

1994

The effect of liquid inundation, vapor shear, and non-condensable gases on the condensation of refrigerants HFC-134a and HCFC-123

Lance Edward Rewerts
Iowa State University

Follow this and additional works at: <https://lib.dr.iastate.edu/rtd>

 Part of the [Mechanical Engineering Commons](#)

Recommended Citation

Rewerts, Lance Edward, "The effect of liquid inundation, vapor shear, and non-condensable gases on the condensation of refrigerants HFC-134a and HCFC-123 " (1994). *Retrospective Theses and Dissertations*. 11311.
<https://lib.dr.iastate.edu/rtd/11311>

This Dissertation is brought to you for free and open access by the Iowa State University Capstones, Theses and Dissertations at Iowa State University Digital Repository. It has been accepted for inclusion in Retrospective Theses and Dissertations by an authorized administrator of Iowa State University Digital Repository. For more information, please contact digirep@iastate.edu.

INFORMATION TO USERS

This manuscript has been reproduced from the microfilm master. UMI films the text directly from the original or copy submitted. Thus, some thesis and dissertation copies are in typewriter face, while others may be from any type of computer printer.

The quality of this reproduction is dependent upon the quality of the copy submitted. Broken or indistinct print, colored or poor quality illustrations and photographs, print bleedthrough, substandard margins, and improper alignment can adversely affect reproduction.

In the unlikely event that the author did not send UMI a complete manuscript and there are missing pages, these will be noted. Also, if unauthorized copyright material had to be removed, a note will indicate the deletion.

Oversize materials (e.g., maps, drawings, charts) are reproduced by sectioning the original, beginning at the upper left-hand corner and continuing from left to right in equal sections with small overlaps. Each original is also photographed in one exposure and is included in reduced form at the back of the book.

Photographs included in the original manuscript have been reproduced xerographically in this copy. Higher quality 6" x 9" black and white photographic prints are available for any photographs or illustrations appearing in this copy for an additional charge. Contact UMI directly to order.

UMI

**A Bell & Howell Information Company
300 North Zeeb Road, Ann Arbor, MI 48106-1346 USA
313/761-4700 800/521-0600**



Order Number 9518434

**The effect of liquid inundation, vapor shear, and non-condensable
gases on the condensation of refrigerants HFC-134a and
HCFC-123**

Rewerts, Lance Edward, Ph.D.

Iowa State University, 1994

U·M·I
300 N. Zeeb Rd.
Ann Arbor, MI 48106



**The effect of liquid inundation, vapor shear, and non-condensable gases on the
condensation of refrigerants HFC-134a and HCFC-123**

by

Lance Edward Rewerts

A Dissertation Submitted to the
Graduate Faculty in Partial Fulfillment of the
Requirements for the Degree of
DOCTOR OF PHILOSOPHY

Department: Mechanical Engineering
Major: Mechanical Engineering

Approved:

Signature was redacted for privacy.

In Charge of Major Work

Signature was redacted for privacy.

For the Major Department

Signature was redacted for privacy.

For the Graduate College

Iowa State University
Ames, Iowa
1994

TABLE OF CONTENTS

ACKNOWLEDGEMENTS	xxi
NOMENCLATURE	xxiii
CHAPTER 1. INTRODUCTION	1
Scope of Research Project	2
Organization of Report	4
CHAPTER 2. LITERATURE REVIEW	5
Introduction	5
Single Tube Condensation	6
Smooth tubes	6
Finned tubes	7
Liquid Inundation	9
Smooth tubes	10
Finned and enhanced tubes	13
Vapor Shear	17
Smooth tubes	17
Finned and enhanced tubes	20
Combined Inundation and Vapor Shear	22
Condensation with Non-condensable Gases	25

CHAPTER 3. EXPERIMENTAL APPARATUS	28
Test Section	30
Tube Bundles	31
Non-condensable gas bundle configuration	35
Liquid inundation and vapor shear bundle configuration	35
Refrigerant Loop	37
Water Loop	39
Glycol Chiller	39
Data Acquisition System	40
CHAPTER 4. EXPERIMENTAL PROCEDURES	43
Water-side Heat Transfer Coefficient	43
Rig Operation	47
Non-condensable gases	49
Liquid inundation with HFC-134a	52
Vapor shear and liquid inundation with HCFC-123	56
Data Reduction	57
Uncertainty of the Shell-side Heat Transfer Coefficients	61
Data Presentation	61
Non-condensable gas results	61
Liquid inundation	62
Combined vapor shear and liquid inundation results	63
CHAPTER 5. THE EFFECT OF NON-CONDENSIBLE GASES ON THE CON-	
DENSATION OF HCFC-123	64
Results of the 26-fpi Geometry	65
Bundle performance	65

Row-by-row performance	67
Results for the 40-fpi Geometry	68
Bundle performance	68
Row-by-row performance	73
Results for the Tu-Cii Geometry	76
Bundle performance	76
Row-by-row performance	77
Results for the G-SC Geometry	82
Bundle performance	82
Row-by-row performance	84
Comparisons Between Test Bundles	85
Summary	90
CHAPTER 6. HFC-134A INUNDATION RESULTS	93
Results for the 26-fpi Geometry	94
Results for the 40-fpi Geometry	100
Results for the Tu-Cii Geometry	105
Results for the G-SC Geometry	109
Comparisons Between Tube Geometries	112
Summary	116
CHAPTER 7. HCFC-123 INUNDATION AND VAPOR SHEAR RESULTS	118
Results for the 26-fpi Geometry	120
Simulated bundle profile	120
Performance as a function of Reynolds number	122
Test bundle row performance	123
Performance as a function of T_{sw}	125

Results for the 40-fpi Geometry	126
Simulated bundle profile	126
Performance as a function of Reynolds number	128
Performance as a function of T_{sw}	129
Test bundle performance	129
Results for the Tu-Cii Geometry	130
Simulated bundle performance	130
Performance as a function of Reynolds number	133
Test bundle performance	134
Performance as a function of T_{sw}	136
Results for the G-SC Geometry	137
Simulated bundle performance	137
Performance as a function of Reynolds number	138
Test bundle performance	139
Performance as a function of T_{sw}	140
Comparisons Between Tube Geometries	142
Summary	145
CHAPTER 8. CONCLUSIONS	147
Summary of HFC-134a Data	147
Summary of HCFC-123 Data	148
Non-condensable gas tests	148
Liquid inundation and vapor shear tests	149
BIBLIOGRAPHY	151
APPENDIX A. DERIVATION OF UNCERTAINTY ANALYSIS EQUATIONS . .	155
APPENDIX B. TABULATED HCFC-123 NON-CONDENSIBLE GAS DATA . .	161

APPENDIX C. TABULATED HFC-134a INUNDATION DATA 178
APPENDIX D. TABULATED HCFC-123 SHEAR AND INUNDATION DATA . . 187

LIST OF TABLES

Table 2.1:	Coefficients and exponents for Equation 2.21 found by Webb (1990) using CFC-11 on five in-line tubes	15
Table 3.1:	Tube geometry specifications	32
Table 3.2:	Tube internal enhancement specifications	33
Table 3.3:	Uncertainties in the measured parameters	41
Table 4.1:	STC for the four tube geometries	47
Table 4.2:	Volumes of N ₂ injected into test section.	50
Table 4.3:	Test section conditions for a 30-row bundle simulation; refrigerant flow rate, water flow rate, water temperature held constant	54
Table 6.1:	Coefficients and exponents for Equation 6.2	115
Table 7.1:	Coefficients and exponents for Equation 7.2	145
Table B.1:	Refrigerant-side data for the 26-fpi geometry with non-condensable gas contamination in HCFC-123 condensation	162
Table B.2:	Water-side data for the 26-fpi geometry with non-condensable gas contamination in HCFC-123 condensation	163
Table B.3:	Row data for the 26-fpi geometry with non-condensable gas contamination in HCFC-123 condensation	164

Table B.4:	Shell-side heat transfer coefficients and uncertainties for the 26-fpi geometry with non-condensable gas contamination in HCFC-123 condensation	165
Table B.5:	Refrigerant-side data for the 40-fpi geometry with non-condensable gas contamination in HCFC-123 condensation	166
Table B.6:	Water-side data for the 40-fpi geometry with non-condensable gas contamination in HCFC-123 condensation	167
Table B.7:	Row data for the 40-fpi geometry with non-condensable gas contamination in HCFC-123 condensation	168
Table B.8:	Shell-side heat transfer coefficients and uncertainties for the 40-fpi geometry with non-condensable gas contamination in HCFC-123 condensation	169
Table B.9:	Refrigerant-side data for the Tu-Cii geometry with non-condensable gas contamination in HCFC-123 condensation	170
Table B.10:	Water-side data for the Tu-Cii geometry with non-condensable gas contamination in HCFC-123 condensation	171
Table B.11:	Row data for the Tu-Cii geometry with non-condensable gas contamination in HCFC-123 condensation	172
Table B.12:	Shell-side heat transfer coefficients and uncertainties for the Tu-Cii geometry with non-condensable gas contamination in HCFC-123 condensation	173
Table B.13:	Refrigerant-side data for the G-SC geometry with non-condensable gas contamination in HCFC-123 condensation	174
Table B.14:	Water-side data for the G-SC geometry with non-condensable gas contamination in HCFC-123 condensation	175

Table B.15:	Row data for the G-SC geometry with non-condensable gas contamination in HCFC-123 condensation	176
Table B.16:	Shell-side heat transfer coefficients and uncertainties for the G-SC geometry with non-condensable gas contamination in HCFC-123 condensation	177
Table C.1:	Refrigerant-side data for the 26-fpi geometry in HFC-134a inundation	179
Table C.2:	Water-side data for the 26-fpi geometry in HFC-134a inundation . .	179
Table C.3:	Row data for the 26-fpi geometry in HFC-134a inundation	180
Table C.4:	Shell-side heat transfer coefficients and uncertainties for the 26-fpi geometry in HFC-134a inundation	180
Table C.5:	Refrigerant-side data for the 40-fpi geometry in HFC-134a inundation	181
Table C.6:	Water-side data for the 40-fpi geometry in HFC-134a inundation . .	181
Table C.7:	Row data for the 40-fpi geometry in HFC-134a inundation	182
Table C.8:	Shell-side heat transfer coefficients and uncertainties for the 40-fpi geometry in HFC-134a inundation	182
Table C.9:	Refrigerant-side data for the Tu-Cii geometry in HFC-134a inundation	183
Table C.10:	Water-side data for the Tu-Cii geometry in HFC-134a inundation . .	183
Table C.11:	Row data for the Tu-Cii geometry in HFC-134a inundation	184
Table C.12:	Shell-side heat transfer coefficients and uncertainties for the Tu-Cii geometry in HFC-134a inundation	184
Table C.13:	Refrigerant-side data for the G-SC geometry in HFC-134a inundation	185
Table C.14:	Water-side data for the G-SC geometry in HFC-134a inundation . . .	185
Table C.15:	Row data for the G-SC geometry in HFC-134a inundation	186
Table C.16:	Shell-side heat transfer coefficients and uncertainties for the G-SC geometry in HFC-134a inundation	186

Table D.1:	Refrigerant-side data for the 26-fpi geometry in HCFC-123 inundation	188
Table D.2:	Water-side data for the 26-fpi geometry in HCFC-123 inundation . . .	188
Table D.3:	Row data for the 26-fpi geometry in HCFC-123 inundation	189
Table D.4:	Shell-side heat transfer coefficients and uncertainties for the 26-fpi geometry in HCFC-123 inundation	189
Table D.5:	Refrigerant-side data for the 40-fpi geometry in HCFC-123 inundation	190
Table D.6:	Water-side data for the 40-fpi geometry in HCFC-123 inundation . .	190
Table D.7:	Row data for the 40-fpi geometry in HCFC-123 inundation	191
Table D.8:	Shell-side heat transfer coefficients and uncertainties for the 40-fpi geometry in HCFC-123 inundation	191
Table D.9:	Refrigerant-side data for the Tu-Cii geometry in HCFC-123 inundation	192
Table D.10:	Water-side data for the Tu-Cii geometry in HCFC-123 inundation . .	192
Table D.11:	Row data for the Tu-Cii geometry in HCFC-123 inundation	193
Table D.12:	Shell-side heat transfer coefficients and uncertainties for the Tu-Cii geometry in HCFC-123 inundation	193
Table D.13:	Refrigerant-side data for the G-SC geometry in HCFC-123 inundation	194
Table D.14:	Water-side data for the G-SC geometry in HCFC-123 inundation . .	194
Table D.15:	Row data for the G-SC geometry in HCFC-123 inundation	195
Table D.16:	Shell-side heat transfer coefficients and uncertainties for the G-SC geometry in HCFC-123 inundation	195

LIST OF FIGURES

Figure 2.1:	Schematic of condensation and condensate flooding of a finned tube (Marto, 1991)	8
Figure 2.2:	Schematic of different condensate flow patterns. (a) Nusselt condensation, (b) staggered bundle flow, (c) turbulent dripping, (d) horizontal vapor flow with shear. (Marto, 1991)	11
Figure 2.3:	Schematic of condensation in the presence of non-condensable gases. Boundary layer temperature and pressure distributions. (Webb and Wanniarachchi (1980))	26
Figure 3.1:	Schematic of experimental test facility	30
Figure 3.2:	Schematic of bundle tube sheet	34
Figure 3.3:	Cross section of test bundle with inundation apparatus	36
Figure 4.1:	Water-side STC data for the 26-fpi and 40-fpi geometries	48
Figure 4.2:	Water-side STC data for the Tu-Cii and G-SC geometries	48
Figure 5.1:	Average shell-side bundle heat transfer coefficient vs. LMTD for the 26-fpi bundle at various nitrogen concentrations during condensation with HCFC-123	66

Figure 5.2: Average shell-side bundle heat transfer coefficient vs. heat flux for the 26-fpi bundle at various nitrogen concentrations in condensation with HCFC-123 66

Figure 5.3: Average shell-side row heat transfer coefficient vs. row number for the 26-fpi bundle at various nitrogen concentrations during condensation with HCFC-123; average bundle heat flux = 20,200 W/m² (6400 Btu/h/ft²) 69

Figure 5.4: Average shell-side row heat transfer coefficient vs. row number for the 26-fpi bundle at various nitrogen concentrations during condensation with HCFC-123; average bundle heat flux = 25,000 W/m² (7920 Btu/h/ft²) 69

Figure 5.5: Average shell-side row heat transfer coefficient vs. row number for the 26-fpi bundle at various nitrogen concentrations during condensation with HCFC-123; average bundle heat flux = 29,300 W/m² (9290 Btu/h/ft²) 70

Figure 5.6: Average shell-side row heat transfer coefficient vs. row number for the 26-fpi bundle at various nitrogen concentrations during condensation with HCFC-123; average bundle heat flux = 33,900 W/m² (10,740 Btu/h/ft²) 70

Figure 5.7: Average shell-side bundle heat transfer coefficient vs. LMTD for the 40-fpi bundle at various nitrogen concentrations during condensation with HCFC-123 71

Figure 5.8: Average shell-side bundle heat transfer coefficient vs. heat flux for the 40-fpi bundle at various nitrogen concentrations in condensation with HCFC-123 71

Figure 5.9: Average shell-side row heat transfer coefficient vs. row number for the 40-fpi bundle at various nitrogen concentrations during condensation with HCFC-123; average bundle heat flux = 20,200 W/m² (6400 Btu/h/ft²) 74

Figure 5.10: Average shell-side row heat transfer coefficient vs. row number for the 40-fpi bundle at various nitrogen concentrations during condensation with HCFC-123; average bundle heat flux = 25,000 W/m² (7920 Btu/h/ft²) 74

Figure 5.11: Average shell-side row heat transfer coefficient vs. row number for the 40-fpi bundle at various nitrogen concentrations during condensation with HCFC-123; average bundle heat flux = 29,300 W/m² (9290 Btu/h/ft²) 75

Figure 5.12: Average shell-side row heat transfer coefficient vs. row number for the 40-fpi bundle at various nitrogen concentrations during condensation with HCFC-123; average bundle heat flux = 33,900 W/m² (10,740 Btu/h/ft²) 75

Figure 5.13: Average shell-side bundle heat transfer coefficient vs. LMTD for the Tu-Cii bundle at various nitrogen concentrations during condensation with HCFC-123 78

Figure 5.14: Average shell-side bundle heat transfer coefficient vs. heat flux for the Tu-Cii bundle at various nitrogen concentrations during condensation with HCFC-123 78

Figure 5.15: Average shell-side row heat transfer coefficient vs. row number for the Tu-Cii bundle at various nitrogen concentrations during condensation with HCFC-123; average bundle heat flux = 20,200 W/m² (6400 Btu/h/ft²) 80

Figure 5.16: Average shell-side row heat transfer coefficient vs. row number for the Tu-Cii bundle at various nitrogen concentrations during condensation with HCFC-123; average bundle heat flux = 25,000 W/m² (7920 Btu/h/ft²) 80

Figure 5.17: Average shell-side row heat transfer coefficient vs. row number for the Tu-Cii bundle at various nitrogen concentrations during condensation with HCFC-123; average bundle heat flux = 29,300 W/m² (9290 Btu/h/ft²) 81

Figure 5.18: Average shell-side row heat transfer coefficient vs. row number for the Tu-Cii bundle at various nitrogen concentrations during condensation with HCFC-123; average bundle heat flux = 33,900 W/m² (10 740 Btu/h/ft²) 81

Figure 5.19: Average shell-side bundle heat transfer coefficient vs. LMTD for the G-SC bundle at various nitrogen concentrations during condensation with HCFC-123 83

Figure 5.20: Average shell-side bundle heat transfer coefficient vs. heat flux for the G-SC bundle at various nitrogen concentrations during condensation with HCFC-123 83

Figure 5.21: Average shell-side row heat transfer coefficient vs. row number for the G-SC bundle at various nitrogen concentrations during condensation with HCFC-123; average bundle heat flux = 20,200 W/m² (6400 Btu/h/ft²) 86

Figure 5.22: Average shell-side row heat transfer coefficient vs. row number for the G-SC bundle at various nitrogen concentrations during condensation with HCFC-123; average bundle heat flux = 25,000 W/m² (7920 Btu/h/ft²) 86

Figure 5.23: Average shell-side row heat transfer coefficient vs. row number for the G-SC bundle at various nitrogen concentrations during condensation with HCFC-123; average bundle heat flux = 29,300 W/m² (9290 Btu/h/ft²) 87

Figure 5.24: Average shell-side row heat transfer coefficient vs. row number for the G-SC bundle at various nitrogen concentrations during condensation with HCFC-123; average bundle heat flux = 33,900 W/m² (10 740 Btu/h/ft²) 87

Figure 5.25: Average shell-side bundle heat transfer coefficient vs. heat flux for the four test bundles at various nitrogen concentrations during condensation with HCFC-123 89

Figure 5.26: Average shell-side bundle heat transfer coefficient vs. LMTD for the four test bundles at various nitrogen concentrations during condensation with HCFC-123 89

Figure 5.27:	Average shell-side row heat transfer coefficient vs. row number for the four test bundles at various nitrogen concentrations during condensation with HCFC-123; average bundle heat flux = 20,200 W/m ² (6400 Btu/h/ft ²)	91
Figure 5.28:	Average shell-side row heat transfer coefficient vs. row number for the four test bundles at various nitrogen concentrations during condensation with HCFC-123; average bundle heat flux = 33,900 W/m ² (10,740 Btu/h/ft ²)	91
Figure 6.1:	26-fpi tube, average shell-side heat transfer coefficient vs. condensate Reynolds number number with HFC-134a	96
Figure 6.2:	26-fpi tube, average shell-side heat transfer coefficient vs. condensate Reynolds number number on row 4 only	96
Figure 6.3:	26-fpi tube, average shell-side heat transfer coefficient vs. condensation temperature difference with HFC-134a	97
Figure 6.4:	26-fpi tube, average shell-side row heat transfer coefficient vs. row number for 15-row simulation with HFC-134a	99
Figure 6.5:	26-fpi tube, average shell-side row heat transfer coefficient vs. row number for 30-row simulation with HFC-134a	99
Figure 6.6:	26-fpi tube, average shell-side row heat transfer coefficient vs. row number for 5-row test bundle with HFC-134a	100
Figure 6.7:	40-fpi tube, average shell-side heat transfer coefficient vs. condensate Reynolds number number with HFC-134a	101
Figure 6.8:	40-fpi tube, average shell-side heat transfer coefficient vs. condensate Reynolds number number with HFC-134, two correlations . . .	101

Figure 6.9: 40-fpi tube, average shell-side row heat transfer coefficient vs. row number, 30-row simulation with HFC-134a 103

Figure 6.10: 40-fpi tube, average shell-side row heat transfer coefficient vs. row number, 5-row test bundle with HFC-134a 103

Figure 6.11: 40-fpi tube, average shell-side heat transfer coefficient vs. condensation temperature difference with HFC-134a 104

Figure 6.12: Tu-Cii tube, average shell-side heat transfer coefficient vs. condensate Reynolds number number with HFC-134a 106

Figure 6.13: Tu-Cii, average shell-side heat transfer coefficient vs. condensation temperature difference with HFC-134a 107

Figure 6.14: Tu-Cii tube, average shell-side row heat transfer coefficient vs. row number for 30-row simulation with HFC-134a 108

Figure 6.15: Tu-Cii tube, average shell-side row heat transfer coefficient vs. row number for 15-row simulation with HFC-134a 108

Figure 6.16: G-SC tube, average shell-side heat transfer coefficient vs. condensate Reynolds number number with HFC-134a 110

Figure 6.17: G-SC, average shell-side heat transfer coefficient vs. condensation temperature difference with HFC-134a 110

Figure 6.18: G-SC tube, average shell-side row heat transfer coefficient vs. row number for 30-row simulation with HFC-134a 111

Figure 6.19: G-SC tube, average shell-side row heat transfer coefficient vs. row number for 5-row test bundle in a 30-row simulation with HFC-134a 111

Figure 6.20: Average shell-side heat transfer coefficient vs. Re_L comparison of all tube geometries 113

Figure 6.21: Average shell-side heat transfer coefficient vs. condensation temperature difference comparison of all tube geometries 113

Figure 7.1: 26-fpi tube, average shell-side row heat transfer coefficient vs. row number for three different vapor velocities with HCFC-123 121

Figure 7.2: 26-fpi tube, average shell-side heat transfer coefficient vs. condensate Reynolds number for all data with HCFC-123 122

Figure 7.3: 26-fpi tube, average shell-side row heat transfer coefficient vs. row number for the 5-row test bundle using HCFC-123, $U_{\infty} = 2.6$ m/s (8.5 ft/s) 124

Figure 7.4: 26-fpi tube, average shell-side row heat transfer coefficient vs. row number for the 5-row test bundle using HCFC-123, $U_{\infty} = 4.3$ m/s (14.1 ft/s) 124

Figure 7.5: 26-fpi tube, average shell-side heat transfer coefficient vs. condensation temperature difference at three vapor velocities using HCFC-123 125

Figure 7.6: 40-fpi tube, average shell-side row heat transfer coefficient vs. row number for three different vapor velocities with HCFC-123 127

Figure 7.7: 40-fpi tube, average shell-side heat transfer coefficient vs. condensate Reynolds number for all data with HCFC-123 128

Figure 7.8: 40-fpi tube, average shell-side heat transfer coefficient vs. condensation temperature difference at three vapor velocities using HCFC-123 130

Figure 7.9: 40fpi tube, average shell-side row heat transfer coefficient vs. row number for the 5-row test bundle using HCFC-123, $U_{\infty} = 2.5$ m/s (8.2 ft/s) 131

Figure 7.10: 40-fpi tube, average shell-side row heat transfer coefficient vs. row number for the 5-row test bundle using HCFC-123, $U_{\infty} = 4.5$ m/s (14.8 ft/s) 131

Figure 7.11: Tu-Cii tube, average shell-side row heat transfer coefficient vs. row number for three different vapor velocities with HCFC-123 132

Figure 7.12: Tu-Cii tube, average shell-side heat transfer coefficient vs. condensate Reynolds number for all data with HCFC-123 133

Figure 7.13: Tu-Cii tube, average shell-side row heat transfer coefficient vs. row number for the 5-row test bundle using HCFC-123, $U_{\infty} = 2.5$ m/s (8.2 ft/s) 135

Figure 7.14: Tu-Cii tube, average shell-side row heat transfer coefficient vs. row number for the 5-row test bundle using HCFC-123, $U_{\infty} = 4.5$ m/s (14.8 ft/s) 135

Figure 7.15: Tu-Cii tube, average shell-side heat transfer coefficient vs. condensation temperature difference at three vapor velocities using HCFC-123 136

Figure 7.16: G-SC tube, average shell-side row heat transfer coefficient vs. row number for three different vapor velocities with HCFC-123 138

Figure 7.17: G-SC tube, average shell-side heat transfer coefficient vs. condensate Reynolds number for all data with HCFC-123 139

Figure 7.18: G-SC tube, average shell-side row heat transfer coefficient vs. row number for the 5-row test bundle using HCFC-123, $U_{\infty} = 2.5$ m/s (8.2 ft/s) 141

Figure 7.19: G-SC tube, average shell-side row heat transfer coefficient vs. row number for the 5-row test bundle using HCFC-123, $U_{\infty} = 4.6$ m/s (15.1 ft/s) 141

Figure 7.20: G-SC tube, average shell-side heat transfer coefficient vs. condensation temperature difference at three vapor velocities using HCFC-123 142

Figure 7.21: Average shell-side heat transfer coefficient vs. condensate Reynolds number comparison of all tubes 144

Figure 7.22: Average shell-side heat transfer coefficient vs. condensation temperature difference comparison of all 30-row simulations 144

ACKNOWLEDGEMENTS

There are many people who deserve recognition for their contributions to this project. First and foremost, I would like to thank ASHRAE for funding this work, the members of ASHRAE TC 8.5, and the members of the Project Monitoring Subcommittee, comprised of Keith Starner, Satish Oza, Fred Scheideman, and Petur Thors, for all their technical support and patience over the course of this study. Thanks also to Dr. Michael Pate for serving as my major professor, and Drs. Howard Shapiro, Greg Maxwell, Richard Seagrave, and Bruce Munson for serving on my Program of Study Committee.

Another person I need to recognize is Joe Huber, a man whose contributions to this project were invaluable. It was he who designed and built the original rig which eventually became our test facility, and it was he who helped teach me the ropes of experimental heat transfer. Many, many thanks to him for his help both in and out of the lab. In addition, I wish to recognize the other members of the Heat Transfer Lab who also provided considerable help and support: Bob Bittle, Shane Moeykens, Duane Wolf, and Wade Huebsch.

I must also give my thanks to Master Pak, my ISU martial arts family, and especially the ISU Hapkido Club. Special and heart-felt thanks to Craig, Gus, Pat (Mr. Air), Amanda, Lily, Jen, and Robin, for actually keeping me sane and on track. It was you who listened to me and reasoned with me when all I wanted to do was quit, beat me when I needed it, and let me beat you when I was in danger of exploding. I know I couldn't have made it without you. Thanks for letting me play. Additional thanks to my favorite trainers, Jay and Mary, for turning the big knots into little knots.

And of course a very special thank you to my parents, George and Judy, without whom any of this would have been possible. You've been supportive, helpful, curious, concerned, and most important, always there when I needed you. I can't begin to tell you how much I appreciate everything you've done for me, but I hope to spend the rest of my life trying. Thank you also to Bruce and Jay, my brothers and my friends, and my extended family in Davenport, the Taylors. Thanks especially to Anne: even though you haven't been in Ames for a while, I've always known you were with me in heart and spirit.

NOMENCLATURE

Symbols

A	area
C_p	specific heat
D	diameter
D_{eq}	equivalent diameter for finned tubes
g	acceleration of gravity
h_o	average shell-side heat transfer coefficient
i	enthalpy
i_{fg}	enthalpy of vaporization
i'_{fg}	modified enthalpy of vaporization
k	thermal conductivity
L	tube length
\bar{L}	effective length of fin side, given by Equation 2.6
LMTD	log-mean temperature difference
m	inundation exponent
\dot{m}	mass flow rate
N	row number
n	exponent for Webb-Murawski correlation
p	pressure

p_f	fin pitch
p_{gb}	refrigerant partial pressure in bulk mixture
p_{gi}	refrigerant partial pressure at condensate interface
p_l	longitudinal pitch
p_t	transverse pitch
q	heat transfer rate
q'	heat transfer rate per unit tube length
q''	heat transfer rate per unit surface area (heat flux)
T	temperature
T_{sw}	$T_{sat} - T_{s,o}$
U	Velocity
V	test section volume
v	specific volume
w	width defined by Equation 4.26
x	mixture quality

Greek symbols

η	efficiency
Γ	flow rate of falling condensate per unit tube length
μ	viscosity
ϕ_f	flooding angle
ρ	density
σ	surface tension
ω	experimental uncertainty

Subscripts

<i>act</i>	actual
<i>atm</i>	atmospheric
<i>c</i>	coolant
<i>B</i>	bundle
<i>D</i>	based on diameter
<i>ef</i>	effective
<i>f</i>	liquid phase
<i>fl</i>	flooded region
<i>fn</i>	finned region
<i>fs</i>	fin sides
<i>ft</i>	fin tips
<i>g</i>	vapor phase
<i>H</i>	based on hydraulic diameter
<i>L</i>	per unit length
<i>N</i>	row number
<i>o</i>	outer
<i>R</i>	row
<i>r</i>	fin root, or refrigerant
<i>s</i>	tube surface
<i>sat</i>	saturation
<i>sh</i>	shear
<i>ts</i>	test section
<i>tot</i>	total
<i>tw</i>	tube wall

<i>uf</i>	unfinned region
<i>w</i>	water
1	row 1

Dimensionless groups

Nu	Nusselt number, $(hD)/k$
P^*	forced convection parameter defined by Equation 2.30
Ph	Phase change number, $C_p\Delta T/i_{fg}$
Pr	Prandtl number, $(\mu C_p)/k$
Re	Reynolds number, $4\dot{m}/(D\mu)$
$\tilde{\text{Re}}$	two-phase Reynolds number, $(U_\infty\rho_f D)/\mu_f$
X_{tt}	Lockhart-Martinelli parameter, defined by Equation 2.37

CHAPTER 1. INTRODUCTION

In the past decade, numerous studies have shown that the ozone layer, a protective layer of gas surrounding the earth high in the atmosphere, has become increasingly thin in places. These ozone "holes" allow dangerous ultraviolet radiation to pass through the atmosphere, where it can have potentially hazardous effects on the environment below. As evidence has grown that these "holes" exist and are in fact growing, evidence has also pointed to chloroflourcarbon (CFC) emissions as a major contributor to their formation. As a result, a global coalition of government and industry has mandated that all CFC-based refrigerants be phased out by 1996, and all new refrigeration equipment be produced with an ozone-safe replacement.

This study was conducted to test the replacements for two of the most commonly used CFC refrigerants, namely CFC-11 and CFC-12. CFC-11 is a low pressure refrigerant (has a saturation pressure at atmospheric temperatures near atmospheric pressure) commonly used in large industrial chillers and as a secondary heat transfer fluid in other processes. CFC-12 is a high pressure refrigerant (has a saturation temperature at atmospheric temperatures of approximately 75 psia (517 kPa)) used extensively in residential and automobile air-conditioners and household refrigerators and freezers. These two refrigerants have been popular because they are in-expensive to produce, non-toxic, and compatible with many elastomers and plastics commonly used in refrigeration equipment.

The choice replacement of CFC-12 is the hydroflouorcarbon (HFC) refrigerant HFC-134a. Both refrigerants behave very similiary thermodynamically, and HFC-134a is non-

toxic, has no ozone depletion potential, and is compatible with many of the commonly used elastomers. In several areas the transition from CFC-12 has already been made, and many types of HFC-134a based air-conditioning and refrigeration equipment are currently in use.

The hydrochloroflourocarbon (HCFC) refrigerant HCFC-123 is the most likely replacement for CFC-11, despite the fact that it has a small but non-zero ozone depletion potential, is not compatible with many common elastomers, and has relatively low allowable exposure limits (30 ppm) compared to other refrigerants (400 ppm for HFC-134a). However, since it is one of only a few chemicals that is thermodynamically similar to CFC-11, great effort has been made to see that most of the compatibility and toxicity problems have been addressed, and HCFC-123 based equipment is now commercially available.

This study was sponsored by the American Society of Heating, Refrigerating, and Air-Conditioning Engineers (ASHRAE) Technical Committee TC 8.5 (Liquid-to-Refrigerant Heat Exchangers) to collect several different types of experimental condensation data of both HFC-134a and HCFC-123 on several commonly used condensation tubes. The data was intended for design engineers who will be designing condensers specifically for use with these new refrigerants. The exact scope of the project is discussed below.

Scope of Research Project

This study was done to collect data on several aspects of the shell-side condensation phenomenon. Specifically, the project was concerned with finding the effect of non-condensable gases on both bundle and row heat transfer performance, determining the effect of liquid inundation, and finding the effect of vapor shear in the presence of high velocity vapor. The data presented in this report is part of the larger ASHRAE research project 676-RP "Experimental determination of shell-side condenser bundle heat transfer design factors for refrigerants R-123 and R-134a".

Shell-side condensation heat transfer data were obtained for the new refrigerants HFC-134a and HCFC-123. Four tube bundles were used to take the data. The four geometries chosen for this study, the 26-fpi, 40-fpi, Turbo C-II, and GEWA SC tubes, have a nominal outer diameter of 19.1 mm (0.75 in) and are all commonly used condensation tubes. The test bundles are 5 rows wide by 5 rows deep and have a triangular tube arrangement with a horizontal pitch of 22.2 mm (0.875 in) and a vertical pitch of 19.1 mm (0.75 in).

Tests were run to determine the effect of small concentrations of non-condensable gases, which have a detrimental effect on the condensation of pure refrigerants, in the condenser. Experiments were conducted using all four bundles and HCFC-123 as the working fluid. HCFC-123 was used because it has an operating saturation pressure below atmospheric pressure and is therefore more susceptible to contamination by outside air. The experiments were conducted at four different heat fluxes ranging between 20,000 and 34,00 W/m^2 (6340 to 10,780 Btu/h/ft^2) with four different non-condensable gas (nitrogen) concentrations of 0.5%, 1.0%, 2.0%, and 5.0%, for a total of sixteen data runs per bundle.

Liquid inundation refers to the effect in the lower rows of an horizontal condenser as condensate from the top of the bundle drains to the bottom. The condensate covers the tube surface and forms a layer which insulates the tube from the vapor and prevents condensation, thus lowering the tubes heat transfer performance.

Tests were conducted to determine the effect of HFC-134a inundation on each of the tube geometries up to a simulated row depth of 30 tubes. Inundation was simulated by producing mixed flows of refrigerant (i.e. liquid and vapor) and condensing the vapor portion while inundating the tubes with the liquid portion. Heat transfer performance was measured as a function of the simulated tube depth as well as the condensate film Reynolds number. Heat fluxes were similar to those used in the non-condensable gas heat flux tests, and Reynolds numbers up to 2900 were produced.

Vapor shear is the effect of high velocity vapor thinning and/or stripping the condensate layer away from the tube, thereby opening up the tube's surface and increasing the heat transfer performance of the tube. This effect tends to work against the effects of inundation, which acts to depress the heat transfer performance.

Vapor shear is only found in the presence of significant vapor velocities. Because of the property differences between HCFC-123 and HFC-134a, only HCFC-123 is capable of producing those kinds of velocities in a normal operating condenser. Therefore, only HCFC-123 was used to conduct shear tests on the four tube geometries. Additionally, inundation tests similar to those using HFC-134a were conducted to determine the combined effects of both liquid inundation and vapor shear.

Experiments were performed to simulate a condenser up to 25 rows deep at three different vapor velocities ranging from 2.5 m/s (8.2 ft/s) to 4.6 m/s (14.8 ft/s). Again, heat fluxes in line with the earlier tests were used, with Reynolds numbers up to 1200 being produced.

Organization of Report

Chapter 2 presents an overview of theoretical and experimental techniques used to analyze shell-side condensation, with particular emphasis on the phenomena of liquid inundation, vapor shear, and non-condensable gas contamination. Chapter 3 describes the test facility used to obtain the experimental heat transfer data presented in this study. Chapter 4 explains the experimental procedures used to obtain the heat transfer data and the data reduction techniques used to calculate the shell-side heat transfer coefficients. Chapter 5 contains the results of the tests with non-condensable gases in HCFC-123. Chapters 6 and 7 present the results of the HFC-134a inundation tests and the HCFC-123 inundation and vapor shear tests, respectively. Chapter 8 gives a summary of the results of the present study.

CHAPTER 2. LITERATURE REVIEW

Introduction

Heat transfer in the refrigeration industry is often accomplished through the process of condensation, where a vapor is cooled below its saturation temperature to form a liquid. Condensation occurs in many different forms. Liquid droplets can form within the vapor, either as a collection of vapor particles, called homogeneous condensation, or by vapor particles attaching themselves to other particles entrained within the vapor, called heterogeneous condensation. Vapor can also condense by coming into direct contact with a cooler liquid. In surface condensation, where condensation occurs as a result of vapor coming into contact with a cold surface, the liquid can take the form of droplets which dot the cold surface, or a film, which wets and covers the surface. Since drop-wise condensation is difficult to maintain, most surface condensation occurs in the film mode.

This study focused on surface condensation of refrigerant vapor on the outer surface of horizontal rows of cooled copper tubes with enhanced enhanced surface geometries. Specifically, the objective was to determine the heat transfer performance of several different tube geometries and the effects on heat transfer performance of liquid draining from the top rows of tubes on to the lower rows (liquid inundation), vapor moving at high velocity past condensation tubes (vapor shear), and non-condensable gases trapped in the vapor.

This chapter will discuss the theoretical and experimental background of film condensation on both smooth and enhanced horizontal tubes. First, a review of the most well known

approaches to single tube condensation will be given. That will be followed by a more detailed discussion of the theoretical and experimental work involving liquid inundation, vapor shear, and non-condensable gases.

Single Tube Condensation

Smooth tubes

Nusselt (1916) was the first to attempted to model the problem of condensation on a smooth, horizontal tube in stationary vapor, performing a differential analysis on the condensate film. Assuming that both liquid and vapor were saturated, the tube surface was isothermal, and the liquid flow was laminar and controlled only by viscous and gravitational forces, Nusselt was able to derive an average heat transfer coefficient over the surface of the tube. This is given by

$$h_o = 0.725 \left[\frac{\rho_f(\rho_f - \rho_g)g i_{fg} k_f^3}{D \mu_f (T_{sat} - T_w)} \right]^{\frac{1}{4}}. \quad (2.1)$$

Rose (1988) notes that the leading coefficient in Equation 2.1 should be changed to 0.728, due to small errors in Nusselt's original calculations.

By assuming that both the liquid and vapor were saturated, heat transfer was restricted to the phase change process of the vapor and no heat transfer was accounted for through subcooling of the liquid. Nusselt tried to account for subcooling by adding a correction to the heat of vaporization,

$$i'_{fg} = i_{fg} + \frac{3}{8} C_{p,f} (T_{sat} - T_{s,o}), \quad (2.2)$$

where the second term in the equation is a result of assuming a linear temperature profile through the liquid layer.

Rosenhow et al. (1956) further proposed that for $Pr > 0.5$ and $C_{p,f}(T_{sat} - T_{s,o})/i'_{fg} <$

1.0, the leading coefficient 0.375 in Equation 2.2 be changed to 0.68 to more closely match experimental data.

Finned tubes

Fins are added to smooth tubes in an effort increase surface area and, hopefully, increase the tubes' overall heat transfer performance. However, the increase in finned-tube performance over smooth tube performance is not proportional to the increase in surface area. Fins also complicate the condensation process by creating spaces in which liquid, known also as condensate, can get trapped.

As the vapor condenses on the tube and fin surfaces, the liquid fills the spaces between the fins along the tube surface. Fin size, fin spacing, liquid surface tension, and liquid viscosity are all factors in determining how much liquid is retained and how much of the inter-fin spaces is filled. When the entire fin space is filled with condensate, the fins are considered flooded. This generally occurs in the lower part of the tube, where gravity has pulled the liquid from the top of the tube and surface tension has held the liquid in the fin spaces. A representation of a finned tube in condensation is shown in Figure 2.1.

Heat transfer in finned tubes is affected by the thickness of the liquid layer being held in the fin spaces. In the top portion of the tube where gravity works to drain the liquid and surface tension acts to thin the liquid layer, heat transfer is generally highest. In the lower portion of the tube, however, where the layer is typically thicker and less of the tube and fin surfaces are exposed to vapor, the heat transfer performance decreases.

Beatty and Katz (1948) were the first to attempt to model the heat transfer performance of a finned tube. By assuming a gravity-driven flow where the fins were treated as vertical plates with negligible tip area and the spaces between the fins as horizontal tubes, they derived an expression for the average heat transfer coefficient composed of the heat transfer coefficients

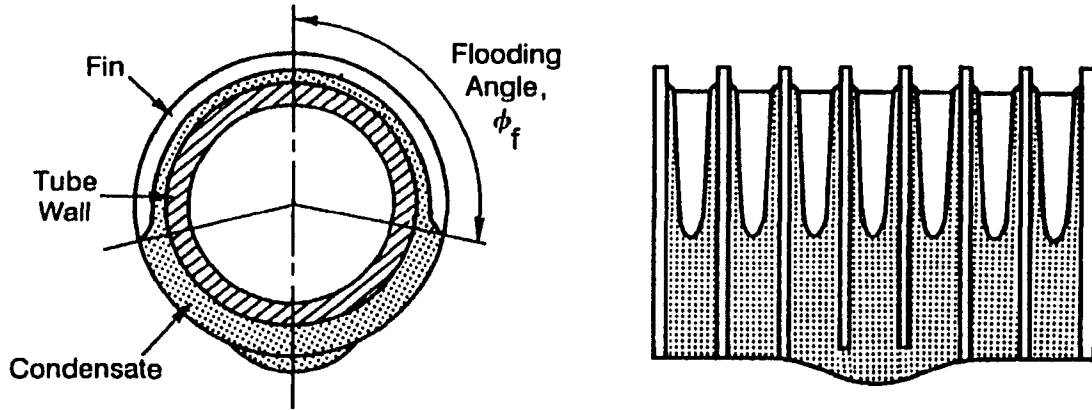


Figure 2.1: Schematic of condensation and condensate flooding of a finned tube (Marto, 1991)

of both the finned and tube areas, given by

$$h_o = \eta_{fn} h_{fn} \frac{A_{fn}}{A_{ef}} + h_{uf} \frac{A_{uf}}{A_{ef}} \quad (2.3)$$

The first term in this expression is related to the fin heat transfer, the second term is related to the tube surface heat transfer, and the factor A_{ef} is an effective total surface area of the whole tube. Using the Nusselt theories for vertical plate and horizontal tube condensation, they developed the following average heat transfer coefficient expression

$$h_o = 0.689 \left[\frac{\rho_f^2 g_i f_g k_f^3}{\mu_f (T_{sat} - T_{s,o}) Deq} \right]^{1/4} \quad (2.4)$$

where

$$\left[\frac{1}{Deq} \right]^{1/4} = 1.30 \eta_{fn} \frac{A_{fn}}{A_{ef}} \frac{1}{\bar{L}^{1/4}} + \frac{A_{uf}}{A_{ef}} \frac{1}{D_r^{1/4}} \quad (2.5)$$

$$\bar{L} = \frac{\pi(D_o^2 - D_r^2)}{4D_o} \quad (2.6)$$

$$A_{ef} = \eta_{fn} A_{fn} + A_{uf} \quad (2.7)$$

The leading coefficient 0.689 was determined by correlating the model with data taken with HCFC-22, propane, *n*-butane, *n*-pentane, and several other low surface tension fluids on 276

and 630 fin per meter (fpm) (7 and 16 fin per inch (fpi)) tubes. Using this expression, the data could be correlated to within 10% for all fluids.

A modification of the Beatty and Katz (1948) model for equivalent diameter was proposed by Smirnov and Lukanov (1972) to account for contributions from the fin tips. This is given by

$$\left[\frac{1}{Deq} \right]^{1/4} = 1.30\eta f_n \frac{A_{fs}}{A_{ef}} \frac{1}{\bar{L}^{1/4}} + \frac{A_{ft}}{A_{ef}} \frac{1}{D_o^{1/4}} + \frac{A_{uf}}{A_{ef}} \frac{1}{D_r^{1/4}} \quad (2.8)$$

$$\bar{L} = \frac{\pi(D_o^2 - D_r^2)}{4D_o} \quad (2.9)$$

$$A_{ef} = \eta A_{fs} + \eta A_{ft} + A_{uf} \quad (2.10)$$

Marto (1988) has noted that the validity of the Beatty and Katz (1948) model is extended by the fact that the model ignores the effects of surface tension, in that surface tension effects on different areas of a finned tube (thinning of the condensate layer on the top of the tube increasing heat transfer and flooding of the fins in the lower part of the tube decreasing heat transfer) tend to cancel each other out. For this reason, the Beatty and Katz model has been used successfully in the refrigeration industry for many years.

Liquid Inundation

Liquid inundation or liquid loading refers to the liquid layer which develops in the lower rows of a multi-row condenser as a result of condensate drainage from the upper rows of the condenser. As vapor is condensed in the top rows of the condenser bundle, the resulting condensate flows around each of the tubes and drips from the tube bottoms on to the rows below. This liquid forms a film, creating an insulating liquid layer on the lower tube rows that reduces the effective area of the tube surface exposed to the vapor, which in turn reduces the tubes' total heat transfer and decreases the tubes' shell-side heat transfer coefficients. For this reason, condenser performance cannot be accurately predicted using single tube models.

Smooth tubes

The first to try to quantify the effect of inundation on a smooth, horizontal tube was Nusselt (1916), who extended his classic model for the average heat transfer on a single horizontal smooth tube, defined by equation 2.1.

To account for inundation in the lower rows of tubes, Nusselt assumed that the condensate would be pulled in a continuous laminar sheet by gravity forces (i.e. no vapor shearing effects) so that all of the condensate from a tube would fall directly onto the tube below it, as seen in Figure 2.2(a). Nusselt also assumed that the wall temperature (thus ΔT_{sw}), would be constant. Under these assumptions the Nusselt single tube equation (Equation 2.1) remains valid and can be used to find the average heat transfer over a bundle of N tube rows, such that

$$\bar{h}_N = \left[\frac{\rho_f(\rho_f - \rho_g)g_i f_g k_f^3}{ND\mu_f(T_{sat} - T_w)} \right]^{\frac{1}{4}}. \quad (2.11)$$

The relationship between average bundle performance and single tube performance can be found by dividing Equation 2.11 by Equation 2.1. This leads to the expression

$$\frac{\bar{h}_N}{h_1} = N^{-m}, \quad (2.12)$$

where \bar{h}_N is the average over N tubes, h_1 is the average of the first tube, and m is the row effect exponent, equal to $\frac{1}{4}$.

By manipulating this expression algebraically, the heat transfer coefficient for any tube N can also be found. The modified form of the equation is

$$\frac{h_N}{h_1} = N^{1-m} - (N-1)^{1-m}. \quad (2.13)$$

Substituting the row effect exponent derived by Nusselt, this is

$$\frac{h_N}{h_1} = N^{\frac{3}{4}} - (N-1)^{\frac{3}{4}}. \quad (2.14)$$

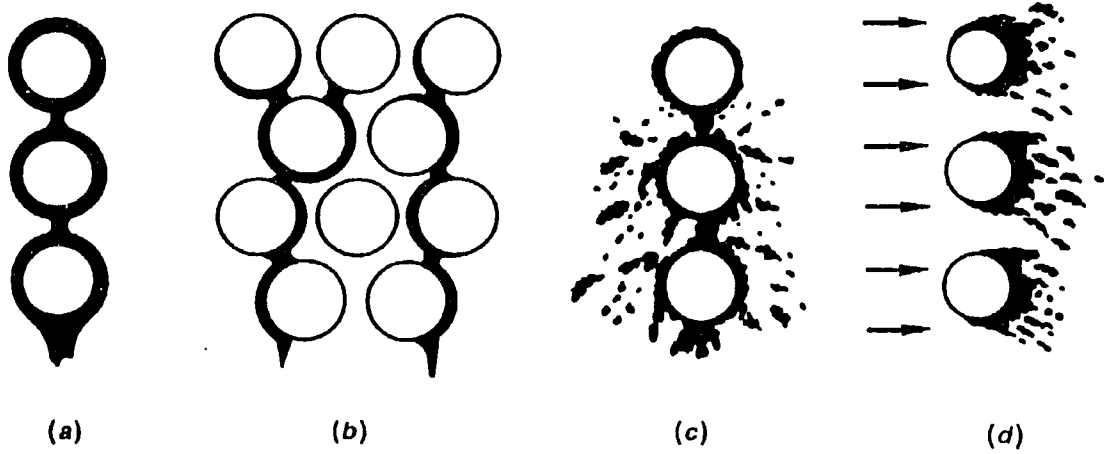


Figure 2.2: Schematic of different condensate flow patterns. (a) Nusselt condensation, (b) staggered bundle flow, (c) turbulent dripping, (d) horizontal vapor flow with shear. (Marto, 1991)

Short and Brown (1951) were the first to experimentally establish the inundation effect on smooth tubes in a quiescent vapor. Condensing CFC-11 and water on a vertical bank of twenty tubes, their data showed that Nusselt's analysis greatly overestimated the effect of inundation in actual tube banks. In large part this was because the condensate tends to fall as discrete droplets and not as a continuous laminar sheet, as Nusselt originally assumed. Based on their data, Short and Brown proposed

$$\frac{\bar{h}_N}{h_1} = 1.24N^{-\frac{1}{4}}. \quad (2.15)$$

In addition, they showed that an alternate form of the Nusselt single tube heat transfer equation, written in terms of the condensate flow rate per length of tube, Γ , can also be applied to any given tube in the bundle. This equation,

$$\frac{h_N}{k_f} \left[\frac{\mu_f^2}{\rho_f(\rho_f - \rho_g)g} \right]^{\frac{1}{3}} = 1.51 \left(\frac{4\Gamma N}{\mu_f} \right)^{-\frac{1}{3}}, \quad (2.16)$$

is true so long as Γ_N is defined as the condensate flowrate from the tube N . The fraction $4\Gamma_N/\mu_f$ is important, as it is defined as the condensate Reynolds number for the flow from a given tube N .

Butterworth (1982) shows how to derive Equation 2.15 for $N \geq 10$ by integrating Equation 2.16. For less than ten rows it was suggested that Equation 2.16 be solved numerically in a step-wise fashion down the bundle.

Kern (1958) improved on Nusselt's work by taking the actual flow patterns of the draining condensate into consideration. Based on his experience, assuming that the liquid falls onto the lower banks of tubes in discrete droplets or columns, and assuming that the falling liquid caused ripples in the film on the lower tubes, Kern proposed a less conservative model. Following the form of Equation 2.12, the model is given by

$$\frac{\bar{h}_N}{h_1} = N^{-\frac{1}{6}}. \quad (2.17)$$

Kern's model was found to closely approximate the Short and Brown (1951) data, and is recommended as the current commercial design standard (Butterworth, 1977). Because experimental data has shown significant deviation from the Nusselt equation at high values of Γ_N/μ_f where the flow transitions to turbulent flow, Webb (1984b) has recommended that Equation 2.17 and Equation 2.15 should only be used for $Re_L < 200$, noting that the resulting predictions should be conservative.

An improvement to the Nusselt model was also offered by Chen (1961), who considered the possibility of additional condensation on the liquid between tubes. Splashing and ripples in the liquid film were ignored due to unpredictability. Assuming all the subcooling was removed in the additional condensation process, Chen arrived at the expression

$$\frac{\bar{h}_N}{h_1} = (1 + 2Ph(N - 1))N^{-\frac{1}{4}} \quad (2.18)$$

where Ph is the phase change number (also known as the Jakob number). Given by

$$Ph = \frac{C_{p,c}\Delta T_c}{i f g}, \quad (2.19)$$

it is defined as the ratio of the heat capacity of the coolant passing through a given tube ($C_p(T_{c,out} - T_{c,in})$) to the latent heat of vaporization of the refrigerant.

As can be seen, this is the original Nusselt equation multiplied by a factor involving the additional condensation. Equation 2.18 provides a good approximation for inundation as long as $Ph < 2.0$ (Roshenow, Hartnett, Ganić, 1985).

None of the work described above, however, was applicable to tubes in anything other than an in-line configuration. In 1972, Eissenberg, working with steam, proposed a model based on the assumption that in a triangular pitch bundle, the condensate does not all drop straight down between tubes. Rather, because of local vapor flow between tubes, the liquid would be diverted laterally and strike the tubes below and on either side of the draining tube, as shown in Figure 2.2(b). As a result, this liquid would strike subsequent tubes on their side rather than their tops, thus minimizing the liquid layer on the top of the tubes, which in turn results in a smaller effect on heat transfer performance. This model is defined by

$$\frac{\bar{h}N}{h_1} = 0.60 + 0.42N^{-\frac{1}{4}}. \quad (2.20)$$

This approach gave reasonable results for steam, although no data indicating its applicability to low surface tension fluids such as refrigerants could be found.

Finned and enhanced tubes

Finned tubes were introduced in the late 1940s for use in shell-and-tube heat exchangers. Although they were not specifically designed for condensation, they were quickly adopted for that use because their larger surface area provided greater heat transfer performance than the plain tubes used at the time. However, very little work was done to determine the effect of liquid inundation.

Following on the finned tube analysis of Beatty and Katz (1948), Katz and Geist (1948) were the first to investigate any possible liquid loading effects. Condensing CFC-11 vapor on six in-line, 12-fpi tubes, they determined an experimental value of $m = 0.04$ for the row effect exponent in Equation 2.12, where the first row heat transfer coefficient was defined by the Beatty and Katz (1948) correlation, Equation 2.4. This smaller coefficient indicated a much smaller inundation effect for finned tubes than for smooth tubes.

Smirnov and Lukanov (1972) studied the effect of inundation by condensing CFC-11 on 20 rows of trapezoidally finned tubes in a staggered arrangement and measuring the local heat transfer coefficient for each row. Interestingly, their data showed that the row-by-row heat transfer coefficients dropped even faster in the first five rows than those predicted by Nusselt (Equation 2.13), and then levelled off sharply, even increasing slightly towards the bottom of the bundle. This data differed from the data taken previously. Fujii and Uehara (1973) suggested that this was probably due to the presence of non-condensable gases in the condenser.

Webb (1990) investigated the effect of inundation on an in-line bundle five rows deep using a standard integral fin tube (26-fpi), three enhanced tubes, and one modified enhanced tube. CFC-11 was used as the working fluid. Five rows were studied for all tubes except the 26-fpi, which was simulated for up to seven rows. Plotting his data in an h_N vs. Re_L format, he was able to develop curves fits of the form

$$h_N = aRe_L^{-n}. \quad (2.21)$$

Table 2.1 shows the empirically determined coefficients and exponents for Equation 2.21 for each tube. Using Equation 2.13 and the data from the first and fifth tubes, Webb also determined the row effect exponent m , at one value of ΔT_{sw} . These values are also listed in Table 2.1.

Webb found that the highest performing tubes during single tube studies, the tubes with

Table 2.1: Coefficients and exponents for Equation 2.21 found by Webb (1990) using CFC-11 on five in-line tubes

Tube	$a \times 10^{-3}$ $W/(m^2 \cdot ^\circ C)$	n	m^a
26-fpi	13.90	0.000	0.00
GEWA-SC	54.14	0.220	0.12
Turbo C	257.80	0.507	0.23
Tred D	269.90	0.576	0.26
Mod. Turbo C	113.30	0.446	0.17

^aAt $\Delta T_{sw} = 5.55^\circ C$, based on rows 1 and 5

enhanced fins, were also the tubes affected the most by inundation. At the same time, the standard fin tube showed no inundation effects at all. This was attributed to channeling of the condensate by the fins as the liquid dropped from row to row. This channeling prevented the condensate from spreading axially along the tube and covering the entire tube surface. The enhanced tubes, on the other hand, showed very little channeling of liquid and allowed a great deal of axial movement by the condensate.

Inundation effects were studied by Murata, Abe, and Hashizume (1990) who condensed HCFC-123 on an in-line bank of stainless steel 26 and 30-fpi low-finned tubes eight rows deep by two columns wide. Tests were performed on single tubes as well as the full bank. Inundation was studied by pumping excess liquid over the first row through a porous plate situated directly over the tube at a distance of 2.5 mm.

Data presented for the first, fourth, and eighth rows showed that during normal condensation on the eight row bundle of 30-fpi tubes, the row-by-row heat transfer coefficient dropped from the first to the fourth row and then increased again in the eighth row to the level of the first row. This was explained by a change in condensate drainage. They noted that near the top of the bundle nearly all the condensate fell on successively lower tubes; however, on the bottom rows the condensate flow became turbulent and the total condensate flow did not hit the next tubes in the column due to its instability.

When the row effect was simulated using only one tube and excess liquid falling from the porous drip tube, Murata et al. (1990) showed that both the 26 and 30-fpi tubes suffered a drop in heat transfer coefficient with increasing condensation rates. The 26-fpi tube showed less dependence on the condensate flowrate than the 30-fpi tube and showed better overall performance at $Re_L > 500$. The heat transfer coefficients of both tubes were also seen to level off at Re_L values of approximately 1500. This was thought to be due to the splashing at the higher flow rates which prevented some of the liquid from reaching tubes in the lower rows.

Additionally, they also determined that for an in-line configuration the condensate flow patterns are related to the vertical pitch. During simulated bundle tests the flow patterns were observed to go from the sheet mode near the top (where the porous plate distributor injected a uniform liquid flow into the bundle) to unstable columns at the bottom. They believed this was due to the large vertical pitch ($2d_o$) and the inability of the liquid to maintain a thin sheet over the distance between the tubes.

An analytical model proposed by Murata et al. (1990) and based on a rectangular shaped fin and a three-region fin surface predicted their single tube data very well. It did, however, underpredict the performance of tubes in the simulated bundles by neglecting heat transfer in the flooded regions of the tubes and splashing on tubes in the lower part of the bundle. Comparisons to other data were not included.

Honda and Uchima (1991, 1992) have conducted the most comprehensive studies to date by investigating the effects of inundation and vapor shear on both in-line and staggered configurations of tube bundles. Six tubes, two standard finned tubes and four enhanced tubes, were studied with CFC-113 in bundles three tubes wide by fifteen rows deep.

The Honda and Uchima (1991, 1992) results were consistent with the Webb (1990) data discussed above. The flat-sided finned tubes showed very little inundation effects at all,

and, as such, performed better under inundation conditions than did those tubes with three dimensional fins. Again, this was attributed to the ability of the finned tubes to prevent the condensate from spreading axially as it fell from tube to tube. The enhanced tubes showed a greater inundation effect, with the in-line bundle being more susceptible than the comparable staggered bundle, particularly at low vapor velocities ($U_{\infty} = 4$ m/s).

Vapor Shear

Much of the research discussed above was conducted under conditions of low vapor velocity. However, when the vapor surrounding a tube is moving at high velocity, the tube's heat transfer performance can be markedly different. The moving vapor interacts with the condensation on the surface of the tube through shear stresses at the vapor/liquid interface. As the velocity increases so do the shear stresses. At lower velocities this interaction can cause waves and ripples in the liquid surface or force the liquid to flow more rapidly around the perimeter of the tube. If the velocity is large the vapor flow may separate from the tube surface and strip some of the liquid away. In both cases the liquid film on the top of the tube is thinned, which causes the heat transfer performance of the tube to increase. This effect is known as vapor shear.

Smooth tubes

While a great deal of smooth tube data has been collected to try to quantify the effect of vapor shear, most of the modeling attempts have taken an analytical approach. The first attempts were extensions of Nusselt's theory to include the shear stresses along the boundary of the condensate/vapor interface. Shekriladze and Gomerlauri (1966) assumed that the major factor in the interfacial shear stress was the change in momentum across the boundary. Using the asymptotic (infinite condensation rate) expression for the shear stress at the condensate

surface and neglecting separation and body forces, they found that for an isothermal tube covered by a laminar film with no waves, the heat transfer could be modeled by

$$\bar{N}u = \frac{\bar{h}D}{k_f} = 0.9\tilde{R}e^{\frac{1}{2}}. \quad (2.22)$$

The value $\tilde{R}e$ is defined as the two-phase Reynolds number and is based on the vapor velocity and the condensate properties, such that

$$\tilde{R}e = \frac{u_g D \rho_f}{\mu_f}. \quad (2.23)$$

If gravity and velocity are both taken into account, Equation 2.22 becomes

$$\bar{N}u\tilde{R}e^{-\frac{1}{2}} = 0.64(1 + (1 + 1.69F)^{\frac{1}{2}})^{\frac{1}{2}} \quad (2.24)$$

where

$$F = \frac{Pr}{Fr \cdot Ph} = \frac{gD\mu_f^i f_g}{u_g^2 k_f \Delta T_{sw}}. \quad (2.25)$$

While still ignoring separation, Fujii and Uehara (1972) took the Shekrladze and Gome-lauri analysis a step farther by matching the shear stress at the condensate/vapor interface and using an approximate integral treatment of the vapor boundary layer. For vertical downward vapor flow over an isothermal tube, they found that the shear effects could be approximated by

$$\bar{N}u\tilde{R}e^{-\frac{1}{2}} = X \left[1 + \frac{0.276F}{X^4} \right]^{\frac{1}{4}}, \quad (2.26)$$

where

$$X = 0.9(1 + \frac{1}{G})^{\frac{1}{3}} \quad (2.27)$$

and

$$G = \frac{k_f \Delta T_{sw}}{\mu_f^i f_g} \left(\frac{\rho_f \mu_f}{\rho_g \mu_g} \right)^{\frac{1}{2}}. \quad (2.28)$$

Equation 2.26 satisfies the limiting cases for both large and small vapor velocities and was found by Lee and Rose (1984) to give reasonable results to existing data. At values of G

greater than 5 (infinite condensation rate), Equation 2.26 almost duplicates the solutions found using Equation 2.24. In the more practical range where G is less than 1.0, Lee and Rose (1984) state that the differences between Equations 2.24 and 2.26 are of the magnitude typical of uncertainties in experimental data.

Equations 2.24 and 2.26 do not consider separation, which at high vapor velocities will occur between 82 and 180 degrees from the stagnation point of the tube. Beyond the separation point the liquid layer thickens and heat transfer is greatly reduced. For a conservative approach, Shekrladze and Gomelauri (1966) suggested that the heat transfer be neglected below the separation point. If 82 degrees is chosen for the separation point, the most conservative model results and Equation 2.24 reduces to

$$\bar{Nu}\bar{Re}^{-\frac{1}{2}} = 0.42(1 + (1 + 1.69F)^{\frac{1}{2}})^{\frac{1}{2}}. \quad (2.29)$$

Both Honda et al. (1982) and Lee and Rose (1984) found that these theories tended to overpredict the experimental Nu values for steam at relatively high vapor velocities and underpredict them for CFC-113 data taken at moderate velocities. Noting these discrepancies, Rose (1984) performed an analysis similar to that of Skedriladze and Gomelauri (1966), but which included the circumferential pressure variation in the condensate film. This analysis defined an additional term, P^* , given by

$$P^* = \frac{\rho g h_f g \nu_f}{k_f \Delta T_{sw}}, \quad (2.30)$$

as part of the momentum equation. It was shown that this term was important when the fraction $F/8P^*$ was significantly less than unity. This meant that for actual condensation processes the pressure gradient was important to refrigerants at lower relative vapor velocities than to steam at comparable temperatures and pressures. The Rose (1984) model predicted higher heat transfer coefficients in the forward (top) part of the tube prior to vapor separation, and it suggested instabilities in the liquid on the lower half of the tube which would also

increase the overall heat transfer coefficient for the tube. In addition, Rose (1984) proposed an alternative equation, defined by

$$\bar{Nu}\tilde{Re}^{-\frac{1}{2}} = \frac{0.9 + 0.728F^{\frac{1}{2}}}{(1 + 3.44F^{\frac{1}{2}} + F)^{\frac{1}{4}}}, \quad (2.31)$$

which satisfied both the zero and infinite velocity asymptotes ($F \rightarrow \infty, F \rightarrow 0$) and agreed with numerical solutions to within 0.4%.

Other attempts to explain the discrepancies between experimental data and theory have also been done. One approach, used by Honda et al. (1979, 1980), used the condition of constant heat flux instead of constant wall temperature. This approach gave values of Nu which were more in line with actual steam data at high vapor velocities. However, Lee and Rose (1982) pointed out that this is more a result of lucky mathematics than a result of a more thorough analysis, since the model lends more weight to the heat transfer calculation on the lower portion of the tube where the condensate thickness is largest and the calculation is least reliable.

Another, more complete approach was used by Honda and Fujii (1980, 1984). This "conjugate" solution treated the heat transfer in the liquid layer, tube wall, and coolant simultaneously under prescribed coolant and vapor conditions, and predicted lower coefficients for steam at high velocities. The model did not account for the discrepancies found in CFC-113 data found by Lee (1982) and Lee and Rose (1984a). Lee and Rose (1984b) note that although this method is sound, it is not entirely satisfactory for detailed comparisons of the condensate film, especially when the coolant-side resistance dominates.

Finned and enhanced tubes

As with liquid inundation, the effect of vapor velocity has been shown experimentally to be significantly less on finned tubes than on smooth tubes. The studies for finned and

enhanced tubes have been entirely experimental, and no correlations equivalent to Equations 2.24 through 2.31, which are for plain tubes, currently exist in the literature.

Gogonin and Dorokhov (1981) condensed CFC-21 on both smooth and finned tubes at a maximum vapor velocity of 8 m/s. Their results showed that the heat transfer coefficients of the finned tubes increased less than 30% when subjected to high velocity vapor. They noted that this increase was within the scatter of data taken by other investigators (Katz and Geist, 1948), Smirnov and Lukanov, 1971) and they concluded that the effect of vapor velocity on the finned tubes was insignificant and that bundle design using finned tubes should be based on data taken for finned tubes in a stationary vapor.

McNaught and Cotchin (1988) found similar results when they condensed CFC-12 on both plain and finned tube bundles. While the plain tube bundles showed an obvious increase in heat transfer coefficient with increasing vapor velocity, the finned tube bundles showed little velocity dependence. They also found that the data for low-fin tubes could be adequately predicted using standard finned tube equations (Beatty and Katz, 1948).

As noted in the discussion of liquid inundation, the most comprehensive studies have been conducted by Honda and Uchima (1991, 1992), who investigated the effects of inundation and vapor shear on both in-line and staggered configurations of tube bundles constructed with two finned tubes and four enhanced tubes. CFC-113 was used as the working fluid during condensation on bundles three tubes wide by fifteen rows deep.

Overall, their data showed that, compared to smooth tubes, the finned tubes were less affected by vapor shear. At the same time, the enhanced tubes appeared to show a greater effect than the finned tubes, although not as large as smooth tubes.

The also showed that at low vapor velocity ($U_{\infty} = 4.0$ m/s) there was very little difference in performance between an in-line bundle and a staggered bundle, although the staggered bundle appeared to perform better in row two and below at higher vapor velocities

($U_{\infty} = 10.1, 18.2$ m/s). Additionally, at low vapor velocities the staggered bundle constructed with enhanced tubes performed better than a comparable square-pitch bundle. In some instances, the first row did not always give the highest heat transfer coefficient. This was more marked in the staggered bundle and was explained by a possible blockage effect in the first row accelerating the vapor flow into the second row. Overall, the best performing tube was found to be a finned-tube with close to optimal dimensions (according to a Honda and Nozu model, 1989) in a staggered arrangement.

Cavallini et al. (1992) conducted a study with a single low-fin 34-fpi tube condensing CFC-11 at velocities up to 26.2 m/s. The data showed that at the highest velocity there was a 50% enhancement in the heat transfer coefficient over the value in stationary vapor. However, while this was found to be significant, Cavallini noted that it was still much less pronounced than the enhancement found for a smooth tube under similar conditions.

Combined Inundation and Vapor Shear

In an actual condenser containing many rows of horizontal tubes, the heat transfer coefficients of individual tube rows are affected by a combination of inundation and vapor shear effects. Theoretically, the vapor shear effect works against the effects of liquid inundation by acting to thin the insulating condensate layer. Webb (1984) states that the different effects should be expected to dominate at different locations in the bundle. Around the outer tubes of the bundle, where there is less inundation and the tubes are subjected to vapor flowing around the perimeter of the condenser shell, shearing effects would be expected to dominate. Conversely, near the center of the bundle most of the vapor should have been condensed, vapor velocity should be relatively small, and inundation effects should dominate.

Very little work has been done to determine the effect of combined inundation and shearing effects, and the majority of that has been done with bundles of smooth tubes and

steam. Butterworth (1977) proposed a model which separates out the two effects. A slightly modified version of this equation, which predicts the local heat transfer coefficient on row N of the condenser, is given by

$$h_N = \left[\frac{1}{2} h_{sh}^2 + \left(\frac{1}{4} h_{sh}^4 + h_1^4 \right)^{\frac{1}{2}} \right]^{\frac{1}{2}} \left[N^{\frac{5}{6}} - (N-1)^{\frac{5}{6}} \right], \quad (2.32)$$

where h_{sh} , the heat transfer coefficient associated with shear forces, is found from

$$\bar{Nu} = 0.59 \bar{Re}^{\frac{1}{2}} \quad (2.33)$$

and h_1 is calculated from the Nusselt equation for a single tube (Equation 2.1).

McNaught (1982) proposed a method that treated the combined effects of inundation and vapor shear as a forced two-phase convection problem. For the local heat transfer coefficient on the N th tube, the model is

$$h_N = (h_{sh}^2 + h_G^2)^{\frac{1}{2}}, \quad (2.34)$$

where h_G is defined by

$$h_G = h_1 (N^{\frac{5}{6}} - (N-1)^{\frac{5}{6}}), \quad (2.35)$$

and h_{sh} is

$$h_{sh} = 1.26 X_{tt}^{-0.78} h_f. \quad (2.36)$$

In the previous two equations the values for X_{tt} and h_f are defined by

$$X_{tt} = \left(\frac{1-x}{x} \right)^{0.9} \left(\frac{\rho_g}{\rho_f} \right)^{0.5} \left(\frac{\mu_f}{\mu_g} \right)^{0.1} \quad (2.37)$$

and

$$h_f = C \frac{k_f}{D} \text{Re}_f^m \text{Pr}_f^n. \quad (2.38)$$

X_{tt} is the Lockhart-Martinelli parameter for two-phase flow and h_l is the liquid-phase forced convection heat transfer coefficient across the tube bank. The coefficients C , m , and n depend on flow conditions through the tube bank.

As noted above, the work used to develop these equations was based on steam condensation on banks of smooth tubes. The only data available for fluids other than water is that of Honda and Uchima (1991, 1992), discussed earlier. Their data showed that under the combined effects of vapor shear and condensate inundation in-line and staggered bundles constructed with the same integral finned tubes have virtually identical performance at low vapor velocities ($U_{\infty} = 3.5$ m/s). At high velocities ($U_{\infty} = 3.5$ m/s) the staggered bundles of finned tubes performed slightly higher than corresponding in-line bundles, while the heat transfer performance of the bundles in general increased slightly over their performance in low velocity conditions. Thus, they concluded that while there is some vapor velocity effect, it is very small for the finned tubes.

Honda and Uchim (1991, 1992) found that the combined effects of shear and inundation were more marked for the tubes with three-dimensional fins. Overall, they found that the staggered bundles performed better than the in-line bundles, regardless of vapor velocity. As noted in the section on inundation effects, the enhanced tubes also showed more susceptibility to condensate buildup. However, at higher velocities, not only did the average heat transfer coefficients of the bundles increase slightly, but the tubes also showed a noticeably smaller dependence on inundation. Therefore, vapor velocity seems to have a much larger effect on the enhanced tubes than on the integral finned tubes.

In terms of row depth, while the staggered bundles showed more shearing effects with increasing vapor velocity than the in-line bundles, the effect became insignificant after approximately row six. They therefore concluded that for a finned tube, the only tube for which they presented row-by-row data, the heat transfer performance was relatively independent of vapor velocity at high inundation rates. No mention was made of the row-by-row performance of the enhanced tubes under conditions of both shear and inundation.

Condensation with Non-condensable Gases

Non-condensable gases, such as air, have a large detrimental effect on the condensation of pure refrigerant in a refrigerant condenser, even in small quantities. The non-condensable gases are drawn to the liquid/vapor interface by motion of the moving refrigerant vapor and accumulate there, creating an insulating layer of gases between the condensate and the refrigerant vapor. This layer acts to severely complicate the condensation process and reduce the heat transfer performance of the condenser.

Figure 2.3, taken from a comprehensive non-condensable gas review by Webb and Wanniarachchi (1980a), gives a schematic representation of condensation on a vertical surface in the presence of non-condensable gases. Webb and Wanniarachchi state that the presence of the gases complicates the condensation process in two ways. First, the refrigerant vapor in the mixture exists at a partial pressure, so its corresponding saturation temperature, T_g , is lower than T_{sat} . Thus, the driving temperature difference ($T_{sat} - T_w$) is reduced to $(T_g - T_w)$ and the heat transfer is diminished. Second, the refrigerant vapor is not in direct contact with the liquid surface and must diffuse through the non-condensable gas layer to the vapor/liquid interface before condensation can occur. Thus, the concentration of non-condensable gas increases closer to the liquid/vapor interface while the concentration of the refrigerant vapor decreases. The driving pressure difference for the diffusion process, $(p_{vi} - p_{vb})$, further lowers the saturation temperature, thereby decreasing the partial pressure and its associated saturation temperature even farther.

Webb also states that vapor shear is important to the effect of non-condensable gases. As vapor in the free stream passes through the bundle, the shear forces in the vapor interact with the gas in the non-condensable gas layer and strip the gas layer from the surface of the tubes, effectively eliminating any detrimental effects associated with their presence.

Almost all investigations related to the effect of non-condensable gases have been directed

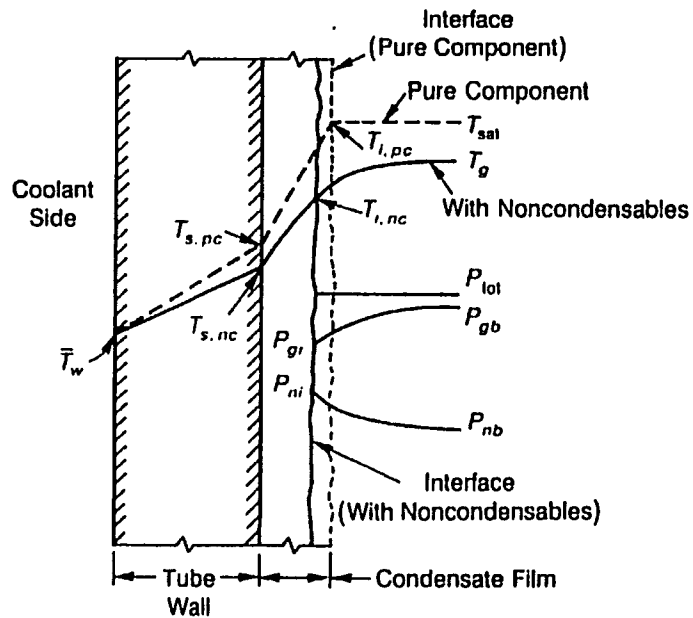


Figure 2.3: Schematic of condensation in the presence of non-condensable gases. Boundary layer temperature and pressure distributions. (Webb and Wanniarachchi, 1980)

at its effect on the condensation of steam. Webb and Wanniarachchi (1980a) did a review of the studies up to that time and found that very little research had been done regarding non-condensable gas effects on refrigerant condensation. A review of the literature since that time has found that almost no studies on non-condensable gas in refrigerant condensation have been done since then. Specifically, at the time of this writing, no studies could be found in the literature which investigated the relationship between non-condensable gas and refrigerant condensation on either finned or enhanced tubes.

The only investigations into the effect of non-condensable gas on refrigerant condensation were conducted by Webb and Wanniarachchi (1980b, 1982), who looked at the effect of non-condensable gas on the performance of a 250-ton CFC-11 water chiller. Their goal was to quantify the penalty in compressor power consumption caused by varying concentrations of

non-condensable gases. They found that at 8% gas concentration and 50% chiller loading the power consumption increased 6.4%. At 70% loading the power consumption increased by 5.9%, which corresponded to a power increase of approximately 8 kW.

They also found that a simplified one-dimensional model based on the Colburn-Hougen equations (developed in Webb and Wanniarachchi, 1980a) predicted the chiller performance to within 10%. A two-dimensional model reported in Webb and Wanniarachchi (1982) predicted the condenser load within -3% to 14% of the experimental values.

CHAPTER 3. EXPERIMENTAL APPARATUS

All of the experiments discussed in this chapter were performed on an experimental refrigeration test facility in the Heat Transfer Laboratory in the Black Engineering Building at Iowa State University. The experimental test apparatus used during this study was originally designed and built by Joseph Huber, a graduate researcher in the Heat Transfer Laboratory, for single tube condensation and evaporation studies with several different types of refrigerants and tube geometries. Modifications to the rig, made by Mr. Huber and the author, were implemented to accommodate ASHRAE project RP-676 "Experimental determination of shell-side condenser bundle design factors for refrigerants R-134a and R-123," while additional system modifications were made by the author to allow data specific to this study to be taken. A complete description of the test facility is discussed below.

To collect the data discussed in this report, the test facility had to be capable of performing experiments with both pure refrigerants and refrigerants contaminated with non-condensable gases, as well as experiments measuring parameters such as liquid inundation rates and vapor velocities through the bundle. Additionally, the ASHRAE RP-676 work statement required that:

1. the test facility be able to provide data for both the average bundle heat transfer coefficient and the average heat transfer coefficients for the middle tube of each row;
2. the average shell-side heat transfer coefficient be measured without relying on tube-wall temperature measurements;

3. the test section accommodate different tube bundles and multiple refrigerants;
4. the test facility be able to accommodate a bundle tube loading of 2400 W per linear meter (2500 BTU/hr per linear foot);
5. the test section be at least 309 mm (12 in) long and accommodate bundles that are 5 columns wide by 5 rows deep;
6. the tube bundles use 19.1 mm (0.75 in) nominal O.D. tubes arranged in a triangular configuration with a horizontal pitch of 22.2 mm (0.875 in) and vertical pitch of 19.1 mm (0.75 in);
7. four different tube geometries be tested; two finned tubes and two enhanced tubes.
8. the temperature rise of the water passing through the test section be greater than 1.11°C (2°F);
9. the refrigerant in the test facility be pure and that the test facility not introduce any oil into the refrigerant;
10. the rig be capable of providing saturated vapor at 35°C (95°F) to the test section.

The test apparatus is composed of several major components. These can be grouped into the the test section, the tube bundles, the refrigerant loop, the closed water loop, and the data acquisition system. A schematic diagram of the test facility is given in Figure 3.1 and shows all the major component groups. The test section shown in the closed water loop does not represent a second test section, but is meant to show the location of the test section within the loop. In the physical system, the closed water loop is attached to the test section and bundle shown in the refrigerant loop.

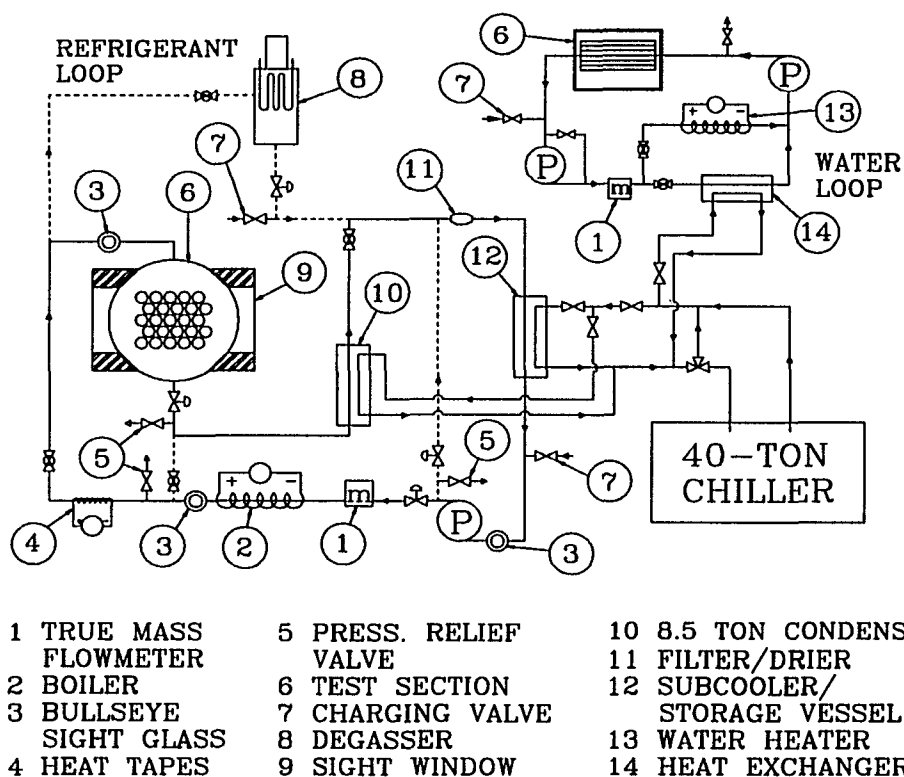


Figure 3.1: Schematic of experimental test facility

The various test facility components are discussed below. The description will begin with the test section, followed by a discussion of the different bundle configurations used to take the various types of data.

Test Section

In the working test facility, the test section refers to the stainless steel pressure vessel where data is collected, the removable tube bundles which are mounted inside, the water-side fixtures mounted on the ends of the pressure vessel, and the instrumentation (pressure transducers, thermistors) which actually measure the condensation data. However, for the

purposes of this discussion, the test section refers solely to the pressure vessel. The other components are discussed below in more detail.

The vessel was constructed from a 660 mm (26 in) section of schedule 40 stainless steel pipe with a 203 mm (8 in) inner diameter. Flanges 25.4 mm (1 in) thick were attached to the ends of the pipe to accommodate the installation of the tube bundles and water-side fixtures. Grooves cut into the flanges allow for the the installation of buna or neoprene o-rings (depending on the refrigerant being tested), which provide the seal between the refrigerant in the vessel and the atmosphere. Two 152 mm (6 in) tall sight windows were installed on either side of the vessel at the midpoint to allow observation of the condensation and drainage processes.

Several (1.5 inch NPT couplings) were also installed on the walls of the vessel. Two ports on the top of the vessel are used as vapor inlets, while a third is used for redundant pressure transducers. Of the three ports placed on the bottom of the vessel, two are unused and the third is used as the refrigerant outlet. Two additional auxilliary ports on the side of the vessel are used for a pressure relief valve and and a refrigerant charging valve, respectively.

Tube Bundles

As required by the ASHRAE work statement, the tube bundles are 5 columns wide by 5 rows deep, were constructed from 2 different finned tube geometries and two different enhanced tube geometries, and have a staggered configuration with a horizontal pitch of 22.2 mm (0.875 in) and a vertical pitch of 19.1 mm (0.75 in). All tubes have a nominal o.d. of 19.1 mm (0.75 in) and are made from standard copper alloys.

The finned geometries tested were the 26 fin per inch (fpi) (1024 fin per meter (fpm)) and the 40-fpi (1575-fpm). The 26-fpi has a standard fin height of 1.45 mm (0.057 in), while the 40-fpi is of the low fin variety and has a fin height of 0.86 mm (0.034 in). For a given

Table 3.1: Tube geometry specifications

Tube	Fin count fins/m	D_o nominal mm	D_i nominal mm	D_r mm	Fin Height mm	A_o nominal m ² /m	A_o actual m ² /m	A_i nominal m ² /m
26-fpi	1024	18.80	14.40	15.90	1.45	0.0588	0.193	0.0454
40-fpi	1575	18.87	15.70	17.10	0.86	0.0594	0.179	0.0493
Tu-Cii	–	18.90	15.54	17.07	0.91	0.0597	–	0.0488
G-SC	1024	18.94	14.17	16.82	1.06	0.0595	0.200	0.0445

Tube	Fin Count fins/in	D_o nominal in	D_i nominal in	D_r in	Fin Height in	A_o nominal ft ² /ft	A_o actual ft ² /ft	A_i nominal ft ² /ft
26-fpi	26	0.739	0.568	0.625	0.057	0.193	0.634	0.149
40-fpi	40	0.743	0.622	0.675	0.034	0.195	0.586	0.163
Tu-Cii	–	0.744	0.612	0.672	0.036	0.196	–	0.160
G-SC	26	0.746	0.558	0.662	0.042	0.195	0.656	0.146

nominal outer diameter, low-fin tubes typically have a larger inner diameter than tubes with standard height fins, and are used in cases where the smaller inner diameter of the standard fin-height tube would cause an excessive pressure drop in the water passing through the tube.

The enhanced geometries tested were the Wolverine Turbo C-II (referred to in this report as Tu-Cii), and the Wieland GEWA SC (call the G-SC). The G-SC is characterized by long, Y-shaped fins, while the Tu-Cii has short fins that have been roughened by mechanical working. The tube geometric specifications for all four geometries are given in Table 3.1.

All four tubes were manufactured with a spiral inner heat transfer enhancement designed to decrease the water-side heat transfer resistance. The internal enhancements consist of several spiral ridges that run axially along the inner surface of the tube. The dimensions of the internal enhancements differ from tube to tube, and are listed in Table 3.2. It should be mentioned that while the enhancements were used to increase the heat transfer coefficients on the water-side of the tubes, only the heat transfer coefficients on the shell-side were measured in this study.

Table 3.2: Tube internal enhancement specifications

Tube	Ridge Count	Ridge Height	Spiral Angle
26-fpi	10	0.381 mm (0.015 in)	40°
40-fpi	10	0.381 mm (0.015 in)	50°
Tu-Cii	38	0.508 mm (0.020 in)	40°
G-SC	25	0.540 mm (0.021 in)	20°

The tubes were mounted by mechanical rolling into tubes sheets constructed of 25.4 mm (1 in) thick 316 stainless steel, shown in Figure 3.2. Original attempts at bundle construction using brazing with brass plates proved unsatisfactory due to warping of the bundle during heating. Since rolling of tubes works best when the tube material is softer than the header material, rolling the tubes into a cheaper and more easily machinable material, such as 6065-T651 aluminum, gave undesirable results due to the small difference in the relative hardnesses between the aluminum and the copper tube alloy.

Mechanical rolling is performed by placing the ends of the tubes, which had been softened by heat treatment, into the tube sheet and expanding the ends with a special rolling device. This produced a friction fit between the tube sheet and the tube which was tight up to a pressure of more than 893 kPa (130 psia). Care was taken not to over-roll the tubes, as this would have caused micro-cracks in the tube material which would have resulted in irreparable leaks in the tube-tube sheet union. A more complete discussion of the tube rolling process can be found in Fisher and Brown (1954).

In order to more adequately disperse the vapor throughout the test section, impingement plates were installed directly under the inlet ports on the top of the bundles. Diversion plates were added to each side of the bundles to prevent the refrigerant vapor from passing around

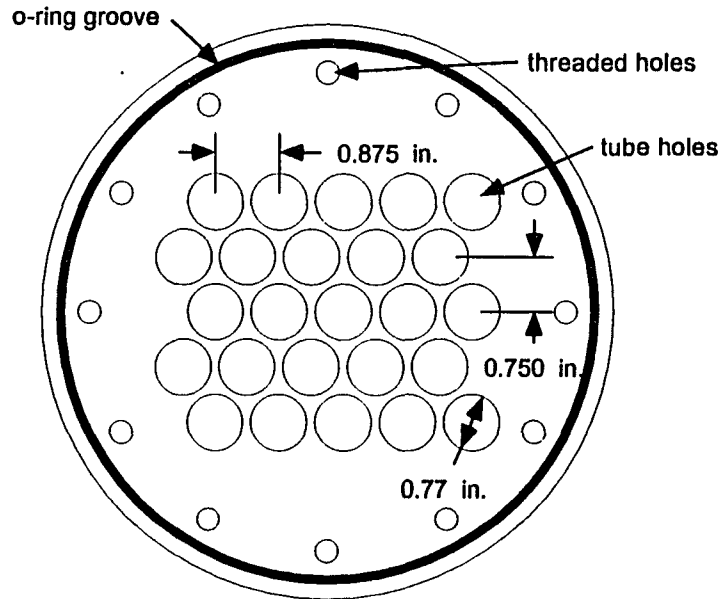


Figure 3.2: Schematic of bundle tube sheet

the bundle along the perimeter of the pressure vessel and insure that all the vapor passed through the tubes. The diversion plates consisted of a steel frame covered with glass plates which allowed inspection of the condensation process through the sight windows placed in the sides of the pressure vessel. The diversion plates were placed 0.318 mm (0.125 in) from the sides of the bundle, a distance equal to the horizontal pitch of the tubes.

Several different types of tests were conducted during the course of this study. Each type of test required a slightly different type of bundle configuration. The next two sections describe the different bundle configurations for the non-condensable gas and liquid inundation/vapor shear tests, respectively.

Non-condensable gas bundle configuration

In the non-condensable gas tests, both bundle and row-by-row data was collected. To accomplish this, all of the tubes in the bundle were left open to water flow and the full bundle was used to condense vapor. The water was run through the bundle in a single-pass arrangement so that each tube saw an equal inlet temperature.

In order to insure that the water flow rate through all tubes was uniform, a large pressure drop was created across the bundle by placing flow restrictors, rubber stoppers containing a 25.4 mm (1 in) long piece of 4.763 mm (0.1875 in) i.d. copper tube, in the water outlet end of each tube. With the restriction on the outlet end, the inlet losses in the tubes became negligibly small, resulting in a uniform pressure drop in each tube and a uniform water distribution through the bundle. Data taken to check this configuration showed that the water flow rates from individual tubes varied by less than 1% across the full range of flow rates used in the condensation tests.

On the shell side, each bundle used the impingement and diversion plate arrangements discussed above.

Liquid inundation and vapor shear bundle configuration

In order to produce the largest possible heat fluxes and still simulate up to thirty rows of tubes, only the middle tubes of each of the five rows in the test bundles were used. Figure 3.3 shows a cross section of the test section as it was used during the inundation and vapor shear testing. The outer four columns (twenty tubes) were plugged with rubber stoppers at both the inlet and outlet ends to prevent water from filling them, thereby preventing secondary condensation from occurring away from the active (i.e. instrumented) tubes.

The screen and impingement plates used to distribute the vapor during the bundle tests were modified so that the refrigerant flow could only enter the bundle over the active center

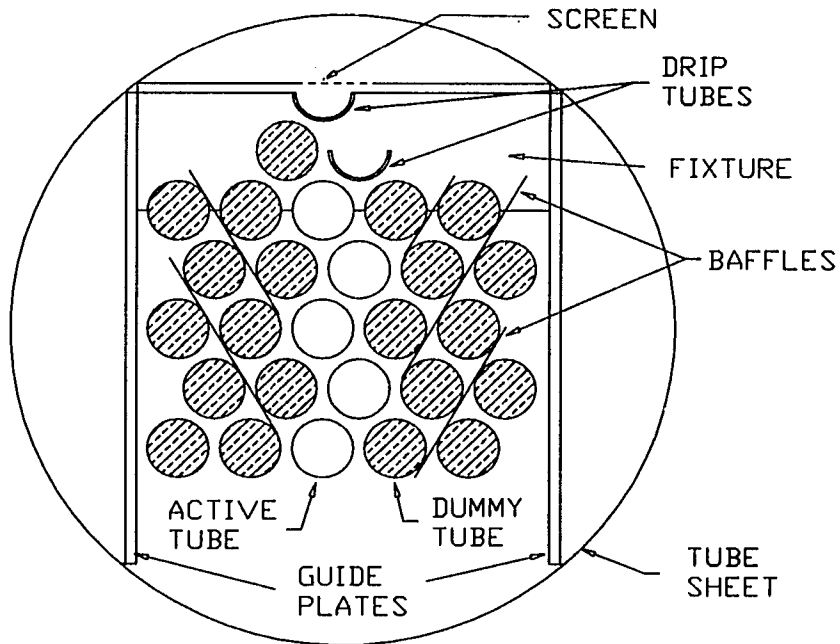


Figure 3.3: Cross section of test bundle with inundation apparatus

column. The liquid flow was directed so that as it passed through the screen the liquid fell into the distribution tubes to be distributed axially in the test section. The areas over the inactive tubes, as well as the ends near the tube sheets, were blocked so liquid could only enter the bundle over the instrumented tubes.

Sheet metal baffles were cut to size and slipped diagonally into the bundle so that the liquid and vapor could not spread laterally through the bundle during each test run. The baffles also acted to channel any liquid that did manage to enter the bundle at any point other than over the active tubes back to the center column. In this way, only the active tubes were subjected to liquid and vapor flow, and all the liquid was forced to flow over the active tubes.

In a bundle with a staggered tube configuration, condensate does not drip directly down onto the next row. Instead, depending on the horizontal pitch of the tubes and the flow rate of the condensate, the liquid drains in one of several ways. One possible flow path is through

the gap between the tubes of the next row and onto the tubes of the third row down. Another possibility, usually associated with very tight triangular configurations, is for the liquid to drain laterally onto the two tubes on either side in the next row down. The condensate may also drain in a combination of both, flowing both sideways and vertically.

In order to simulate this phenomenon, two drip tubes were used to simulate inundation. The first was directly above the first tube of the bundle at a distance of 38.1 mm (1.50 in) center to center, or two times the longitudinal (vertical) pitch, p_l . The second was directly above the active tube in the second row, again at a distance of $2p_l$. Figure 3.3 shows the arrangement of these tubes, along with the rest of the distribution system.

The drip tubes themselves were constructed from 40-fpi tubes which had been cut in half axially. Semi-circular copper pieces were attached to over each end, forming a trough. Holes 0.79 mm (0.031 in) in diameter were drilled along the bottom at 4.8 mm (0.1875 in) intervals for the inundation tests with HFC-134a. The diameter of these holes was increased to 1.3 mm (0.051 in) for tests with HCFC-123 because the higher viscosity and surface tension of HCFC-123 would not allow it to flow through the smaller holes. Additionally, a groove 0.63 mm (0.025 in) wide was cut axially through the fins along the bottom (underside) of the tube in such a way that the afore-mentioned holes emptied into the groove. During low inundation flow rate testing, this groove allowed the liquid to move axially along the underside of the tube. Thus, gravity was the driving force in forming the drip patterns, not the artificial drip points created by the holes. At high flow rates the holes tended to drain the liquid in columnar mode with marginal interaction between columns.

Refrigerant Loop

The refrigerant loop is used to set the refrigerant inlet condition to the test section. Refrigerant is pumped into the boiler, which is a 7.32 m (24 ft) long section of 19.1 mm

(0.75 in) o.d. stainless steel tube. The refrigerant is boiled by passing electrical current from a 40 kVA SCR-controlled rectifier through the walls of the boiler tube.

After leaving the boiler, the refrigerant passes into a section of 1.83 m (6 ft) 38.1 mm (1.5 in) i.d. copper pipe wrapped with electric heat tapes. This is used to add additional heat to the refrigerant at the exit of the boiler and allow for greater control of the state of the refrigerant entering the test section. The exit from the boiler is at a slightly higher elevation than the inlet to the test section. This prevents any liquid holdup in the piping upstream of the test section during liquid inundation tests and insures that all the flow measured through the flowmeter at the inlet to the boiler reaches the test section.

From the superheater, the refrigerant flows into the test section and condenses on the tube bundle. The condensed refrigerant leaving the test section flows through a nominal 8.5 ton shell-and-tube condenser and then into a chilled storage tank which is located at the inlet of the pump. Since the inundation tests require only partial condensation in the test section, the condenser is needed to completely condense the vapor leaving the test section so that the refrigerant can be pumped. The condenser is not used during full bundle tests, as all condensation takes place in the test section. The storage vessel insures that the liquid remains subcooled and that pump will never be starved for liquid.

A diaphragm-type positive displacement pump is used to circulate the refrigerant. The diaphragm pump is well suited to the present study for several reasons. First, the diaphragm pump prevents any oil from entering the refrigerant, as would be the case if a compressor was used to circulate the refrigerant. Second, the diaphragm pump is not plagued by the shaft seal leakage problems which affect conventional centrifugal and gear pumps. Third, the diaphragm pump does not require the working fluid to provide lubrication for its internal moving parts, as gear pumps do. Final, the diaphragm pump can withstand pressures up to 6890 kPa (1000 psia) and is significantly cheaper than magnetically coupled centrifugal

pumps of the same pressure capabilities.

The refrigerant loop also contains a degassing tower, which is a 1.52 m (5 ft) high length of 102 mm (4 in) i.d. copper pipe mounted vertically. During a degassing cycle, refrigerant is boiled and fed into the middle of the tower. The heavier vapor refrigerant condenses on a small coil installed in the top of the tower and falls to the bottom, while the lighter non-condensable gases collect in the top of the tower and are periodically purged.

Water Loop

Water is pumped through the tube bundle to cool the tube surfaces during condensation and remove energy from the refrigerant vapor during the condensation process. The water leaving the tube bundle is then split into two streams. One stream passes through a set of liquid-to-liquid heat exchangers, where the energy added to the water as it passes through the tube bundles is removed. The other stream passes through an SCR-controlled electric heater, which allows the water temperature at the test section inlet to be precisely controlled. The two streams then merge and flow into the test section. Two centrifugal pumps are used to circulate the water.

The water loop also contains an in-line filtration system. Eight cartridge-type household water filters are connected in a parallel arrangement just upstream of the test section. These filters remove any mineral impurities from the water, which would otherwise become rusty after a short period of use, and prevent mineral deposits from forming on the tube and water box surfaces.

Glycol Chiller

The source of cold glycol for the liquid-to-liquid heat exchangers, the refrigerant sub-coolers, and the condenser in the de-gassing tower is a nominal 141 kW (480,000 Btu/hr)

packaged chiller unit capable of supplying 35 kW (120,000 Btu/hr) at an evaporator temperature of -17.7°C (0°F). The chiller unit has a 4 cylinder compressor equipped with unloading and a 1140 l (300 gal) water/glycol storage tank.

Data Acquisition System

The data acquisition system consists of two switch/control units and a high resolution digital multimeter controlled by an 80386 SX computer. Three computer programs, one for each of the three different types of tests, control the system and make the water and refrigerant energy transfer rate calculations needed to monitor the system.

The refrigerant and water inlet and outlet temperatures necessary for the calculation of the shell-side heat transfer coefficient were measured with thermistors calibrated to an accuracy of $\pm 0.025^{\circ}\text{C}$ (0.045°F); other temperatures were measured with Type-T thermocouples.

Pressures were measured with strain gage pressure transducers having accuracies of $\pm 0.25\% \times (\text{full scale})$. Since the saturation pressure is a critical parameter, a redundant measurement was taken by a capacitance-type pressure transducer. Because the strain-gage transducer has a higher accuracy than the capacitance-type transducer, only the pressure measurements obtained from the strain gage transducer were used in the heat transfer coefficient calculations; the redundant measurement was only used as a check. Because HFC-134a has higher vapor pressure than HCFC-123, transducers with different ranges were used to minimize the experimental uncertainty. Strain-gage transducers with a range of 0-1034 kPa (0-150 psia) were used during the HFC-134a tests, and strain-gage transducers with a range of 0-345 kPa (0-50 psia) were used during the HCFC-123 tests.

The saturation pressure was used to calculate the saturation temperature via the refrigerant saturation temperature-pressure relationship. Since a phase change was taking place in the test section, the test section pressure was the saturation pressure. It was assumed there was

Table 3.3: Uncertainties in the measured parameters

Measurement	Transducer	Uncertainty
refrigerant inlet temperature	thermistor	$\pm 0.025^{\circ}\text{C}$ (0.045°F)
refrigerant outlet temperature	thermistor	$\pm 0.025^{\circ}\text{C}$ (0.045°F)
bulk water inlet temperature	thermistor	$\pm 0.025^{\circ}\text{C}$ (0.045°F)
bulk water outlet temperature	thermistor	$\pm 0.025^{\circ}\text{C}$ (0.045°F)
tube water outlet temperatures	thermistor	$\pm 0.025^{\circ}\text{C}$ (0.045°F)
HFC-134a pressure	strain gage	± 2.59 kPa (0.375 psia)
HCFC-123 pressure	strain gage	± 0.862 kPa (0.125 psia)
refrigerant mass flow rate	coriolis effect	$\pm(0.002\dot{m}_{ref} + 0.002 \text{ kg/min})$ $\pm(0.002\dot{m}_{ref} + 0.004 \text{ lbm/min})$
water mass flow rate	coriolis effect	$\pm(0.002\dot{m}_w + 0.150 \text{ kg/min})$ $\pm(0.002\dot{m}_w + 0.331 \text{ lbm/min})$

negligible pressure drop through the bundle and that the pressure was uniform throughout the test section.

Even though highly accurate pressure transducers were used, the sensitivity of the saturation pressure to the saturation temperature for the refrigerants used in this study caused the uncertainty in the derived saturation temperature to be relatively high compared to the other measured temperatures. For instance, $\partial T_{sat}/\partial P_{sat}$ at 35°C (95°F) for HFC-134a is $0.041^{\circ}\text{C/kPa}$ ($0.51^{\circ}\text{F/psia}$) and 0.22°C/kPa (2.7°F/psia) for HCFC-123. The uncertainty in the derived saturation temperature was approximately $\pm 0.11^{\circ}\text{C}$ (0.2°F) for HFC-134a, and approximately $\pm 0.2^{\circ}\text{C}$ (0.36°F) for HCFC-123. The derivation of the saturation temperature uncertainty can be found in Appendix A.

The uncertainty in the calculated shell-side heat transfer coefficient (ω_{h_o}) is quite sensitive to the uncertainty in the saturation temperature. At low heat fluxes, nearly 75% of ω_{h_o} is due to the uncertainty in the saturation temperature. At high heat fluxes, approximately 60% of ω_{h_o} is due to the uncertainty in the saturation temperature.

The refrigerant and water flow rates were measured by coriolis-effect mass flow meters having an accuracy of $\pm(0.2\% \times (\text{flow rate}) + (\text{meter zero stability}))$. A summary of the

measurement uncertainties is given in Table 3.3. Since the test facility has nearly 50 different transducers, about 1 minute is required to scan through all the transducers.

CHAPTER 4. EXPERIMENTAL PROCEDURES

Because the effect of several phenomena were being studied in this investigation (non-condensable gases, liquid inundation, and vapor shear), different experimental procedures were used to collect heat transfer data. This chapter describes the procedures used for each type of experiment and the data reduction techniques used to calculate the bundle and row heat transfer coefficients and other parameters of interest.

The first section describes the techniques used to determine the water-side heat transfer coefficient (also referred to in this report as the inside heat transfer coefficient), which is needed to calculate the refrigerant-side heat transfer coefficients for condensation. The following three sections detail the experimental procedures used to take bundle and individual tube data with non-condensable gases, liquid inundation, and vapor shear experiments, respectively. The final two sections detail the methods used to calculate the heat transfer coefficients and other relevant parameters and to determine the experimental uncertainties of the heat transfer coefficients.

Water-side Heat Transfer Coefficient

One of the values needed to calculate the shell-side heat transfer coefficients was the inside (water-side) heat transfer coefficient of the condensation tubes. Since the inner surfaces of all four tube geometries were enhanced with spiral ridges to reduce the water-side resistance and increase the water-side heat transfer performance, traditional smooth-tube correlations

(e.g. Gnielinski (1976)) could not be used. This required that the water-side heat transfer coefficients be found experimentally for each tube. Correlations for several tubes (26-fpi, 40-fpi, Tu-Cii) were already available from the manufacturer; however, new correlations were developed to eliminate any discrepancies induced by tube-length differences between the manufacturer's test tubes and the tubes used in this study, which were considerably shorter, and to give correlations specific to the conditions being used in these tests.

The water-side heat transfer coefficients for the Tu-Cii also needed to be found experimentally for another reason. The spiral heat transfer enhancement of the Tu-Cii is designed for water flows with $Re_D > 20,000$. However, the water-side flow range of interest in this study was approximately $9000 < Re_D < 18,000$. As a result, the flows were not fully turbulent. This created very high water-side resistance, which made accurate calculation of the shell-side heat transfer coefficient nearly impossible.

To alleviate the problem, a spring-type turbulator used by a large refrigeration equipment manufacturer (Glamm, 1993) was installed over the spiral fins which already existed on the inside surface. This spring, made of a small diameter wire and held in place by friction fit, worked to continually trip the water into turbulent flow over the full length of the tube. In turn, this increased the tubes' inside heat transfer coefficients, decreased the water-side thermal resistance, and allowed the Tu-Cii to be used over the full range of water flow rates used in these tests.

The procedures used to calculate the inside heat transfer coefficient were based on a modified-Wilson technique (Thors, 1992). HFC-134a was boiled at constant heat flux while heated water was circulated through two tubes, connected in series, submerged in the refrigerant. The water flow rate and temperature were allowed to vary, while the heat flux on the tubes and refrigerant saturation temperature were held constant.

The saturation temperature in the test section was held constant at $14^{\circ}\text{C} \pm 0.2^{\circ}\text{C}$ (57.2°F)

$\pm 0.36^\circ\text{F}$) while the heat flux was held at $27,000 \text{ W/m}^2$ ($8700 \text{ Btu}/(\text{hr}\cdot\text{ft}^2)$) and allowed to vary no more than 5%. This produced water temperatures which were similar to those found during actual condensation tests ($\approx 24 - 31^\circ\text{C}$ ($75.2 - 87.8^\circ\text{F}$)). Saturation temperature was maintained at a constant value by controlling the temperature of the glycol flowing to the downstream condenser, which in turn controlled the saturation pressure in the test section. The water temperature was held constant by holding the saturation temperature constant and by adding a constant amount of heat in the electric water heater. Water flow rates were varied over and beyond the range of flow rates found during actual condensation tests, from 5 - 23 kg/min (11 - 51 lb/min).

The heat transfer of the water flowing through the tubes was determined using the following equations:

$$q = \dot{m}_w C_p (T_{w,in} - T_{w,out}) = U_o A_o \times \text{LMTD} \quad (4.1)$$

where

$$\text{LMTD} = \frac{(\Delta T_1 - \Delta T_2)}{\ln(\Delta T_1 / \Delta T_2)} \quad (4.2)$$

$$\frac{1}{U_o} = \frac{A_o}{A_i} \frac{1}{h_i} + \frac{1}{h_o} + A_o R_{tw} \quad (4.3)$$

$$h_i = \text{STC} \frac{k_w}{D_i} \text{Re}_w^8 \text{Pr}_w^{33} \left(\frac{\mu_w}{\mu_{tw}} \right)^{.14}, \quad (4.4)$$

the thermal resistance of the wall R_{tw} in Equation 4.3 is

$$R_{tw} = \frac{\ln(D_r / D_i)}{2\pi k_{tw} L}, \quad (4.5)$$

and the temperature differences ΔT_1 and ΔT_2 in Equation 4.2 are defined by

$$\begin{aligned} \Delta T_1 &= T_{w,in} - T_{sat} \\ \Delta T_2 &= T_{w,out} - T_{sat}. \end{aligned} \quad (4.6)$$

Equation 4.4 is a form of the Sieder-Tate equation for flow in circular ducts, where STC is the Sieder-Tate coefficient, a value which varies for different geometries. In this equation, all water properties should be evaluated at the average bulk temperature $(T_{w,in} + T_{w,out})/2$, except for the parameter μ_{tw} , which should be evaluated at the tube wall temperature. However, since the tube wall temperature could not be calculated for these tests, μ_{tw} was evaluated at $(T_{sat} + T_{w,bulk})/2$.

The functional equation for the experiment is found by substituting Equation 4.4 into Equation 4.3:

$$\underbrace{\frac{1}{U_o} - A_o R_{tw}}_Y = \underbrace{\frac{1}{h_o}}_a + \underbrace{\frac{1}{STC} \frac{A_o/A_i}{\frac{k_w}{D_i} Re_w^{.8} Pr_w^{.33} \left(\frac{\mu_w}{\mu_{tw}}\right)^{.14}}}_X \quad (4.7)$$

Equation 4.7 has the form

$$Y = a + bX, \quad (4.8)$$

a linear relationship between X and Y , where Y is the dependent variable (a function of the overall heat transfer coefficient) and X is the independent variable (a function of water mass flow rate and temperature). Both X and Y could be calculated from the data and plotted for each test point.

The unknowns in Equation 4.7, represented by the intercept a and the slope b in Equation 4.8, are the inverse of the shell-side heat transfer coefficient for boiling and the inverse of the STC , respectively. They were calculated by plotting the X - Y pairs and doing a linear regression through the data points. Ideally, with both the heat flux and saturation temperature held constant through the course of each test both a and b should also be constant.

Figures 4.1 and 4.2 show the test results for the four different tube geometries. Figure 4.1 shows the results for the 26-fpi and 40-fpi tubes while Figure 4.2 shows the Tu-Cii and G-SC results. As can be seen in both figures, the STC appears to remain constant over the flow

Table 4.1: STC for the four tube geometries

Tube	Re_D Range	STC
26-fpi	$8100 < Re_D < 34,000$	0.058
40-fpi	$7500 < Re_D < 26,000$	0.055
Tu-Cii	$7100 < Re_D < 26,000$	0.065
G-SC	$8000 < Re_D < 34,000$	0.054

rate range of interest for all four tube geometries. The calculated STCs are also tabulated in Table 4.1 over the specific test Re_D ranges of each tube. For the fin tubes, the experimentally determined values of STC differ from the manufacturer's values by less than 5%.

Rig Operation

Before data could be taken, the system had to be leak tested and charged with refrigerant. First, the system was charged with high pressure (110 psia) air and let set for eight to twelve hours. If negligible pressure loss was found, the system was evacuated under high-vacuum for another eight hours and allowed to set again to check for leaks under vacuum. If still no leaks were found, the system was charged with refrigerant and the refrigerant de-gassed for eight hours. De-gassing removed any air that may have leaked into the system during charging, and, in the case of HCFC-123, removed any residual nitrogen that may have dissolved into the refrigerant during shipping. The refrigerant was then checked for the presence of non-condensable gases by storing the refrigerant in the test section, where it was allowed to come to thermal equilibrium with the environment. Its saturation temperature was computed from the saturation pressure and checked against the thermistor probes in the test section. If differences outside the accuracy of the transducers was found, the de-gassing procedure was repeated.

Once the system had been charged and de-gassed, condensation data could be taken. The different procedures used are outlined in the following sections.

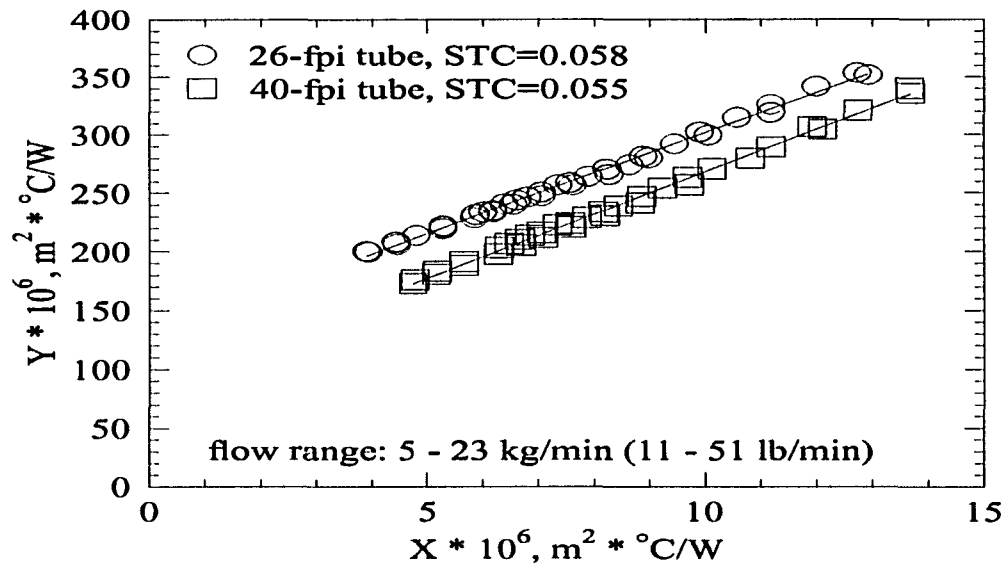


Figure 4.1: Water-side STC data for the 26-fpi and 40-fpi geometries

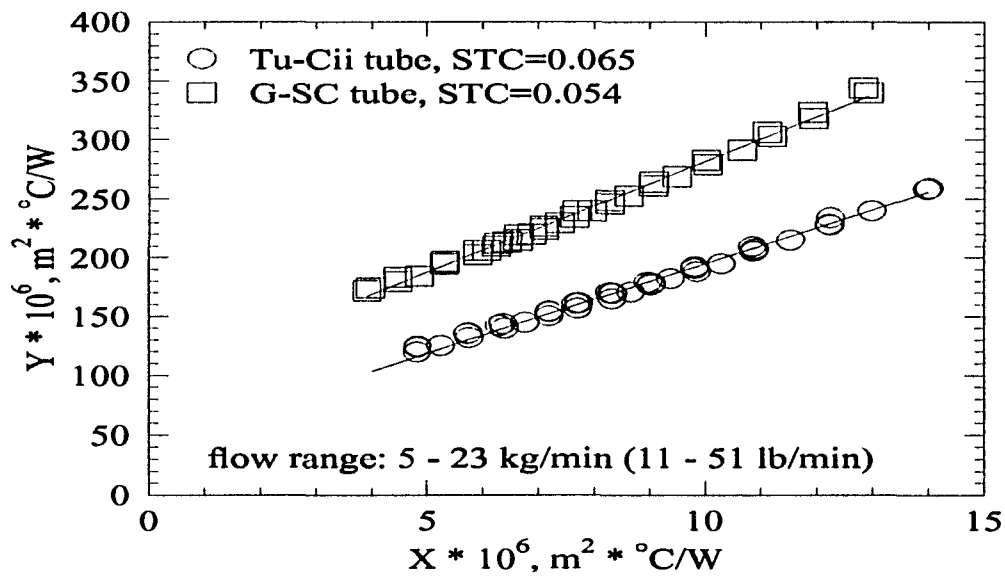


Figure 4.2: Water-side STC data for the Tu-Cii and G-SC geometries

Non-condensable gases

Tests were performed with 25-tube bundles of each tube geometry to determine the effect of non-condensable gases on the condensation of HCFC-123. Data were recorded at four different values of nominal bundle energy rate transfer from 18 kW (60,750 Btu/hr) to 30 kW (102,000 Btu/hr) at increasing increments of 4 kW (13,600 Btu/hr). Four different concentrations of non-condensable gas, 0.5%, 1.0%, 2.0%, and 5.0% were tested, using nitrogen as the non-condensable gas.

Nitrogen concentrations were based on the volume of the test section and the diameter of the tubes being tested. The total volume of the test section was calculated using

$$V_{ts} = \frac{\pi}{4} L (D_{ts}^2 - 25D_o^2) \quad (4.9)$$

where D_{ts} is the inner diameter of the test section, D_o is the outer diameter of the tubes in the bundle, and L is the length of the test bundle. The condenser volume, which was very similar for all four bundles, was approximately 15,500 cm³. Nitrogen volumes were calculated at test conditions for HCFC-123 ($T_{sat} = 35^\circ\text{C}$ (95°F), $p_{sat} = 130.3$ kPa (18.90 psia)) and then determined at laboratory atmospheric conditions, the condition at which the nitrogen was injected, using the ideal gas law:

$$V_{N_2,atm} = V_{N_2,sat} \frac{p_{sat}}{p_{atm}} \frac{T_{atm}}{T_{sat}}. \quad (4.10)$$

Values for the volume of nitrogen injected at the various concentrations for all bundles are presented in Table 4.2.

Condensation tests with concentrations of nitrogen were conducted using the following procedure:

1. The water pump was activated and the water temperature controller and the water flow rate were set to the levels corresponding to the energy transfer rate being tested. Water

Table 4.2: Volumes of N₂ injected into test section.

% N ₂	$V_{N_2,ts}$ cm ³	$V_{N_2,atm}^a$ cm ³
26-fpi		
0.5%	77.8	98.6
1.0%	155.5	197.2
2.0%	311.0	394.3
5.0%	777.6	985.8
40-fpi		
0.5%	77.5	97.6
1.0%	155.1	195.2
2.0%	310.1	390.4
5.0%	775.3	975.9
Tu-Cii		
0.5%	77.5	97.6
1.0%	154.9	195.2
2.0%	309.9	390.4
5.0%	774.7	976.0
G-SC		
0.5%	77.4	98.0
1.0%	154.7	195.9
2.0%	309.4	391.8
5.0%	773.6	979.5

^aCalculated at laboratory conditions

- temperature was adjusted to maintain a saturation temperature in the test section of $35^{\circ}\text{C} \pm 0.1^{\circ}\text{C}$ ($95^{\circ}\text{F} \pm 0.18^{\circ}\text{F}$). Water flow rate was set to keep the temperature rise of the water across the test section to $2^{\circ}\text{C} \pm 0.1^{\circ}\text{C}$ ($3.6^{\circ}\text{F} \pm 0.18^{\circ}\text{F}$).
2. The refrigerant pump was started and the boiler and superheaters activated at low power levels. These levels were slowly increased over approximately ten minutes to the appropriate levels for the test, which at final steady state conditions were set to produce inlet vapor to the test section with between $3 - 5^{\circ}\text{C}$ ($5.4 - 9^{\circ}\text{F}$) superheat.
 3. The throttling valve at the exit to the test section was adjusted to keep a small, constant

level of refrigerant liquid at the bottom of the test section. This forced all condensation to occur in the test section and prevented any non-condensable gas from escaping over the duration of the experiment.

4. Once a constant level of liquid had been established in the test section, an appropriate volume of nitrogen was injected into the test section through a charging valve placed in an auxilliary port of the pressure vessel.
5. Final adjustments were made to the water temperature controller, boiler, and superheaters, and the test section was allowed to come to steady state. Steady conditions were indicated by negligible changes in inlet water temperature and saturation temperature over several scans of the rig transducers.
6. At steady state, ten scans were made by the data acquisition system and recorded to five separate files on the controlling computer's hard drive. Approximately 12 minutes were required to make all ten scans.
7. After ten scans had been recorded, the water and refrigerant flow rates, boiler and superheater power levels, and water temperature controller were adjusted to levels for the next data point. Steps 3, 5, and 6 were repeated until data at four different nominal energy transfer rates had been recorded at a single non-condensable gas concentration.
8. The data files corresponding to each of the data points were moved to another computer for data analysis. A spreadsheet program was used to sort the data, look for anomalies, and average the ten scans, while a FORTRAN program was used take the averaged data and calculate the bundle and row-by-row heat transfer coefficients and their associated experimental uncertainties.
9. Steps 1 through 7 were repeated until data had been collected at all nominal energy

transfer rates and nitrogen concentrations with all four tube geometries.

In order to calculate the shell-side condensing coefficients, the following parameters were measured: the temperature of the refrigerant entering and leaving the test section, the bulk temperature of the water entering and leaving the test section, the temperature of the water leaving the middle tube of each bundle row, the refrigerant pressure in the test section, and the refrigerant and water mass flow rates.

Liquid inundation with HFC-134a

As discussed in the previous chapter, the same five tube rows were used to simulate up to thirty tube rows in an actual condenser. As a result, the experimental procedures had to be modified from those used to take the full bundle data for non-condensable gas contamination discussed above.

In order to maintain constant conditions during each test run and produce data which could be compared on the basis of constant test conditions, the water inlet temperatures were held constant. This procedure simulated a single-pass condenser with constant water inlet temperature. Thus, while the quality of the refrigerant passing through the condenser at any given time could vary, individual tubes undergoing varying inundation rates could be compared on the basis of constant water-side inlet conditions and flow rate.

Refrigerant flow of known vapor quality was produced in the boiler of the refrigerant flow loop. This mixed flow was then introduced into the test section where the liquid portion was collected and distributed. A combination of impingement plates, a screen, and a row of drip tubes with holes drilled along the bottom (discussed in Chapter 3 and shown in Figure 3.3) insured that the liquid was collected and distributed evenly along the length of the test section. This mixed flow approach guaranteed that the liquid and vapor portions were in equilibrium during each test run.

Inundation was simulated by artificially controlling the refrigerant inlet conditions during each test run. At any given water flow rate and inlet water temperature, only a portion of the vapor in the test section was condensed on the tube bundle. The energy transfer rate from the vapor to the cooling liquid was calculated from the water-side temperature rise using

$$q_w = \dot{m}_w C_{p,w} (T_{w,out} - T_{w,in}). \quad (4.11)$$

Assuming all the energy transferred to the water was from refrigerant phase change, the refrigerant enthalpy at the exit could be calculated from

$$i_{out} = i_{in} - \frac{q_w}{\dot{m}_r}. \quad (4.12)$$

The exit quality was calculated by a computer refrigerant-property subroutine which determined the quality iteratively, based on the saturation pressure in the test section and refrigerant enthalpy calculated above. During the next test run, the exit quality could then be reproduced at the inlet to the test section to simulate the conditions at the bottom of the test section during the previous test run. The liquid portion of the flow was distributed over the active tubes of the bundle to simulate the condensate flowing off the bottom row of tubes. Thus, it was possible to simulate a continuous quality change from 100% to 0% through the entire course of the test.

Test runs could be performed for a variety of heat flux loads and inundation rates. By setting the refrigerant loop at a maximum flow rate and maximum boiler energy input, and varying the water inlet temperature and flow rate, it was possible to simulate a range of heat fluxes. At higher water inlet temperatures, T_{sw} was reduced and less energy was removed from the refrigerant. This meant that more test iterations, or refrigerant passes, were required to go from 100% saturated vapor to completely saturated liquid. For example, by condensing all the vapor in three passes (i.e. condensing approximately 33% of the vapor during each pass) and taking measurements on five rows of tubes per pass, a total of fifteen tube rows could

Table 4.3: Test section conditions for a 30-row bundle simulation; refrigerant flow rate, water flow rate, water temperature held constant

Test Pass	Quality ^a x_{in}	Quality ^b x_{out}	T_{sat} ^c °C	Simulated Tubes
1	100%	84%	35.0	1 - 5
2	84%	66%	35.0	6 - 10
3	66%	50%	35.0	11 - 15
4	50%	34%	35.0	16 - 20
5	34%	16%	35.0	21 - 25
6	16%	0%	35.0	26 - 30

^aSet using boiler

^bDetermined by water flow rate and temperature

^cControlled by downstream condenser

be simulated. This is analogous to having three condensers in series which have identical water flow rates and inlet temperatures, each of which condense approximately 33% of the vapor. By running each experiment with more refrigerant passes (i.e. adding more condensers in the series connection) a larger number of overall tube rows could be simulated. An example 30-row simulation test is outlined in Table 4.3, with the relevant test section conditions noted for each phase of the test.

Values in the table are based on a test with no apparent inundation effects. Thus, each refrigerant pass condenses equally, regardless of the liquid loading on the tubes. In a bundle simulation with large inundation effects, the percentage of vapor condensed in each pass would be expected to decrease as the inundation flow rate increased and heat transfer performance on lower tube rows decreased.

The following procedure was used to simulate inundation in the test section:

1. The water loop was started and the water temperature controller and water pump were set to levels corresponding to the number of tubes being simulated. For example, during a test simulating a 15-row condenser, the water flow rate and inlet temperature were

set so that the bulk water temperature change across the test section was approximately 2°C and three different tests, or refrigerant passes, would be required to go from 100% saturated vapor to 0% vapor.

2. The glycol pump was activated and glycol was pumped to the refrigerant storage vessel/subcooler and to the glycol-to-water heat exchanger in the water loop. This cooled the refrigerant liquid sufficiently to begin pumping and helped control the temperature in the water loop, which was being heated by the electric water heaters.
3. The refrigerant pump was activated and the boiler turned on at low power levels to begin the boiling process and start a small amount of condensation in the test section. Boiler inlet energy and total refrigerant flow rate were slowly increased to test levels over the course of about ten minutes.
4. Glycol circulation to the secondary condenser downstream from the test section was started to control the saturation pressure in the test section. The cooled glycol flow guaranteed that any excess vapor not condensed in the test section would be returned to liquid form prior to circulation by the refrigerant pump. The total glycol flow rate to this condenser was slowly adjusted to maintain the proper saturation temperature in the test section once a steady inlet water temperature to the test section had been reached.
5. Vapor quality from the boiler was calculated using the inlet refrigerant temperature to the boiler, the mass flow rate of refrigerant entering the boiler, the electrical energy supplied to the boiler, and the boiler exit pressure. For the first pass, the quality was set at between 99%-100% to minimize any liquid or superheated vapor entering the test section. A section of electrically heated piping originally used for superheating was turned on at low power to maintain a constant piping wall temperature of T_{sat} between the boiler and the test section and to prevent any losses to the environment.

6. The system was allowed to come to steady state at constant $T_{sat} = 35^{\circ}\text{C}$ (95°F), constant test section inlet refrigerant quality of 99%-100%, and constant water inlet temperature. These parameters were allowed to vary no more than 0.1°C (0.18°F), .5%, and 0.1°C (0.18°F), respectively.
7. Once steady state had been reached, as defined by minimum variations in the saturation temperature and water inlet temperature, ten scans of all measuring devices (thermocouples, thermistors, flowmeters, etc.) were made using the computerized data acquisition system. Approximately 12 minutes were required to make all ten scans. Data was written to five separate data files, which were sorted and averaged using a spreadsheet macro during the data reduction phase.
8. The exit quality was recorded. Once ten measurement scans were completed, the boiler energy was reduced in order to reduce the vapor quality at the inlet to the test section to the level of the exit quality just recorded. Glycol flow to the downstream condenser was decreased to maintain T_{sat} , which fell due to the lower boiler energy input.
9. Steps 5 through 8 above were repeated at the new inlet condition until the vapor was completely condensed. Water inlet temperature, water flow rate per tube, and saturation temperature were kept constant during the course of the entire experiment.

Vapor shear and liquid inundation with HCFC-123

Combined shear and inundation tests were conducted in a similar manner to the tests for liquid inundation alone, except that the velocity entering the top row of the bundle was also varied by increasing the refrigerant flow rate. Three different flow rates were used to produce three different vapor velocities. Inundation tests identical to those discussed above were conducted at each refrigerant flow rate for a combination vapor shear and inundation

test. However, due to large uncertainties in the water temperature difference at low heat fluxes (i.e. low refrigerant flow rates), simulations were limited to 25-row bundles.

Data Reduction

The data from the 10 scans were loaded into a spreadsheet to be inspected for any anomalies. Each type of experiment (non-condensable gas, liquid inundation, vapor shear) used a spreadsheet specific to that test. The data was then averaged and the averages written to another data file. Finally, this file of averaged data was read by a FORTRAN program which computed the shell-side heat transfer coefficients using the equations listed below.

The shell-side heat transfer coefficient was calculated using the log-mean temperature difference (LMTD) method. In this approach, the heat transfer rate for the heat exchanger is found by

$$q = U_o A_o \times \text{LMTD}. \quad (4.13)$$

The log-mean temperature difference (LMTD) is defined as

$$\text{LMTD} = \frac{(\Delta T_1 - \Delta T_2)}{\ln(\Delta T_1 / \Delta T_2)} \quad (4.14)$$

where

$$\Delta T_1 = T_{sat} - T_{w,in} \quad (4.15)$$

$$\Delta T_2 = T_{sat} - T_{w,out}, \quad (4.16)$$

while the overall heat transfer coefficient of the heat exchanger U_o is defined by

$$\frac{1}{U_o} = \frac{A_o}{A_i} \frac{1}{h_i} + \frac{1}{h_o} + A_o R_{tw}, \quad (4.17)$$

where h_i is the water-side heat transfer coefficient defined by Equation 4.4.

The energy transfer rate q can be calculated from either the refrigerant energy transfer rate

$$q = \dot{m}_{ref}(i_{ref,out} - i_{ref,in}) \quad (4.18)$$

or the water energy transfer rate

$$q = \dot{m}_w C_p (T_{w,out} - T_{w,in}). \quad (4.19)$$

For the bundle heat transfer coefficient calculations, the refrigerant energy transfer rate and the bulk water-side energy transfer rate typically differed by less than 5%, so the two values were averaged to determine the energy transfer rate for the bundle. For the row heat transfer coefficient calculations, the energy transfer rate could only be determined from the water-side flow. In the case of the row coefficients, the tube flow rate was assumed to be 1/25th of the bulk flow rate. Experimental measurement of the water flow rates from the middle tube of each row indicated that the actual flow rate differed from the assumed tube flow rate by less than 1%.

Following the calculation of q , U_o was calculated from Equation 4.13. The shell-side heat transfer coefficient, h_o , was then calculated by rearranging Equation 4.17:

$$h_o = \left[\frac{1}{U_o} - \frac{A_o}{A_i} \frac{1}{h_i} - A_o R_{tw} \right]^{-1} \quad (4.20)$$

The temperature of the outer tube surface, which was used to find the driving temperature difference ($T_{sat} - T_{s,o}$), was calculated using

$$T_{s,o} = T_{w,bulk} + q \left(\frac{1}{\pi D_i L h_i} + \frac{\ln(D_r/D_i)}{2\pi k_{tw} L} \right) \quad (4.21)$$

This method was used to calculate the average shell-side heat transfer coefficients for the middle tube of each row as well as the average shell-side bundle heat transfer coefficients. The length of enhanced tube surface exposed to the refrigerant (603 mm (23.75 in)) and the

nominal outer tube diameter were used in the calculation of the outer surface area. This area, which is equivalent to the area of a smooth tube with the same outer diameter, was used in place of the actual surface area, since the actual areas of the enhanced tubes were not known. Using the nominal outer surface area allowed comparisons to be made between all the geometries tested on a nominal area and a unit length basis. The tube dimensions used in the heat transfer coefficient calculations are given in Table 3.1.

As a check on the tube energy transfer rates, the FORTRAN program computed an estimate of bundle heat flux based on the middle tube heat fluxes by multiplying each tube heat flux by five, adding the weighted tube heat fluxes together, and dividing the result by 25. The actual bundle heat flux and estimated heat flux generally differed by less than 5%.

The condensate Reynolds number, Re_L , used to characterize the flow of refrigerant liquid from each tube during the inundation and vapor shear portions of the study, is defined by

$$Re_L = \frac{4\Gamma}{\mu_f} \quad (4.22)$$

where Γ is the condensate flow rate from the tube per unit length of the tube.

The condensate flow rate from each tube was based on the inlet quality and the amount of energy removed from the tube during the test. For each of rows one and two, the inundation rate was assumed to be equal and was calculated as approximately half (47.5%) the flow rate from the liquid portion ($\dot{m}_{f,in}$) of the refrigerant entering the test section, given as

$$\dot{m}_{f,in} = \dot{m}_{r,tot} - x_{in}\dot{m}_{r,tot} \quad (4.23)$$

The total condensate flow for tubes one and two, then, was the amount of liquid inundating that tube plus the liquid condensed on the tube during the test, assuming minimal subcooling of the condensate:

$$\Gamma_N = \frac{\dot{m}_{f,in}}{L} + \frac{q_{w,N}}{i_{fg}L} \quad (4.24)$$

As noted in Chapter 3, the drainage in a staggered bundle is not from the first to the second rows, but from the first to the third to the fifth rows, etc. Therefore, the inundation rates for rows three through five were governed by

$$\Gamma_N = \Gamma_{N-2} + 0.95 \frac{q_{w,N}}{i_{fg}L} \quad (4.25)$$

assuming that 95% of the liquid coming off tube $N - 2$ reaches tube N by draining vertically, and the rest drains sideways to the dummy tubes in row $N - 1$.

The mean local vapor velocity of the refrigerant was calculated using the method of Nobbs and Mayhew (1976), in which velocity is based on the mean flow width between tubes. The width is defined by

$$w = \frac{p_l p_t - \pi \frac{D_o^2}{4}}{p_l} \quad (4.26)$$

where p_l and p_t are the longitudinal and transverse pitches of the tubes, respectively, and D_o is the tube outer diameter. Using this approach with a nominal 19.1 mm (0.75 in) o.d. tube and longitudinal and transverse pitches of 19.1 mm (0.75 in) and 22.2 mm (0.875 in), respectively, yields a mean flow width of 7.26 mm (0.286 in). This compares to 3.18 mm (0.125 in), which is the minimum flow width between tubes in the same row based solely on the transverse (horizontal) pitch. Thus, the velocities calculated using mean flow width are approximately 2.3 times smaller than those calculated using the minimum flow width between adjacent tubes in the same row.

The mean flow area A is based on the number of tubes of the bundle. The vapor flow passed only one active tube in the top row of the bundle, corresponding to a flow area of $2wL$.

Given the flow area, the average velocity was calculated using the one-dimensional conservation of mass equation:

$$U_\infty = \dot{m}_r v_r A \quad (4.27)$$

The specific volume of the refrigerant, v_r , was based on the inlet quality of the flow and the

saturation pressure in the test section and was calculated by the refrigerant-property subroutine mentioned above.

Uncertainty of the Shell-side Heat Transfer Coefficients

Since the transducers used to obtain parameter measurements from the experimental test facility are real devices, the measurements returned by the transducers are subject to some uncertainty. Thus, the calculated shell-side heat transfer coefficients based on transducer measurements are also subject to experimental uncertainty.

The method of propagation of errors (Holman (1984)) is used to determine the experimental uncertainty in the calculated heat transfer coefficients. This method calculates the uncertainty in the heat transfer coefficients as a function of the sum of the squares of the uncertainties in the independent variables. A derivation of the equations used to calculate the experimental uncertainty in the shell-side heat transfer coefficients is given in Appendix A, while the calculated uncertainties for each of the individual tests are given in Appendices B, C, and D, along with the measured parameters and calculated data in tabular form.

Data Presentation

Data is presented differently for each of the different types of condensation tests. The different graphical presentation styles for these tests are described in the following paragraphs.

Non-condensable gas results

Results of the tests conducted to determine the effect of the presence of non-condensable gases on the condensation of HCFC-123 are presented in several forms. Average shell-side condensation heat transfer coefficients for the bundle are plotted as function of the percentage of non-condensable gas against the driving water-refrigerant temperature difference (h_o vs.

LMTD) and the average bundle heat flux (h_o vs. q''). Average condensation heat transfer coefficients for the middle tube of each row are presented as a function of the percentage of non-condensable gas by volume and the row number (h_o vs. tube row). Data is presented for all four types of condensation tube geometries.

Liquid inundation

Because only the five center tubes of each row were being used to collect data to simulate drainage in bundles up to the thirty rows deep, the form of the data presentation for the liquid inundation tests is quite different from that of the bundle tests conducted with non-condensable gases.

For several of the tubes, most notably the two tubes with enhanced shell-side geometries, the drip pattern was as important to the overall performance of the tube as was the condensate flow rate over the tube. This meant that even though the condensate flow rate over the tube was controlled, the heat transfer coefficients from the tubes were not believed to be accurate unless the drip patterns were indicative of the actual patterns in a condenser at that particular flow rate.

For this reason, the data from all the tubes were not used for presentation and correlations. Rather, only the data from the last two tube rows were used. The first three tube rows, while also instrumented, were used to establish drip patterns. During the first run of a test, with a 100% inlet quality and no inundation, the flow patterns for all five tubes were believed to be accurate. Thus, for any given test, the data from the five tubes in the first pass and the data from tubes four and five in subsequent passes were used. For example, in a 30-row simulation only the data from tubes 1 through 5, 9, 10, 14, 15, 19, 20, 24, 25, 29, and 30 were used.

Plots are presented to show the effect of tube row (h_o vs. tube row) for both the 5-row test bundle and the simulated bundles. Two different tests, a 15-row and 30-row simulation, are

given for each tube. Figures showing the effect of condensate inundation rate (h_o vs. Re_L) are also shown, along with plots of the average tube heat transfer coefficients as a function of the temperature difference T_{sw} (h_o vs. $(T_{sat} - T_{s,o})$). As noted above, tube surface areas are based on the outer diameter of the tube fins to allow comparison on a per length of tube basis.

Combined vapor shear and liquid inundation results

Presentation of the results of the vapor shear portion of the study is very similar to that used for the liquid inundation results described above. In addition, plots showing the combined effect of vapor velocity through the first row of each of the bundles and inundation in the lower rows of simulated bundles are shown for both the 5-row test bundle and the simulated bundles. Because of large uncertainties associated with low heat fluxes, only 25-row simulations are shown. This is discussed in more detail in Chapter 7.

CHAPTER 5. THE EFFECT OF NON-CONDENSIBLE GASES ON THE CONDENSATION OF HCFC-123

Non-condensable gases, or gases which do not condense under the conditions normally found in refrigeration condensers, have a detrimental effect on the condensation of pure refrigerants. First, they lower the effective saturation pressure and temperature of the refrigerant vapor, thereby reducing the driving condensation temperature difference ($T_{sat} - T_g$) and, as a consequence, the overall heat transfer performance of the tube. Second, the motion of the refrigerant vapor draws the gases to the condensation surface of the tube where they collect and form a thin layer through which the refrigerant vapor must pass in order to condense. This inhibits the condensation process and decreases the heat transfer performance by lowering the effective vapor saturation pressure and temperature even further.

Tests were conducted to determine the effect of varying nitrogen concentrations (based on condenser volume) in the condenser using all four tube geometries. Nitrogen concentrations of 0.5, 1.0, 2.0, and 5.0% were tested with HCFC-123 at heat fluxes between approximately 20,000 and 34,000 W/m² (6340 and 10,780 Btu/h/ft²). These results were then compared to pure refrigerant data reported by Huber (1995a, 1995b).

Both the heat transfer coefficient and heat flux calculations are based on the nominal tube surface area, or envelope area, of each tube. This area is calculated with the outer fin diameter of the tube and is used so that the heat transfer performance of the tubes may be compared, as it is not possible to calculate the actual surface area of the Tu-Cii. Using the nominal area also allows the tubes to be compared on a unit length basis.

Results of the 26-fpi Geometry

Bundle performance

The performance of the 26-fpi bundle was characterized by a gradual decrease in average bundle heat transfer coefficients with increasing concentrations of nitrogen. Figures 5.1 and 5.2 illustrate this gradual decrease. Figure 5.1 presents the average bundle heat transfer coefficients as a function of the LMTD across the condenser, while Figure 5.2 presents the same coefficients in terms of the overall bundle heat flux. The pure refrigerant data were reported by Huber (1995a).

Both figures show the drop in heat transfer coefficient with the addition of only a small amount nitrogen. Comparing the data taken at the lowest heat flux to the comparable data for 0% non-condensable gas concentration, there is a 19% decrease in heat transfer coefficient for 0.5% concentration, a 26% decrease for 1.0% concentration, a 37% for 2.0% concentration, and a nearly 57% decrease at a 5.0% N₂ concentration. At the highest heat fluxes these decreases are approximately 12%, 17%, 24%, and 40% at the same concentrations, respectively. Thus, the effect of non-condensable gases is not as large at the higher heat flux.

This trend towards lower dependence on gas concentration at higher heat fluxes can be seen in both figures, particularly at the highest nitrogen concentrations, where the trends tend to have positive slopes and the average heat transfer coefficients increase with increasing heat flux. This trend is believed to be caused by a vapor shearing effect in the gas layer surrounding the tube surface. An increasing heat flux corresponds to an increase in refrigerant mass flow rate and an increase in the vapor velocity through the test section. At higher velocities, the refrigerant vapor strips some of the non-condensable gas layer away from the surface of the tube, which allows more vapor to condense and increases the overall tube heat transfer performance.

At the high heat fluxes, where these same trends begin to level off, it is believed that

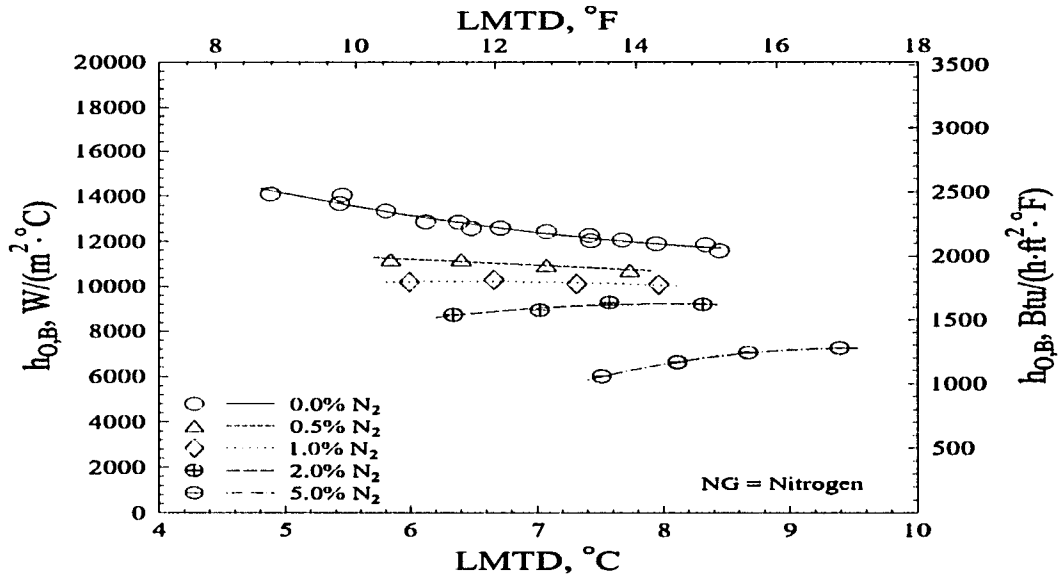


Figure 5.1: Average shell-side bundle heat transfer coefficient vs. LMTD for the 26-fpi bundle at various nitrogen concentrations during condensation with HCFC-123

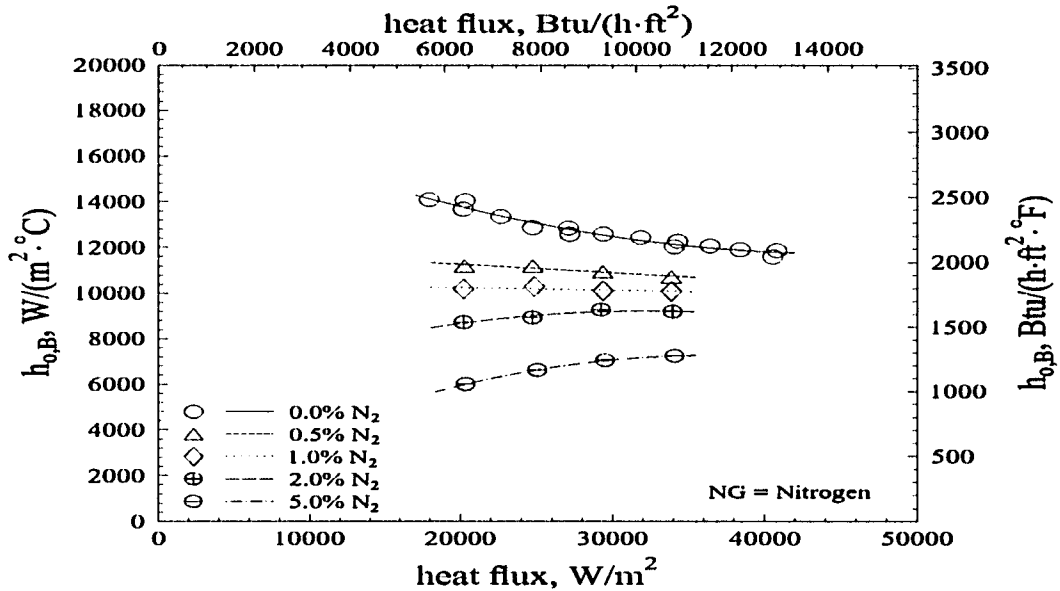


Figure 5.2: Average shell-side bundle heat transfer coefficient vs. heat flux for the 26-fpi bundle at various nitrogen concentrations in condensation with HCFC-123

liquid loading on the tube surface becomes more important and the shearing effects in the non-condensable gas layer no longer dominate. It is believed that at even higher heat fluxes, beyond the range of this data, the effects will slowly reverse so that resistance to heat transfer in the liquid layer will begin to dominate, resulting in a drop in the non-condensable gas shearing effects and a decrease in the heat transfer performance.

At the lower N_2 concentrations (0.5 and 1.0%) there is no increase in heat transfer performance with increasing heat flux. This could be caused by one of two phenomena. First, it may indicate that at low concentrations the non-condensable gases are trapped within the fin spaces below the boundary layer and are not easily stripped from the tube surface by increasing vapor velocities. Second, it may be that most, but not all, of the non-condensable gas gets stripped from the tube at low concentrations, thereby producing a trend similar to that at 0% concentration. For whichever reason, the fact that the trends at these low concentrations actually decrease slightly would also seem to indicate that once the heat transfer has been decreased at low non-condensable gas concentrations, liquid loading dominates, and shearing effects in the gas layer are for the most part negligible.

Row-by-row performance

The row-by-row behavior of the tube bundle is shown in Figures 5.3 through 5.6. The decrease in performance with increasing non-condensable gas concentration, discussed above for the full bundle, is also apparent in these figures for the individual tube rows. The multiple curves which appear in Figures 5.3 and 5.6 for the pure refrigerant data are indicative of repeatability tests during the pure refrigerant experiments. Contamination with 0.5%, 1.0%, 2.0%, and 5.0% N_2 causes drops in individual row heat transfer coefficients of approximately 16%, 25%, 39%, and 60%, respectively, from the performance for pure refrigerant.

It is interesting to note that while the overall heat transfer coefficients drop, the row-by-

row bundle profile stays relatively the same throughout the course of the test at all heat fluxes and N₂ concentrations. It may be that the relatively large fin spaces (compared to the short finned 40-fpi tube) allowing shearing effects to keep the gas layer around each tube relatively small uniform throughout the bundle. Thus, it is believed that the consistent profile indicates a relatively even vertical distribution of nitrogen within the test section, so that no one row or group of two or three rows near the top of the condenser is more affected.

Results for the 40-fpi Geometry

Bundle performance

The 40-fpi bundle appeared to be slightly more affected by the presence of nitrogen than was the 26-fpi bundle, particularly at low (0.5%) concentrations. The overall bundle performance is shown as a function of the refrigerant-to-water temperature difference (LMTD) and the average heat flux in Figures 5.7 and 5.8, respectively. As with the 26-fpi data, the pure refrigerant data was reported earlier by Huber (1995a).

The data in both figures show the initial drop in heat transfer performance with the addition of a small amount of nitrogen. The drop is particularly apparent at the lowest heat flux (smallest LMTD). With the addition of only 0.5% nitrogen by volume, the average bundle heat transfer coefficient drops nearly 26%. At higher concentrations, the performance continues to drop, but at smaller relative amounts with respect to the increases in gas concentration. The performance with a 1.0% nitrogen contamination drops approximately 31% compared to the performance of pure refrigerant, while the performance with 2.0% and 5.0% nitrogen concentrations drops 43% and 63%, respectively. This can be compared to the much smaller decreases in performance at the highest heat flux (largest LMTD). At nitrogen concentrations of 0.5%, 1.0%, 2.0%, and 5.0% the average bundle heat transfer coefficients compared to those of pure HCFC-123 drop by 9%, 14%, 24%, and 43%.

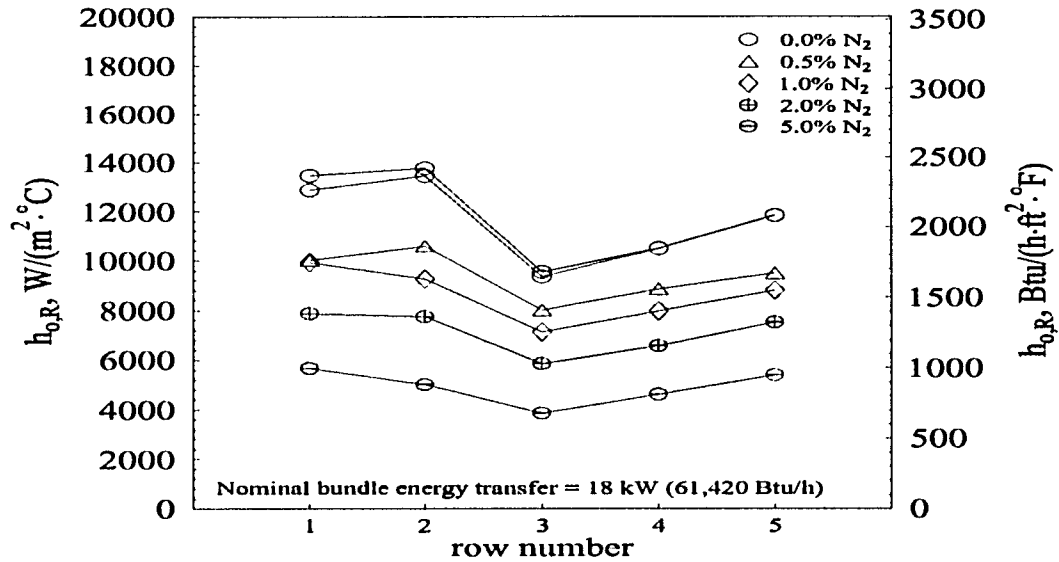


Figure 5.3: Average shell-side row heat transfer coefficient vs. row number for the 26-fpi bundle at various nitrogen concentrations during condensation with HCFC-123; average bundle heat flux = $20,200 W/m^2$ ($6400 Btu/h/ft^2$)

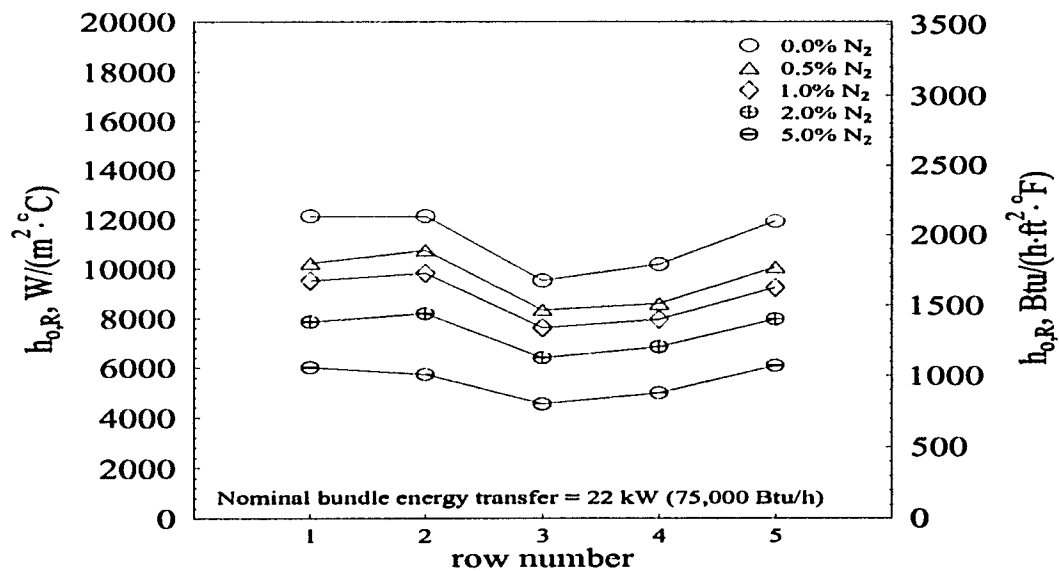


Figure 5.4: Average shell-side row heat transfer coefficient vs. row number for the 26-fpi bundle at various nitrogen concentrations during condensation with HCFC-123; average bundle heat flux = $25,000 W/m^2$ ($7920 Btu/h/ft^2$)

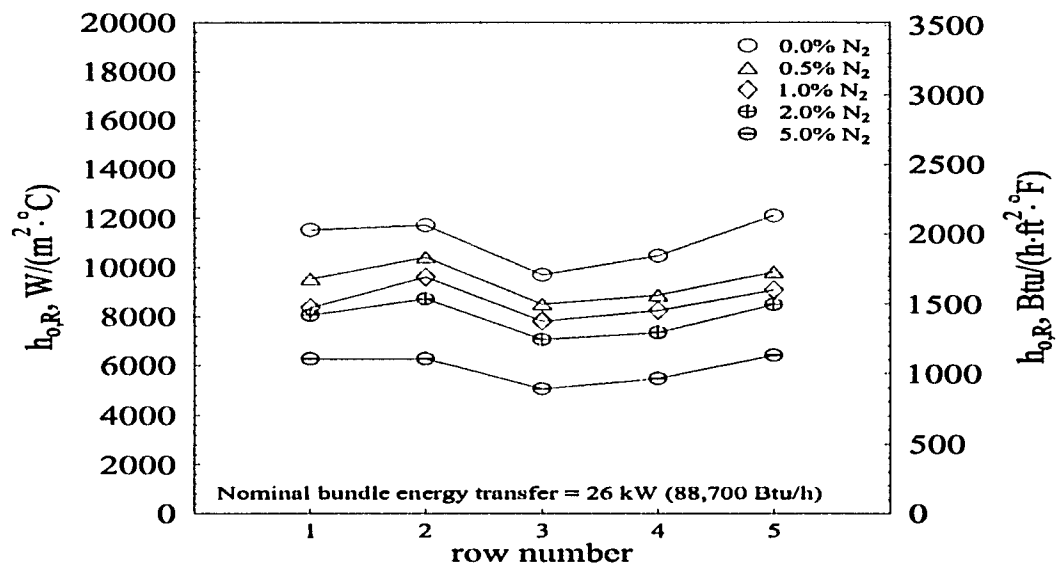


Figure 5.5: Average shell-side row heat transfer coefficient vs. row number for the 26-fpi bundle at various nitrogen concentrations during condensation with HCFC-123; average bundle heat flux = $29,300 \text{ W/m}^2$ (9290 Btu/h/ft^2)

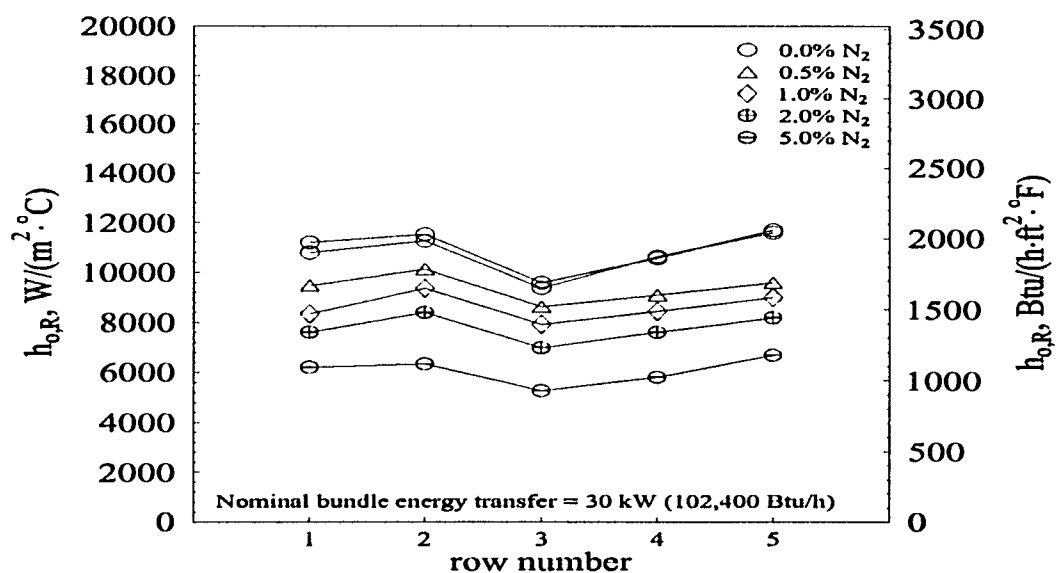


Figure 5.6: Average shell-side row heat transfer coefficient vs. row number for the 26-fpi bundle at various nitrogen concentrations during condensation with HCFC-123; average bundle heat flux = $33,900 \text{ W/m}^2$ ($10,740 \text{ Btu/h/ft}^2$)

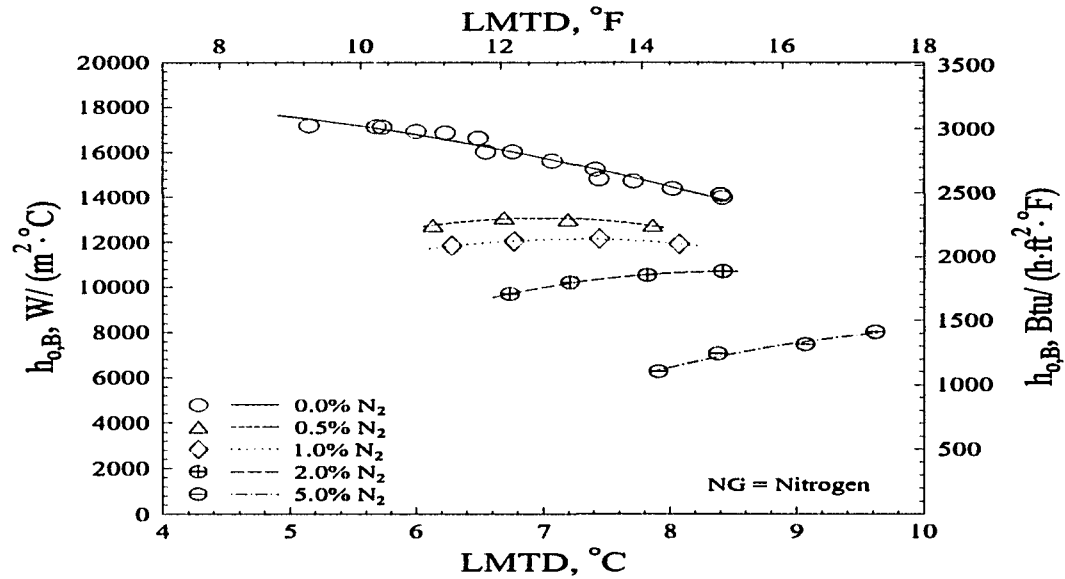


Figure 5.7: Average shell-side bundle heat transfer coefficient vs. LMTD for the 40-fpi bundle at various nitrogen concentrations during condensation with HCFC-123

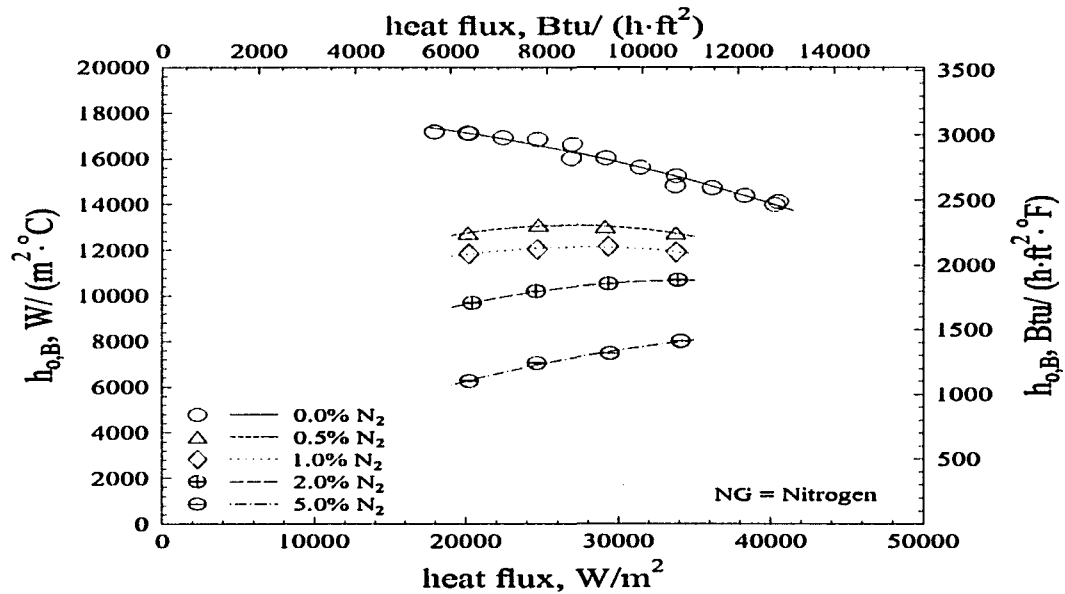


Figure 5.8: Average shell-side bundle heat transfer coefficient vs. heat flux for the 40-fpi bundle at various nitrogen concentrations in condensation with HCFC-123

Again, the increase in heat transfer performance with increasing heat flux is believed to be an effect of vapor shear in the gas layer. However, unlike the 26-fpi geometry which showed a gradual decrease in performance with increasing gas concentrations and relatively little shear dependence below 1.0% gas concentration, the 40-fpi is affected at all heat fluxes and at all gas concentrations. As heat flux, and consequently vapor velocity increase, so does the average bundle performance. Thus, the trends of the data at different gas concentrations seen in Figures 5.7 and 5.8 all have positive slopes, where increasing heat flux corresponds to increasing heat transfer coefficients.

The effects of shear also appear to be slightly more prevalent with the 40-fpi geometry than with the 26-fpi geometry. While the 26-fpi data has decreasing trends (i.e. negligible shear) at the lowest gas concentrations (0.5% and 1.0%), the 40-fpi data show a shallow peak in the data, where the liquid loading effects, which decrease performance, are offset by shear in the non-condensable gas layer, which increases performance. Thus, shear appears to be a contributing factor to the performance of the 40-fpi at low gas concentrations, where liquid loading was the dominating phenomenon with the 26-fpi.

The fact that the 40-fpi appears to be more susceptible to vapor shear in the gas layer is believed to be a result of its shorter, more tightly packed fins, compared to the 26-fpi geometry. With shorter, more closely spaced fins, there is less space between fins for the nitrogen to collect, which means that more of the gas must collect around the perimeter of the tube near the fin tips, where it is more easily stripped from the tubes surface. At the same time, the large initial drop in tube performance at small gas concentrations would seem to indicate the nitrogen that does collect between the fins is held there very closely and is not easily removed by vapor shear effects. Thus, the performance of the low-fin 40-fpi geometry is a balance between two opposing phenomena: nitrogen retention in the inter-fin spaces that is unaffected by shear, and relatively small total inter-fin area which causes a large fraction of the gas to be

collected near the fin tips, where it can be stripped away by vapor shear.

Row-by-row performance

The average row heat transfer coefficients and the row-by-row performance of the tube bundle are shown in Figures 5.9 through 5.12. The decrease in performance in the individual tube rows with increasing non-condensable gas concentration is apparent in each figure, as well as the effect on the highest performing tubes in the bundle. As with the 26-fpi data, those figures with multiple curves for the pure refrigerant data indicate repeatability tests with 0% nitrogen concentrations.

Unlike the row-by-row profiles of 26-fpi bundle, which changed very little from the lowest to the highest gas concentrations, those of the 40-fpi bundle change gradually with increasing nitrogen contamination, until the profiles at the highest concentration (5.0%) are noticeably different from those found with pure refrigerant. The profile of the 40-fpi bundle at 0.0% nitrogen concentration is characterized by peaks in both the first and third rows. However, with the injection of 0.5% nitrogen the first peak seems to nearly disappear. With further contamination, the peak in the third row decreases at a higher rate than that of the performance of the bundle in general. At the highest concentration the profile is much flatter and is characterized by a general decrease from the first through the fifth rows. The first and third rows still outperform the other rows, but only by a very small margin.

This change in row-by-row behavior is thought to be caused by a combination of stratification in the nitrogen in the test section and nitrogen retention in the inter-fin spaces on the tube surface, discussed above. At small concentrations the nitrogen is believed to migrate to the top of the test section in the top rows of the bundle, where it collects in the fin spaces of the first row, dropping its performance. With increasing nitrogen concentrations, the nitrogen moves lower in the test section, collecting in inter-fin spaces, until the spaces of the third row

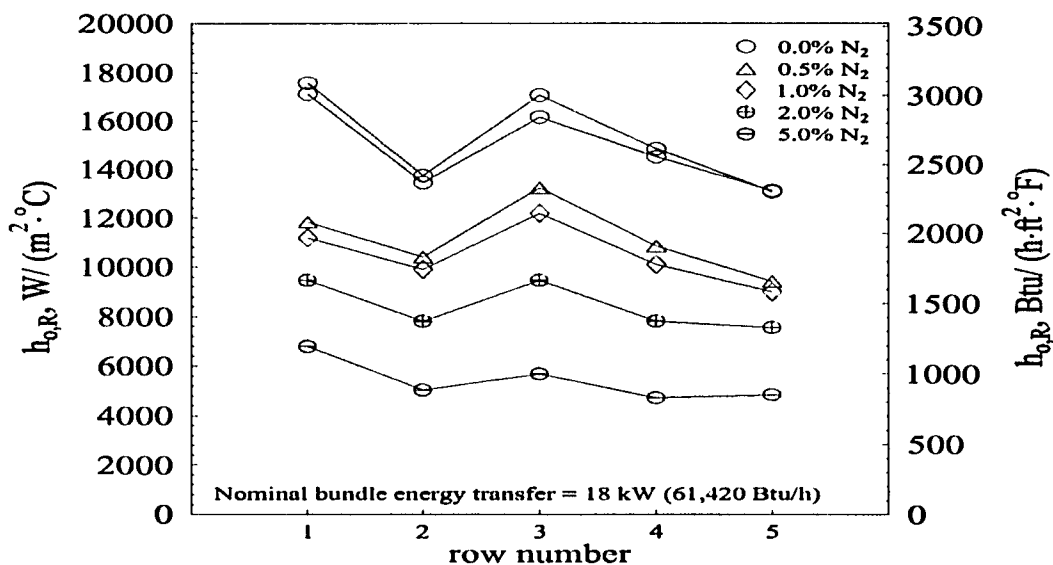


Figure 5.9: Average shell-side row heat transfer coefficient vs. row number for the 40-fpi bundle at various nitrogen concentrations during condensation with HCFC-123; average bundle heat flux = $20,200 \text{ W/m}^2$ (6400 Btu/h/ft^2)

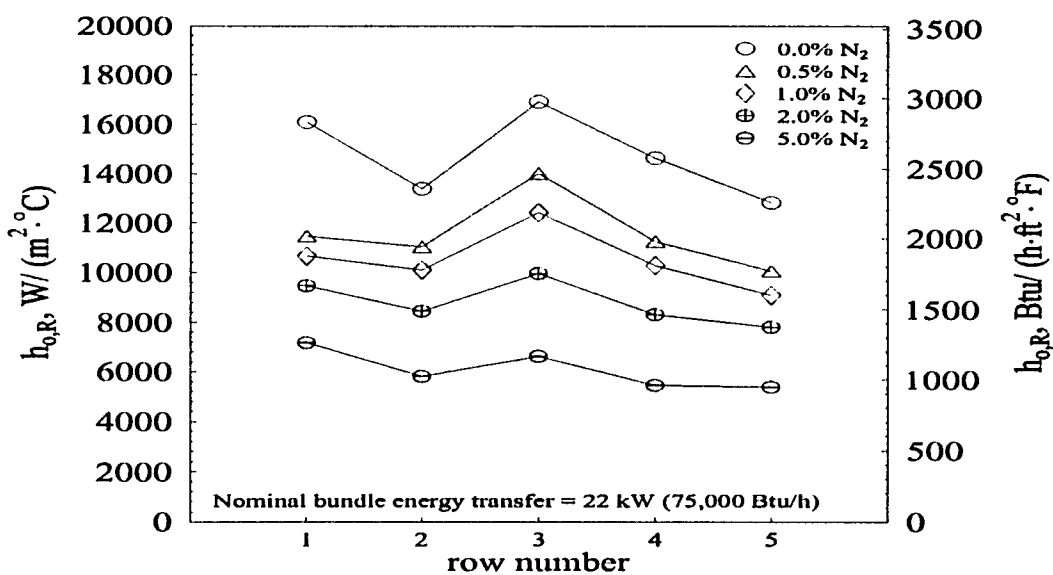


Figure 5.10: Average shell-side row heat transfer coefficient vs. row number for the 40-fpi bundle at various nitrogen concentrations during condensation with HCFC-123; average bundle heat flux = $25,000 \text{ W/m}^2$ (7920 Btu/h/ft^2)

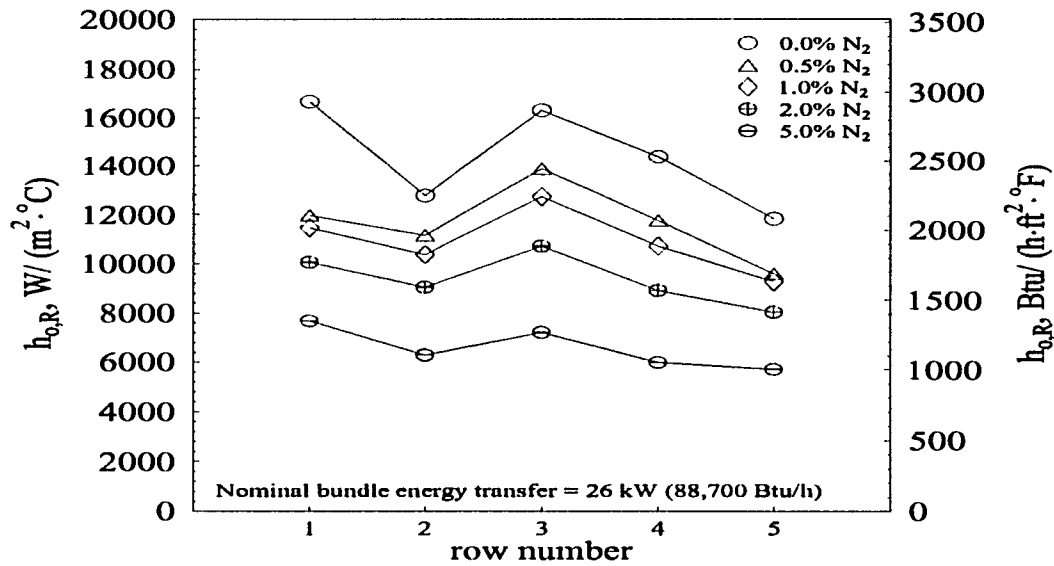


Figure 5.11: Average shell-side row heat transfer coefficient vs. row number for the 40-fpi bundle at various nitrogen concentrations during condensation with HCFC-123; average bundle heat flux = $29,300 \text{ W/m}^2$ (9290 Btu/h/ft^2)

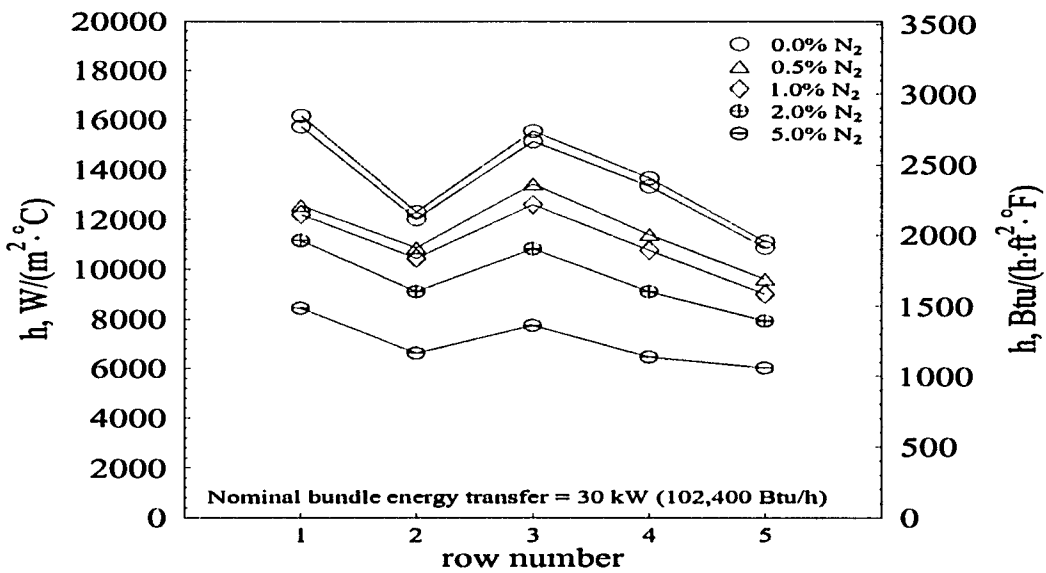


Figure 5.12: Average shell-side row heat transfer coefficient vs. row number for the 40-fpi bundle at various nitrogen concentrations during condensation with HCFC-123; average bundle heat flux = $33,900 \text{ W/m}^2$ ($10,740 \text{ Btu/h/ft}^2$)

have been filled, significantly decreasing its performance. This supposition makes further sense when considering that the peak performances of the first and third rows are probably caused by vapor shearing effects on the liquid layer as the vapor is forced through the bundle, and that filling the inter-fin spaces with a non-condensable gas which is only slightly affected by vapor shear would have a very large detrimental effect on that performance.

Results for the Tu-Cii Geometry

Bundle performance

The tests conducted using the Tu-Cii showed that there was a very large decrease with even small concentrations of non-condensable gases, but that additional gas contamination caused a gradual heat transfer performance decrease. Figures 5.13 and 5.14 show the effect of varying concentrations of nitrogen on the average bundle heat transfer coefficients as functions of the bundle LMTD and the heat flux, respectively. As is obvious from both figures, even non-condensable gas contamination as small as 0.5% causes a large drop in the bundle heat transfer performance.

At the lowest heat flux the bundle heat transfer coefficient drops more than 51% with a non-condensable gas concentration of only 0.5%, compared to that with no non-condensibles at all. With the increasing concentrations of N_2 the heat transfer coefficients continue to decrease, but at a much slower rate. A concentration of 1.0% decreases the performance by 57%, a 2.0% concentration decreases the performance by 66%, and a 5.0% concentration decreases the performance by more than 78%. These decreases are much more significant than those found for the 26-fpi and 40-fpi tubes discussed above.

As with the two previous tubes, there is a definite shearing effect in the non-condensable gas layer surrounding the tubes at the higher heat fluxes that strip some of the gas away from the tube surface and allows the tubes' performance to increase at higher vapor velocities. This,

in addition to the Tu-Cii's susceptibility to liquid loading effects at 0% gas concentrations, means that the decrease in the heat transfer performance at the highest heat fluxes due to non-condensable gas is much smaller than at low heat fluxes. At the highest heat flux, concentrations of 0.5%, 1.0%, 2.0%, and 5.0% drop the average bundle heat transfer coefficients by approximately 35%, 41%, 49%, and 64%, respectively. These decreases are significantly smaller than the decreases at the low heat fluxes discussed above.

The Tu-Cii's large dependence on non-condensable gas contamination is believed to be caused by the knurled geometry of the fins. The non-condensibles are drawn toward the fin roots by the motion of the condensing vapor and get trapped there by the three-dimensional structure of the fins. Then, even with shearing effects around the outer surface of the tube and along the fins tips, there is always a non-condensable gas layer along the tube surface which prevents condensation and cuts the tubes performance by more than 50%, even at small non-condensable gas concentrations. This is similar to the phenomenon discussed for the 40-fpi tube above, but to a much higher degree.

The shearing effect, which helps to improve the heat transfer performance in the presence of non-condensable gases, also appears to dominate over the effect of liquid loading, which acts to depress the heat transfer performance, throughout the range of heat fluxes used in these tests. All the heat transfer coefficient trends at gas concentrations greater than 0% are increasing at the point of the highest heat flux and have not yet begun to level off, as was seen with the 26-fpi tube. This indicates that the effect of liquid loading has not become significant enough to counter the shearing occurring in the non-condensable gas layer.

Row-by-row performance

The bundle row-by-row heat transfer coefficient profiles are shown in Figures 5.15 through 5.18. The most notable aspect of each figure is the effect of the N₂ contamination on

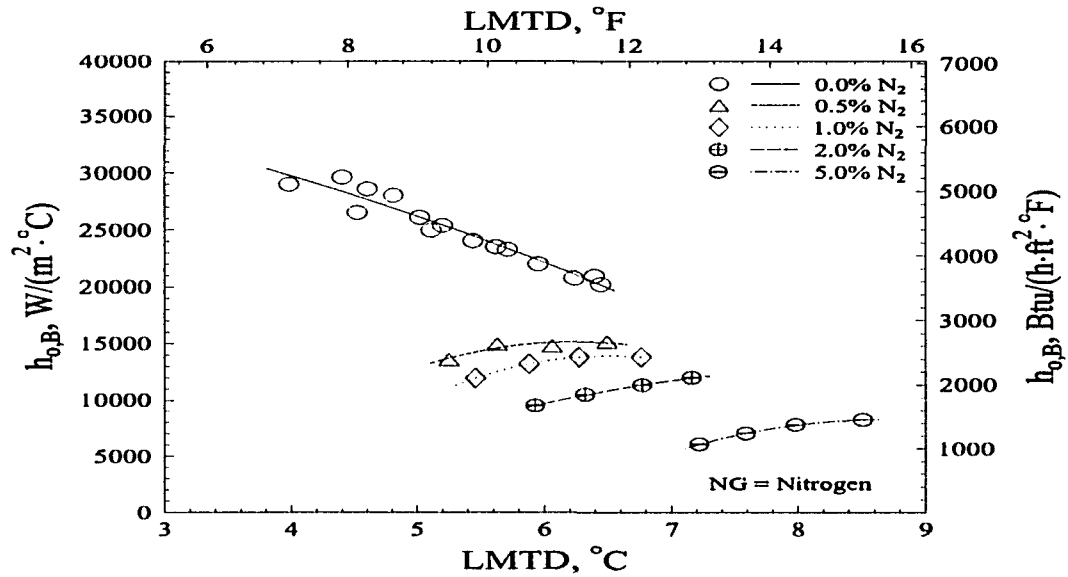


Figure 5.13: Average shell-side bundle heat transfer coefficient vs. LMTD for the Tu-Cii bundle at various nitrogen concentrations during condensation with HCFC-123

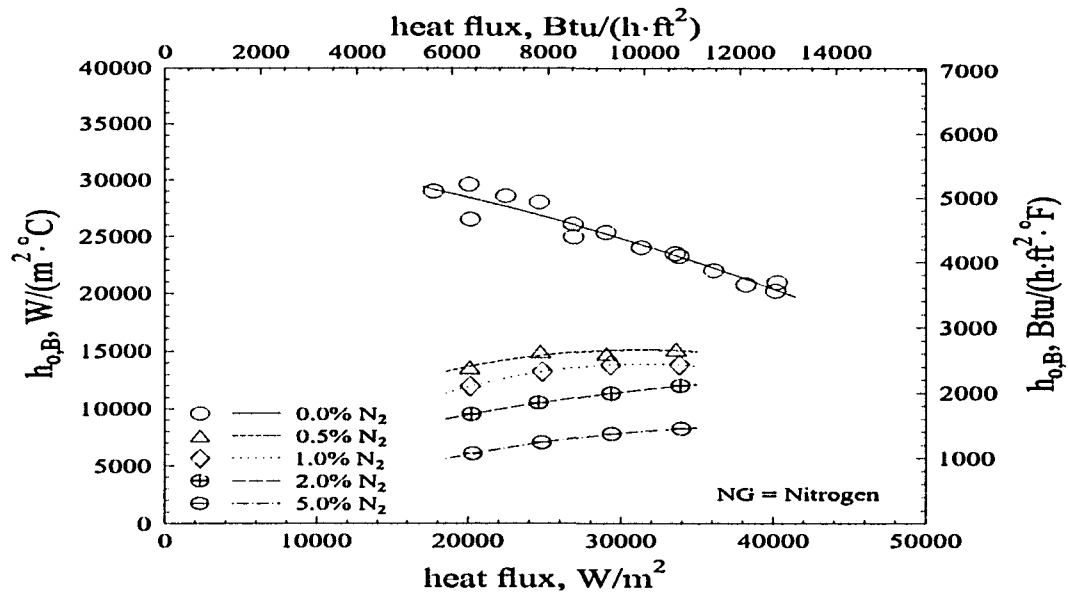


Figure 5.14: Average shell-side bundle heat transfer coefficient vs. heat flux for the Tu-Cii bundle at various nitrogen concentrations during condensation with HCFC-123

the bundle profile even at low concentrations. The profile at 0% concentration is characterized by a peak in heat transfer coefficient in the second row which is believed to be caused by a vapor shearing effect on the condensate layer as the refrigerant is accelerated through the gap in the first row to impinge on the second row. However, this peak is completely absent in the presence of any non-condensable gas contamination, even with shearing effects in the gas layer at higher heat fluxes. This would seem to support the supposition, discussed above, that non-condensibles get trapped within the fins next to the tube surface and prevent normal condensation even at low non-condensable gas concentrations and high vapor velocities. Thus, the heat transfer is decreased and inundation patterns normally seen on smooth tubes are allowed to form.

It is also interesting to note that at the highest N_2 concentrations the profile begins to flatten out so that all the tubes rows appear to perform more equally. It is believed that this is caused by a concentration gradient in non-condensable gases from the top to the bottom of the bundle which acts to even the effects of the non-condensable gas and liquid loading. The $Tu-C_{ii}$ is very dependent on condensate flow rate. This means that near the bottom of the bundle the liquid film inhibits condensation and forces more condensation to occur on the better performing tubes at the top of the bundle. However, this excess condensation in the top rows draws more of the non-condensibles in the vapor flow, so that the gas layer on the top tubes is relatively thicker than on the bottom rows. Thus, the gas layer dominates and decreases the heat transfer performance in the top rows, while liquid loading effects dominate and suppress heat transfer at the bottom of the bundle.

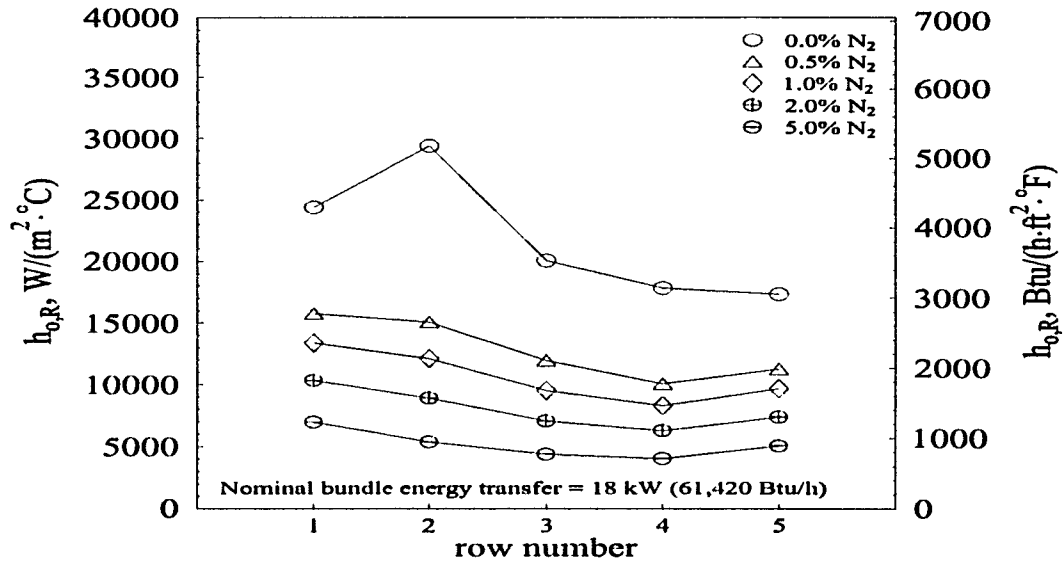


Figure 5.15: Average shell-side row heat transfer coefficient vs. row number for the Tu-Cii bundle at various nitrogen concentrations during condensation with HCFC-123; average bundle heat flux = $20,200 W/m^2$ ($6400 Btu/h/ft^2$)

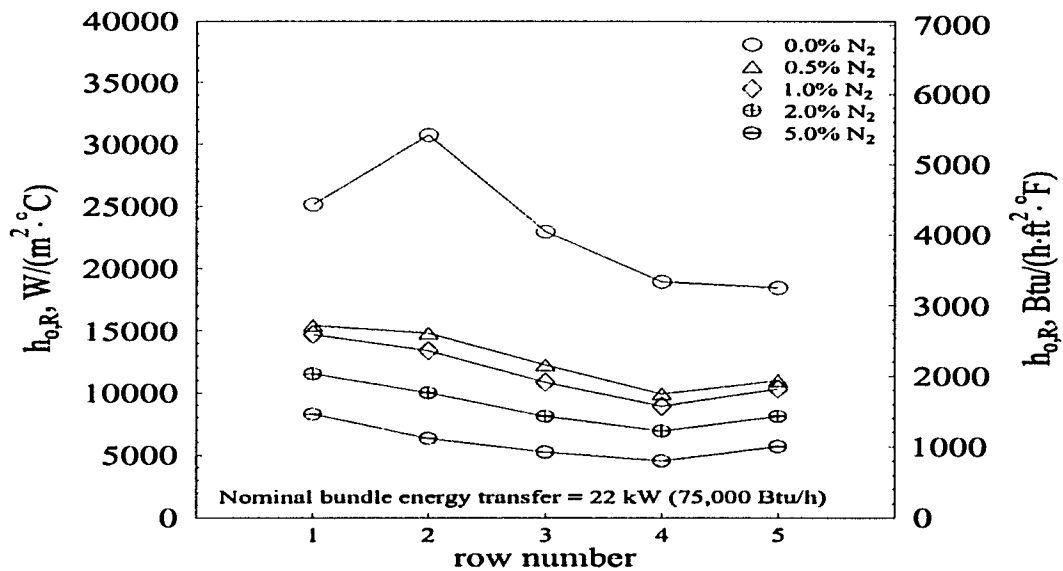


Figure 5.16: Average shell-side row heat transfer coefficient vs. row number for the Tu-Cii bundle at various nitrogen concentrations during condensation with HCFC-123; average bundle heat flux = $25,000 W/m^2$ ($7920 Btu/h/ft^2$)

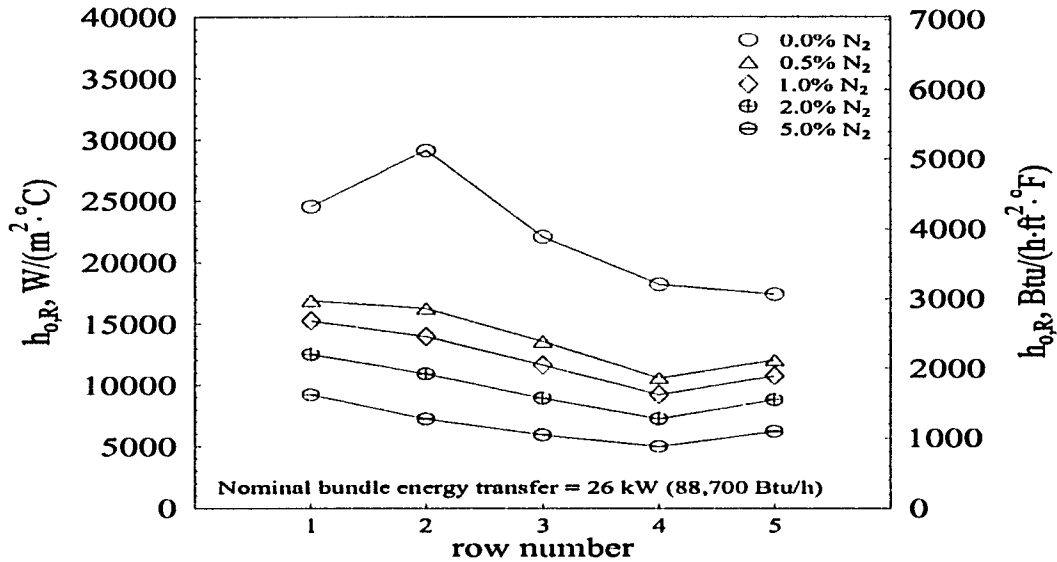


Figure 5.17: Average shell-side row heat transfer coefficient vs. row number for the Tu-Cii bundle at various nitrogen concentrations during condensation with HCFC-123; average bundle heat flux = $29,300 \text{ W/m}^2$ (9290 Btu/h/ft^2)

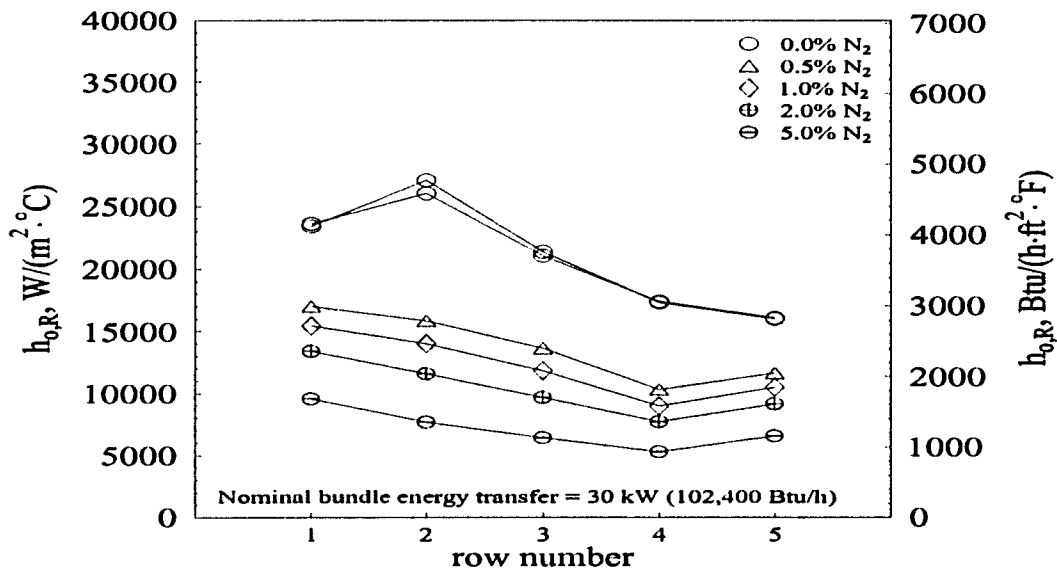


Figure 5.18: Average shell-side row heat transfer coefficient vs. row number for the Tu-Cii bundle at various nitrogen concentrations during condensation with HCFC-123; average bundle heat flux = $33,900 \text{ W/m}^2$ ($10,740 \text{ Btu/h/ft}^2$)

Results for the G-SC Geometry

Bundle performance

The performance of the G-SC tube bundle indicates that it is the least susceptible to low (< 1.0%) concentrations of non-condensable gases of the four tubes tested. At the 0.5% concentration level, all the data fell within the experiential uncertainty of the pure refrigerant data. The trends in its performance were also found to be similar to the performances of both the 26-fpi and 40-fpi bundles discussed earlier. Like the 26-fpi bundle, the G-SC bundle was characterized by a gradual decrease in performance with increasing concentrations of nitrogen. At the same time, the G-SC performed like the 40-fpi by showing shear effects in the non-condensable gas layer even at the lowest nitrogen concentrations and by being dominated by shear in the higher concentrations.

The overall average bundle performance is shown in Figures 5.19 and 5.20. Both figures show the gradual decrease in average bundle heat transfer coefficients at the lower concentrations, with larger decreases at the highest concentrations. At the lowest heat flux (smallest LMTD), there is only a 9% decrease with a 0.5% N₂ concentration. These become 19%, 33%, and finally 58% decreases at 1.0%, 2.0%, and 5.0% nitrogen concentrations, respectively. The decrease with the addition of 0.5% nitrogen is the smallest decrease found for any of the geometries tested. The next smallest decrease at comparable heat fluxes was found with the 26-fpi bundle, which had a 19% decrease. At the highest concentration, however, the decrease is comparable to both the 26-fpi (57%) and the 40-fpi (63%).

As with the other tubes in the study, the decreases at the highest heat fluxes are much smaller (compared to the decreases at low heat fluxes) due to shearing effects in the non-condensable gas layer. At the lowest concentrations, the effect of non-condensable contamination is almost negligible. At a heat flux of approximately 33,800 kW/m² (10,700 Btu/h/ft²), the bundle performance drops 4% with 0.5% N₂, 10% with 1.0% N₂, 21% with 2.0% N₂,

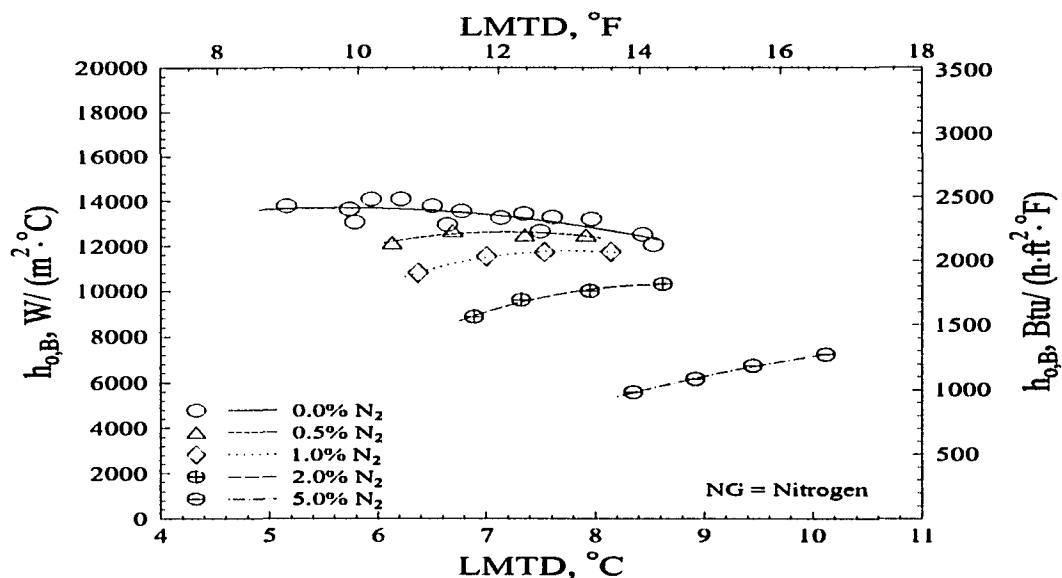


Figure 5.19: Average shell-side bundle heat transfer coefficient vs. LMTD for the G-SC bundle at various nitrogen concentrations during condensation with HCFC-123

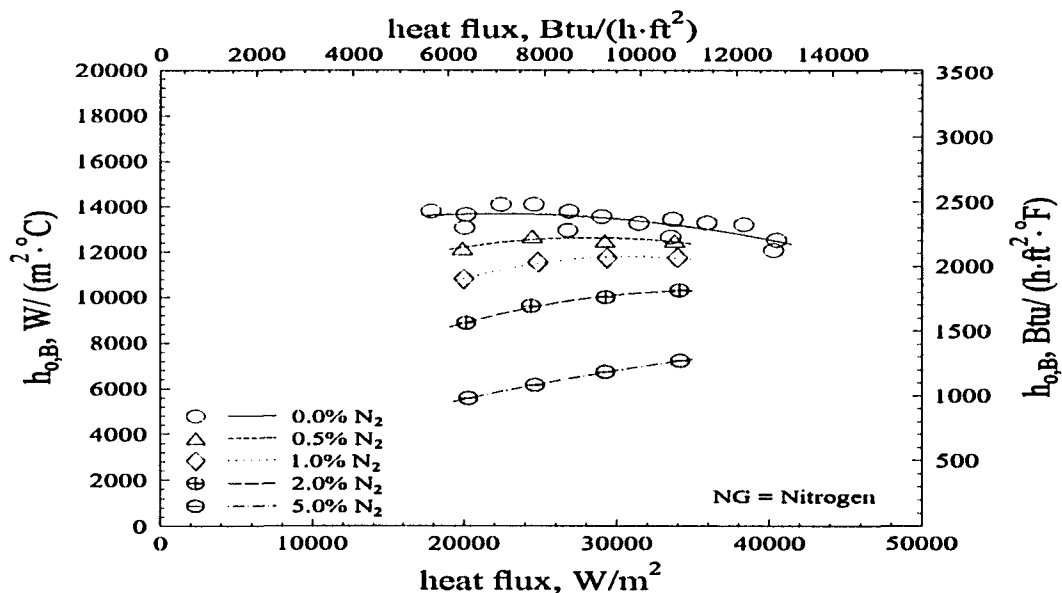


Figure 5.20: Average shell-side bundle heat transfer coefficient vs. heat flux for the G-SC bundle at various nitrogen concentrations during condensation with HCFC-123

and 45% with 5.0% N₂. Again, the decreases with the lowest concentrations are the smallest of any of the tubes tested.

As noted in earlier sections, shear in the non-condensable gas layer is not the only factor affecting the heat transfer performance at low N₂ concentrations. Figures 5.19 and 5.20 both show that the trends at the 0.5% and 1.0% levels begin to level off at the highest heat fluxes, which is believed to indicate a transition from shear dominated performance to liquid layer dominated performance. As liquid covers the tube surface, the heat transfer resistance of the liquid layer becomes more important and the resistance of the non-condensable gas layer decreases. At concentrations greater than 1% where the nitrogen layer around the tube is thicker, shear effects becomes much more important. Thus, the trends for the 2.0 and 5.0% data increase with increasing heat flux and increasing vapor velocity. It is believed that at still higher heat fluxes where liquid inundation rates are higher, these trends will begin to level off much like the trends of the lower gas concentrations.

Row-by-row performance

The effect of non-condensable gases on the row-by-row performance of the G-SC is identical to its effect on the Tu-Cii geometry. In both cases, the presence of even small concentrations of gas serve to remove any significant peaks in the performance profile and flatten the profile across the whole bundle. Figures 5.21 through 5.24 illustrate the performance of the G-SC bundle at four different heat fluxes at each different nitrogen concentration level. Each of these figures shows the flattening of the bundle row-by-row profiles.

This behavior (flattening of the profile) is believed to be a result of non-condensable gas migrating beneath the Y-shaped fins of the G-SC where it gets trapped, even with small N₂ concentrations and in the presence of high vapor velocities. This serves to equalize the performance of every row in the bundle by giving each tube nearly identical heat transfer

resistances from non-condensable contamination. The only difference between tubes then becomes the resistance due to the liquid layer on the tube, with the tubes in the lower rows having a thicker layer than the tubes in the top rows, and the tubes' access to vapor, with the tubes at the top and bottom having more surface area open to the vapor space. This would explain highest heat transfer coefficients being in the top row of the bundle and the slight upward curve of the trends at the highest concentrations across the whole range of heat fluxes, and is consistent with the results of both the 26-fpi and Tu-Cii geometries, as shown in Figures 5.3 and 5.15.

Comparisons Between Test Bundles

Of the four bundles, the Tu-Cii bundle displayed the highest average heat transfer performance, followed generally by the 40-fpi, 26-fpi, and G-SC bundles. This ranking varied slightly depending on the gas concentration, and is not absolute through the ranges of non-condensable gas concentration. At the same time, the Tu-Cii was found to be the most susceptible to performance degradation as a result of non-condensable gas contamination. The G-SC bundle, on the other hand, showed the least susceptibility, particularly at low gas concentrations, yet generally had the worst performance of the the four tubes at the highest concentrations.

Comparisons are shown in Figures 5.25 through 5.26 in terms of heat flux and LMTD for the smallest (0.5%) and largest (5.0%) gas concentrations. Both figures indicate that at small concentrations the performance differences between tube geometries were relatively well defined, with the Tu-Cii bundle having the best performance, followed by the 40-fpi, G-SC, and 26-fpi bundles, respectively. However, at the 5.0% non-condensable concentration all the bundles performed very similarly to each other. Average bundle heat transfer coefficients were all within approximately 13% of each other. The average bundle coefficients of the best

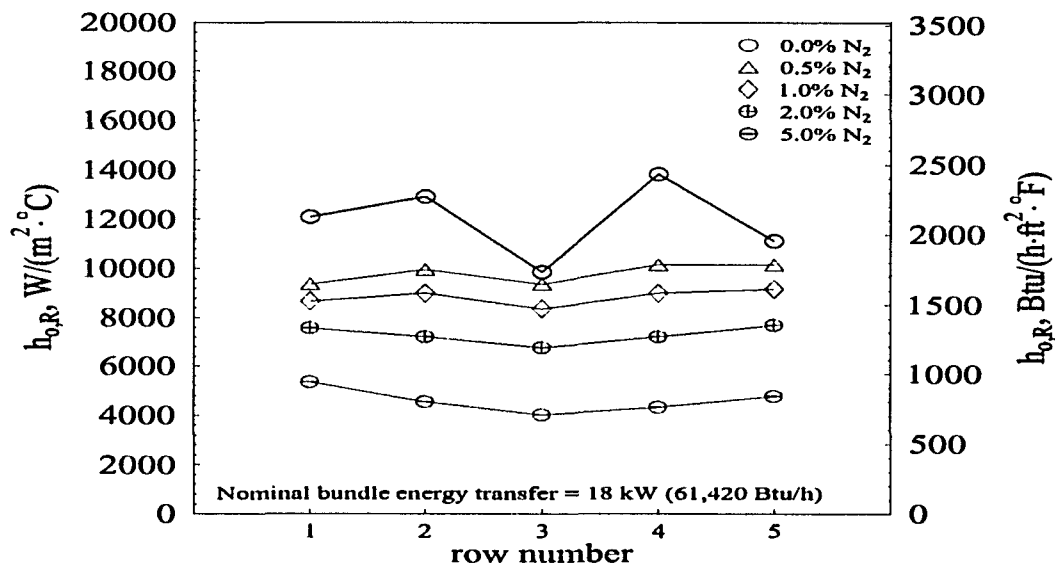


Figure 5.21: Average shell-side row heat transfer coefficient vs. row number for the G-SC bundle at various nitrogen concentrations during condensation with HCFC-123; average bundle heat flux = $20,200 \text{ W/m}^2$ (6400 Btu/h/ft^2)

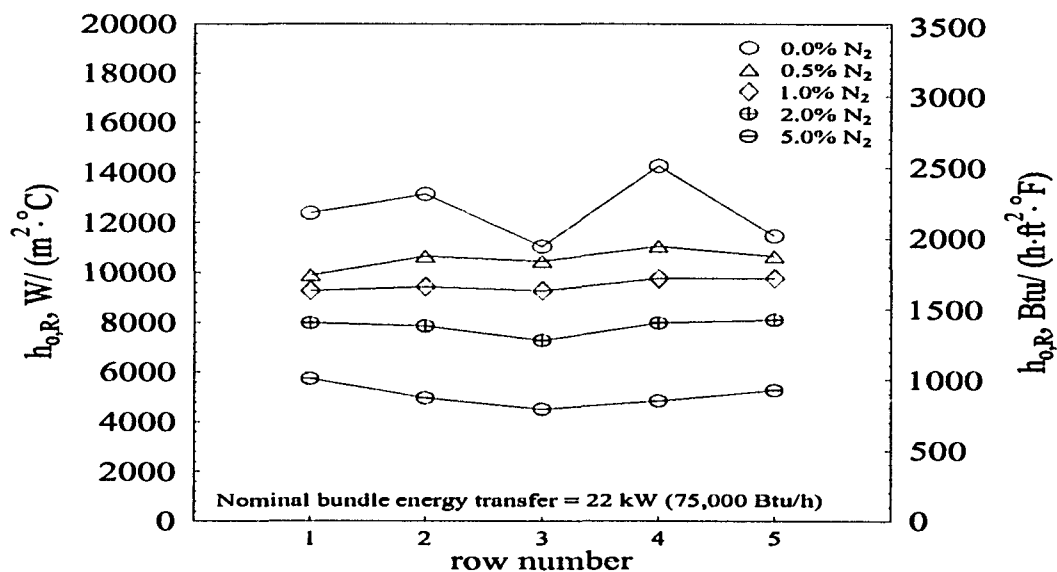


Figure 5.22: Average shell-side row heat transfer coefficient vs. row number for the G-SC bundle at various nitrogen concentrations during condensation with HCFC-123; average bundle heat flux = $25,000 \text{ W/m}^2$ (7920 Btu/h/ft^2)

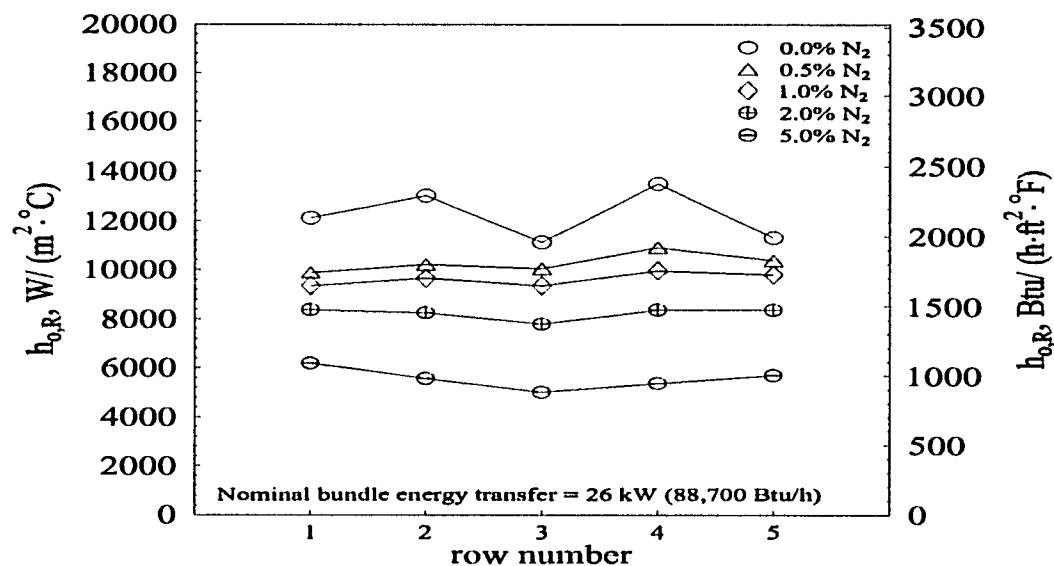


Figure 5.23: Average shell-side row heat transfer coefficient vs. row number for the G-SC bundle at various nitrogen concentrations during condensation with HCFC-123; average bundle heat flux = $29,300 \text{ W/m}^2$ (9290 Btu/h/ft^2)

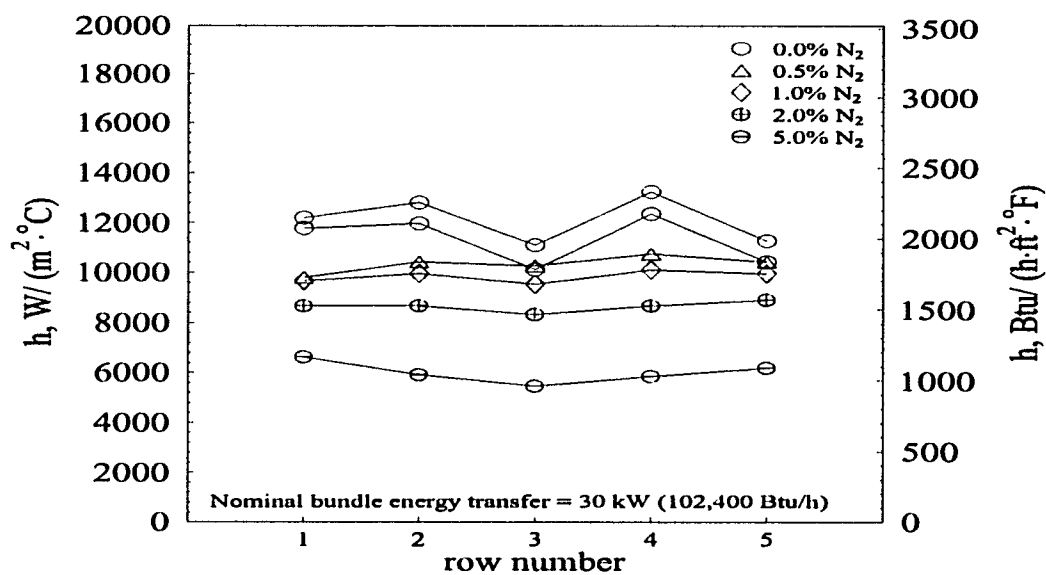


Figure 5.24: Average shell-side row heat transfer coefficient vs. row number for the G-SC bundle at various nitrogen concentrations during condensation with HCFC-123; average bundle heat flux = $33,900 \text{ W/m}^2$ ($10,740 \text{ Btu/h/ft}^2$)

(40-fpi) and the worst (G-SC) performing tubes differed by only 11% at the lowest heat flux. At the highest heat flux the Tu-Cii was the best performing tube, and the difference between it and the G-SC, still the worst performing tube, was approximately 13%.

This similarity in heat transfer coefficients would seem to indicate that high concentrations of non-condensable gas effectly nullify any advantages gained by tubes with enhanced surface geometries. However, Figure 5.26 also shows that even with similar average bundle coefficients, the Tu-Cii outperforms the other bundles by condensing the vapor at a smaller refrigerant-to-water temperature difference. Thus, warmer water can be used with the Tu-Cii to get the same amounts of condensation. Interestingly, by this comparison, the 26-fpi was the next best performing bundle, followed by the 40-fpi and G-SC bundles, respectively.

Figures 5.27 and 5.28 compare the bundles in terms of row-by-row performance at the lowest and highest concentrations and heat fluxes, and illustrate the effect of increasing gas concentrations and increasing vapor velocities. From these figures, two important things should be noted.

First, Figure 5.27 very clearly demonstrates the effect of increasing gas concentration on the respective bundle profiles. At the lowest concentration the profiles have flattened from their various pure refrigerant profiles (not shown here), but are still clearly distinguishable from each other. At the same time, there is a marked difference in the average performances of the bundles. However, at the 5.0% concentration level, the profiles have collapsed to nearly the same trend. With the exception of a small peak in the third row of the 40-fpi bundle, all the bundles have nearly identical curved row-by-row profiles which have a peak in the first row and slightly smaller peak in the fifth row. As noted earlier, this is believed to indicate that the presence of non-condensibles masks geometry effects within the condenser bundle, leaving only liquid layer thickness and access to the vapor as driving parameters in individual row performance. Thus, there is a peak in the first row where the liquid layer is smallest and

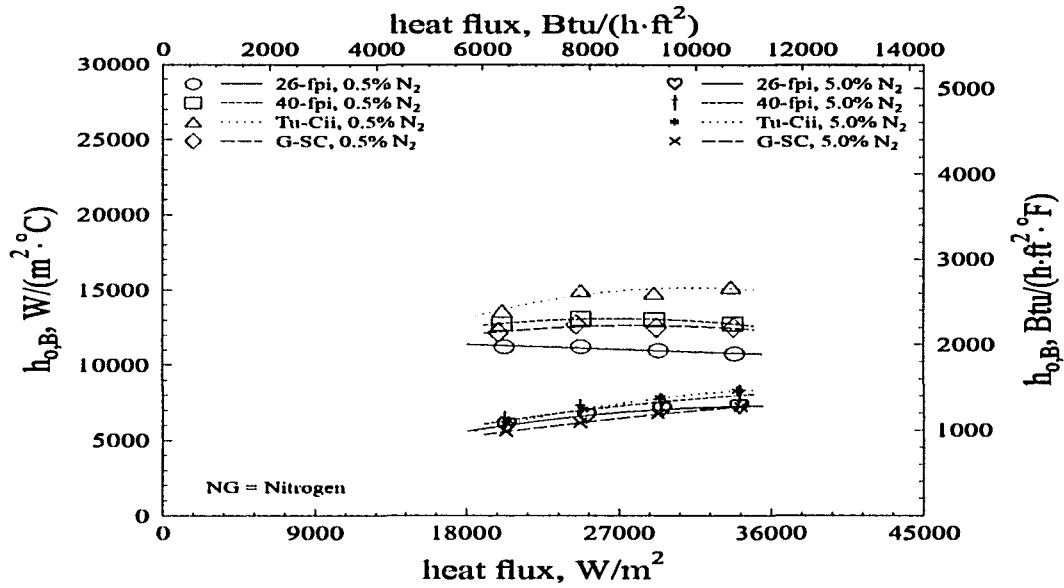


Figure 5.25: Average shell-side bundle heat transfer coefficient vs. heat flux for the four test bundles at various nitrogen concentrations during condensation with HCFC-123

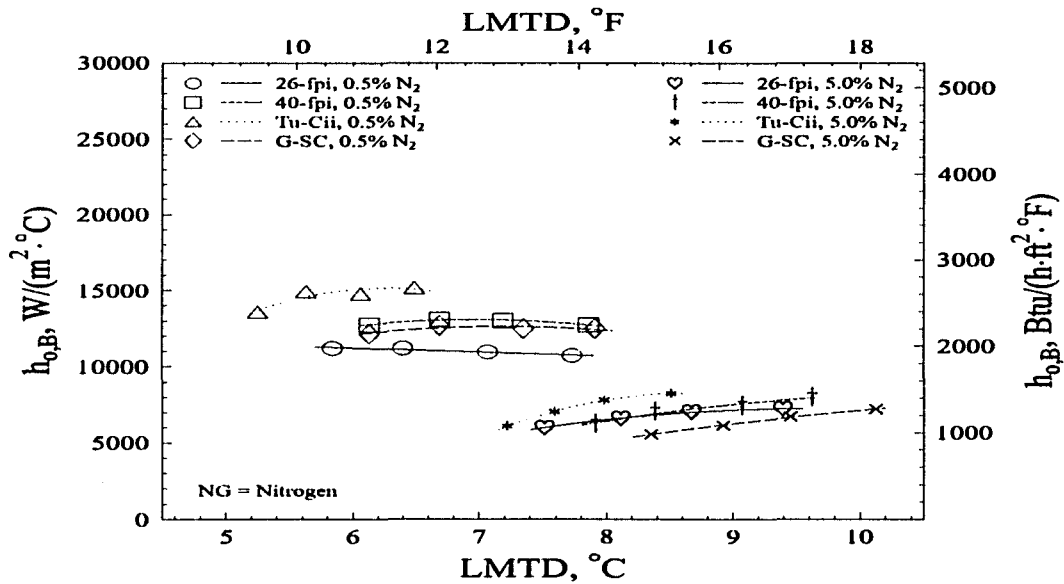


Figure 5.26: Average shell-side bundle heat transfer coefficient vs. LMTD for the four test bundles at various nitrogen concentrations during condensation with HCFC-123

the tubes have access to the vapor space at the top of the condenser, and another smaller peak in the fifth row, where the liquid layer is thicker, but where the tube also has access to the vapor space at the bottom of the test section.

The second important aspect to note can be seen clearly in Figure 5.28. As with Figure 5.27, the changes caused by increasing gas concentration can be seen. However, Figure 5.28 also shows the effect of vapor shear in the nitrogen layer at the higher heat flux, and consequently higher vapor velocity, condition. It is particularly apparent at the highest gas concentration level. The bottom rows of tubes of all four bundles can be seen to perform very closely. A look at the data shows that the bottom rows all perform within 10% of each other. However, in the top rows, particularly of the Tu-Cii and 40-fpi bundles, there is a marked increase in heat transfer performance. This is thought to be a result of large shearing effects in the non-condensable gas layer at the top of the bundle where the vapor velocity is highest, stripping some of the gas from the tubes in the top rows and allowing more condensation to take place.

The reason for the relatively shear-independent behavior of the 26-fpi and G-SC bundles in the top rows is not known. While shear in the overall bundle performance can be seen in Figures 5.25 and 5.26, it does not appear to have much effect on individual tube rows.

Summary

Tests were performed on four bundles, two finned and two enhanced, to determine the effect of non-condensable gases on the condensation of pure HCFC-123. Data was taken at four heat fluxes and four concentrations of non-condensable gas (nitrogen) and compared to data taken at 0% gas concentration. From the data the following conclusions were drawn.

1. The Tu-Cii bundle performs better than the other bundles through non-condensable gas concentrations of 5% and heat fluxes of $33,900 \text{ W/m}^2$ ($10,740 \text{ Btu/h/ft}^2$).

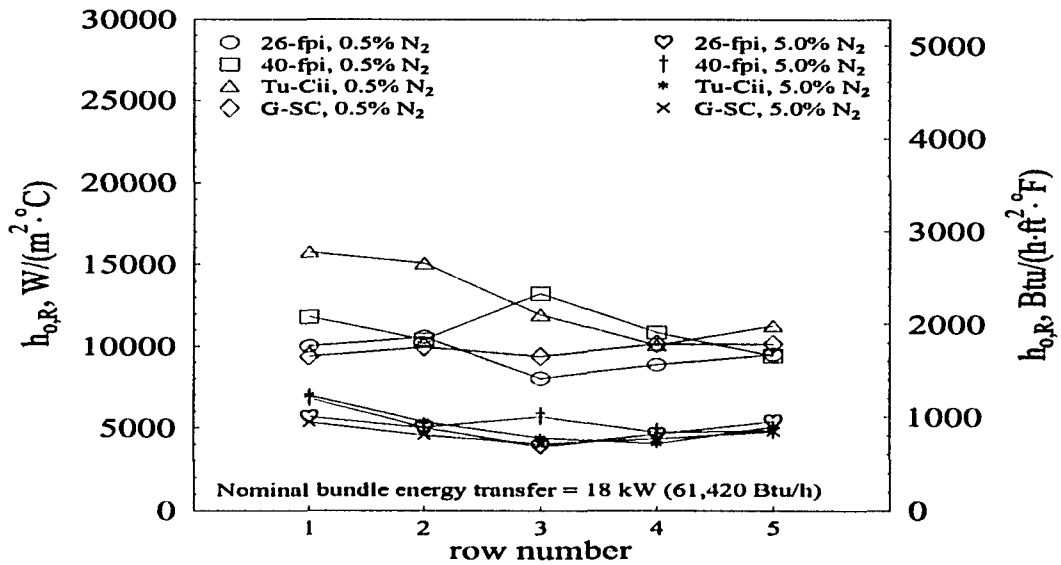


Figure 5.27: Average shell-side row heat transfer coefficient vs. row number for the four test bundles at various nitrogen concentrations during condensation with HCFC-123; average bundle heat flux = 20,200 W/m² (6400 Btu/h/ft²)

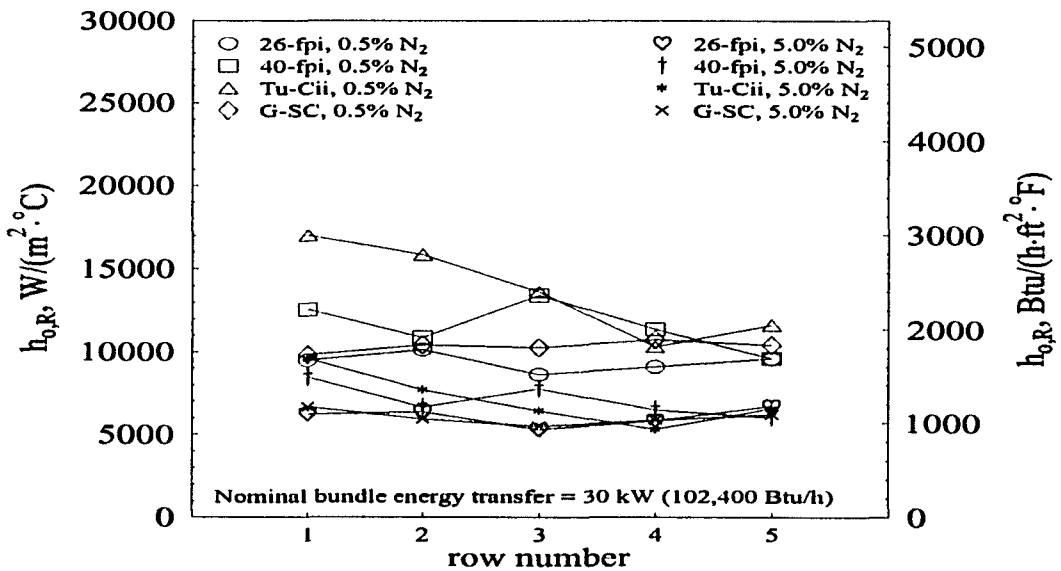


Figure 5.28: Average shell-side row heat transfer coefficient vs. row number for the four test bundles at various nitrogen concentrations during condensation with HCFC-123; average bundle heat flux = 33,900 W/m² (10,740 Btu/h/ft²)

2. The Tu-Cii geometry is susceptible to the presence of even small amounts of non-condensable gas. At high heat fluxes, 0.5% non-condensable gas contamination causes a decrease of 35% in the overall bundle heat transfer coefficient. At low heat fluxes where there is very little shearing in the non-condensable gas layer, the decrease in heat transfer coefficient is more than 50%.
3. All four tube geometries benefit from shearing effects in the non-condensable gas layer, which helps to offset some of the non-condensable gas effects at high heat fluxes.
4. The G-SC is on mildly dependent on the presence of small concentrations of non-condensable gas. At the lowest gas concentration the average bundle heat transfer coefficient decreases by between 4% and 9%, at the highest and lowest heat fluxes respectively. These values are within the experimental uncertainty of the data with pure refrigerant.
5. The 26-fpi is dependent on vapor shear in the non-condensable gas layer only at gas concentrations above 1.0%. Below 1.0% concentration there is a steady decrease in overall bundle heat transfer performance with increasing heat flux.
6. The presence of even small concentrations of non-condensable gases works to even the performance of all the tubes in a bundle and flatten the overall bundle profile. High concentrations bring the performances of the bundles to within 13% of each other.

CHAPTER 6. HFC-134A INUNDATION RESULTS

As refrigerant vapor condenses in multi-row condensers, the resulting condensate drains from the top rows and falls onto the lower rows of tubes where it forms an insulating liquid layer. The condensate film reduces the total surface area of the tube exposed to vapor, which lowers the tubes' overall heat transfer performance and decreases the condensation heat transfer coefficients found on the shell-side of each tube. This process of condensate-inhibited condensation in the lower rows is referred to as liquid inundation.

Heat fluxes were varied between approximately 26 kW/m^2 (8640 Btu/h/ft^2) for the 30-row simulations and 56 kW/m^2 ($17,750 \text{ Btu/h/ft}^2$) for the 15-row simulations. Envelope areas are used for the tube surface areas in heat flux and heat transfer coefficient calculations. This area is based on the outer fin diameter of each tube and is equivalent to a smooth tube having the same outer diameter as the fins. The condensate Reynolds numbers ranged from approximately 200 to 2900.

Inundation tests were performed on all four tube bundles to simulate both 15 and 30-row condensers. Data were taken to determine the relationship between the shell-side heat transfer coefficient and both row number and inundation rate as represented by the condensate Reynolds number. Results of the tests for each tube bundle are presented below. Raw data for each tube, along with all calculated values and experimental uncertainties, are presented in tabular form in Appendix C.

Results for the 26-fpi Geometry

In general, the 26-fpi bundle showed very little inundation effect on heat transfer performance over the range of heat fluxes and inundation rates covered in these tests. Figure 6.1 shows the effect of condensate inundation rate in the form of film Reynolds number on the row-by-row heat transfer coefficient. Data for both 15 and 30-row simulations are shown. As discussed in Chapter 4, drainage patterns are as important to determining a tube's heat transfer performance as the condensate flow rate is. Therefore, the data from the first five tubes from the first refrigerant pass (100% saturated vapor at the inlet) and the fourth and fifth tubes from subsequent refrigerant passes are presented, since these tubes are believed to most accurately represent the drainage patterns found in actual multi-row condensers.

Figure 6.1 shows that for this tube there is negligible inundation effect. This is consistent with the findings of both Webb (1990) and Honda et al. (1987a), who found no row effect when condensing CFC-11 and CFC-113, respectively, on standard 26-fpi tubes. Additionally, Honda et al. (1991, 1992), condensing CFC-113 on both staggered and in-line bundles of two unspecified finned tubes, found negligible inundation effects.

This inundation-independent behavior is connected to the ability of the tube's continuous fins to channel the liquid as it falls from tube to tube and prevent it from moving axially along the tube surface. By preventing axial movement, the fins direct the condensate around the tube across a very small percentage of the tube's surface area in the quickest way possible. This keeps the majority of the tube's surface free from condensate build-up and exposed to vapor, thus providing greater surface area for condensation. The flat-sided fins also work to promote drainage of condensate which forms on that tube so that there is very little liquid holdup in the upper portion of the tube.

An alternate form of the Nusselt single-tube heat transfer equation can be written in terms of the condensate Reynolds number, $Re_{L,N}$, from a given tube N . This expression is given

by

$$\frac{h_{o,N}}{k_f} \left[\frac{\mu_f^2}{\rho_f(\rho_f - \rho_g)g} \right]^{1/3} = 1.51 (\text{Re}_{L,N})^{-1/3} \quad (6.1)$$

and shown in Figure 6.1. At steady-state thermodynamic conditions when the refrigerant properties are constant, this equation can also be written in the general form

$$h_{o,N} = a \text{Re}_{L,N}^{-n} \quad (6.2)$$

Webb (1990), fitting a line of this form to his CFC-11 data, found an exponent of $n = 0.000$ for a Reynolds range up to approximately 600. Plotting a similar line through the current HFC-134A data, the exponent was found to be $n = 0.0267$. This value, while greater than zero, represents a very mild slope and indicates a negligible inundation effect up through a film Reynolds number of approximately 2900.

Data presented by Huber (1994a, 1994b, 1995a, 1995b) show that bundles with constant water inlet temperature do not always display row-by-row heat transfer coefficients which decrease steadily from the top to the bottom of the bundle. In some cases, the best performing tube is not in the first row. Bundles constructed from different tubes in the same configuration often show different row-by-row heat transfer trends which are consistent within that bundle, independent of the working fluid. Thus, it was not simply the conditions in the condenser (pressure, coolant flow rate and temperature, refrigerant flow rate, etc.) which affect the heat transfer on a given tube, but also its surface geometry and placement within a bundle.

Figure 6.2 shows the results of removing tube placement as a variable in the 26-fpi data. Heat transfer coefficient as a function of Reynolds number is plotted only for the fourth tube in the test bundle for both 15 and 30-row simulations. For the 30-row simulation, these tubes represent rows 4, 9, 14, 19, 24, and 29. As can be seen, a single row shows even less inundation effect than the total bundle. A line of the form of Equation 6.2 fitted to this data produces an exponent n equal to 0.0111. This value is smaller than the exponent ($n = 0.0267$)

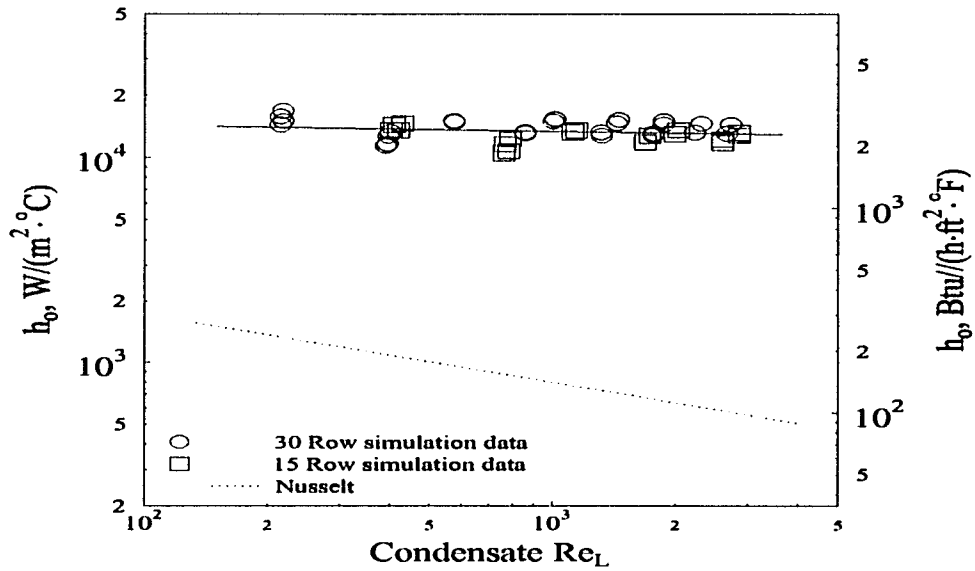


Figure 6.1: 26-fpi tube, average shell-side heat transfer coefficient vs. condensate Reynolds number number with HFC-134a

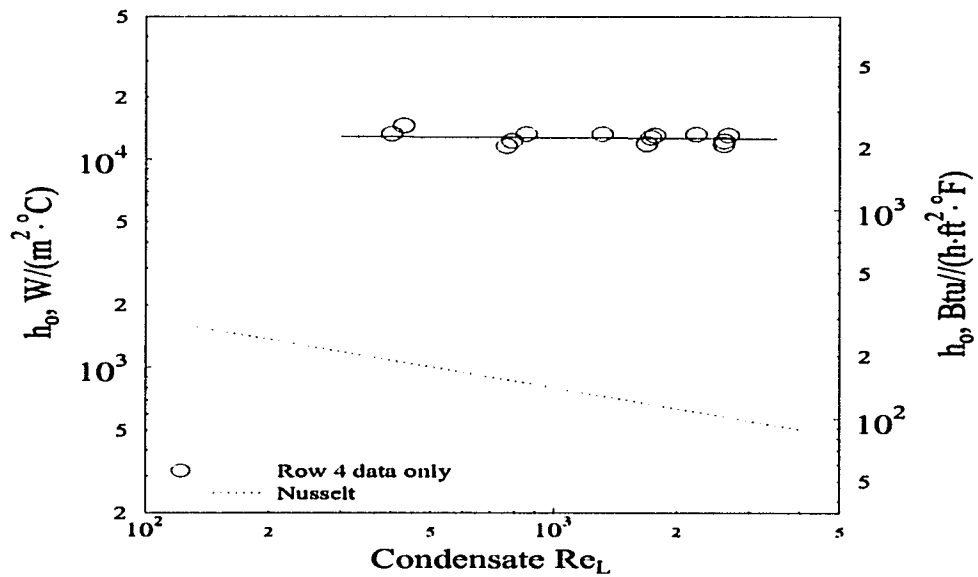


Figure 6.2: 26-fpi tube, average shell-side heat transfer coefficient vs. condensate Reynolds number number on row 4 only

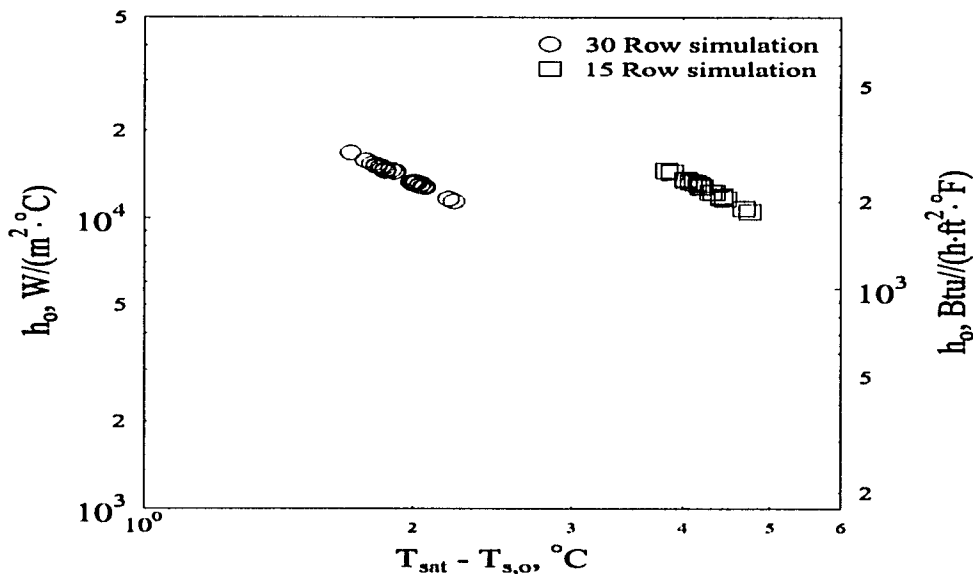


Figure 6.3: 26-fpi tube, average shell-side heat transfer coefficient vs. condensation temperature difference with HFC-134a

calculated for the full bundle and further verifies that the heat transfer performance of this tube is independent of liquid loading rate.

Figure 6.3 plots the row-by-row heat transfer coefficient as a function of the temperature difference $T_{sat} - T_{s,o}$. As noted in the data reduction section in Chapter 2, wall temperatures were not measured directly, but rather were calculated from the water-side energy balance. This explains the apparent lack of experimental variation which would normally be expected in the data. However, the relatively small range of temperature differences in both sets of simulations also indicates the relative steadiness of the heat transfer coefficients of the individual rows with increasing inundation rates. For the 30-row simulation, the vapor-to-wall temperature difference only varied from 1.65 to 2.2°C (3.0 to 4.0°F) from the best performing tube to the poorest performing tube over the full 30-row simulation. For the 15-row simulations, which were conducted at higher heat fluxes, the temperature differences ranged from 3.8 to 4.75°C (6.84 to 8.55°F).

If the data from all the runs in a given simulation are plotted, a trend for the whole condenser can be seen. Figures 6.4 and 6.5 show the bundle profiles generated for the 15 and 30-row simulations, respectively. The trends predicted by Nusselt (1916) and the Katz and Geist (1948) data, discussed in Chapter 2, are shown for comparison. Again, these figures show only the data points from the the first five tube rows of the first refrigerant pass and rows four and five from each subsequent pass.

The line representing the Nusselt correlation is for a smooth tube with a diameter equal to the outer diameter of the finned tube and having the same temperature difference as the finned tube in the first row of the bundle. The correlation for the Katz and Geist (1948) data uses the first tube in the finned bundle as a starting point and calculates the row-by-row heat transfer coefficients using the relation

$$h_N = h_1 \cdot (N^{1-m} - (N - 1)^{1-m}) \quad (6.3)$$

where N is the row number and m is equal to 0.06.

These two figures indicate that the heat transfer coefficients for the individual tube rows stay relatively constant throughout the bundle simulations with respect to their bundle placement, i.e., the fourth and fifth rows of the test bundle exhibit the same heat transfer performance independent of their simulated depths.

Figure 6.4 also shows the repeatability of two separate test runs of the 15-row simulation. As can be seen from the plot, all points were repeatable and showed little variation from run to run. Repeatability tests with other bundles showed similar results.

Figure 6.6 is a plot of the heat transfer coefficients for the tubes in the five-row test bundle as a function of the inlet quality during the 15-row simulations. Two such simulations were performed for a total of six refrigerant passes. As this figure demonstrates, the five-row bundle pattern does not change significantly with increasing liquid inundation rates, and as mentioned above, gives a good indication of the repeatability of the data. As with the figures

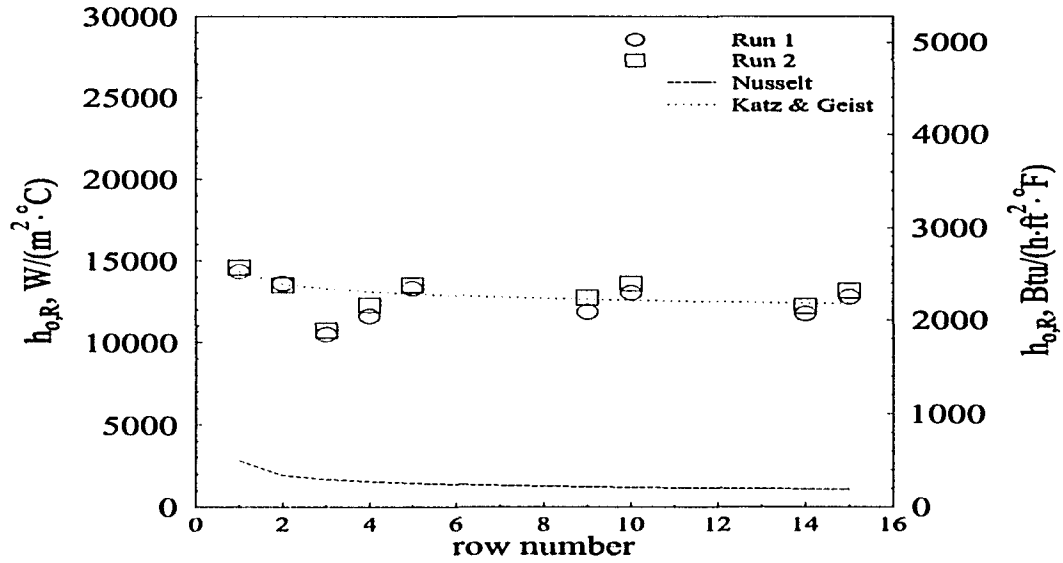


Figure 6.4: 26-fpi tube, average shell-side row heat transfer coefficient vs. row number for 15-row simulation with HFC-134a

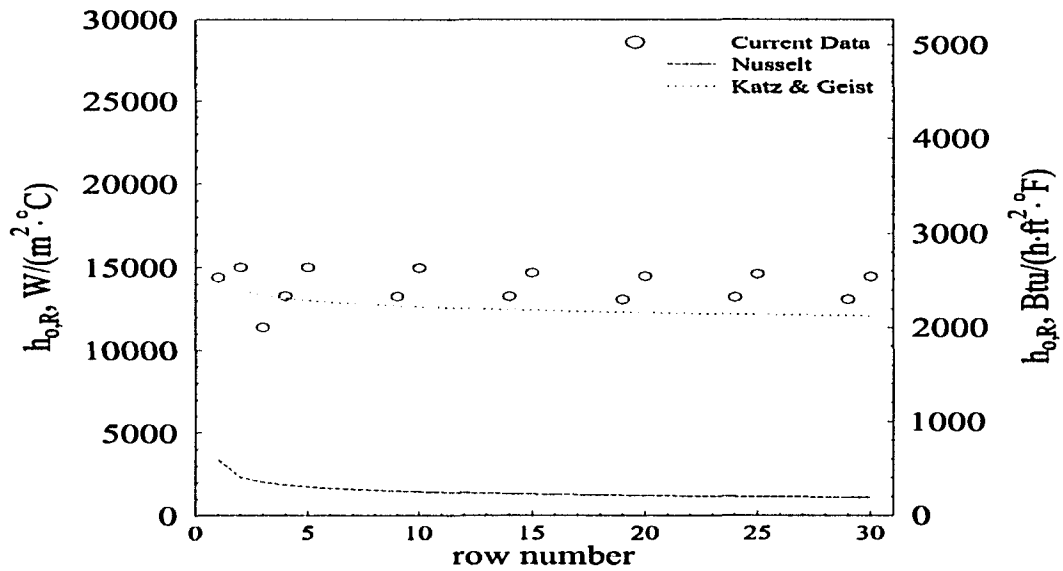


Figure 6.5: 26-fpi tube, average shell-side row heat transfer coefficient vs. row number for 30-row simulation with HFC-134a

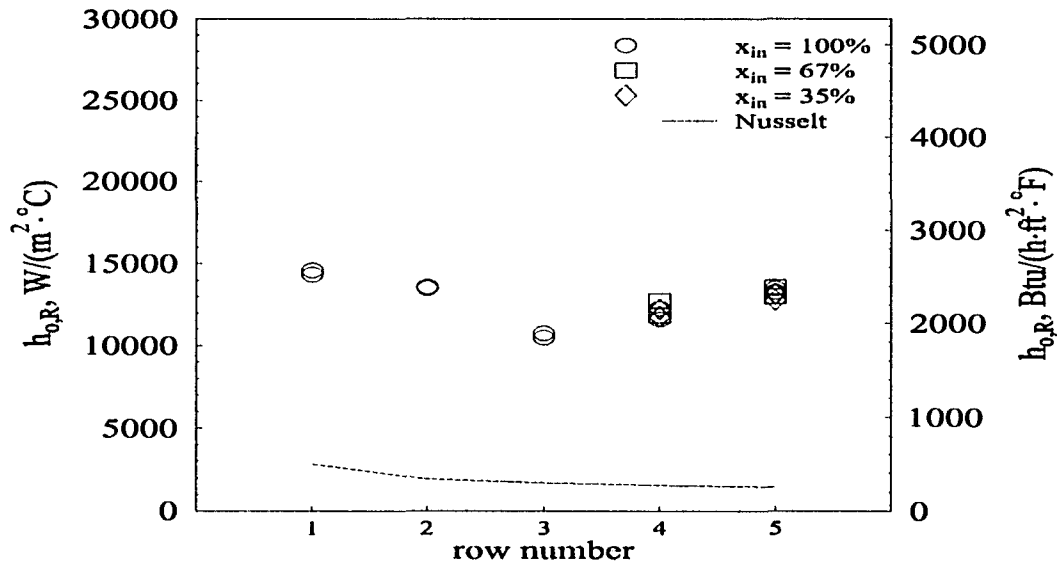


Figure 6.6: 26-fpi tube, average shell-side row heat transfer coefficient vs. row number for 5-row test bundle with HFC-134a

above, the first three rows of each pass are not shown except in the first pass ($x_{in} = 100\%$).

Results for the 40-fpi Geometry

The results from the tests with the 40-fpi tube bundle varied slightly from those of the 26-fpi tests. The 40-fpi tube, which is of the low-fin variety, showed only a slight inundation effect up to a certain critical condensate flow rate, at which point the inundation effect became much more noticeable and pronounced.

Figure 6.7 and 6.8 are plots of the heat transfer coefficient as a function of the condensate film Reynolds number. Two figures are presented to demonstrate two approaches to correlating the data. Figure 6.7 has a single regression line based on Equation 6.2 drawn through the data points. Figure 6.8 has two such lines, connected at a transition point of $Re_L = 1200$.

As can be seen from these two plots, this Reynolds number is the point at which the effect of increasing film flow rate becomes much more apparent on the heat transfer coefficient. The

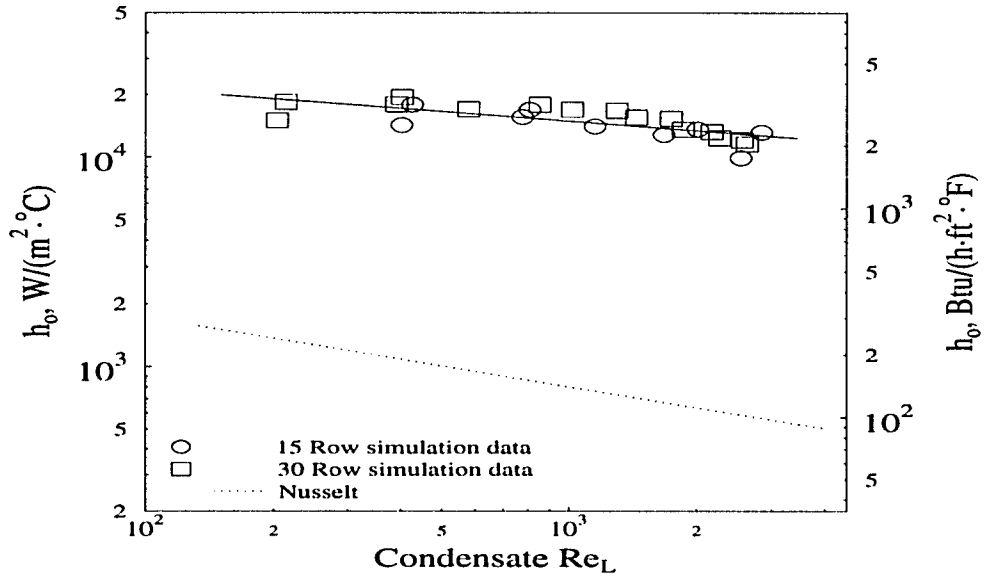


Figure 6.7: 40-fpi tube, average shell-side heat transfer coefficient vs. condensate Reynolds number number with HFC-134a

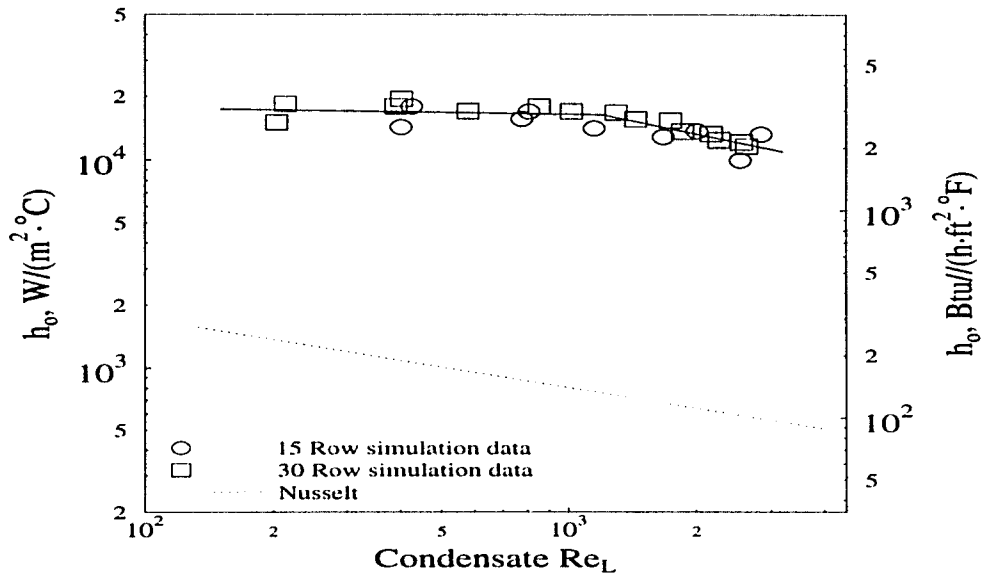


Figure 6.8: 40-fpi tube, average shell-side heat transfer coefficient vs. condensate Reynolds number number with HFC-134, two correlations

exponent for Equation 6.2 for the range $Re_L < 1200$ is 0.0290, compared to 0.413 for $Re_L > 1200$. These two exponents indicate that in the Reynolds range $Re_L < 1200$ the tube has very little dependence on the condensate flow rate and channels the liquid much like the 26-fpi tube. However, for $Re_L > 1200$ the 40-fpi tube's dependence on the inundation rate increases dramatically.

Because the condensation taking place during these tests occurred on the center tube of each row, it was not possible to observe the flow patterns and the transition points between various flow regimes. However, judging from the flow patterns observed leaving the bottom row of tubes during each refrigerant pass, it is believed that this change in heat transfer behavior corresponds to the point where the shorter, more closely spaced fins of the 40-fpi tube (with respect to the 26-fpi tube discussed above) become completely flooded along the bottom surface of the tube and the liquid begins to move axially. As a result of this axial condensate movement, the liquid is no longer channelled between the fins and a more of the tube's surface area is covered in liquid. Thus, the point at which the heat transfer behavior changes is also believed to be the transition between the column and sheet modes of condensate flow.

The drop in heat transfer coefficient in the lower portion of the simulated bundle can also be seen in Figures 6.9 and 6.10, which show the row-by-row heat transfer coefficients for the 30-row simulation. Figure 6.9 shows the full condenser profile for the 30-row simulation while Figure 6.10 plots all the 5-row test bundle runs simultaneously. In both figures only the first five tubes and rows four and five of the 5-row test bundle are presented, as these tubes are believed to most accurately represent the flow patterns in a real condenser.

Figure 6.9 shows clearly where inundation becomes a factor and the heat transfer begins to drop much more rapidly. The heat transfer coefficient stays relatively constant for each tube row through approximately the third refrigerant pass, which, as noted earlier, corresponds to

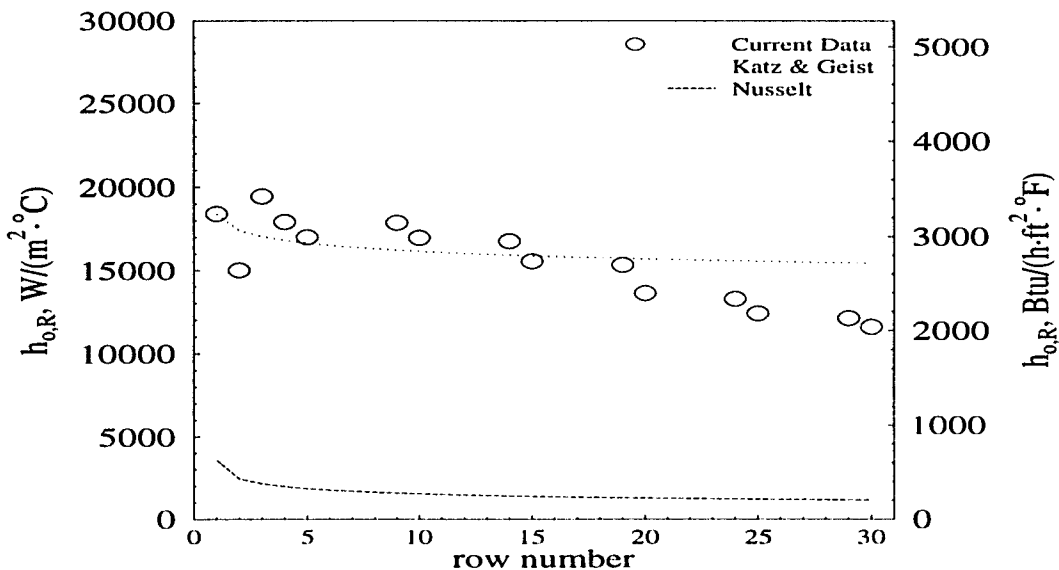


Figure 6.9: 40-fpi tube, average shell-side row heat transfer coefficient vs. row number, 30-row simulation with HFC-134a

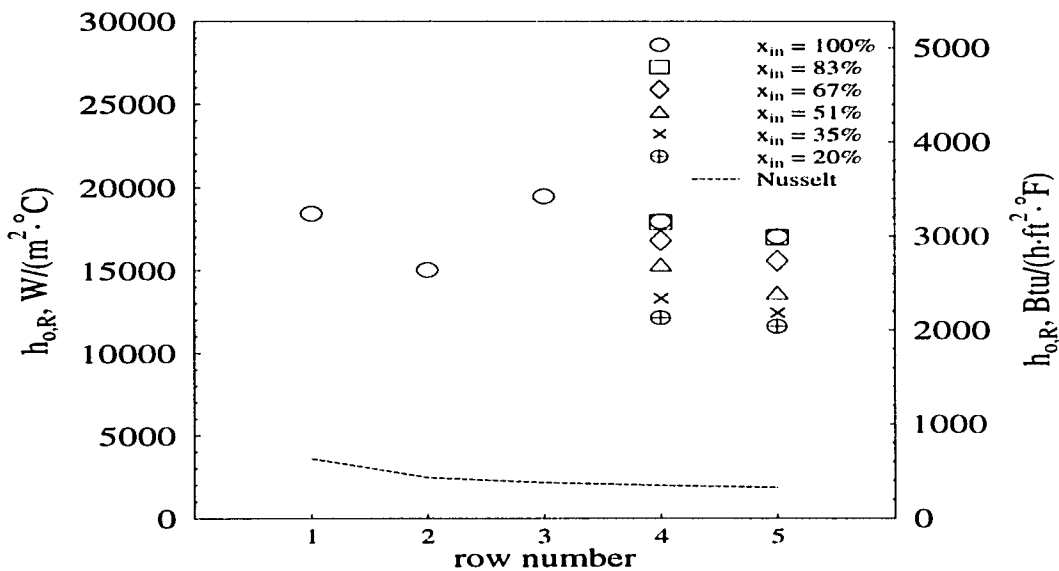


Figure 6.10: 40-fpi tube, average shell-side row heat transfer coefficient vs. row number, 5-row test bundle with HFC-134a

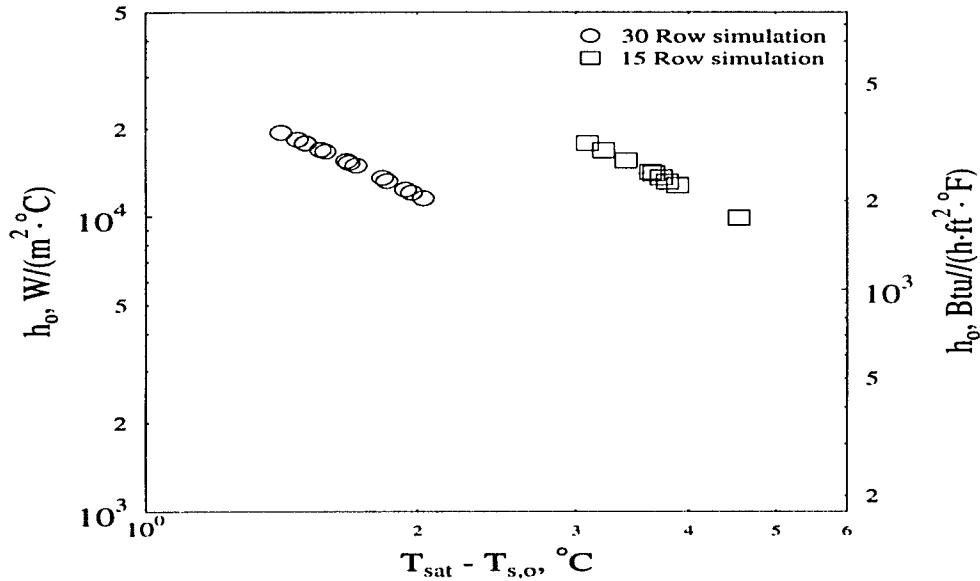


Figure 6.11: 40-fpi tube, average shell-side heat transfer coefficient vs. condensation temperature difference with HFC-134a

row 15 and a condensate Reynolds number of 1200. The drop in the last two tube rows of the test bundle are also seen in Figure 6.10. This is particularly apparent for the first two test runs, marked by $x_{in} = 100\%$ and 83% , which completely overlap each other.

The heat transfer coefficient is plotted against T_{sw} in Figure 6.11. Comparing this to the same figure for the 26-fpi tube, namely Figure 6.3, it is obvious that the inundation effect causes the temperature difference to increase in comparison to the best performing tubes at the top of the bundle. As the liquid flow rate increases on lower tube rows, the driving temperature difference increases, thereby decreasing the heat transfer coefficient for that tube. The temperature difference for the best to worst performing tubes over the full range of the tests is 1.47 to 2.03°C (2.65 to 3.65°F) for the 30-row simulation and 3.09 to 4.55°C (5.56 to 8.19°F) for the 15-row simulation.

Results for the Tu-Cii Geometry

The Tu-Cii tube is referred to as an enhanced tube because of its three-dimensional fin geometry. This three-dimensional fin provides greater surface area for condensation than traditional flat-sided fins and thus, offers the possibility of improved heat transfer performance. However, the results of inundation experiments discussed below show that these features also make this tube more susceptible to liquid loading effects.

Unlike the two finned tubes, the Tu-Cii showed an immediate degradation in heat transfer performance with increasing liquid inundation. Figure 6.12 shows the heat transfer coefficient as a function of the film Reynolds number and indicates that the heat transfer drops steadily with increasing condensate flow.

However, the figure also shows that, like the 40-fpi discussed in the previous section, the Tu-Cii appears to have a dual performance range as a function of the condensate film Reynolds number. The transition point in Figure 6.12 can be found at $Re_L = 1250$. A line drawn through the points below $Re_L = 1250$ has a slope of $n = 0.3640$, larger than found for either the 26-fpi tube ($n = 0.0268$) or the 40-fpi tube ($n = 0.0290$) in its respective low Reynolds range. Above the critical Reynolds number the exponent for Equation 6.2 increases dramatically to $n = 0.9059$. Thus, even in its highest performance range the Tu-Cii is more dependent on condensate flow rate than the two finned tubes. Interestingly, the exponent in both the Reynolds ranges is even larger than that predicted by the Nusselt theory for smooth tubes, where $n = 0.333$, as shown in Equation 6.1.

The poor inundation behavior is believed to be a result of the saw-tooth shape of the tube's three-dimensional fins. The saw-tooth geometry not only allows the draining condensate to move more easily in the axial direction, it also slows the drainage of liquid from between the fins, which contributes to axial movement along the tube. Webb (1990), working with an earlier version of the same tube, also observed this when he noted that the time between

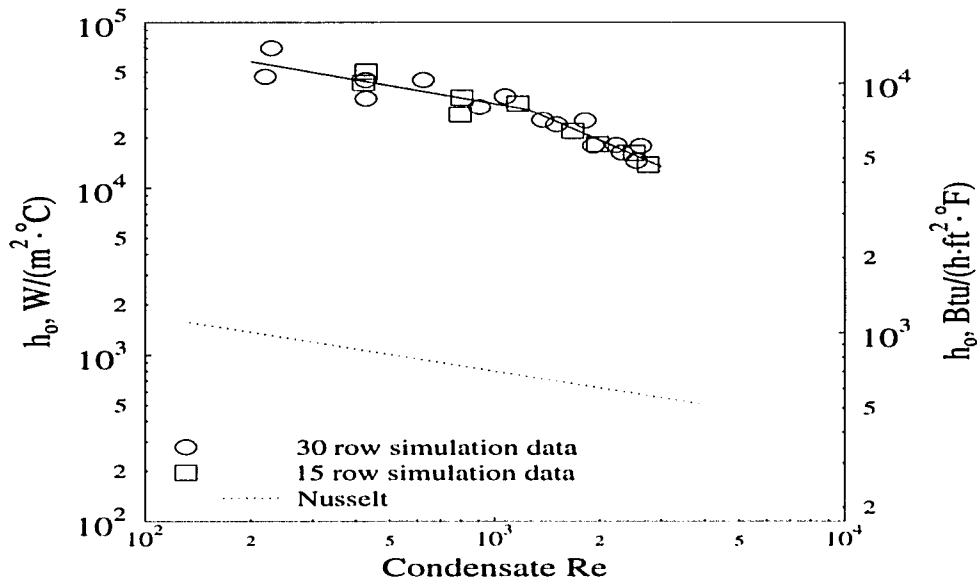


Figure 6.12: Tu-Cii tube, average shell-side heat transfer coefficient vs. condensate Reynolds number with HFC-134a

condensate impingement at the top of the tube and condensate separation from the bottom of the tube was much larger than that for the standard 26-fpi tube.

It is interesting to note at this point that the dripping patterns for the Tu-Cii differed from the other tubes. As described earlier, because of the physical arrangement of the active tubes in the test section, it was only possible to observe the drainage patterns from the bottom row of each test bundle. However, every tube bundle except the Tu-Cii began each run in either the drip or drip/column mode at the bottom of the fifth row. The Tu-Cii, on the other hand, began in the column mode. This would seem to support the supposition that the three-dimensional fins are holding liquid in greater volume. The larger body forces then pull greater amounts of liquid from the fin spaces, creating columns instead of individual drips.

Figure 6.13 indicates how the heat transfer coefficient is spread over a larger range of temperature difference. The temperature difference range for the 30-row simulation is from 0.50 to 1.60°C (0.9 to 2.88°F), while it ranges from 1.2 to 3.16°C (2.16 to 5.69°F) for the

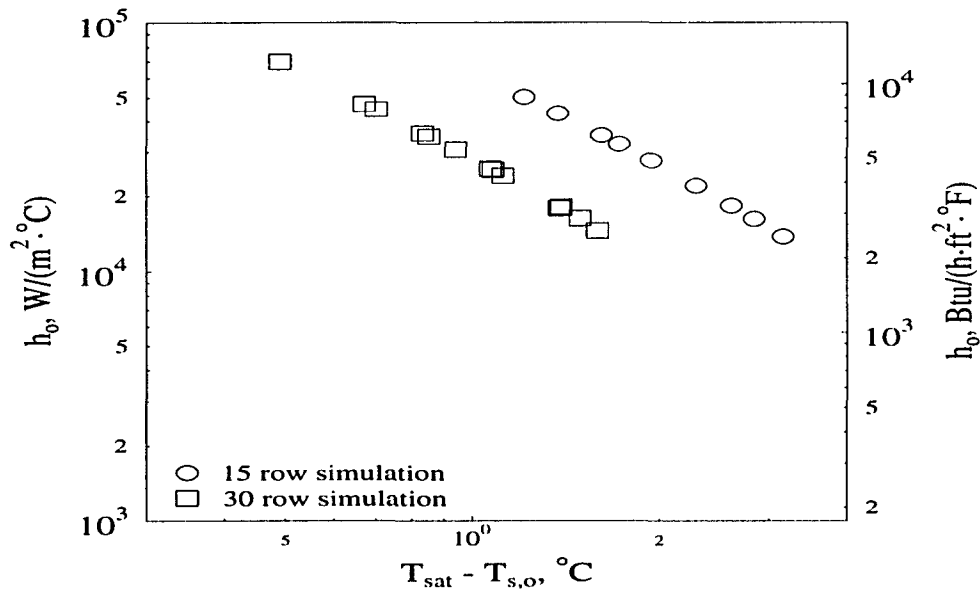


Figure 6.13: Tu-Cii, average shell-side heat transfer coefficient vs. condensation temperature difference with HFC-134a

15-row simulation. At the same time, the heat transfer coefficients drop from a high of near 70,000 W/(m² · °C) (12,325 Btu/(h·ft² · °F)) to a low of approximately 14,000 W/(m² · °C) (2465 Btu/(h·ft² · °F)).

Figures 6.14 and 6.15 show the overall bundle profiles for the 30 and 15-row bundle simulations, respectively. Comparing these to the corresponding figures for the 26 and 40-fpi tubes, it can be seen how much more susceptible the Tu-Cii tube is to inundation effects. In both simulations, the heat transfer coefficient increases from the first to the second rows and then drops off rapidly. This same behavior was seen by Honda et al. (1992) when condensing CFC-113 on staggered bundles of enhanced tubes and was explained by a possible blockage effect in the first row accelerating the vapor into the second row.

Again, the correlations of both Nusselt and Katz and Geist are shown for comparison. As the figures indicate, and as was pointed out earlier, the heat transfer drops off at a rate even greater than predicted by either correlation.

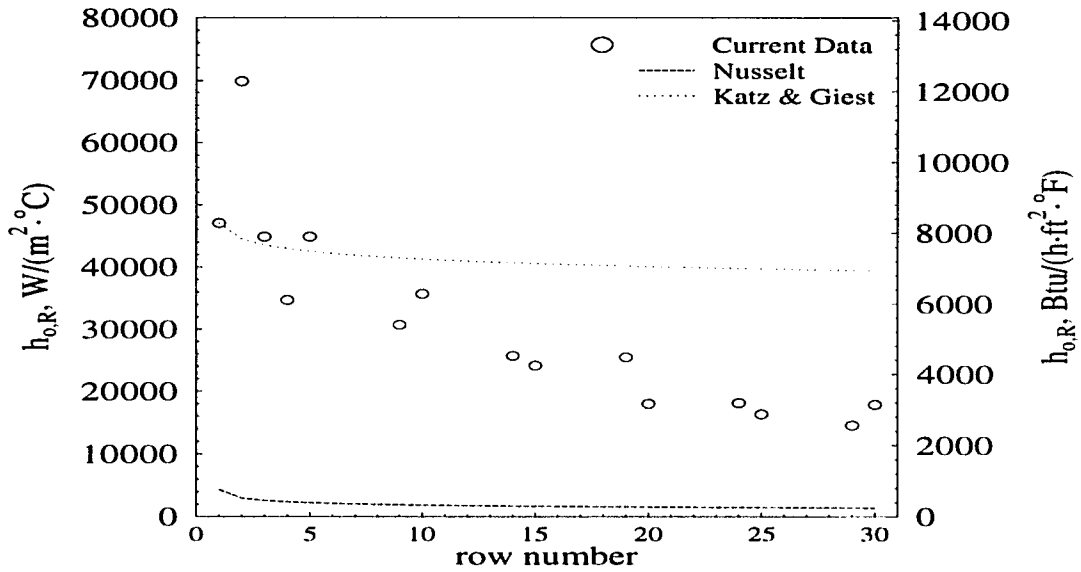


Figure 6.14: Tu-Cii tube, average shell-side row heat transfer coefficient vs. row number for 30-row simulation with HFC-134a

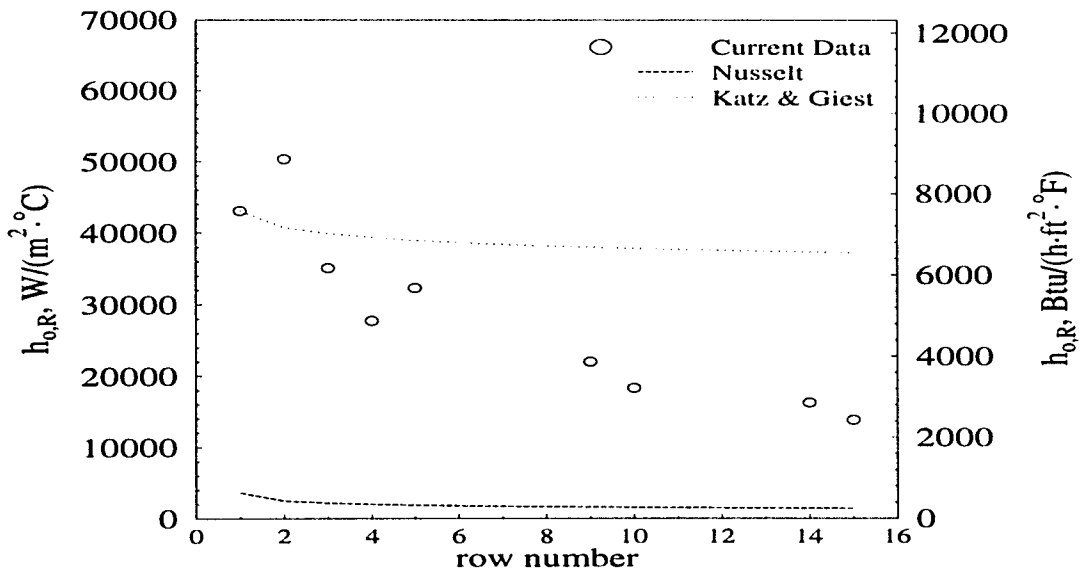


Figure 6.15: Tu-Cii tube, average shell-side row heat transfer coefficient vs. row number for 15-row simulation with HFC-134a

Results for the G-SC Geometry

The G-SC enhanced tube is distinguished by its continuous Y-shaped fins. During inundation tests, these fins allowed the tube to perform similarly to the finned tubes discussed earlier.

Figure 6.16 shows the relationship between the shell-side heat transfer coefficient and the condensate Reynolds number. Data points are plotted for two 30-row simulations and one 15-row simulation. As with the corresponding figures for the other tube geometries, only data for all 5-rows from the first refrigerant pass (100% saturated vapor at the inlet) are presented, along with data from the fourth and fifth tubes from subsequent passes.

Figure 6.16 shows that the heat transfer coefficient decreases slowly with increasing Reynolds number. Compared to Figures 6.1, 6.8, and 6.12, the decline is much less dramatic than for the Tu-Cii, but slightly higher than for the finned tubes. The change in heat transfer coefficient also appears to be relatively steady over the full range of condensate flow rate.

Webb (1990), in a study with CFC-11 on the G-SC tube, observed condensate drainage around the circumference in the Y-shaped fin as well as channeling of condensate between the fins. It is assumed that this phenomenon also occurred during the current study even though it could not be observed first-hand. This drainage pattern would explain the relatively small drop in heat transfer coefficients over the full range of condensate flow.

Figure 6.17 presents the heat transfer coefficient as a function of the temperature difference ($T_{sat} - T_{s,o}$). The appearance of this figure is similar to the comparable figures for the other tubes, showing a steady decrease in heat transfer coefficient with increasing T_{sw} . For the 30-row simulation the temperature differences ranged from 1.3 to 1.94°C (2.34 to 3.49°F), while T_{sw} ranged from approximately 3.0 to 4.1°C (5.4 to 7.38°F) during the 15-row simulation.

The overall 30-row bundle profile is presented in Figure 6.18. The G-SC bundle acted

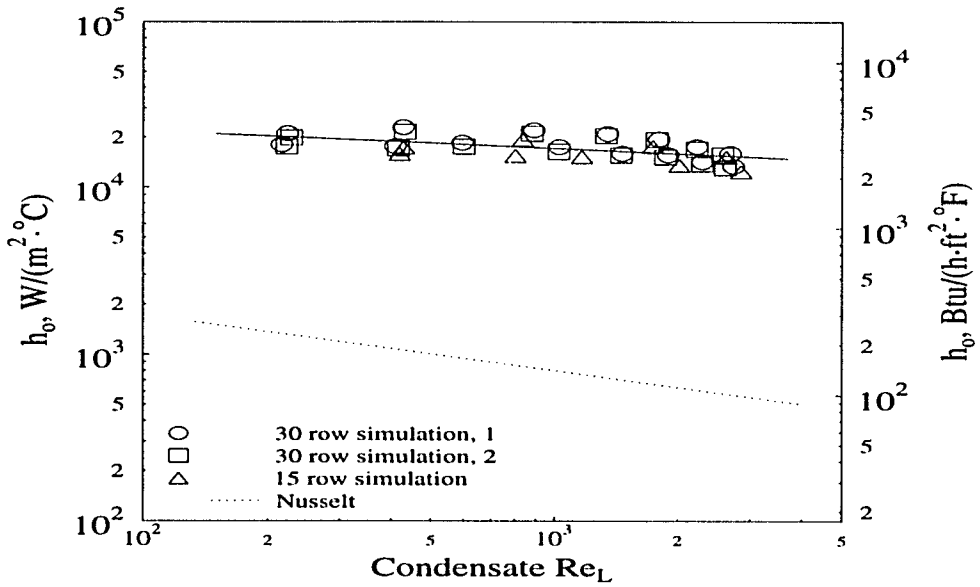


Figure 6.16: G-SC tube, average shell-side heat transfer coefficient vs. condensate Reynolds number with HFC-134a

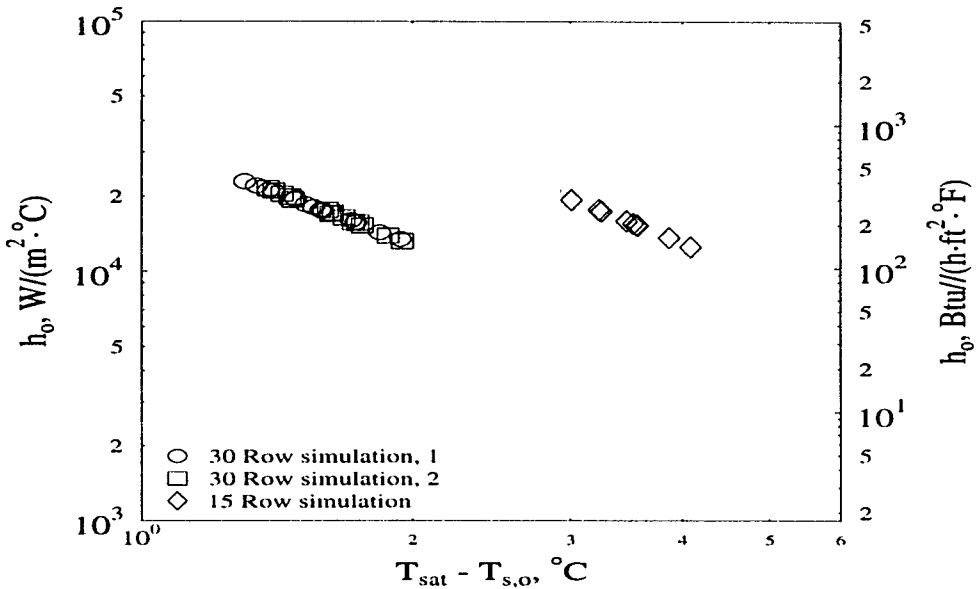


Figure 6.17: G-SC, average shell-side heat transfer coefficient vs. condensation temperature difference with HFC-134a

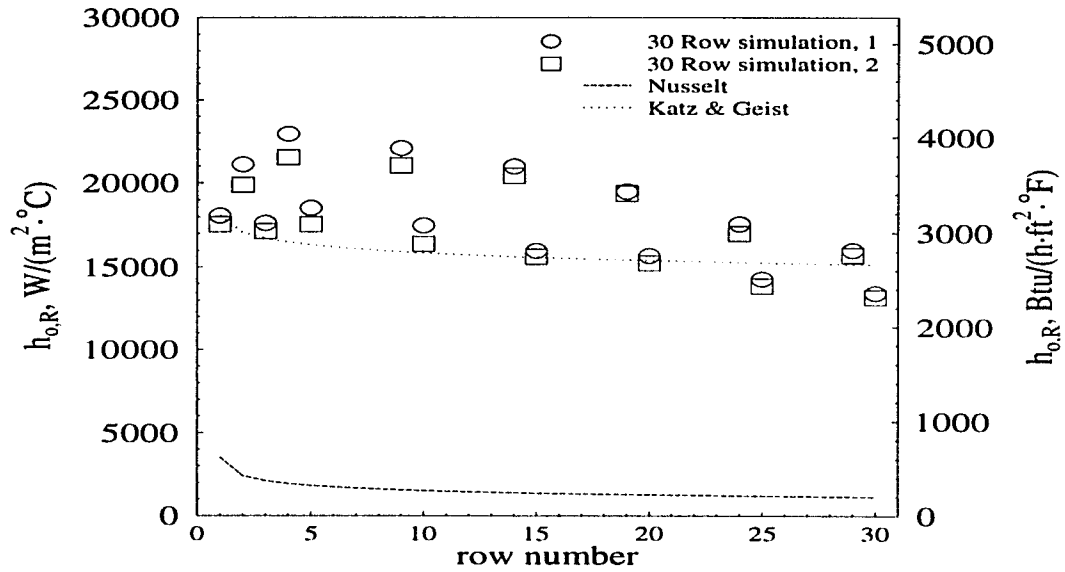


Figure 6.18: G-SC tube, average shell-side row heat transfer coefficient vs. row number for 30-row simulation with HFC-134a

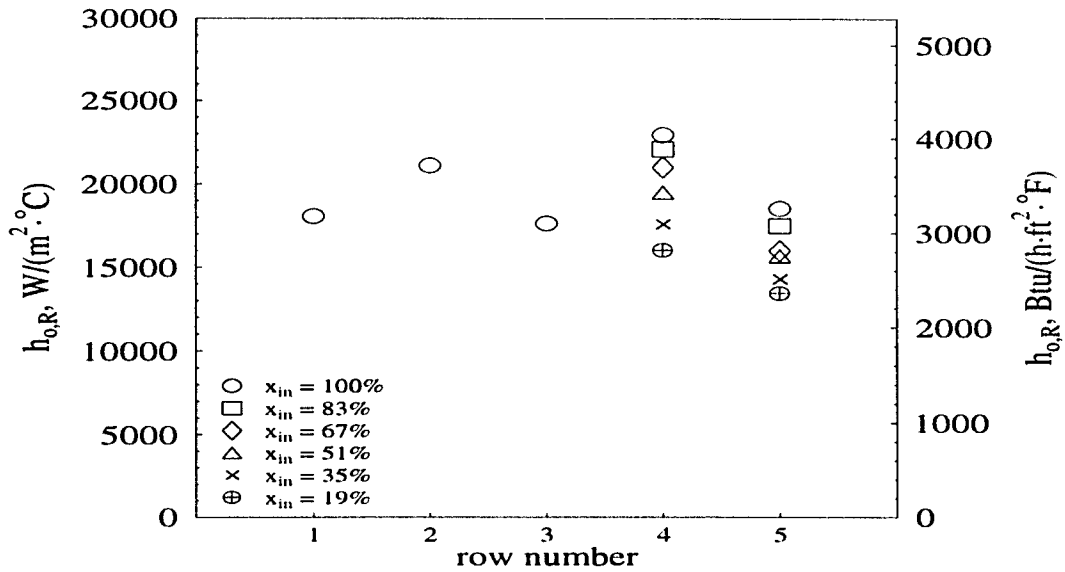


Figure 6.19: G-SC tube, average shell-side row heat transfer coefficient vs. row number for 5-row test bundle in a 30-row simulation with HFC-134a

differently from the other bundles in that the fourth row of the 5-row test bundle was often the highest performing tube through the entire range of tests. This behavior can also be plainly seen in Figure 6.19, which presents all the 30-row simulation runs overlapping. The steady decrease in heat transfer coefficient in the fourth and fifth rows with increasing inundation can clearly be seen in both figures. The data for the first three rows are not presented in either figure as it is believed that the flow rate patterns on those tubes do not represent those found in an actual condenser.

The apparent sudden increase in heat transfer coefficient in the first four rows, seen in Figure 6.18, is not so much an increase in heat transfer coefficient with increasing condensate flow as it is indicative of the “signature”, or row-by-row heat transfer performance trend, of the 5-row G-SC test bundle. The “signature” is unique to the bundle and remains constant, independent of the working fluid. This row-by-row signature is shown in Figure 6.19 and is distinguished by the lines marked with \circ . The true effect of the inundation is shown in the same figure in rows 4 and 5, which decrease steadily from the first through the last run of the test.

Comparisons Between Tube Geometries

The heat transfer performance of all the tube geometries tested is compared in Figures 6.20 and 6.21. Figure 6.20 compares the geometries in terms of h_o vs. Re_L , while Figure 6.21 compares them on the basis of h_o vs. T_{sw} . As is apparent from both figures, the Tu-Cii performs better than the other geometries in terms of overall heat transfer performance and higher heat transfer coefficients, even though it showed the largest inundation effects and the largest drops in heat transfer performance with increasing condensate flow rate.

In general, the Tu-Cii performed the best of the four tube geometries, particularly at $Re_L < 2000$ and $T_{sw} < 1.5^\circ\text{C}$ (2.7°F). For $Re_L > 2000$ the Tu-Cii shows heat transfer

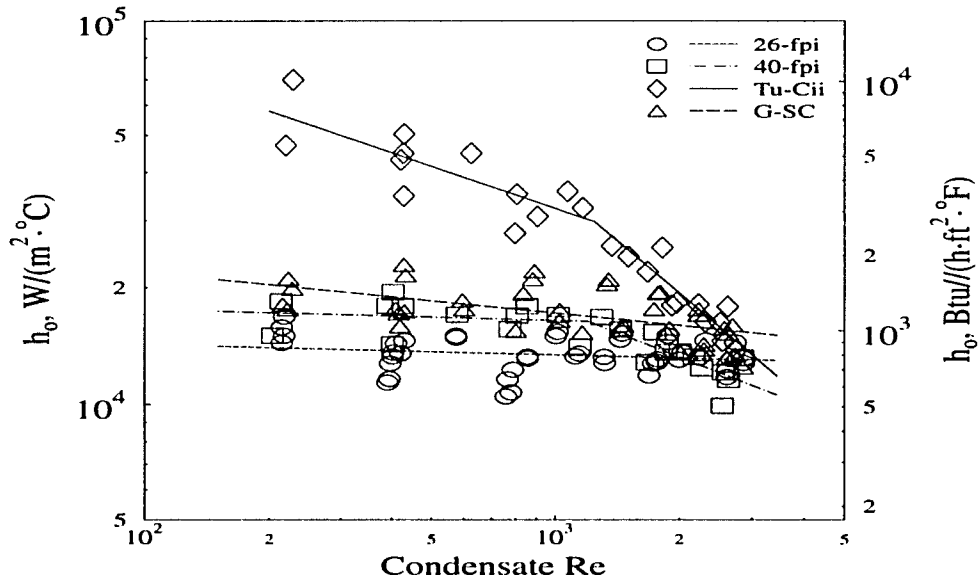


Figure 6.20: Average shell-side heat transfer coefficient vs. Re_L comparison of all tube geometries

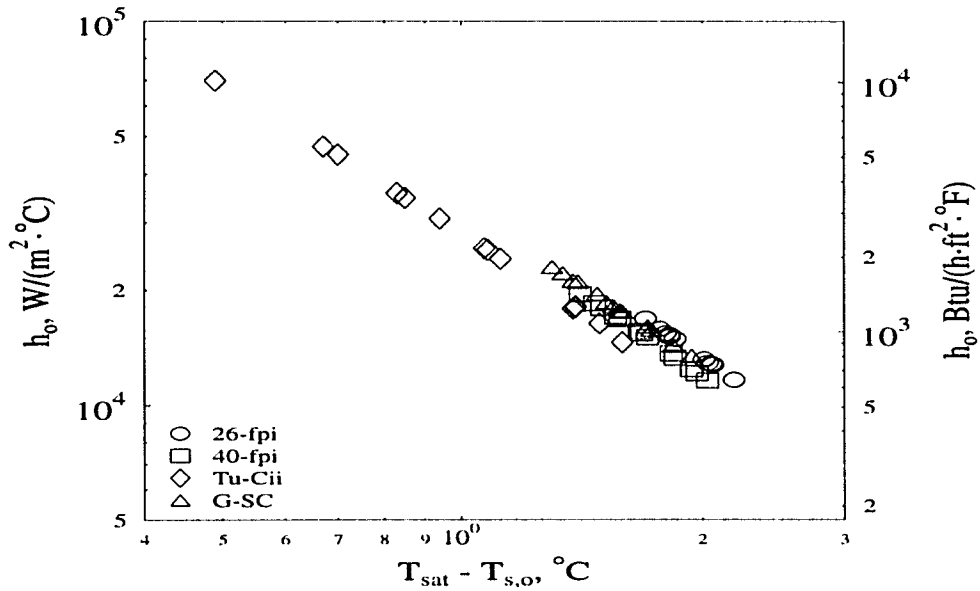


Figure 6.21: Average shell-side heat transfer coefficient vs. condensation temperature difference comparison of all tube geometries

performance within 10% of the other tubes. Both the high heat transfer coefficients and large row effect trends are believed to be related to the geometry of the tube's three-dimensional fins, which provide greater surface area for condensation, but also tend to retain the condensate for a longer time before drainage, thus allowing the liquid to move axially along the tube surface.

The Tu-Cii's best performance was found to be below Reynolds numbers of approximately 1250. Below this flow rate the tube's performance was highest and its dependence on condensate flow rate was much smaller than for $Re_L > 1250$.

The G-SC was the next best performer, showing a much lower heat transfer coefficient at low Reynolds numbers than the Tu-Cii but also showing much less dependence on condensate flow rate. At the lowest flow rate, the G-SC tube had a heat transfer coefficient that was approximately 30% of the Tu-Cii's, but was 75% of the Tu-Cii value at the highest flow rate because of the large decrease in the Tu-Cii's performance.

The G-SC also performed better than both the finned tubes by a small margin. Compared to the 26-fpi tube, it showed heat transfer coefficients that were approximately 23% higher, while compared to the 40-fpi tube the heat transfer performance was within about 10%, particularly as $Re_L \rightarrow 1200$. However, at $Re_L > 1200$, where the 40-fpi showed a much higher row effect, the G-SC was clearly better, having a heat transfer coefficient approximately 20% higher at the largest condensate flow rate .

While the G-SC is considered an enhanced tube, it performed much more like the two finned tubes than it did the Tu-Cii, the other enhanced tube. This is due to the fact that the G-SC has continuous fins which act to channel the liquid as it falls from row to row and prevent the condensate from moving axially.

The standard 26-fpi showed the best characteristics in terms of liquid inundation, even though its heat transfer performance was nearly 18% lower than the next highest tube. Very little change was seen in the heat transfer coefficient for each tube over the entire range of

Table 6.1: Coefficients and exponents for Equation 6.2

Tube	$a \times 10^{-3}$ W/(m ² · °C)	n
26-fpi	16.122	0.0267
G-SC	35.650	0.1055
40-fpi ($Re_L < 1200$)	20.065	0.0289
40-fpi ($Re_L > 1200$)	304.74	0.4126
Tu-Cii ($Re_L < 1250$)	398.32	0.3640
Tu-Cii ($Re_L > 1250$)	18935	0.9059

inundation rate. Again, this is attributed to the tubes ability to channel the flow and keep a large surface area free for condensation, even at high condensate flow rates.

The low-fin 40-fpi tube and the enhanced Tu-Cii showed the strangest behavior, with performance trends which were distinctly different in two different Reynolds ranges. The 40-fpi tube performed like the standard 26-fpi tube at flow rates with $Re_L < 1200$ but acted like the enhanced Tu-Cii at higher Reynolds numbers. The performance of the Tu-Cii, on the other hand, was much more sensitive to the condensate flow rate than the 40-fpi tube in its respective low Reynolds range. However, above its critical Reynolds number the Tu-Cii's performance dropped much more dramatically, as its exponent n for Equation 6.2 is more than twice that of the 40-fpi in it highest Reynolds range.

While it was not observed directly, this change in behavior is thought to represent the point at which the condensate flow rate moves from the column/sheeting mode of drainage to the full sheeting mode. During this mode of condensate flow, the fins do not channel the liquid as effectively and allow much greater axial movement of the liquid. The relatively tight bundle pitch (19.1 mm vertical, 22.2 mm horizontal) may also play a part by allowing full columns and sheets of liquid to exist where they would not otherwise form in larger distances.

Table 6.1 contains the coefficients and exponents for Equation 6.2 for each of the tubes tested. The individual equations are plotted in Figure 6.20.

Summary

Tests were run on four different condensation tubes, two standard finned tubes and two enhanced tubes, using HFC-134a as the working fluid. Tests were performed to simulate both a 15-row and a 30-row condenser. From the data, the following conclusions were made.

1. The enhanced tubes, in particular the Tu-Cii, show better overall performance during inundation tests, displaying higher overall heat transfer coefficients through the full range of condensate flow rates tested.
2. The finned tubes show the best performance in terms of row effect behavior, displaying very little dependence on condensate flow rate. The 26-fpi in particular showed negligible inundation effects through the full range of inundation flow rates.
3. In general, those tubes with continuous fins have better drainage effects and show the least dependence on inundation flow rates.
4. The Tu-Cii shows the greatest inundation effects, with heat transfer coefficients dropping almost 80% from the top to the bottom of the bundle in a 30-row simulation.
5. The Tu-Cii performs best at $Re_L < 1250$. For $Re_L > 1250$, it is believed the fins become flooded so that the tube performance degrades more rapidly with increasing condensate flow rate.
6. The G-SC tube performs much like a finned tube when used for condensation of HFC-134a, showing only slight degradation of heat transfer performance with increasing condensate flow.
7. The 40-fpi tube performs best at $Re_L < 1200$ where it shows very little row effect. This row effect is on the same order as the 26-fpi tube. It is believed the fins become

flooded at $Re_L > 1200$, where the tube performance degrades markedly with increasing condensate flow rate.

CHAPTER 7. HCFC-123 INUNDATION AND VAPOR SHEAR RESULTS

Vapor shear occurs on a tube when the shearing stresses in the condensate layer, caused by high velocity vapor, act to thin the layer by either forcing the liquid to flow around the perimeter of the tube or by completely stripping the liquid from the surface. Because vapor shear acts to thin the liquid layer and promote the removal of condensate it has a positive effect on the heat transfer performance of the tube. This is in contrast to liquid inundation, which acts to thicken the liquid layer in the lower rows of tube bundles and decrease performance.

The effects of shear and inundation vary with different refrigerant types even though the cooling capacities may be the same. The physical properties of HCFC-123 and HFC-134a differ markedly even though their enthalpies of vaporization are very similar (within 0.5%). While HCFC-123's liquid density is nearly 25% larger than that of HFC-134a, its vapor density is approximately 1/5 that of HFC-134a at the same saturation conditions. These differences mean that for similar cooling capacity under the same saturation conditions, the vapor volume of HCFC-123 is nearly five times that of the HFC-134a, and its subsequent velocity under flow conditions is approximately five times as high. Thus, effects due to vapor shear become much more likely when HCFC-123 is used as the working fluid.

Inundation and vapor shear tests were performed on all four tube bundles to simulate a 25-row condenser with vapor velocities through the first tube row ranging from 2.5 m/s (8.2 ft/s) to 4.6 m/s (15.1 m/s). Heat fluxes in the tubes varied from approximately 16,500 W/m² (5230 Btu/h/ft²) to 30,000 W/m² (9510 Btu/h/ft²). These vapor velocities and heat fluxes are representative of HCFC-123 bundles used in industry. Data were taken to determine

the relationship between the shell-side heat transfer coefficient and row number, inundation rate (condensate Reynolds number), and vapor velocity. The condensate Reynolds numbers ranged from approximately 100 to 1200.

Vapor velocities were calculated using the method of Nobbs and Mayhew (1976), who based the vapor velocity on the mean flow width between tubes. This width is also defined by Equation 4.26 and is written as

$$w = \frac{p_l p_t - \pi \frac{D_o^2}{4}}{p_l} \quad (7.1)$$

In this equation, p_l and p_t are the longitudinal and tangential tube pitches, respectively, and D_o is the tube outer diameter. The width calculated using this method with a nominal 19.1 mm (0.75 in) o.d. tube is approximately 2.3 times larger than the value of the minimum width (3.18 mm (0.125 in)) based on the distance between adjacent tubes in the same row. The velocities determined using the mean flow width, therefore, are about 2.3 times smaller than the velocities found when using the minimum flow width.

The mean flow area is calculated using this width and the number of tubes in the first row. For these tests, only one tube in the top row was active and open to vapor flow, so the mean flow area was calculated to be $2wL$.

Heat transfer coefficients are calculated based on the nominal surface area of the tube using the diameter of the tube at the fin tips. This surface area is also known as the envelope area. Area calculations using this method allow the enhanced tubes, for which the actual surface area is not known, to be compared to the finned tubes. It also allows all the tubes to be compared on a unit length basis.

Inundation simulations were conducted by introducing refrigerant flows of known quality into the test section. The vapor portion of the flow was condensed on the test bundle while the liquid portion was screened off, distributed, and dripped onto the active tubes to simulate inundation. Quality changes of near 100% were produced in a series of five refrigerant passes

(approximately 18% quality change per test) to complete condensation through the simulated 25-row bundles. A more complete description of the inundation apparatus and test procedures can be found in Chapter 4.

Overall, there were no shear effects seen on any of the tubes for the range of vapor velocities produced in these tests. However, at the same time, each tube showed a noticeable drop in heat transfer performance due to liquid inundation. Results of the tests for each tube bundle are presented below.

Results for the 26-fpi Geometry

Simulated bundle profile

The 26-fpi bundle showed no shearing effects through the range of vapor velocities used in these tests. Figure 7.1 presents the heat transfer performance of the simulated 25-row bundle as a function of the vapor velocity entering the top row of the bundle. Following the analysis discussed in Chapter 6, only data for simulated tube rows 1 through 5, 9, 10, 14, 15, 19, 20, 24, and 25 are presented. Lines regressed through the data points for each velocity show the trend of the data. These trends indicate that with increasing vapor velocity, which corresponds to an increase in both refrigerant flow rate and heat flux, the heat transfer coefficients decrease through the full depth of the simulated bundle.

The figure also shows that the decrease at each velocity through row 25 is relatively consistent from one inlet velocity to another. This is particularly true at the middle and high velocities, where the trends are almost completely parallel. Overall, the average heat transfer coefficient dropped approximately 20% from the lowest to the highest inlet velocity.

The apparent decrease in heat transfer coefficient with increasing vapor velocity seen in Figure 7.1 is not a function of the vapor velocity, but an effect of higher condensation rates (and thus increasing inundation) which corresponds to increasing heat flux and refrigerant

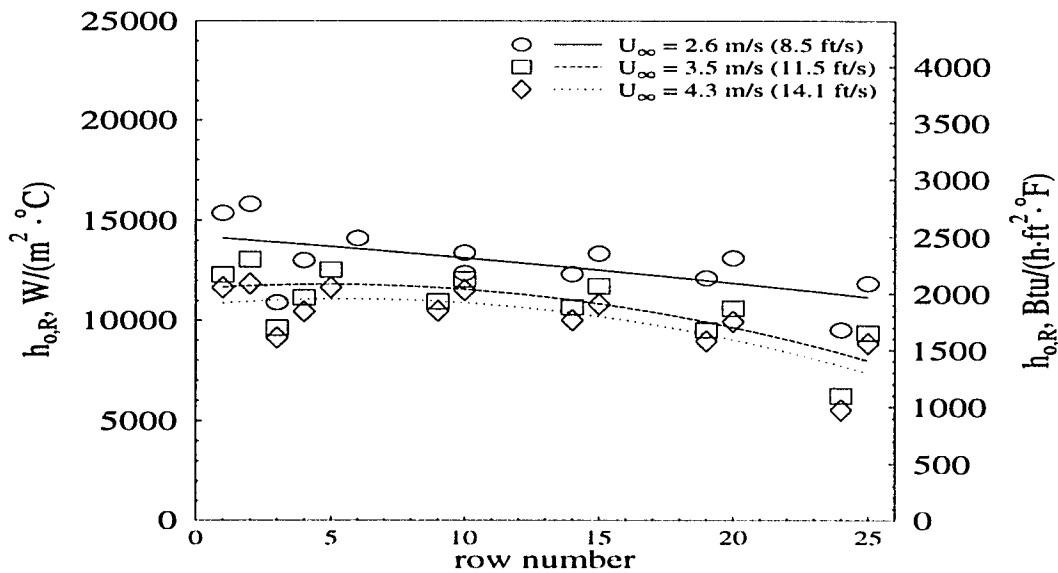


Figure 7.1: 26-fpi tube, average shell-side row heat transfer coefficient vs. row number for three different vapor velocities with HCFC-123

flow rate. This inundation effect can be seen most readily near a simulated tube depth of row 20 in the data at the highest vapor velocity, where the heat transfer coefficients begin to decrease at a faster rate than the simulations at lowest flow rate.

The decrease in the average heat transfer coefficients displayed at the different velocities seems to show that the increase in condensate flow rate from the first to the second vapor velocity has a larger detrimental effect on the performance than does the increase from the second to the third velocity. This is thought to be a function of the liquid retention between the tube fins at the different condensate flow rates. It is believed that at the first vapor velocity there is very little condensate flooding in the lower part of the tube, but with an increase in inundation rate the fins become significantly more flooded, so that with another (equal) increase in flow rate, there is much less area to flood, resulting in a smaller decrease in the overall heat transfer performance.

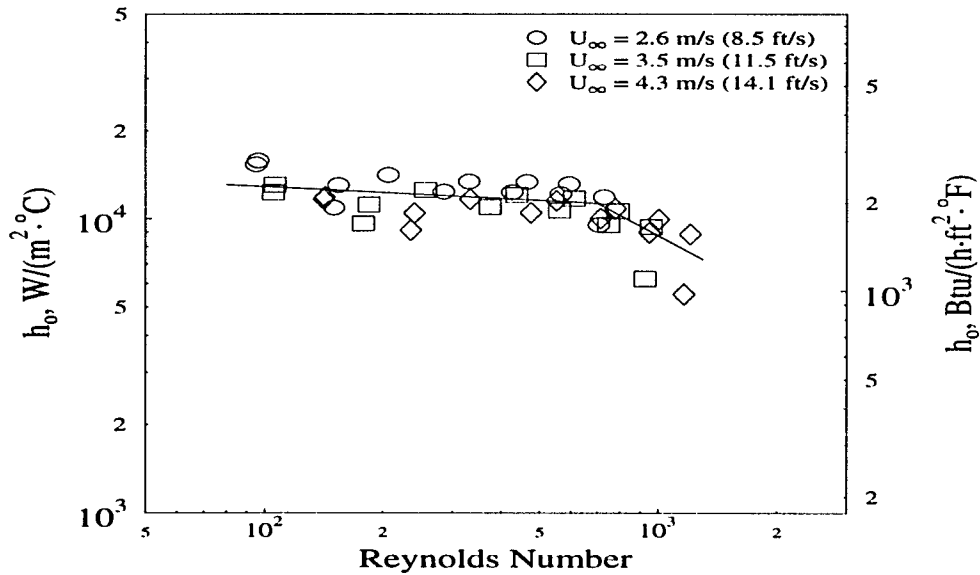


Figure 7.2: 26-fpi tube, average shell-side heat transfer coefficient vs. condensate Reynolds number for all data with HCFC-123

Performance as a function of Reynolds number

Figure 7.2 is a plot of all the data as a function of condensate Reynolds number. This figure shows that there is very little dependence on condensate Reynolds number, with only a slight decrease in heat transfer coefficient up to a Reynolds number of approximately 700. Above this value the heat transfer performance drops off more drastically. Correlations of the form

$$h_o = aRe_L^{-n} \quad (7.2)$$

(discussed in Chapter 6) plotted through the two different ranges of condensate Reynolds number ($Re_L < 700$, $Re_L > 700$) produce values of n equal to 0.0669 and 0.7186, respectively.

The large difference in the exponential values for Equation 7.2 indicates the large difference in heat transfer performance as a function of Reynolds number in the different Reynolds

ranges. Through the range of $Re_L < 700$ the tube is relatively independent of liquid loading effects, while at $Re_L > 700$ the tube is much more susceptible to condensate flow.

The behavior of the 26-fpi tube seen in Figure 7.2 is similar to the behavior of the 40-fpi and Tu-Cii tubes during HFC-134a inundation discussed in the previous chapter. In both cases the heat transfer coefficients showed a small, steady decrease through a critical value of condensate Reynolds number. Above this critical value the performance degraded much more rapidly and the heat transfer coefficients underwent a dramatic decrease through the rest of the Reynolds number range. This two-region trend is believed to be caused by the beginning of axial movement of the condensate along the lower tube surface as the fins become completely flooded along the lower portion of the tube. This change in heat transfer performance may also correspond to a transition in condensate flow pattern from the column mode to the column/sheet mode. This conclusion is based on the observed flow patterns leaving the bottom row of the 5-tube test bundle and the bundle's tight triangular pitch, even though the flow patterns in the middle of the test bundle could not be viewed directly.

The fact that this two-region behavior was not observed with the 26-fpi tube when inundating with HFC-134a is attributed to the higher viscosity and surface tension of HCFC-123, which tends to hold the liquid in the fins longer and allows the condensate film to build up to the point that axial movement becomes possible.

Test bundle row performance

Figures 7.3 and 7.4 are plots of the heat transfer coefficients of the 5-tube test bundle at the lowest and highest vapor velocities. Data is plotted as a function of the test section inlet quality. As with the Figures 7.1 and 7.2, only the data from the first pass is shown in its entirety, along with tubes 4 and 5 from each subsequent pass.

These two figures show how the heat transfer coefficients drop off in rows 4 and 5

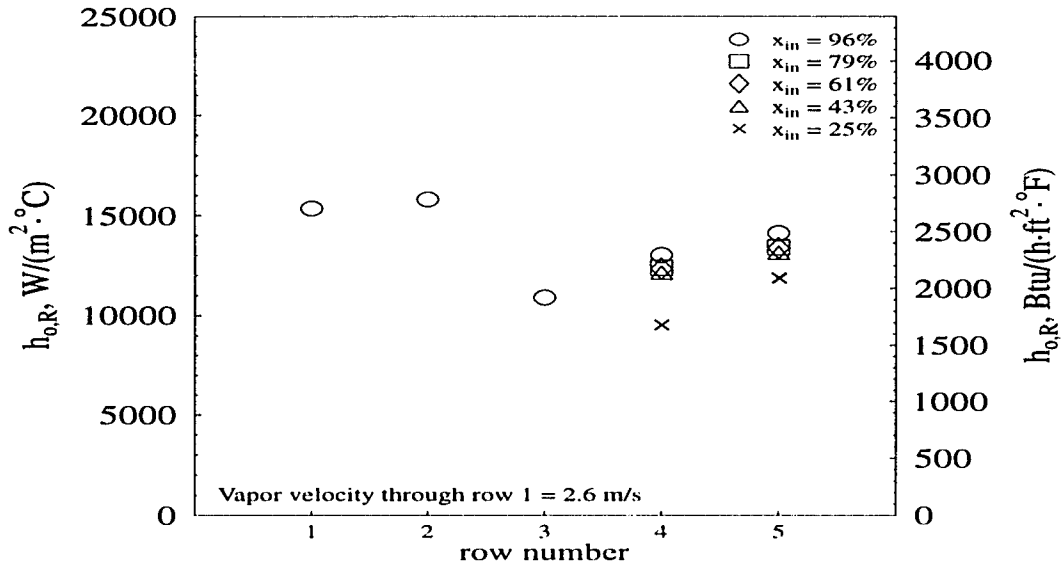


Figure 7.3: 26-fpi tube, average shell-side row heat transfer coefficient vs. row number for the 5-row test bundle using HCFC-123, $U_{\infty} = 2.6$ m/s (8.5 ft/s)

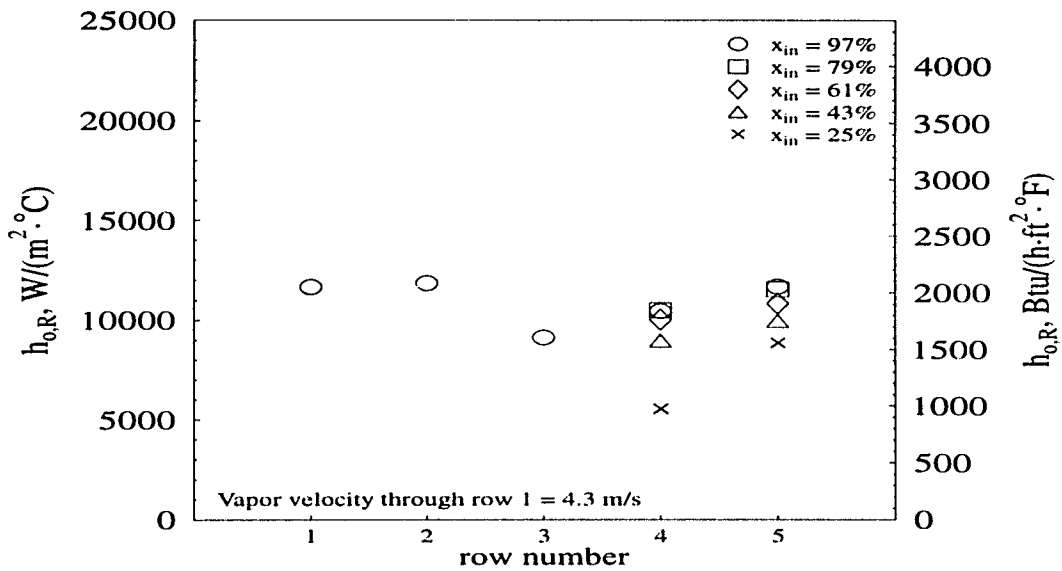


Figure 7.4: 26-fpi tube, average shell-side row heat transfer coefficient vs. row number for the 5-row test bundle using HCFC-123, $U_{\infty} = 4.3$ m/s (14.1 ft/s)

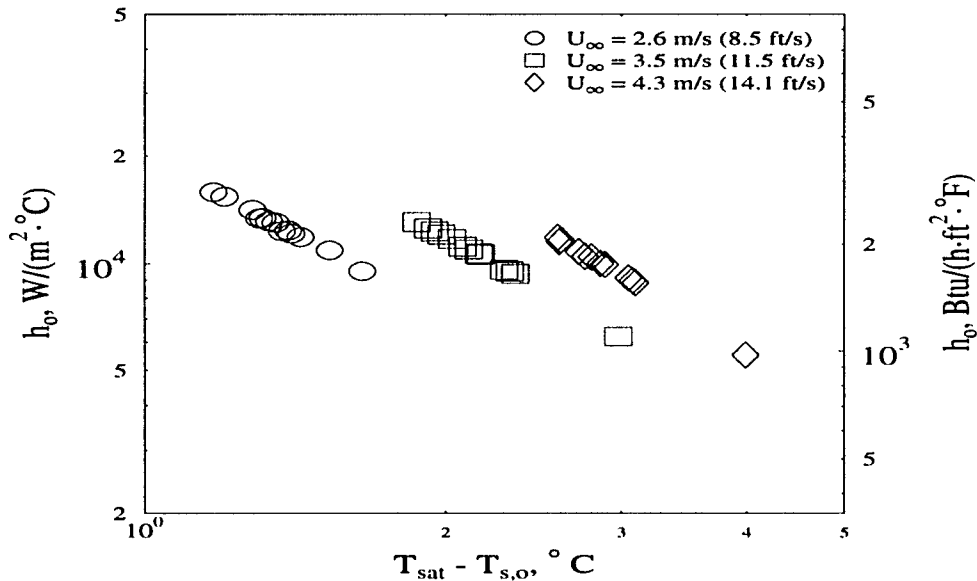


Figure 7.5: 26-fpi tube, average shell-side heat transfer coefficient vs. condensation temperature difference at three vapor velocities using HCFC-123

with decreasing inlet quality (increasing inundation flow rate), particularly at the highest inundation flow rate, designated by $x_{in} = 25\%$. A comparison of the figures also shows that the performance of the tubes decreases with an increase in the heat flux (refrigerant flow rate), even though this also corresponds to an increase in vapor velocity through the bundle. Thus, the dominant effect appears to be due to liquid inundation.

Performance as a function of T_{sw}

Figure 7.5 plots the row-by-row heat transfer coefficient as a function of the temperature difference ($T_{sat} - T_{s,o}$) for the three vapor velocities tested. As noted earlier, wall temperatures were calculated and not measured directly.

The figure indicates how the driving temperature difference increases with increasing heat flux. At the lowest heat flux, the temperature difference ranged from 1.15 to 1.64°C (2.07 to 2.95°F) from the best to the poorest performing tubes, respectively, while at the

highest heat flux the temperature difference ranged from 2.56 to 3.98°C (4.61 to 7.16°F). The effect of liquid inundation can be seen in the decrease in the heat transfer coefficient of the best performing tube at each of the different flow rates and in the rate of decrease of the heat transfer coefficient with increasing temperature difference at each flow rate. Lines drawn through the data have the general form $h_o = a\Delta T_{sw}^{-s}$. If this equation is used to represent the data in Figure 7.5 the value of the exponent, s , at the lowest vapor velocity is 1.431, while at the highest velocity the exponent increases to 1.715.

Experimental uncertainties in the calculated values of heat transfer coefficients for the tubes ranged from near $\pm 20\%$ at the lowest refrigerant flow rate (i.e. lowest vapor velocity) to approximately $\pm 9\%$ at the highest flow rate. The difference in these heat transfer coefficient uncertainty values is due to the higher uncertainties associated with the lower water and refrigerant flow rates and the subsequently smaller water temperature differences across the test section at the lowest vapor velocity. The uncertainties in these variables increase as the values become smaller, producing the relatively larger uncertainties found in the low velocity data.

Results for the 40-fpi Geometry

Simulated bundle profile

The 40-fpi tubes showed no shearing effects up through the highest vapor velocity $U_\infty = 4.5$ m/s (14.8 ft/s) tested. At the same time, condensate inundation was found to have a definite effect through the full range of refrigerant flow rates tested, particularly at $Re_L > 480$.

Figure 7.6 is a plot of the overall simulated 25-row bundle profile at three different vapor velocities, as calculated for the area between the tubes in the top row of the bundle. Trends drawn through the data at each velocity show that the average heat transfer coefficient

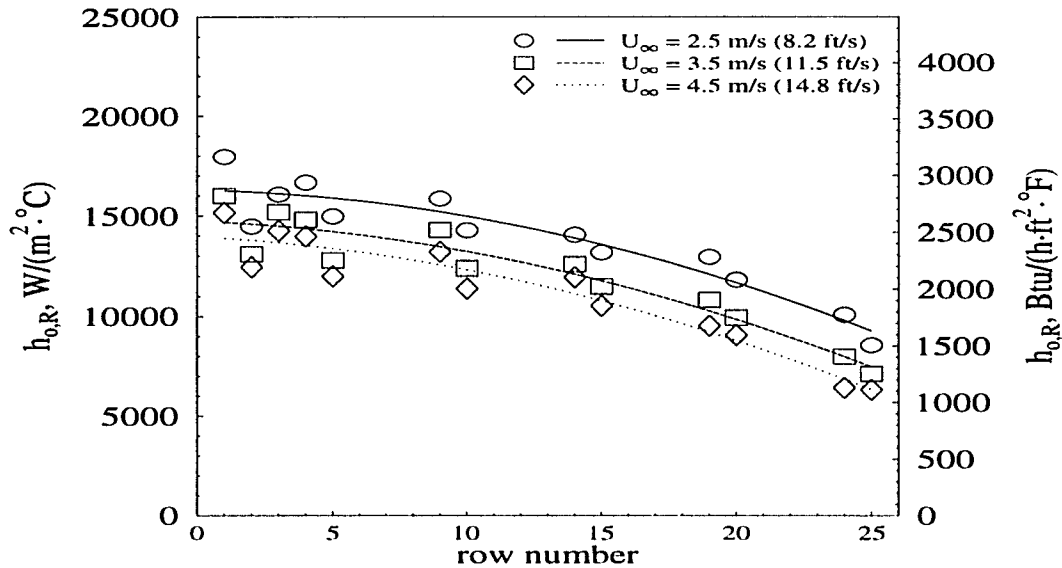


Figure 7.6: 40-fpi tube, average shell-side row heat transfer coefficient vs. row number for three different vapor velocities with HCFC-123

decreases steadily from the top to the bottom of the bundle at each vapor velocity (refrigerant flow rate), while the overall bundle performance decreases with increasing vapor velocity (increasing refrigerant flow rate and increasing heat flux). In general, the average heat transfer coefficient trend shown in Figure 7.6 at the highest vapor velocity ($U_{\infty} = 4.5$ m/s (14.8 ft/s)) is approximately 20% lower than the same trend at the lowest vapor velocity ($U_{\infty} = 2.5$ m/s (8.2 ft/s)).

It is also apparent from the figure that, like the 26-fpi tube, the increase in condensate flow rate from the first to the second vapor velocity has a larger detrimental effect on the performance than does the increase from the second velocity to the third. As was noted above, this is believed to be related to the liquid retention between the tube fins at the different condensate flow rates.

As with the 26-fpi tube, the drop in heat transfer performance is also relatively consistent from the top to the bottom of the bundle. As can be seen in the figure, the trends representing

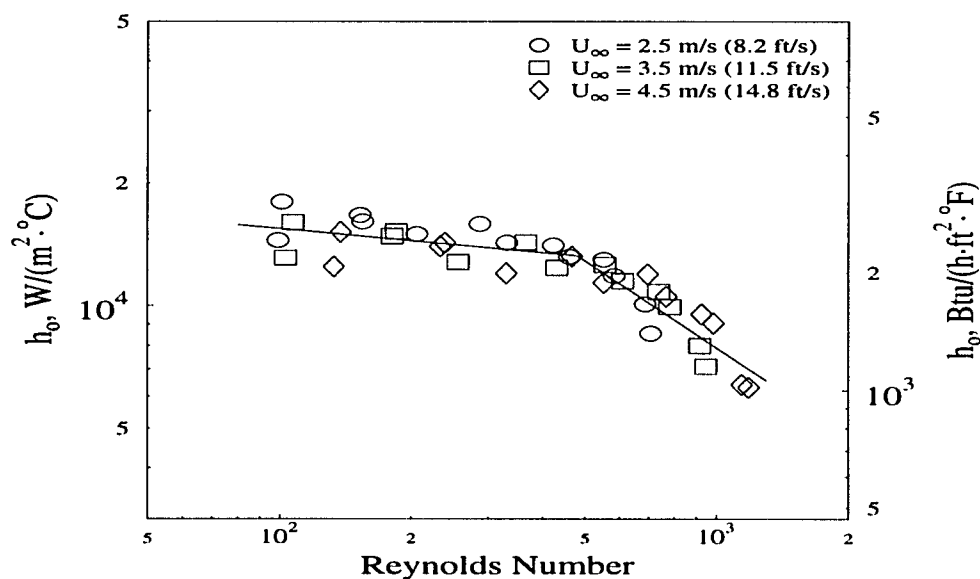


Figure 7.7: 40-fpi tube, average shell-side heat transfer coefficient vs. condensate Reynolds number for all data with HCFC-123

the different vapor velocities are parallel through the full depth of the bundle.

Performance as a function of Reynolds number

A plot of the heat transfer coefficients as a function of the condensate film Reynolds number for all three vapor velocities is shown in Figure 7.7. Differing behavior in two regions can be observed. This behavior was reported earlier for the 40-fpi tube in inundation with HFC-134a and discussed earlier for the 26-fpi tube using HCFC-123.

At $Re_L < 480$, the tube appears to be only slightly dependent on the condensate flow rate. A correlation like Equation 7.2 drawn through the data gives an exponent of $n = 0.097$. For $Re_L > 480$ the tube becomes much more inundation-dependent, showing a row-effect exponent equal to 0.706, which is very close to the value of $n = 0.719$ found for the 26-fpi tube at $Re_L > 700$. As with the 26-fpi tube, this behavior is believed to be a result of condensate flooding the fins along the lower part of the tube which allows axial movement

of the condensate and marks the transition between different condensate drainage patterns. It is of interest to note that this transition point occurs at much lower condensate Reynolds numbers than it does for the 26-fpi tube. This is probably due to the 40-fpi tube's shorter fins and tighter fin spacing which allows flooding of the fins much sooner than with the 26-fpi tube.

Performance as a function of T_{sw}

The row-by-row heat transfer coefficient as a function of the temperature difference ($T_{sat} - T_{s,o}$) is plotted in Figure 7.5 for the three different vapor velocities. The effect of increasing vapor-to-wall temperature difference is illustrated, along with the effect of increasing condensation rates on the overall performance of the tube. The larger temperature differences at the higher vapor velocities are due to the higher heat fluxes at those points. The effect of increasing condensation rates and inundation flow rates can be seen by comparing the data from the best and worst performing tubes at the different vapor velocities. As noted above, the average tube heat transfer coefficients dropped approximately 20% from the lowest to the highest refrigerant flow rates.

Test bundle performance

The row-by-row performance of the 5-row test bundle at the highest and lowest vapor velocities is illustrated in Figures 7.9 and 7.10. Data is presented as a function of the inlet quality to the test section. Similar to the plots of the data for the 26-fpi tube shown in Figures 7.3 and 7.4, only the data from the first pass is shown in its entirety (designated by \circ), along with tubes 4 and 5 from each subsequent pass.

The effect of increasing condensation rate is readily apparent in Figures 7.9 and 7.10. The data for rows 4 and 5 drop steadily with decreasing inlet quality. This drop is particularly

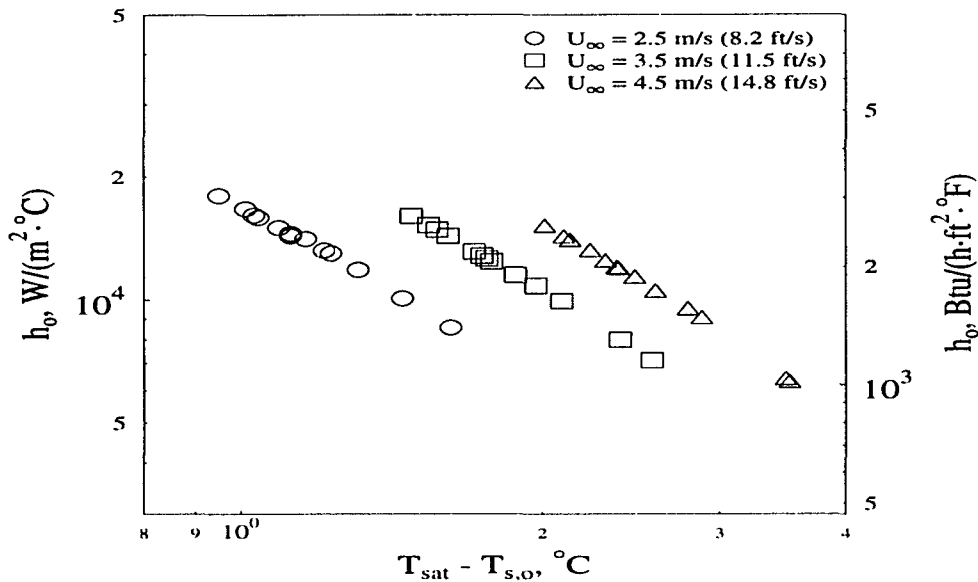


Figure 7.8: 40-fpi tube, average shell-side heat transfer coefficient vs. condensation temperature difference at three vapor velocities using HCFC-123

noticeable at the lowest inlet quality, where in the fourth and fifth rows there is an approximate 40% drop in heat transfer coefficient from the value at the highest inlet quality.

Uncertainties in the row-by-row heat transfer coefficients varied from approximately $\pm 23\%$ in the low velocity data to $\pm 10\%$ in the high velocity data. As explained earlier, the higher uncertainties at the low velocities is due to the larger uncertainties of the lowered refrigerant and water flow rates, and the subsequently smaller temperature increase in the water flowing through the bundles.

Results for the Tu-Cii Geometry

Simulated bundle performance

Figure 7.11 is a plot of the row-by-row heat transfer coefficients for the simulated 25-row Tu-Cii bundle at three different vapor velocities. This figure is markedly different from the

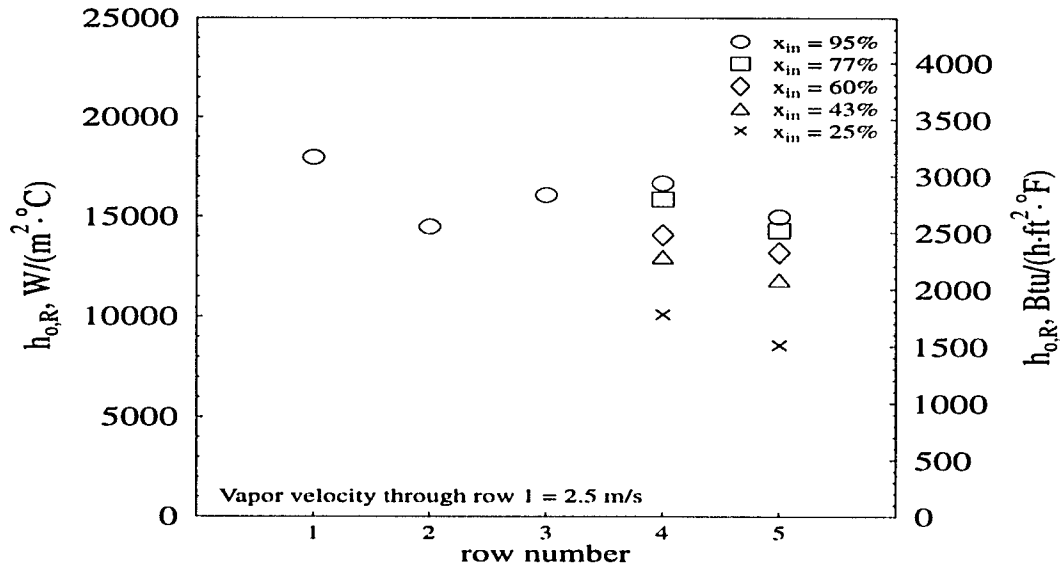


Figure 7.9: 40-fpi tube, average shell-side row heat transfer coefficient vs. row number for the 5-row test bundle using HCFC-123, $U_\infty = 2.5$ m/s (8.2 ft/s)

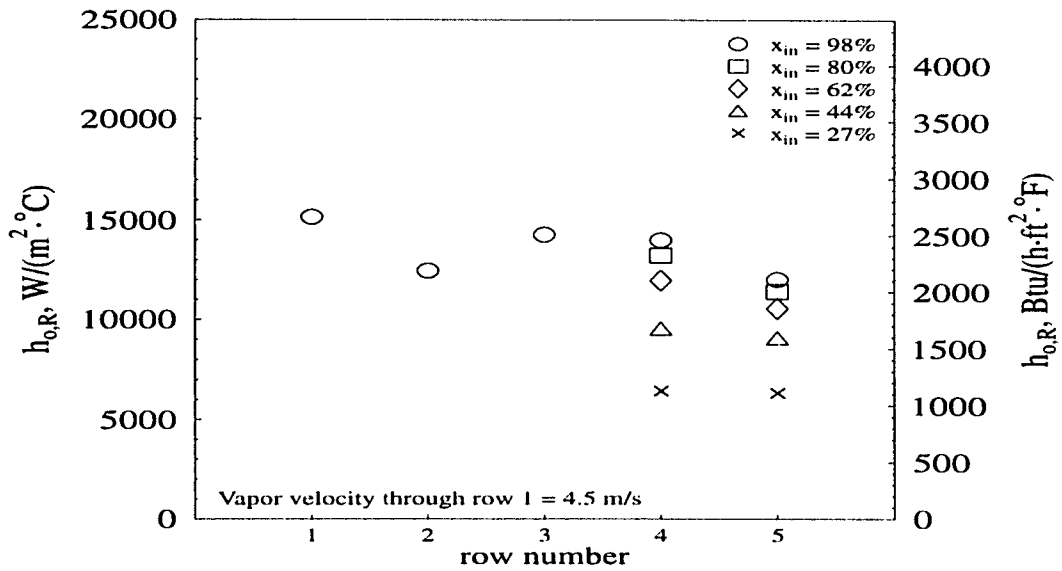


Figure 7.10: 40-fpi tube, average shell-side row heat transfer coefficient vs. row number for the 5-row test bundle using HCFC-123, $U_\infty = 4.5$ m/s (14.8 ft/s)

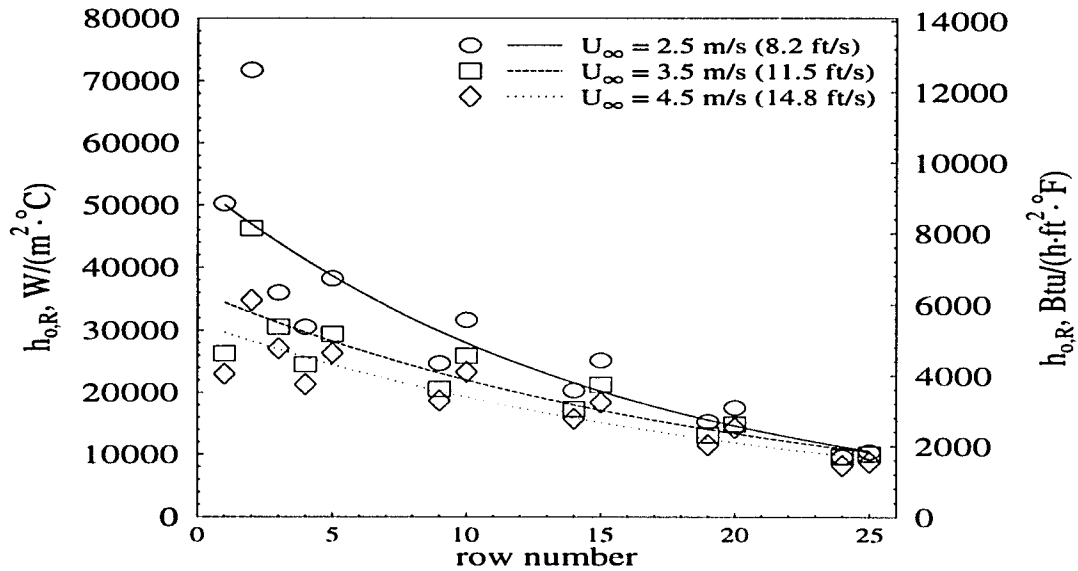


Figure 7.11: Tu-Cii tube, average shell-side row heat transfer coefficient vs. row number for three different vapor velocities with HCFC-123

plots of the same data for the 26-fpi and 40-fpi tubes shown in Figures 7.1 and 7.6, respectively, shown earlier.

As with the other tubes, the heat transfer performance drops with increasing vapor velocity (i.e. increasing heat flux and refrigerant mass flow rate) indicating negligible vapor shearing effects. However, unlike the finned tubes, the effect of inundation is readily apparent in the top rows of the bundle. The figure shows how the heat transfer performance drops off more rapidly in the first fifteen to twenty rows of the simulated bundle and then begins to level off near the bottom. This trend in heat transfer performance is often associated with the behavior of smooth tubes undergoing liquid inundation, as shown by Nusselt's original analysis along with other investigators.

Additionally, Figure 7.11 shows that the performance of the tubes converges near the bottom of the bundle, regardless of the inundation flow rate. At the top of the simulated bundle the heat transfer coefficient drops more than 50% with an increase in vapor velocity

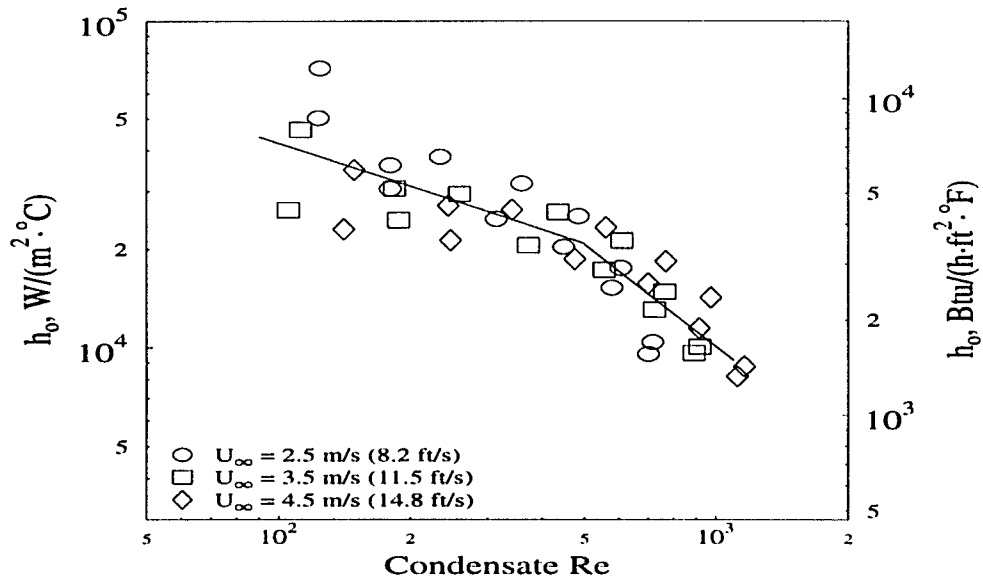


Figure 7.12: Tu-Cii tube, average shell-side heat transfer coefficient vs. condensate Reynolds number for all data with HCFC-123

from $U_{\infty} = 2.5$ m/s (8.2 ft/s) to 4.6 m/s (15.1 ft/s). At the bottom of the bundle, however, the heat transfer coefficients differ by less than 16%. This would seem to indicate that the tube has become critically flooded, and no more liquid can be held within its three-dimensional fin structure. As a result, an increase in condensate flow rate on these tubes has only a small effect on the tube's heat transfer performance.

Performance as a function of Reynolds number

Figure 7.12 is a plot of all the data as a function of condensate Reynolds number. As with the finned tubes, the figure shows that the Tu-Cii also appears to perform differently in two distance Reynolds number ranges. This behavior is also consistent with its behavior when inundated with HFC-134a as reported in Chapter 6.

The figure shows that the effect of inundation is immediate and pronounced, and that after the critical Reynolds range is reached (near $Re_L = 500$), the effect on heat transfer performance

is even more dramatic. Regression using Equation 7.2 reveals row-effect exponents of $n = 0.4365$ in the range $Re_L < 500$ and $n = 1.0345$ at $Re_L > 500$. These are considerably larger than the values found for the finned tubes and are even larger than those found when using the Tu-Cii with HFC-134a. This large change in behavior between the two refrigerants is associated with the higher viscosity and surface tension of HCFC-123 holding the liquid in the fin structure longer, thus allowing more condensate build-up and greater axial movement.

Test bundle performance

Figures 7.13 and 7.14 are plots of the heat transfer performance of the 5-row test bundle at the lowest and highest vapor velocities. The dependence of the heat transfer performance on condensate inundation noted above can easily be seen.

The most marked difference between the two plots is the performance drop in the first two tubes with an increase in total refrigerant mass flow rate from 6.1 kg/min (13.4 lb/min) to 10.4 kg/min (22.9 lb/min), which corresponds to an increase in the vapor velocity from 2.5 to 4.6 m/s (8.2 to 15.1 ft/s). This large drop is due to the increase in heat flux and the subsequent increase in the amount of condensate on the tubes. Apparently HCFC-123's relatively higher viscosity prevents the tube from draining, thus causing a larger decrease in the tube's heat transfer performance.

The convergence noted in Figure 7.11 can also be seen by comparing the heat transfer performance of tubes 4 and 5 at the lower inlet qualities. At the lower heat flux, the difference in performance between different inlet quality flows is very pronounced, dropping nearly 7000 $W/m^2/^\circ C$ for every drop in inlet quality. However, at the higher heat flux the drop is much smaller at only about 4000 $W/m^2/^\circ C$, so that at the bottom of the simulated bundle the heat transfer performances are very similar.

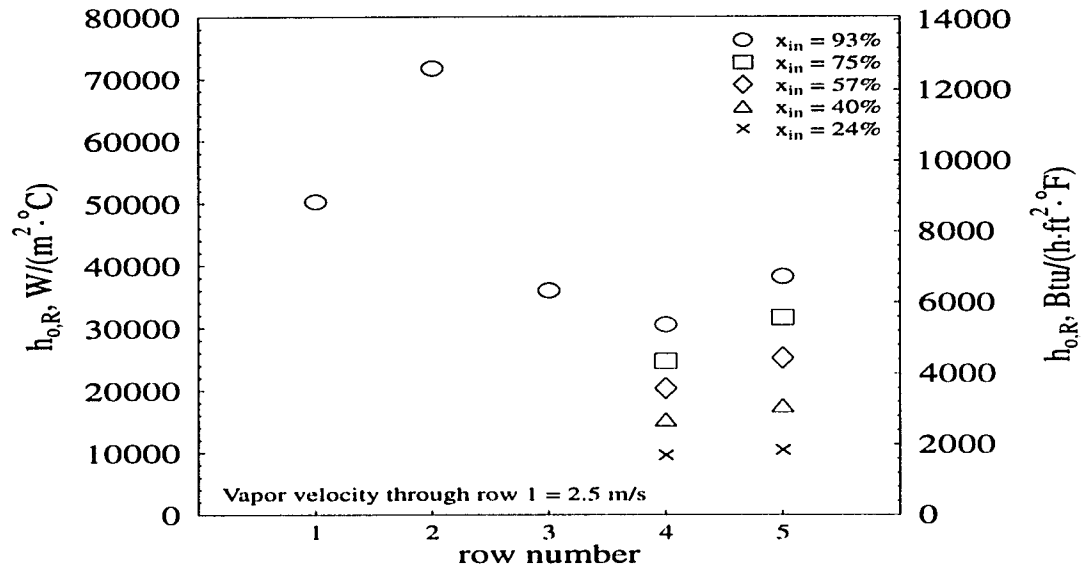


Figure 7.13: Tu-Cii tube, average shell-side row heat transfer coefficient vs. row number for the 5-row test bundle using HCFC-123, $U_\infty = 2.5$ m/s (8.2 ft/s)

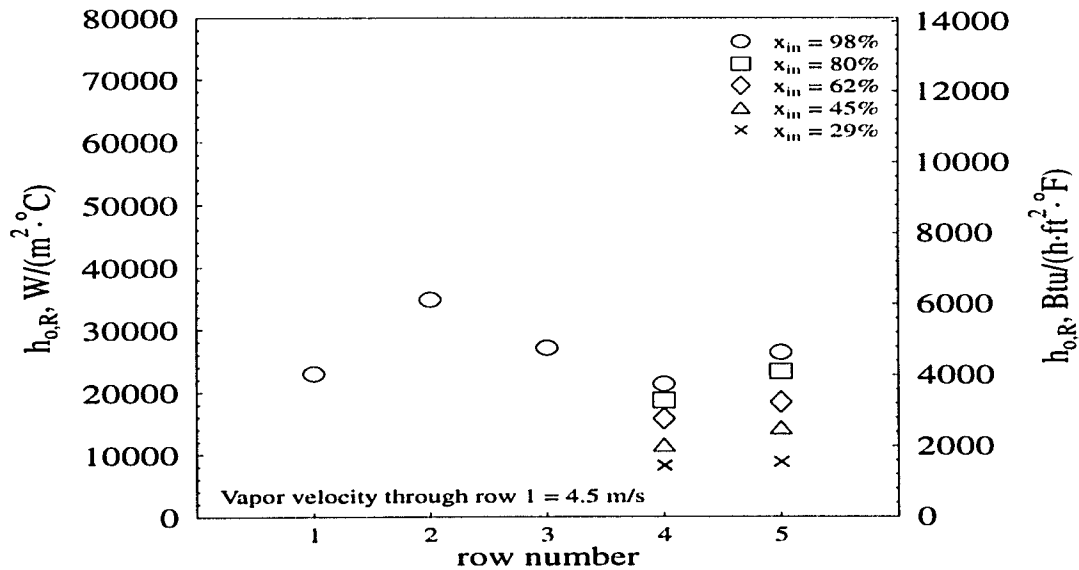


Figure 7.14: Tu-Cii tube, average shell-side row heat transfer coefficient vs. row number for the 5-row test bundle using HCFC-123, $U_\infty = 4.5$ m/s (14.8 ft/s)

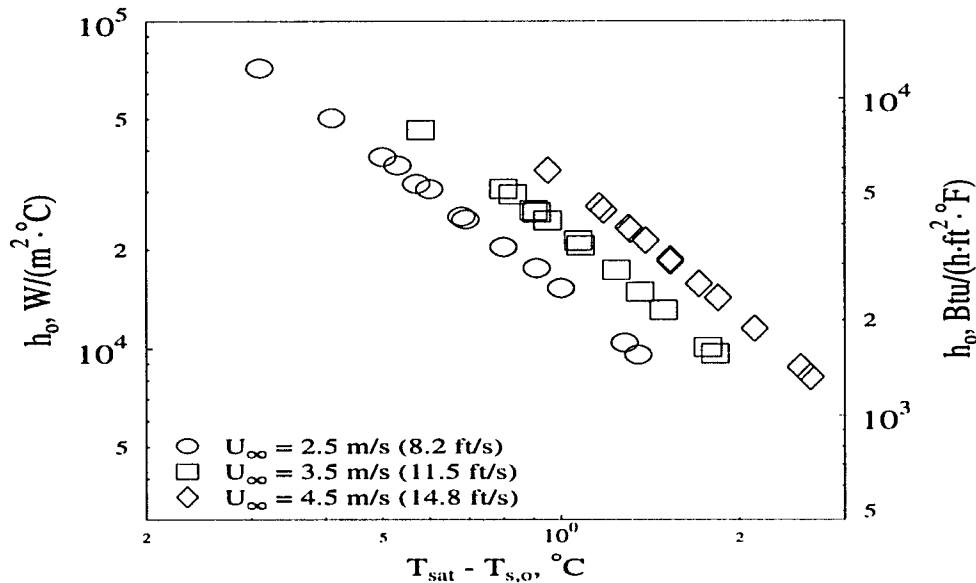


Figure 7.15: Tu-Cii tube, average shell-side heat transfer coefficient vs. condensation temperature difference at three vapor velocities using HCFC-123

Performance as a function of T_{sw}

The heat transfer coefficients as a function of the vapor-to-wall temperature difference are shown in Figure 7.15. The figure shows the large drop in heat transfer coefficients as well as the trends for the three different vapor velocities. At the lowest vapor velocity the vapor-to-surface temperature difference varied from 0.31 to 1.4°C (0.56 to 2.52°F). Temperature differences ranged from 0.95 to 1.77°C (1.71 to 3.19°F) at the highest velocities.

The experimental uncertainties for the Tu-Cii data are much higher than for the finned tubes discussed above. Uncertainties are calculated using a propagation-of-error technique (Holman (1984)) which uses the squares of the uncertainties of measured parameters to determine the uncertainty in the computed values. The uncertainty in the heat transfer coefficient is sensitive to the ratio of the water-side and shell-side resistances. As the ratio increases, so does the uncertainty in the shell-side heat transfer coefficient calculation. Since

the performance of the Tu-Cii is much higher than the finned tubes discussed above, the ratio of the water-side to the shell-side resistances is also much larger, and thus so are the uncertainties.

For the top rows of the bundle at the lowest flow rates, where the temperature differences are also smallest and the heat transfer coefficients are the highest, the experimental uncertainty in the heat transfer coefficients can be as high as $\pm 84\%$. Below row 10 the uncertainty drops to below $\pm 50\%$, and at the highest flow rates and lowest heat transfer coefficients the uncertainty is approximately $\pm 10 - 20\%$.

Results for the G-SC Geometry

Simulated bundle performance

The G-SC bundle performance characteristics are similar to both of the finned tubes and the Tu-Cii tube. Overall, the G-SC showed no shear effects and significant effects due to liquid inundation.

Figure 7.16 plots the row-by-row heat transfer performance of the 25-row simulated G-SC bundle as a function of three different vapor velocities. The figure shows that while the G-SC tends to have a bundle profile similar to the finned tubes discussed above (little inundation effects near the top of the bundle with much larger effects near the bottom), it also tends to converge to the same performance at the bottom of the bundle at different heat fluxes, much as the Tu-Cii did. The figure also shows that the G-SC is only slightly affected by an increase in heat flux, and its corresponding increase in condensation rate.

Near the top of the bundle, the heat transfer coefficients drop approximately 11% from the lowest to the highest heat flux (i.e. vapor velocity). At the bottom of the bundle, this difference drops to less than 5%. Overall, the heat transfer performance drops approximately 40% and 50% from the top of the bundle to the bottom at the lowest and highest heat fluxes,

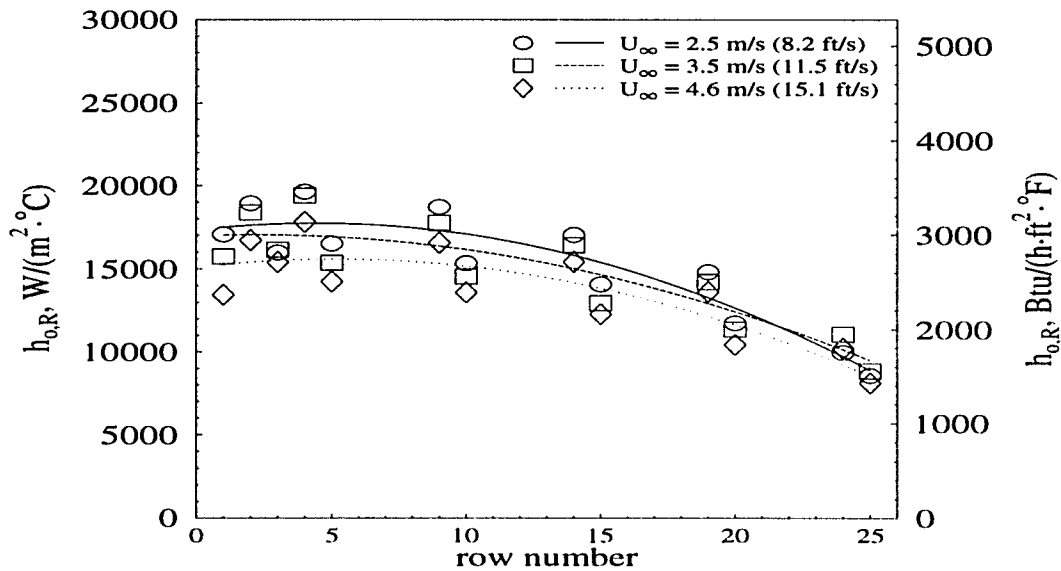


Figure 7.16: G-SC tube, average shell-side row heat transfer coefficient vs. row number for three different vapor velocities with HCFC-123

respectively.

Performance as a function of Reynolds number

The relationship between heat transfer performance and the condensate film Reynolds number is plotted in Figure 7.17. As with the tubes discussed above, the heat transfer performance of the G-SC appears to correlate to a dual Reynolds number-range using Equation 7.2. Using a critical Reynolds number near 600, the data separates into two regions defined by exponents for Equation 7.2 of $n = 0.1329$ at $Re_L < 610$ and $n = 0.7014$ at $Re_L > 610$. These numbers are very close to those found for both 26-fpi and 40-fpi discussed earlier.

The relatively small exponent used to define the performance in the lower range indicates that the G-SC is only marginally dependent on the condensate flow rate. At these low flow rates, the continuous fins act to channel the liquid and prevent any axial movement along the lower surface of the tube. Above the critical Reynolds number, it is believed the fins have

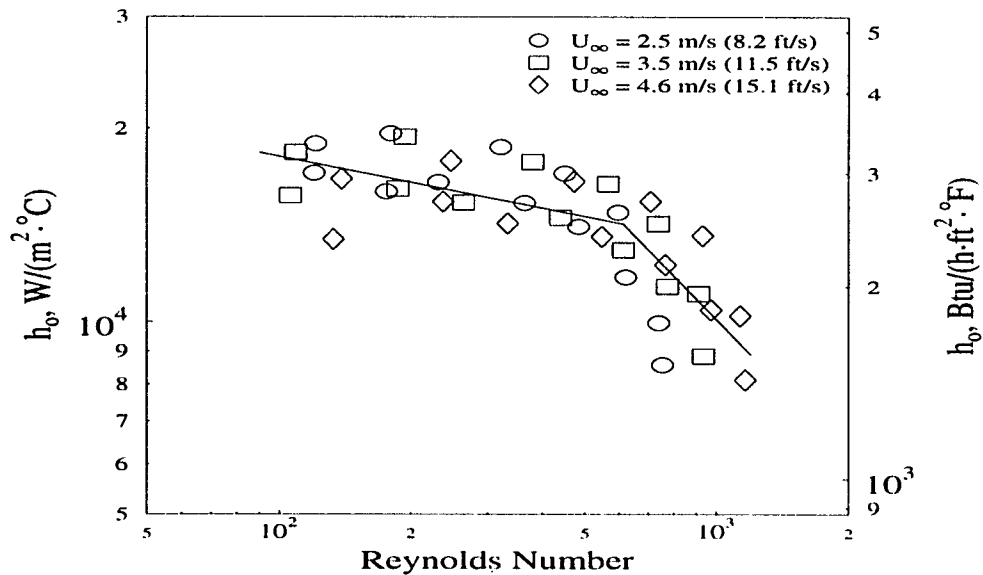


Figure 7.17: G-SC tube, average shell-side heat transfer coefficient vs. condensate Reynolds number for all data with HCFC-123

become flooded along the tube's lower surface and the liquid has begun to flow axially, thus decreasing the tube's effective condensation surface and allowing the individual columns to interact and form sheets.

Test bundle performance

The row-by-row heat transfer coefficients for the 5-row test bundle are presented in Figures 7.18 and 7.19 as functions of the inlet quality. The figures represent data taken at the lowest and highest vapor velocities, respectively. Only the data from the first pass is shown in its entirety, along with tubes 4 and 5 from each subsequent pass.

These two figures are very similar to Figures 7.3 and 7.4, 7.9 and 7.10, and 7.13 and 7.14 which plot the same type of data for the 26-fpi, 40-fpi, and Tu-Cii tubes. The most notable aspect of Figures 7.18 and 7.19 is the sudden drop in heat transfer performance in the lower rows of the simulated bundle, discussed in relation to Figure 7.17 and marked in these figures

by \times and Δ . In the upper rows of the simulated bundle the heat transfer is only slightly affected by the condensate flow rate. Between the first and second refrigerant passes (i.e. $x_{in} = 93$ and 75%) at the lowest heat flux, the heat transfer coefficient drops approximately 1200 $W/(m^2 \cdot ^\circ C)$ (211 $Btu/(h \cdot ft^2 \cdot ^\circ F)$). However, between the third and fourth passes ($x_{in} = 58$ and 40%), the coefficient drops by more than 2300 $W/(m^2 \cdot ^\circ C)$ (405 $Btu/(h \cdot ft^2 \cdot ^\circ F)$), and between the fourth and fifth passes ($x_{in} = 40$ and 21%), the heat transfer coefficient decreases by more than 3000 $W/(m^2 \cdot ^\circ C)$ (530 $Btu/(h \cdot ft^2 \cdot ^\circ F)$).

As with the other tubes, no shearing effect can be seen in the two figures. Liquid inundation appears to be the dominating effect in all cases tested for the G-SC tube.

Performance as a function of T_{sw}

Figure 7.20 plots the dependence of heat transfer coefficient on the temperature difference T_{sw} for the three different velocities. The figure further illustrates an aspect noted in Figure 7.16, namely, the decrease in heat transfer performance near the top of the bundle at increasing heat flux (i.e. increasing vapor velocity) and the apparent convergence of the performance near the bottom of the bundle for all heat flux data. Figure 7.20 also demonstrates the relatively large range in heat transfer coefficients from the top to the bottom of the bundle. At the lowest velocity the temperature difference increased from 0.91 to 1.75 $^\circ C$ (1.64 to 3.15 $^\circ F$) for the highest and poorest performing tubes in the bundle, respectively. At the highest velocity this temperature difference increased from 1.81 to 3.02 $^\circ C$ (3.26 to 5.44 $^\circ F$).

Experimental uncertainties in the heat transfer coefficients ranged from near $\pm 25\%$ at the lowest heat fluxes to approximately $\pm 11\%$ at the highest heat fluxes. These values are less than those found for the Tu-Cii, and are more in line with those found for the finned tubes.

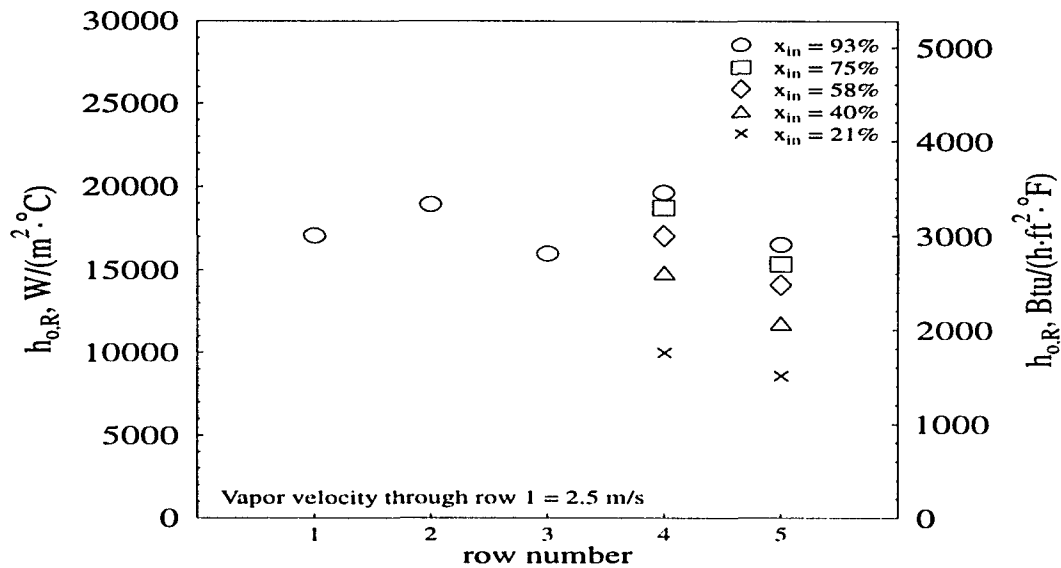


Figure 7.18: G-SC tube, average shell-side row heat transfer coefficient vs. row number for the 5-row test bundle using HCFC-123, $U_\infty = 2.5$ m/s (8.2 ft/s)

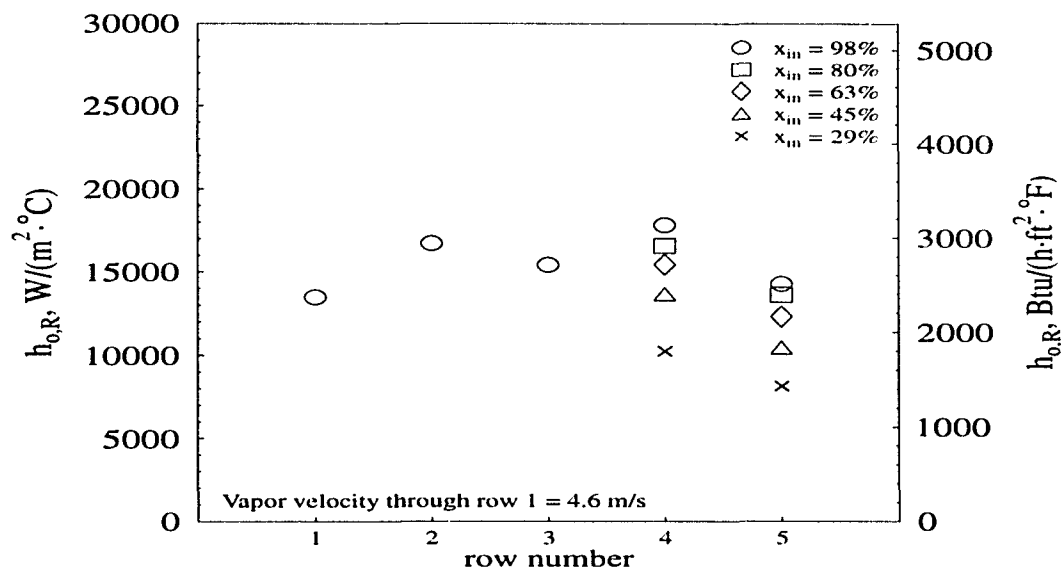


Figure 7.19: G-SC tube, average shell-side row heat transfer coefficient vs. row number for the 5-row test bundle using HCFC-123, $U_\infty = 4.6$ m/s (15.1 ft/s)

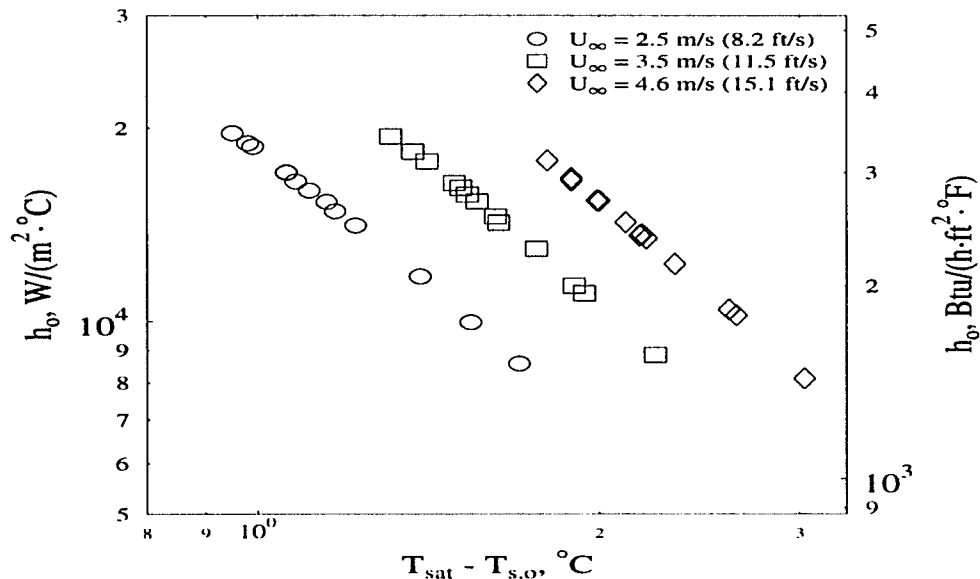


Figure 7.20: G-SC tube, average shell-side heat transfer coefficient vs. condensation temperature difference at three vapor velocities using HCFC-123

Comparisons Between Tube Geometries

Comparisons between the four test bundles are made in Figures 7.21 and 7.22. Figure 7.21 compares the heat transfer performance of the different geometries as a function of the condensate Reynolds number; Figure 7.22 shows performance of the different geometries on the basis of the calculated vapor-to-surface temperature difference at the highest vapor velocity (i.e. highest refrigerant flow rate and heat flux).

Both figures indicate that the best overall heat transfer performance is shown by the Tu-Cii, particularly at low condensate flow rates. Near the top of the simulated 25-row bundle, the next closest performing tube (G-SC) has average heat transfer coefficients (based on the correlation fits through the data) that are still nearly 57% those of Tu-Cii. At the bottom of the simulated bundle, where the effects of inundation are most pronounced, the Tu-Cii and G-SC perform almost identically, differing by less than 5%. The worst performing tube, the

26-fpi, is almost 70% lower than the Tu-Cii at the top of the bundle, but approximately 8% lower near the bottom. At the top of the bundle, the 40-fpi tube has heat transfer coefficients that are nearly 60% below the Tu-Cii, which places the 40-fpi tube performance between the 26-fpi and the G-SC. However, because the 26-fpi is not affected by liquid inundation until near the bottom of the bundle, the 40-fpi tube performs worse than the 26-fpi in the lower rows and has heat transfer coefficients that are nearly 20% lower than the Tu-Cii.

Figure 7.21 also shows that all four tubes seem to be affected by the inundation rate in two distinct Reynolds ranges and compares the critical Reynolds numbers of these transition points for all four geometries. Correlations developed using Equation 7.2 and plotted through the data indicate the general trends of the data and illustrate the critical Reynolds numbers more clearly. Table 7.1 lists the coefficients and exponents for the equations plotted in Figure 7.21.

The dual range of Reynolds number dependence is attributed to the relatively high viscosity and surface tension of HCFC-123, as compared to HFC-134a. These two properties affect the performance of the tubes under condensate inundation by decreasing the flooding angle of the finned tubes and preventing the liquid film from draining as rapidly. This allows the liquid to build up and begin moving axially along the lower surface of the tube, which in turn decreases the effective condensation surface area and promotes the onset of sheet-mode drainage patterns. Since this dual range behavior was only seen on two of the tubes (40-fpi and Tu-Cii) when condensing HFC-134a (see the Chapter 6 for further discussion), the conclusion drawn that this is an effect related to the refrigerant and not the tubes is believed to be accurate.

In general, the 26-fpi tube is the least dependent on condensate flow rate of the four tubes tested and stays relatively independent for the longest time before becoming flooded. The 40-fpi and G-SC tubes are affected almost equally by the film flow rate in the low Reynolds range, having only a very small dependence on inundation. However, the 40-fpi has the lowest

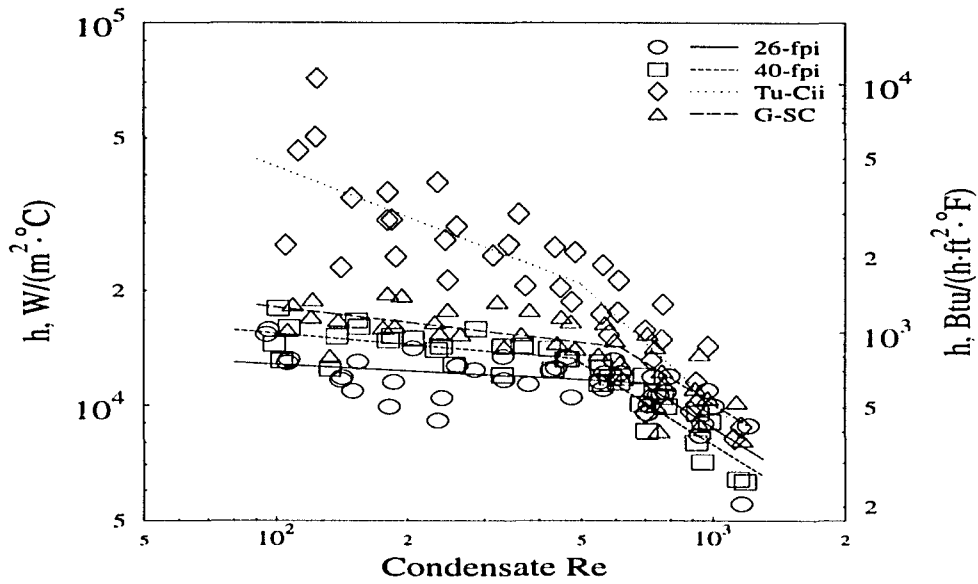


Figure 7.21: Average shell-side heat transfer coefficient vs. condensate Reynolds number comparison of all tubes

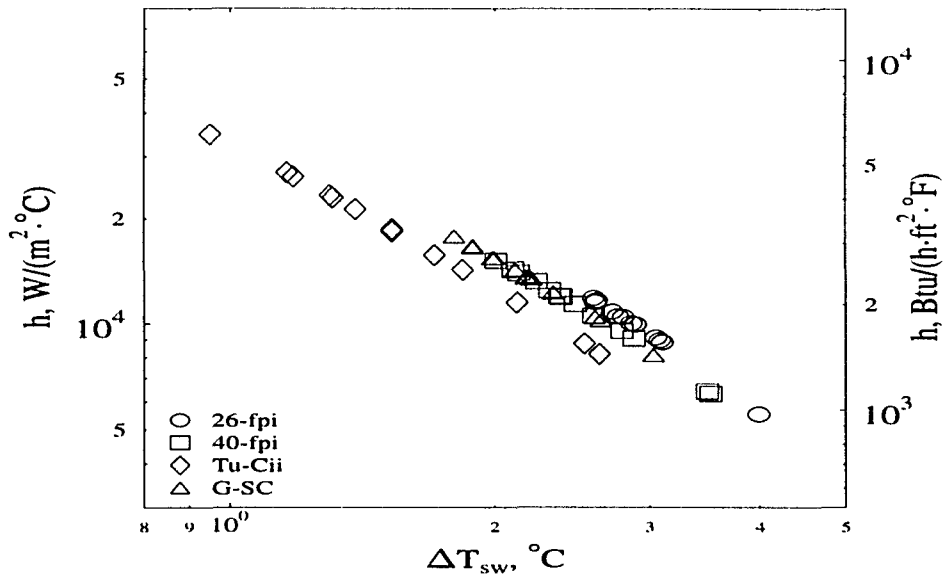


Figure 7.22: Average shell-side heat transfer coefficient vs. condensation temperature difference comparison of all 30-row simulations

Table 7.1: Coefficients and exponents for Equation 7.2 using HCFC-123

Tube	Re_L Range	$a \times 10^{-3}$ $W/(m^2 \cdot ^\circ C)$	n
26-fpi	<700	17.519	0.0669
26-fpi	>700	1252.6	0.7186
40-fpi	<480	24.156	0.0970
40-fpi	>480	1038.0	0.7063
Tu-Cii	<500	313.84	0.4365
Tu-Cii	>500	12838	1.0347
G-SC	<610	33.377	0.1329
G-SC	>610	1283.5	0.7014

critical Reynolds number and, therefore, becomes negatively affected sooner than does the G-SC. At the same time the 26-fpi, 40-fpi, and G-SC tubes show almost identical inundation effects in their respective low Reynolds ranges even though these ranges are separated at different critical Reynolds numbers for each tube. The Tu-Cii is most affected by condensate inundation, compared to the other tubes, with higher row effect exponents in both the high and low Reynolds number ranges than any of the other tubes in their comparable ranges.

Figure 7.22 also shows how closely the 40-fpi and G-SC perform to each other in terms of the vapor-to-wall temperature difference. Over a large range of heat transfer coefficients and T_{sw} values, the data for the two tubes completely overlaps. While the G-SC performs better than the 40-fpi overall, it is interesting to note how closely they perform as a function of temperature difference.

Summary

Condensation tests were run on two finned tubes and two enhanced tubes using HCFC-123 as the working fluid. Tests were performed to simulate a 25-row condenser at three different vapor velocities. From the data, the following conclusions were made.

1. The enhanced Tu-Cii showed the best overall heat transfer performance, particularly at film Reynolds numbers below 500. At the same time, the tube was most affected by condensate inundation and suffered the largest degradations in heat transfer performance with increasing condensate flow rate.
2. The high relative viscosity and surface tension of HCFC-123 (as compared to HFC-134a) promotes a heat transfer performance which can be defined in terms of two distinct condensate Reynolds number ranges where the performance is markedly different. Each range is quantifiable and can be correlated using an equation of the form $h_o = a\text{Re}_L^{-n}$. Ranges are separated at a unique critical Reynolds number for each tube.
3. The finned tubes show the lowest dependence on condensate flow rate, particularly below their critical Reynolds number.
4. In general, those tubes with continuous fins, including the G-SC, have better drainage effects and show the least dependence on inundation flow rates, particularly below that tube's critical Reynolds number.
5. The Tu-Cii tube shows the greatest inundation effects, with heat transfer coefficients dropping almost 80% from the top to the bottom of the bundle in a 25-row simulation.
6. The G-SC tube performs much like the finned tube when used for condensation of HCFC-123 throughout the full range of condensate flow rates.
7. Both enhanced tubes appear to become critically flooded at a point near the bottom of the simulated 25-row bundle, such that the heat transfer coefficients collapse to the same performance trend near the bottom of the bundle independent of heat flux or condensate flow rate.

CHAPTER 8. CONCLUSIONS

The purpose of the current study was to measure shell-side heat transfer coefficients for the condensation of HFC-134a and HCFC-123 on tube bundles using a staggered tube arrangement and determine the effects of non-condensable gas contamination, liquid inundation, and vapor shear on the condensation process. The average shell-side bundle heat transfer coefficient and the shell-side heat transfer coefficient for the middle tube of each row were computed. The tube bundles were constructed from 4 different tube geometries of the type commonly used in the refrigeration industry. The data were obtained at a saturation temperature of 35°C (95°F) and over a wide heat flux range, depending on the type of experiment being conducted. The conditions were typical of those found in refrigerant condensers.

Summary of HFC-134a Data

In general, the effects of inundation with HFC-134a are small for those tubes with continuous fins, particularly the 26-fpi and the GEWA-SC. The 40-fpi also showed a low condensate flow rate dependence of the order of the 26-fpi tube, but only through a Reynolds number up to approximately 1200, at which point the 40-fpi tube's heat transfer performance decreased rapidly. This trend was believed to be a result of flooding of the fins on the 40-fpi tube and the subsequent axial movement of the condensate along the tube surface. It may also correspond to a transition between liquid drip modes from the columnar to the sheet mode.

The Turbo C-II was greatly affected by HFC-134a inundation, although it still performed

better than any of the other tubes throughout the full range of condensate flow rates tested. Specifically, at the lowest inundation rates the Turbo C-II showed heat transfer coefficients that were more than double those of the other tubes. However, at the highest flowrates, above a Reynolds number of about 2000, the Turbo C-II performance fell to approximately the same levels (within 10%) as those of the other tubes. The Turbo C-II also showed performance similar to the 40-fpi tube, which had distinctly different heat transfer performance in different ranges of condensate Reynolds number.

The large drop in performance for the Turbo C-II is believed to be caused by liquid retention in the tube's three-dimensional fins which slows drainage and floods the tube. The tube's tendency to perform differently at different condensate flow rates is thought to be caused by the onset of axial movement of the condensate along the bottom of the tube and a subsequent change in film drainage patterns.

Summary of HCFC-123 Data

Non-condensable gas tests

The presence of non-condensable gases had a noticeable effect on the condensation of HCFC-123 on all four of the geometries tested. The effect was much more striking with the Turbo C-II, especially at very low concentrations; however, the Turbo C-II also outperformed the other tube bundles through a nitrogen concentration of 5.0% by volume. Generally, the performance of Turbo C-II was followed by the 40-fpi, GEWA SC, and 26-fpi geometries.

At the 0.5% nitrogen contamination and the lowest heat flux, the heat transfer coefficients of the Turbo C-II bundle are approximately 50% higher than the 26-fpi bundle, the worst performing bundle at that concentration and heat flux. At the highest concentration (5.0%), the Turbo C-II still outperforms the other bundles, but is only approximately 13% higher than the worst performing tube, the GEWA SC.

Non-condensable gas contamination was found to affect the individual row performance of a given bundle, particularly at high gas concentrations, by evening the performance of the individual rows in the bundle, so that each row performed almost equally well. At 5% non-condensable concentration, where the average bundle performances of the four bundles are very similar, row-by-row coefficient profiles for each tube are also very similar, having a slightly curved trend with peaks in the first and fifth rows. This indicates that the presence of non-condensibles removes most of the bundle geometry effects, since the all the profiles are dissimilar at 0% gas concentration.

The data also suggests that each tube is affected by the presence of vapor shear in the non-condensable gas layer. At high gas concentrations, the performance of each bundle increases with increasing heat fluxes, which correspond to increasing vapor velocity through the bundle. This behavior is also found at low heat fluxes in all bundles, except the 26-fpi bundle at concentrations below 1.0%, which shows decreasing performance with increasing heat flux. This is believed to indicate that in that range the increasing thickness of the liquid layer on the tubes dominates over the effects of shear in the non-condensable gas layer.

Liquid inundation and vapor shear tests

The higher viscosity and surface tension of HCFC-123 (as compared to HFC-134a) make the inundation effects with HCFC-123 much more pronounced than with HFC-134a. All the tubes appeared to flood so that there was a very definite transition point between the flooded and unflooded performance in each tube. The Turbo C-II performance dropped nearly 80% from the lowest to the highest condensate Reynolds numbers. Decreases of approximately 20%, 20%, and 45% were seen for the 26-fpi, 40-fpi, and GEWA SC tubes, respectively, over the same Reynolds number range.

Inundation also appeared to be the dominating factor with respect to the effects of

vapor shear. While the constriction in flow area above row 2 due to the staggered bundle arrangement appears to cause vapor velocity effects to become noticeable for the 26-fpi, Turbo C-II, GEWA SC tubes during full bundle tests, additional tests found that average row-by-row coefficients decrease with increasing vapor velocity and liquid inundation. Thus, the heat transfer performance of the tubes appears to be much more strongly affected by inundation than by vapor velocity.

Overall, the Turbo C-II had the highest heat transfer coefficients, followed by the GEWA SC, the 40-fpi, and the 26-fpi tubes. At the lowest inundation rates the Turbo C-II had almost double the heat transfer performance of the GEWA SC and more than triple that of the 26-fpi. However, at the highest inundation rates the Turbo C-II outperformed the other tubes by less than 10%.

BIBLIOGRAPHY

- Beatty, Kenneth O. Jr., and Donald L. Katz. "Condensation of Vapors on Outside of Finned Tubes." *Chemical Engineering Progress* 44, no. 1 (1948): 55–70.
- Butterworth, D. "Developments in the Design of Shell and Tube Condensers." *ASME Winter Annual Meeting, Atlanta* ASME Reprint 77-WA/HT-24 (1977).
- Butterworth, D. "Film Condensation of Pure Vapor." In *Heat Exchanger Design Handbook*, ed. E. Schlunder. Washington: Hemisphere Publishing Company, 1983.
- Cavallini, A., B. Bella, G. A. Longo, and L. Rosetta. "Forced Convection Condensation on Horizontal Low Integral Fin Tubes." *Institution of Chemical Engineers Symposium Series* 129, no. 2 (1992): 829–835.
- Chen, Michael Ming. "An Analytical Study of Laminar Film Condensation: Part 2—Single and Multiple Horizontal Tubes." *Transactions of the ASME, Journal of Heat Transfer* 83, (1961): 55–60.
- Fisher, F. F., and G. J. Brown. "Tube Expanding and Related Subjects." *Transactions of the ASME* 76, (1954): 563–575.
- Fujii, T., and H. Uehara. "Laminar Film Condensation on a Vertical Surface." *International Journal of Heat and Mass Transfer* 15 (1972): 217–234.
- Glaum, Paul. The Trane Company. Personal communication. 1993.
- Gnielinski, V. "New Equations for Heat and Mass Transfer in Turbulent Pipe and Channel Flow." *International Chemical Engineering* 16, no. 2, (1976): 359–368.
- Gogonin, I. I., and A. R. Dorokhov. "Enhancement of Heat Transfer in Horizontal Shell-and-tube Condensers." *HEAT TRANSFER—Soviet Research* 13, no. 3 (1981): 119–125.
- Gregorig, Von Romano. "Hautkondensation an feingewellten Oberflächen bei Berücksichtigung der Oberflächenspannungen." *Zeitschrift für angewandte*

Mathematik und Physik 5, (1954): 36–49.

- Honda, H., and T. Fujii. “Condensation of Flowing Vapor on a Horizontal Tube—Numerical Analysis as a Conjugate Heat Transfer Problem.” *Transactions of the ASME, Journal of Heat Transfer* 106, (1984): 841–848.
- Honda, H., and S. Nozu. “A Prediction Method for Heat Transfer During Film Condensation on Horizontal Low Integral-Fin Tubes.” *Transactions of the ASME, Journal of Heat Transfer* 109, (1987): 218–225.
- Honda, H., S. Nozu, and B. Uchima. “A Generalized Prediction Method for Heat Transfer During Film Condensation on a Horizontal Low Finned Tube.” In *Proceedings of the 2nd ASME-JSME thermal engineering joint conference*, edited by P. Marto and I. Tanasawa. JSME 4, (1987): 385–392.
- Honda, H., S. Nozu, and Y. Takeda. “A Theoretical Model of Film Condensation in a Bundle of Horizontal Low Finned Tubes.” *Transactions of the ASME, Journal of Heat Transfer* 111, (1989): 525–532.
- Honda, H., B. Uchima, S. Nozu, H. Nakata, and E. Torigoe. “Film Condensation of R-113 on In-Line Bundles of Horizontal Finned Tubes.” *Transactions of the ASME, Journal of Heat Transfer* 113, (1991): 479–486.
- Honda, H., B. Uchima, S. Nozu, E. Torigoe, and S. Imai. “Film Condensation of R-113 on Staggered Bundles of Horizontal Finned Tubes.” *Transactions of the ASME, Journal of Heat Transfer* 114, (1992): 442–449.
- Incropera, Frank P., and David P. De Witt. *Fundamentals of Heat and Mass Transfer*. 3rd ed. New York: John Wiley & Sons, 1990.
- Ishihara, K. I., and J. W. Palen. “Condensation of Pure Fluids on Horizontal Finned Tube Bundles.” In *Proceedings of the Symposium on Condensers: Theory and Practice*, Institution of Chemical Engineers Symposium Series No. 75, (1983): 429–446.
- Karkhu, V. A., and V. P. Borovkov. “Film Condensation of Vapor at Finely-Finned Horizontal Tubes.” *HEAT TRANSFER—Soviet Research* 3, no. 2 (1971): 183–191.
- Katz, D. L., and J. M. Geist. “Condensation on Six Finned Tubes in a Vertical Row.” *Transactions of the American Society of Mechanical Engineers* 70, (1948): 907–914.
- Kern, Donald Q. “Mathematical Development of Tube Loading in Horizontal Condensers.” *A.I.Ch.E. Journal* 4, no. 2 (1958): 157–160.

- Lee, W. C., S. Rahbar, and J. W. Rose. "Film Condensation of Refrigerant-113 and Ethenediol on a Horizontal Tube – Effect of Vapor Velocity." *Journal of Heat Transfer* 106, (1984): 524–530.
- McNaught, J. M., and C. D. Cotchin. "Heat Transfer and Pressure Drop in a Shell and Tube Condenser with Plain and Low-fin Tube Bundles. *Chemical Engineers Research and Design* 67, (1989): 127–133.
- McNaught, J. M. "Two-Phase Forced Convection Heat Transfer During Condensation on Horizontal Tube Bundles." *Proceedings of the Seventh International Heat Transfer Conference, Munich*. 5, (1982): 125-131.
- Marto, P. J. "Heat Transfer in Condensation." In *Boilers, Evaporators, and Condensers* ed. S. Kakac, 525–570. New York: John Wiley & Sons, Inc., 1991.
- Marto, P. J. "An Evaluation of Film Condensation on Horizontal Integral-Fin Tubes." *Transactions of the ASME, Journal of Heat Transfer* 110, (1988a): 1287-1305.
- Marto, P.J. "Fundamentals of Condensation." In *Two-Phase Flow Heat Exchangers* ed. S. Kakac et al., 221-290. Dordrecht: Kluwer Academic Publishers, 1988b.
- Marto, P. J. "Heat Transfer and Two-Phase flow During Shell-side Condensation." *Heat Transfer Engineering* 5, (1984): 31-61.
- Murata, Keiji, Norimitsu Abe, and Kenichi Hashizume. "Condensation Heat Transfer in a Bundle of Horizontal Integral-fin Tubes." In *Proceedings – 9th International Heat Transfer Conference* 4, (1990): 259–264.
- Nobbs, D. W., and Mayhew, Y. R. "Effect of Downward Vapor Velocity and Inundation on Condensation rates on Horizontal Tube Banks." *Steam Turbine Condensers*, NEL Report 619: 39-52.
- Nusselt, Wilhelm. "The Condensation of Steam on Cooled Surfaces". *Chemical Engineering Fundamentals* 1, no. 2 (1982): 6–19. Translated by D. Fullarton.
- Rohsenow, W. M., J.M. Weber, and A.T. Ling. "Effect of Vapor Velocity on Laminar and Turbulent Film Condensation." *Transactions of the ASME* 78, (1956): 1637-1774.
- Rose, J. W. "Effect of Pressure Gradient in Forced Convection Film Condensation on a Horizontal Tube." *International Journal of Heat and Mass Transfer* 27, no. 1 (1984): 39–47.
- Rose, J. W. "Fundamentals of Condensation Heat Transfer: Laminar Film Condensation." *JSME International Journal Series II*, 31, no. 3 (1988): 357–375.

- Shekriladze, I. G. and V. I. Gomelaui. "Theoretical Study of Laminar Film Condensation of Flowing Vapour." *International Journal of Heat and Mass Transfer* 9 (1966): 581–591.
- Short, B. E., and H. E. Brown. "Condensation of Vapors on Vertical Banks of Horizontal Tubes." *Institution of Mechanical Engineers. Proceedings of the General Discussion of Heat Transfer*, (1951): 27–31.
- Smirnov, G. F., and I. I. Lukanov. "Study of Heat Transfer from Freon-11 Condensing on a Bundle of Finned Tubes." *HEAT TRANSFER–Soviet Research* 4, no. 3 (1972): 51–55.
- Thors, Petur. Wolverine Tube, Inc. Personal Communication. 1992.
- Webb, R. L. "The Effects of Vapor Velocity and Tube Bundle Geometry on Condensation in Shell-side Refrigeration Condensers." *ASHRAE Transactions* 90 part 1, (1984a): 5–25.
- Webb, R. L. "Shell-side Condensation in Refrigerant Condensers." *ASHRAE Transactions* 90 part 1, (1984b): 39–59.
- Webb, R. L., and A. S. Wanniarachchi. "The Effect of Noncondensable Gases in Water Chiller Condensers – Literature Survey and Theoretical Predictions." *ASHRAE Transactions* 86, (1980): 142–159.
- Webb, R. L., A. S. Wanniarachchi, and T. M. Rudy. "The Effect of Noncondensable Gases on the performance of an R-11 Centrifugal Water Chiller Condenser." *ASHRAE Transactions* 86, (1980): 57–67.
- Webb, R. L., and A. S. Wanniarachchi. "Noncondensable Gases in Shell-Side Refrigerant Condensers." *ASHRAE Transactions* 88, (1982): 170–184.
- Webb, R. L., T. M. Rudy, and M. A. Kedzierski. "Prediction of the Condensation on Horizontal Integral-Fin Tubes." *Transactions of the ASME, Journal of Heat Transfer* 107, (1985): 369–376.
- Webb, R. L., and C. G. Murawski. "Row Effect for R-11 Condensation on Enhanced Tubes." *Transactions of the ASME, Journal of Heat Transfer* 112, (1990): 768–776.

APPENDIX A. DERIVATION OF UNCERTAINTY ANALYSIS EQUATIONS

The propagation of errors method (Holman (1984)) is used to determine the experimental uncertainty in the heat transfer coefficients calculated in this report. This method uses the squares of the uncertainties in the independent parameters to compute the uncertainty in the calculated quantity. For any calculated quantity y , the uncertainty in the calculated value of y , ω_y , is calculated from

$$\omega_y = \left[\left(\frac{\partial y}{\partial x_1} \omega_{x_1} \right)^2 + \left(\frac{\partial y}{\partial x_2} \omega_{x_2} \right)^2 + \cdots + \left(\frac{\partial y}{\partial x_n} \omega_{x_n} \right)^2 \right]^{1/2} \quad (\text{A.1})$$

where $x_1 \cdots x_n$ are the independent parameters which are used to calculate y , and $\omega_{x_1} \cdots \omega_{x_n}$ are the uncertainties in the independent parameters.

The shell-side heat transfer coefficient is calculated using Equation 4.20. Substitution of Equation 4.13 into Equation 4.20 yields

$$h_o = \left[A_o \left(\frac{(\Delta T_1 - \Delta T_2)}{q \cdot \ln \left(\frac{\Delta T_1}{\Delta T_2} \right)} - \frac{1}{A_i h_i} - R_{tw} \right) \right]^{-1} \quad (\text{A.2})$$

where

$$\begin{aligned} \Delta T_1 &= T_{sat} - T_{w,i} \\ \Delta T_2 &= T_{sat} - T_{w,o} \end{aligned} \quad (\text{A.3})$$

and

$$\Delta T_1 - \Delta T_2 = T_{w,o} - T_{w,i}. \quad (\text{A.4})$$

In order to find the uncertainty in h_o , Equation A.2 must be differentiated with respect to the independent variables T_{sat} , $T_{w,in}$, $T_{w,out}$, A_o , A_i , R_{tw} , q , and h_i . The partial derivatives are then used to calculate ω_{h_o} by the method of Equation A.1. Since the parameters A_o , A_i , and R_{tw} are based on arbitrary nominal diameters and a nominal tube length, their partial derivatives are neglected. The governing uncertainty equation then becomes

$$\omega_{h_o} = \left[\left(\frac{\partial h_o}{\partial T_{sat}} \omega_{T_{sat}} \right)^2 + \left(\frac{\partial h_o}{\partial T_{w,in}} \omega_{T_{w,in}} \right)^2 + \left(\frac{\partial h_o}{\partial T_{w,out}} \omega_{T_{w,out}} \right)^2 + \left(\frac{\partial h_o}{\partial q} \omega_q \right)^2 + \left(\frac{\partial h_o}{\partial h_i} \omega_{h_i} \right)^2 \right]^{1/2}. \quad (\text{A.5})$$

Each of the terms in the right side of the above equation will be discussed in detail in the following sections.

Uncertainty Due To Saturation Temperature

The partial derivative of Equation A.2 with respect to T_{sat} is given by

$$\begin{aligned} \frac{\partial h_o}{\partial T_{sat}} &= \frac{1}{A_o} \left[\frac{(\Delta T_1 - \Delta T_2)}{q \cdot \ln \left(\frac{\Delta T_1}{\Delta T_2} \right)} - \frac{1}{A_i h_i} - R_{tw} \right]^{-2} \\ &\times \left[\frac{(\Delta T_1 - \Delta T_2)}{q \cdot \ln \left(\frac{\Delta T_1}{\Delta T_2} \right)^2} \right] \left[\frac{\left(\frac{1}{\Delta T_2} - \frac{\Delta T_1}{\Delta T_2^2} \right)}{\left(\frac{\Delta T_1}{\Delta T_2} \right)} \right]. \end{aligned} \quad (\text{A.6})$$

As discussed in Chapter 4, the saturation temperature is calculated from the saturation pressure.

By Equation A.1, the uncertainty in T_{sat} is then

$$\omega_{T_{sat}} = \frac{\partial T_{sat}}{\partial p_{sat}} \omega_{p_{sat}}. \quad (\text{A.7})$$

The partial derivative is computed by the computerized refrigerant property routines, and $\omega_{p_{sat}}$ is given by either of the following values

$$\begin{aligned}\omega_{p_{sat}} &= \pm 2.585 \text{ kPa, HFC-134a} \\ \omega_{p_{sat}} &= \pm 0.8618 \text{ kPa, HCFC-123.}\end{aligned}\tag{A.8}$$

The uncertainties in the inlet and outlet water temperatures are given by

$$\begin{aligned}\omega_{T_{w,in}} &= \pm 0.025^\circ\text{C} \\ \omega_{T_{w,out}} &= \pm 0.025^\circ\text{C.}\end{aligned}\tag{A.9}$$

Uncertainty Due To Water Inlet Temperature

The partial derivative of Equation A.2 with respect to $T_{w,in}$ is given by

$$\begin{aligned}\frac{\partial h_o}{\partial T_{w,in}} &= \frac{1}{A_o} \left[\frac{(\Delta T_1 - \Delta T_2)}{q \cdot \ln\left(\frac{\Delta T_1}{\Delta T_2}\right)} - \frac{1}{A_i h_i} - R_{tw} \right]^{-2} \\ &\times \left[\frac{-1}{q \cdot \ln\left(\frac{\Delta T_1}{\Delta T_2}\right)} + \frac{(\Delta T_1 - \Delta T_2)}{q \cdot \Delta T_1 \ln\left(\frac{\Delta T_1}{\Delta T_2}\right)^2} \right].\end{aligned}\tag{A.10}$$

The uncertainty in the inlet water temperature is noted in Equation A.9.

Uncertainty Due To Water Outlet Temperature

The partial derivative of Equation A.2 with respect to $T_{w,out}$ is given by

$$\frac{\partial h_o}{\partial T_{w,out}} = \frac{1}{A_o} \left[\frac{(\Delta T_1 - \Delta T_2)}{q \cdot \ln\left(\frac{\Delta T_1}{\Delta T_2}\right)} - \frac{1}{A_i h_i} - R_{tw} \right]^{-2}$$

$$\times \left[\frac{1}{q \cdot \ln \left(\frac{\Delta T_1}{\Delta T_2} \right)} - \frac{(\Delta T_1 - \Delta T_2)}{q \cdot \Delta T_2 \ln \left(\frac{\Delta T_1}{\Delta T_2} \right)^2} \right]. \quad (\text{A.11})$$

The uncertainty in the outlet water temperature is given above in Equation A.9.

Uncertainty Due To Heat Transfer Rate

The partial derivative of Equation A.2 with respect to q is given by

$$\frac{\partial h_o}{\partial q} = \frac{1}{A_o} \left[\frac{(\Delta T_1 - \Delta T_2)}{q \cdot \ln \left(\frac{\Delta T_1}{\Delta T_2} \right)} - \frac{1}{A_i h_i} - R_{tw} \right]^{-2} \left[\frac{(\Delta T_1 - \Delta T_2)}{q^2 \ln \left(\frac{\Delta T_1}{\Delta T_2} \right)} \right] \quad (\text{A.12})$$

As discussed in Chapter 4, the energy transfer rate can be calculated from either the refrigerant energy transfer rate

$$q_{ref} = \dot{m}_{ref}(i_{ref,out} - i_{ref,in}) \quad (\text{A.13})$$

or the water energy transfer rate

$$q_w = \dot{m}_w C_p (T_{w,out} - T_{w,in}) \quad (\text{A.14})$$

By using a repeated application of Equation A.1, ω_q can be calculated using the following equations.

For the calculating the uncertainty of the average bundle heat transfer coefficient, which is based on both q_w and q_{ref} , the equations

$$q = (q_{ref} + q_w)/2 \quad (\text{A.15})$$

$$\omega_q = \frac{1}{2} \left[\omega_{q_{ref}}^2 + \omega_{q_w}^2 \right]^{1/2} \quad (\text{A.16})$$

were used. For the calculation of an average row heat transfer coefficient, which is based on q_w only, this becomes

$$q = q_w \quad (\text{A.17})$$

$$\omega_q = \omega_{qw} \quad (\text{A.18})$$

Applying the method of Equation A.1 to Equations A.13 and A.14, $\omega_{q_{ref}}$ and ω_{qw} can be calculated as follows:

$$\omega_{q_{ref}} = [((i_{ref,out} - i_{ref,in})\omega_{\dot{m}_{ref}})^2 + (\dot{m}_{ref}\omega_{i_{ref,out}})^2 + (\dot{m}_{ref}\omega_{i_{ref,in}})^2]^{1/2} \quad (\text{A.19})$$

$$\omega_{qw} = [(C_p(T_{w,out} - T_{w,in})\omega_{\dot{m}_w})^2 + (\dot{m}_w C_p \omega_{T_{w,out}})^2 + (\dot{m}_w C_p \omega_{T_{w,in}})^2]^{1/2} \quad (\text{A.20})$$

where the uncertainties in the water temperature measurements are given in Equation A.9 and the uncertainties in the mass flow rates are

$$\begin{aligned} \omega_{\dot{m}_{ref}} &= \pm(0.002\dot{m}_{ref} + 0.002\text{kg/min}) \\ \omega_{\dot{m}_w} &= \pm(0.002\dot{m}_w + 0.150\text{kg/min}); \text{ bulk flow rate} \\ \omega_{\dot{m}_w} &= \pm 0.01\dot{m}_w; \text{ tube flow rate.} \end{aligned} \quad (\text{A.21})$$

The uncertainty in C_p is neglected.

The enthalpy i is a function of temperature and pressure. Therefore, by Equation A.1

$$\omega_{i_{ref,in}} = \left[\left(\frac{\partial i_{ref,in}}{\partial p_{sat}} \omega_{p_{sat}} \right)^2 + \left(\frac{\partial i_{ref,in}}{\partial T_{ref,in}} \omega_{T_{ref,in}} \right)^2 \right]^{1/2} \quad (\text{A.22})$$

and

$$\omega_{i_{ref,out}} = \left[\left(\frac{\partial i_{ref,out}}{\partial p_{sat}} \omega_{p_{sat}} \right)^2 + \left(\frac{\partial i_{ref,out}}{\partial T_{ref,out}} \omega_{T_{ref,out}} \right)^2 \right]^{1/2} \quad (\text{A.23})$$

where the uncertainties in the saturation pressure measurements are listed above and the uncertainties in the inlet and outlet refrigerant temperatures are given by

$$\begin{aligned} \omega_{T_{ref,in}} &= \pm 0.025^\circ\text{C} \\ \omega_{T_{ref,out}} &= \pm 0.025^\circ\text{C.} \end{aligned} \quad (\text{A.24})$$

The enthalpy partial derivatives are computed by using the computerized property equations and applying a finite difference method centered around p_{sat} , $T_{ref,in}$, and $T_{ref,out}$. For p_{sat} , a grid size of 40 kPa is used. For $T_{ref,in}$ and $T_{ref,out}$, a grid size of 10°C is used.

Uncertainty Due To the Water-side Heat Transfer Coefficient

The partial derivative of Equation A.2 with respect to h_i is given by

$$\frac{\partial h_o}{\partial h_i} = - \left[\left(\frac{(\Delta T_1 - \Delta T_2)}{q \cdot \ln \left(\frac{\Delta T_1}{\Delta T_2} \right)} - \frac{1}{A_i h_i} - R_{tw} \right)^2 (A_o A_i h_i^2) \right]^{-1}. \quad (\text{A.25})$$

The inside (water-side) heat transfer coefficient is defined by Equation 4.4, while the uncertainty in the water-side heat transfer coefficient, ω_{h_i} , is taken to be $0.005h_i$.

APPENDIX B. TABULATED HCFC-123 NON-CONDENSIBLE GAS DATA

Table B.1: Refrigerant-side data for the 26-fpi geometry with non-condensable gas contamination in HCFC-123 condensation

run	q W	T_{sat} °C	inlet outlet		middle tube $T_{s,o}$					\dot{m} kg/min
			sh °C	sc °C	row 1 °C	row 2 °C	row 3 °C	row 4 °C	row 5 °C	
0% N ₂ Concentration, Run 1										
bf16	16080	35.02	3.43	.03	33.68	33.68	33.28	33.41	33.50	5.68
bf18	18060	35.03	4.14	.06	33.43	33.48	33.03	33.18	33.33	6.36
bf20	20250	35.06	5.03	.09	33.21	33.28	32.88	32.98	33.18	7.10
bf22	22070	35.05	4.07	.09	33.00	33.00	32.64	32.74	32.97	7.77
bf24	24160	35.07	5.81	.08	32.86	32.84	32.50	32.60	32.84	8.44
bf26	26150	35.04	4.65	.03	32.53	32.55	32.23	32.37	32.61	9.19
bf28	28360	35.02	5.73	.14	32.22	32.24	31.95	32.14	32.33	9.91
bf30	30450	34.97	6.31	.13	31.97	32.03	31.67	31.86	32.06	10.62
bf32	32370	35.00	7.04	.11	31.80	31.85	31.46	31.68	31.82	11.25
bf34	34070	34.99	7.58	.19	31.49	31.66	31.26	31.49	31.60	11.81
bf36	36170	35.01	8.03	.16	31.33	31.47	31.02	31.27	31.42	12.52
0% N ₂ Concentration, Run 2										
bf18	18180	34.91	5.32	-.09	33.37	33.39	32.95	33.07	33.22	6.37
bf24	24240	35.09	4.75	.05	32.77	32.74	32.40	32.53	32.82	8.51
bf30	30280	35.01	5.98	.20	31.94	32.02	31.66	31.91	32.07	10.57
bf36	36010	35.04	8.60	.24	31.24	31.41	30.99	31.24	31.39	12.43
0.5% N ₂ Concentration										
bf18	18100	35.00	5.70	.47	33.00	33.07	32.67	32.82	32.92	6.31
bf22	22080	35.03	4.43	.46	32.64	32.72	32.30	32.35	32.61	7.74
bf26	26140	35.04	4.49	.42	32.07	32.23	31.86	31.94	32.13	9.17
bf30	30060	34.98	3.78	.60	31.53	31.67	31.34	31.45	31.56	10.56
1.0% N ₂ Concentration										
bf18	18050	34.95	4.65	.40	32.89	32.79	32.39	32.56	32.71	6.33
bf22	22140	35.06	4.78	.55	32.47	32.52	32.08	32.16	32.42	7.75
bf26	26130	35.02	4.13	.52	31.72	31.99	31.58	31.69	31.88	9.17
bf30	30070	35.01	4.27	.57	31.22	31.47	31.11	31.25	31.38	10.54
2.0% N ₂ Concentration										
bf18	18060	35.04	4.13	.69	32.51	32.49	32.01	32.21	32.44	6.33
bf22	22070	34.96	4.60	.73	31.91	31.99	31.52	31.65	31.94	7.72
bf26	26020	35.03	3.09	.78	31.55	31.72	31.29	31.37	31.66	9.16
bf30	30210	34.96	3.64	.81	30.81	31.03	30.62	30.81	30.98	10.60
5.0% N ₂ Concentration										
bf18	18130	35.01	3.97	1.21	31.46	31.21	30.65	31.03	31.36	6.34
bf22	22280	34.99	4.59	1.23	30.95	30.85	30.32	30.53	30.98	7.77
bf26	26210	35.03	4.47	1.27	30.54	30.54	30.02	30.21	30.59	9.14
bf30	30260	35.02	4.24	1.24	29.88	29.94	29.46	29.72	30.08	10.57

Table B.2: Water-side data for the 26-fpi geometry with non-condensable gas contamination in HCFC-123 condensation

run	q W	$T_{bulk,in}$ °C	$T_{bulk,out}$ °C	LMTD °C	\dot{m}_{bulk} kg/min	\dot{m}_{tube} kg/min	Re	$\frac{h_i}{W}$ $\frac{m^2}{K}$
0% N ₂ Concentration, Run 1								
bf16	15840	29.17	30.99	4.92	125.22	5.01	9330	6540
bf18	17840	28.55	30.52	5.47	130.28	5.21	9590	6710
bf20	20070	28.20	30.20	5.83	144.58	5.78	10570	7270
bf22	21930	27.88	29.88	6.14	157.86	6.31	11460	7780
bf24	24040	27.64	29.63	6.39	173.64	6.95	12540	8370
bf26	26110	27.28	29.28	6.72	187.21	7.49	13410	8860
bf28	28320	26.89	28.91	7.09	201.02	8.04	14280	9340
bf30	30550	26.50	28.54	7.42	215.41	8.62	15170	9830
bf32	32450	26.28	28.29	7.69	231.19	9.25	16200	10380
bf34	34290	25.99	28.01	7.97	243.70	9.75	16970	10790
bf36	36460	25.61	27.68	8.35	252.95	10.12	17470	11080
0% N ₂ Concentration, Run 2								
bf18	17950	28.41	30.40	5.49	129.63	5.19	9520	6680
bf24	24110	27.56	29.57	6.49	172.24	6.89	12420	8310
bf30	30350	26.53	28.56	7.44	215.06	8.60	15160	9820
bf36	36140	25.51	27.61	8.46	247.63	9.91	17070	10880
0.5% N ₂ Concentration								
bf18	17930	28.11	30.11	5.88	128.58	5.14	9380	6610
bf22	21930	27.58	29.57	6.44	158.42	6.34	11420	7770
bf26	26060	26.92	28.92	7.11	187.05	7.48	13290	8820
bf30	30200	26.19	28.21	7.78	215.17	8.61	15050	9790
1.0% N ₂ Concentration								
bf18	17890	27.91	29.90	6.04	129.27	5.17	9390	6630
bf22	22060	27.34	29.35	6.70	157.19	6.29	11280	7710
bf26	26110	26.66	28.67	7.35	187.01	7.48	13220	8790
bf30	30210	26.00	28.03	8.00	214.51	8.58	14940	9750
2.0% N ₂ Concentration								
bf18	17920	27.65	29.64	6.39	129.34	5.17	9340	6610
bf22	21940	26.89	28.89	7.07	157.25	6.29	11170	7670
bf26	26020	26.41	28.42	7.61	186.27	7.45	13090	8740
bf30	30250	25.61	27.62	8.36	215.50	8.62	14870	9740
5.0% N ₂ Concentration								
bf18	18090	26.44	28.46	7.57	128.50	5.14	9040	6500
bf22	22290	25.83	27.84	8.15	158.46	6.34	10990	7640
bf26	26310	25.31	27.33	8.72	187.60	7.50	12860	8690
bf30	30420	24.58	26.61	9.43	215.53	8.62	14530	9640

Table B.3: Row data for the 26-fpi geometry with non-condensable gas contamination in HCFC-123 condensation

run	row 1		row 2		row 3		row 4		row 5	
	$T_{w,out}$ °C	q'' W/m ²								
0% N ₂ Concentration, Run 1										
bf16	30.99	17830	30.99	17830	30.83	16260	30.88	16750	30.92	17150
bf18	30.50	19880	30.52	20080	30.34	18250	30.40	18860	30.46	19470
bf20	30.16	22170	30.19	22510	30.03	20700	30.07	21160	30.15	22060
bf22	29.85	24330	29.85	24330	29.71	22600	29.75	23100	29.84	24210
bf24	29.62	26770	29.61	26630	29.48	24860	29.52	25410	29.61	26630
bf26	29.23	28570	29.24	28710	29.12	26950	29.17	27690	29.26	29000
bf28	28.84	30670	28.85	30830	28.74	29100	28.81	30200	28.88	31300
bf30	28.48	33210	28.50	33540	28.37	31350	28.44	32530	28.51	33710
bf32	28.24	35460	28.26	35820	28.12	33290	28.20	34730	28.25	35640
bf34	27.92	36800	27.98	37950	27.84	35280	27.92	36800	27.96	37570
bf36	27.60	39390	27.65	40380	27.49	37210	27.58	39000	27.63	39980
0% N ₂ Concentration, Run 2										
bf18	30.39	20080	30.40	20180	30.22	18360	30.27	18870	30.33	19470
bf24	29.53	26550	29.52	26420	29.39	24660	29.44	25340	29.55	26820
bf30	28.48	32820	28.51	33320	28.38	31130	28.47	32650	28.53	33660
bf36	27.51	38760	27.57	39920	27.42	37010	27.51	38760	27.56	39730
0.5% N ₂ Concentration										
bf18	30.06	19620	30.09	19920	29.93	18310	29.99	18910	30.03	19320
bf22	29.52	24050	29.55	24420	29.39	22440	29.41	22680	29.51	23920
bf26	28.83	27960	28.89	28830	28.75	26780	28.78	27220	28.85	28250
bf30	28.11	32330	28.16	33170	28.04	31150	28.08	31820	28.12	32500
1.0% N ₂ Concentration										
bf18	29.89	20030	29.85	19620	29.69	18000	29.76	18710	29.82	19320
bf22	29.30	24230	29.32	24480	29.15	22390	29.18	22750	29.28	23980
bf26	28.53	27360	28.63	28830	28.48	26630	28.52	27220	28.59	28240
bf30	27.88	31390	27.97	32900	27.84	30720	27.89	31560	27.94	32400
2.0% N ₂ Concentration										
bf18	29.58	19530	29.57	19430	29.38	17510	29.46	18320	29.55	19230
bf22	28.80	23630	28.83	23990	28.65	21780	28.70	22390	28.81	23750
bf26	28.31	27690	28.37	28570	28.21	26240	28.24	26670	28.35	28280
bf30	27.47	31370	27.55	32720	27.40	30190	27.47	31370	27.53	32380
5.0% N ₂ Concentration										
bf18	28.41	19910	28.31	18900	28.09	16690	28.24	18200	28.37	19510
bf22	27.76	24060	27.72	23560	27.52	21080	27.60	22070	27.77	24180
bf26	27.22	28040	27.22	28040	27.03	25250	27.10	26280	27.24	28330
bf30	26.46	31710	26.48	32050	26.31	29180	26.40	30700	26.53	32890

Table B.4: Shell-side heat transfer coefficients and uncertainties for the 26-fpi geometry with non-condensable gas contamination in HCFC-123 condensation

run	bundle				row 1		row 2		row 3		row 4		row 5	
	q'' W/m ²	q' W/m	h_o $\frac{W}{m^2 K}$	w ± %										
0% N ₂ Concentration, Run 1														
bf16	17940	1060	14090	16.	13780	17.	13780	17.	9580	13.	10660	14.	11660	15.
bf18	20170	1190	13660	14.	12870	15.	13440	15.	9350	12.	10480	13.	11820	14.
bf20	22650	1340	13350	13.	12280	13.	13030	13.	9660	11.	10380	11.	12050	13.
bf22	24720	1460	12860	11.	12140	12.	12140	12.	9530	10.	10190	10.	11920	12.
bf24	27080	1600	12850	10.	12400	11.	12190	11.	9820	10.	10470	10.	12190	11.
bf26	29360	1730	12590	9.	11530	10.	11710	10.	9710	9.	10480	9.	12100	10.
bf28	31840	1870	12430	9.	11100	9.	11270	9.	9570	8.	10610	9.	11800	9.
bf30	34270	2020	12270	8.	11200	8.	11530	9.	9580	8.	10580	8.	11700	9.
bf32	36420	2150	12070	7.	11200	8.	11520	8.	9490	7.	10590	8.	11360	8.
bf34	38400	2270	11900	7.	10610	7.	11510	8.	9540	7.	10610	7.	11200	8.
bf36	40800	2400	11860	7.	10790	7.	11520	7.	9380	7.	10510	7.	11220	7.
0% N ₂ Concentration, Run 2														
bf18	20300	1200	14050	15.	13450	15.	13750	16.	9530	12.	10490	13.	11830	14.
bf24	27160	1610	12570	10.	11650	10.	11450	10.	9290	9.	10050	10.	12050	11.
bf30	34060	2010	12030	8.	10790	8.	11270	8.	9380	8.	10640	8.	11600	9.
bf36	40530	2390	11590	7.	10290	7.	11110	7.	9200	7.	10290	7.	10970	7.
0.5% N ₂ Concentration														
bf18	20240	1190	11200	12.	10010	12.	10580	12.	8000	10.	8850	11.	9490	11.
bf22	24730	1460	11200	10.	10230	10.	10750	10.	8330	9.	8590	9.	10060	10.
bf26	29320	1730	10950	8.	9540	8.	10420	9.	8510	8.	8870	8.	9820	9.
bf30	33850	2000	10720	7.	9470	8.	10130	8.	8630	7.	9090	7.	9590	8.
1.0% N ₂ Concentration														
bd18	20190	1190	10200	11.	9920	12.	9250	11.	7120	9.	7960	10.	8790	11.
bf22	24830	1460	10300	9.	9520	9.	9820	10.	7610	8.	7950	9.	9230	9.
bf26	29350	1730	10120	8.	8360	8.	9610	8.	7810	7.	8250	8.	9080	8.
bf30	33870	2000	10090	7.	8330	7.	9360	7.	7920	7.	8440	7.	9000	7.
2.0% N ₂ Concentration														
bf18	20210	1190	8730	9.	7870	10.	7750	9.	5850	8.	6570	9.	7510	9.
bf22	24730	1460	8930	8.	7850	8.	8190	8.	6400	7.	6840	8.	7960	8.
bf26	29240	1720	9280	7.	8050	7.	8720	8.	7070	7.	7350	7.	8490	8.
bf30	33960	2000	9200	6.	7610	6.	8390	7.	6990	6.	7610	6.	8190	7.
5.0% N ₂ Concentration														
bf18	20350	1200	6000	7.	5670	7.	5020	7.	3850	6.	4610	7.	5400	7.
bf22	25040	1480	6610	6.	6010	7.	5740	6.	4540	6.	4990	6.	6080	7.
bf26	29510	1740	7050	6.	6280	6.	6280	6.	5060	6.	5480	6.	6430	6.
bf30	34090	2010	7240	5.	6210	6.	6340	6.	5270	5.	5810	5.	6700	6.

Table B.5: Refrigerant-side data for the 40-fpi geometry with non-condensable gas contamination in HCFC-123 condensation

run	q W	T_{sat} °C	inlet outlet		middle tube $T_{s,o}$					\dot{m} kg/min
			sh °C	sc °C	row 1 °C	row 2 °C	row 3 °C	row 4 °C	row 5 °C	
0% N ₂ Concentration, Run 1										
bg18	18130	34.99	3.50	.08	33.76	33.51	33.70	33.59	33.48	6.40
bg24	24090	34.96	4.55	.19	33.23	32.88	33.23	33.08	32.85	8.46
bg30	30160	35.01	6.34	.18	32.79	32.33	32.73	32.52	32.15	10.51
bg36	35970	35.02	9.88	.22	32.36	31.76	32.13	31.85	31.47	12.35
0% N ₂ Concentration, Run 2										
bg16	16110	34.93	4.24	.02	33.82	33.63	33.77	33.66	33.58	5.67
bg18	18080	34.97	2.94	.07	33.77	33.52	33.74	33.60	33.46	6.39
bg20	20130	34.96	5.68	.14	33.59	33.36	33.56	33.42	33.25	7.03
bg22	22150	34.95	5.30	.06	33.38	33.15	33.44	33.27	33.10	7.76
bg24	24170	34.97	5.94	.12	33.32	33.00	33.32	33.15	32.88	8.44
bg26	26160	35.02	6.11	.15	33.21	32.82	33.18	33.00	32.70	9.13
bg28	28160	35.00	5.24	.09	32.98	32.59	32.95	32.80	32.44	9.86
bg30	30250	35.03	6.32	.06	32.86	32.41	32.80	32.59	32.23	10.55
bg32	32330	35.00	7.72	.17	32.70	32.17	32.54	32.30	31.92	11.20
bg34	34220	34.96	7.49	.28	32.49	31.90	32.28	32.02	31.68	11.86
bg36	36170	34.99	8.68	.26	32.35	31.71	32.12	31.84	31.43	12.47
0.5% N ₂ Concentration										
bg18	18050	35.02	4.33	.49	33.30	33.13	33.43	33.19	32.99	6.33
bg22	22180	35.03	4.39	.49	32.91	32.85	33.19	32.88	32.70	7.78
bg26	26060	34.99	3.20	.38	32.57	32.46	32.81	32.54	32.19	9.19
bg30	30170	35.07	3.63	.49	32.36	32.08	32.48	32.17	31.84	10.61
1.0% N ₂ Concentration										
bg18	18120	34.94	4.07	.53	33.12	32.95	33.23	32.98	32.81	6.36
bg26	26230	35.07	3.43	.57	32.52	32.34	32.69	32.40	32.13	9.23
bg30	30130	35.00	2.76	.74	32.17	31.87	32.23	31.93	31.56	10.62
bg22	22090	34.96	3.83	.59	32.69	32.60	32.92	32.63	32.43	7.76
2.0% N ₂ Concentration										
bg18	18310	34.96	4.90	.61	32.77	32.47	32.77	32.47	32.41	6.40
bg22	22060	35.04	4.35	.62	32.46	32.26	32.55	32.23	32.11	7.73
bg26	26230	35.06	2.81	.83	32.15	31.94	32.27	31.91	31.70	9.24
bg30	30290	35.06	3.53	.90	31.94	31.51	31.88	31.51	31.20	10.63
5.0% N ₂ Concentration										
bg18	18120	34.99	4.31	1.17	31.89	31.27	31.52	31.13	31.19	6.33
bg26	26300	35.05	2.99	1.27	31.13	30.65	30.98	30.53	30.41	9.23
bg22	22060	35.07	3.68	1.30	31.58	31.11	31.40	30.96	30.94	7.72
bg30	30490	35.03	4.75	1.36	30.87	30.25	30.66	30.19	30.00	10.62

Table B.6: Water-side data for the 40-fpi geometry with non-condensable gas contamination in HCFC-123 condensation

run	q W	$T_{bulk,in}$ °C	$T_{bulk,out}$ °C	LMTD °C	\dot{m}_{bulk} kg/min	\dot{m}_{tube} kg/min	Re	$\frac{h_i}{W}$ m ² K
0% N ₂ Concentration, Run 1								
bg18	17940	28.21	30.20	5.78	129.36	5.17	8620	5340
bg24	23990	27.36	29.36	6.63	172.20	6.89	11260	6650
bg30	30170	26.52	28.53	7.54	215.76	8.63	13850	7900
bg36	36110	25.54	27.60	8.51	251.29	10.05	15790	8840
0% N ₂ Concentration, Run 2								
bg16	15890	28.82	30.63	5.19	125.75	5.03	8480	5250
bg18	17860	28.25	30.22	5.74	130.31	5.21	8690	5370
bg20	19950	27.90	29.90	6.06	143.22	5.73	9480	5770
bg22	21980	27.67	29.66	6.29	158.38	6.34	10430	6240
bg24	24010	27.43	29.43	6.58	172.93	6.92	11330	6680
bg26	25980	27.21	29.20	6.84	187.90	7.52	12250	7120
bg28	28030	26.89	28.89	7.16	201.62	8.06	13050	7510
bg30	30190	26.57	28.58	7.50	214.76	8.59	13800	7880
bg32	32360	26.24	28.25	7.82	231.26	9.25	14750	8330
bg34	34300	25.89	27.91	8.12	244.29	9.77	15460	8670
bg36	36310	25.52	27.58	8.51	253.00	10.12	15890	8880
0.5% N ₂ Concentration								
bg18	17940	27.84	29.83	6.21	129.56	5.18	8560	5330
bg22	22070	27.29	29.29	6.77	158.21	6.33	10330	6210
bg26	26020	26.76	28.75	7.29	188.33	7.53	12150	7100
bg30	30240	26.16	28.18	7.96	214.87	8.59	13690	7850
1.0% N ₂ Concentration								
bg18	18010	27.62	29.61	6.35	129.80	5.19	8540	5320
bg26	26230	26.58	28.60	7.53	187.08	7.48	12030	7050
bg30	30320	25.88	27.91	8.18	214.61	8.58	13580	7810
bg22	22050	27.16	29.12	6.86	161.24	6.45	10500	6300
2.0% N ₂ Concentration								
bg18	18230	27.17	29.18	6.82	130.29	5.21	8490	5310
bg22	21960	26.79	28.78	7.30	158.41	6.34	10230	6190
bg26	26280	26.19	28.20	7.92	187.64	7.51	11960	7040
bg30	30400	25.59	27.61	8.54	215.43	8.62	13540	7810
5.0% N ₂ Concentration								
bg18	18080	26.04	28.05	8.01	129.21	5.17	8210	5220
bg26	26410	24.93	26.95	9.19	187.46	7.50	11610	6940
bg22	22060	25.65	27.66	8.49	157.84	6.31	9940	6100
bg30	30550	24.36	26.40	9.75	215.15	8.61	13150	7710

Table B.7: Row data for the 40-fpi geometry with non-condensable gas contamination in HCFC-123 condensation

run	row 1		row 2		row 3		row 4		row 5	
	$T_{w,out}$ °C	q'' W/m ²								
0% N ₂ Concentration, Run 1										
bg18	30.21	20130	30.12	19230	30.19	19930	30.15	19530	30.11	19120
bg24	29.36	26800	29.24	25190	29.36	26800	29.31	26130	29.23	25060
bg30	28.56	34250	28.41	31730	28.54	33910	28.47	32740	28.35	30720
bg36	27.68	41850	27.49	38130	27.61	40480	27.52	38720	27.40	36370
0% N ₂ Concentration, Run 2										
bg16	30.64	17810	30.57	17120	30.62	17610	30.58	17220	30.55	16930
bg18	30.23	20180	30.14	19260	30.22	20080	30.17	19570	30.12	19060
bg20	29.91	22400	29.83	21510	29.90	22290	29.85	21730	29.79	21060
bg22	29.65	24400	29.57	23410	29.67	24650	29.61	23910	29.55	23170
bg24	29.43	27050	29.32	25570	29.43	27050	29.37	26240	29.28	25030
bg26	29.22	29390	29.09	27490	29.21	29240	29.15	28360	29.05	26900
bg28	28.90	31530	28.77	29490	28.89	31380	28.84	30590	28.72	28710
bg30	28.62	34260	28.47	31750	28.60	33920	28.53	32750	28.41	30750
bg32	28.31	37250	28.14	34190	28.26	36350	28.18	34910	28.06	32750
bg34	27.98	39730	27.79	36120	27.91	38400	27.83	36880	27.72	34790
bg36	27.66	42130	27.46	38190	27.59	40750	27.50	38980	27.37	36420
0.5% N ₂ Concentration										
bg18	29.80	19760	29.74	19150	29.85	20260	29.76	19360	29.69	18650
bg22	29.23	23880	29.21	23640	29.33	25110	29.22	23760	29.16	23020
bg26	28.70	28430	28.66	27840	28.78	29600	28.69	28280	28.57	26520
bg30	28.17	33610	28.08	32100	28.21	34280	28.11	32600	28.00	30760
1.0% N ₂ Concentration										
bg18	29.59	19900	29.53	19290	29.63	20300	29.54	19390	29.48	18790
bg26	28.56	28820	28.50	27950	28.62	29700	28.52	28240	28.43	26930
bg30	27.91	34070	27.81	32400	27.93	34400	27.83	32730	27.71	30730
bg22	29.06	23840	29.03	23460	29.14	24840	29.04	23590	28.97	22710
2.0% N ₂ Concentration										
bg18	29.17	20280	29.06	19160	29.17	20280	29.06	19160	29.04	18960
bg22	28.74	24040	28.67	23170	28.77	24410	28.66	23050	28.62	22560
bg26	28.17	28910	28.10	27890	28.21	29490	28.09	27740	28.02	26720
bg30	27.64	34370	27.50	32020	27.62	34030	27.50	32020	27.40	30340
5.0% N ₂ Concentration										
bg18	28.11	20810	27.89	18600	27.98	19510	27.84	18100	27.86	18300
bg26	26.97	29760	26.81	27430	26.92	29030	26.77	26840	26.73	26260
bg22	27.67	24810	27.51	22850	27.61	24070	27.46	22230	27.45	22110
bg30	26.44	34830	26.24	31480	26.37	33650	26.22	31140	26.16	30140

Table B.8: Shell-side heat transfer coefficients and uncertainties for the 40-fpi geometry with non-condensable gas contamination in HCFC-123 condensation

run	bundle				row 1		row 2		row 3		row 4		row 5	
	q'' W/m ²	q' W/m	h_o $\frac{W}{m^2 K}$	w ± %										
0% N ₂ Concentration, Run 1														
bg18	20150	1240	17110	18.	17110	20.	13450	16.	16160	19.	14510	17.	13120	16.
bg24	26860	1660	16010	13.	15880	14.	12330	12.	15880	14.	14230	13.	12090	12.
bg30	33700	2080	14810	10.	15730	11.	12010	10.	15150	11.	13330	10.	10870	9.
bg36	40270	2490	13980	8.	15960	10.	11810	8.	14220	9.	12360	8.	10340	8.
0% N ₂ Concentration, Run 2														
bg16	17880	1100	17170	20.	16930	22.	13730	18.	15900	21.	14130	19.	12990	18.
bg18	20080	1240	17130	18.	17570	20.	13740	17.	17060	20.	14850	18.	13070	16.
bg20	22390	1380	16920	16.	17040	18.	13930	15.	16590	17.	14620	16.	12700	14.
bg22	24650	1520	16860	15.	16090	16.	13380	14.	16910	16.	14640	15.	12820	13.
bg24	26920	1660	16620	13.	16900	15.	13270	13.	16900	15.	14750	14.	12240	12.
bg26	29130	1800	16030	12.	16670	14.	12760	11.	16310	13.	14370	12.	11830	11.
bg28	31390	1940	15620	11.	15910	12.	12400	11.	15590	12.	14130	11.	11340	10.
bg30	33760	2080	15240	10.	16170	12.	12290	10.	15560	11.	13660	10.	11110	9.
bg32	36140	2230	14710	9.	16460	11.	12230	9.	15020	10.	13070	10.	10750	9.
bg34	38280	2360	14380	8.	16400	11.	11940	9.	14520	10.	12720	9.	10710	8.
bg36	40490	2500	14110	8.	16180	10.	11770	8.	14410	9.	12510	8.	10310	8.
0.5% N ₂ Concentration														
bg18	20100	1240	12740	14.	11810	14.	10400	13.	13230	15.	10840	13.	9410	12.
bg22	24720	1530	13080	12.	11460	12.	11030	11.	14010	13.	11240	12.	10060	11.
bg26	29090	1800	13000	10.	11960	10.	11150	10.	13860	12.	11750	10.	9580	9.
bg30	33750	2080	12730	8.	12550	10.	10860	9.	13420	10.	11390	9.	9600	8.
1.0% N ₂ Concentration														
bg18	20180	1250	11840	13.	11180	13.	9900	12.	12180	14.	10100	12.	8990	12.
bg26	29310	1810	12150	9.	11460	10.	10360	9.	12720	11.	10710	10.	9260	9.
bg30	33780	2080	11910	8.	12190	9.	10440	8.	12590	9.	10760	9.	9000	8.
bg22	24660	1520	12040	11.	10660	11.	10090	11.	12410	12.	10280	11.	9080	10.
2.0% N ₂ Concentration														
bg18	20420	1260	9690	10.	9460	11.	7800	10.	9460	11.	7800	10.	7550	10.
bg22	24590	1520	10200	9.	9460	10.	8440	9.	9950	10.	8310	9.	7800	9.
bg26	29330	1810	10520	8.	10050	9.	9030	8.	10710	9.	8900	8.	8020	8.
bg30	33900	2090	10690	7.	11150	8.	9100	8.	10820	8.	9100	8.	7920	7.
5.0% N ₂ Concentration														
bg18	20220	1250	6260	7.	6790	8.	5040	7.	5680	8.	4720	7.	4850	7.
bg26	29440	1820	7470	6.	7670	7.	6280	6.	7200	7.	5980	6.	5700	6.
bg22	24650	1520	7050	7.	7170	8.	5810	7.	6620	7.	5450	7.	5380	7.
bg30	34100	2110	8000	6.	8440	7.	6620	6.	7740	6.	6470	6.	6020	6.

Table B.9: Refrigerant-side data for the Tu-Cii geometry with non-condensable gas contamination in HCFC-123 condensation

run	q W	T_{sat} °C	inlet outlet		middle tube $T_{s,o}$					\dot{m} kg/min
			sh °C	sc °C	row 1 °C	row 2 °C	row 3 °C	row 4 °C	row 5 °C	
0% N ₂ Concentration, Run 1										
bc18	18170	34.97	3.98	.15	34.09	34.21	33.95	33.86	33.83	6.39
bc24	24230	35.08	4.91	.29	33.91	34.06	33.76	33.58	33.56	8.49
bc30	30180	35.04	6.80	.37	33.57	33.67	33.44	33.21	33.10	10.48
bc36	36190	35.06	8.99	.53	33.16	33.24	33.00	32.65	32.49	12.45
0% N ₂ Concentration, Run 2										
bc16	16110	34.92	3.52	.08	34.20	34.34	34.10	34.01	33.96	5.68
bc18	18120	34.98	3.83	.10	34.16	34.33	34.09	34.00	33.93	6.38
bc20	20250	34.95	4.00	.14	34.04	34.19	33.95	33.83	33.75	7.13
bc22	22240	34.95	4.12	.17	33.93	34.08	33.86	33.69	33.66	7.82
bc24	24220	35.08	4.95	.23	33.98	34.13	33.85	33.68	33.63	8.49
bc26	26120	35.06	4.14	.26	33.84	33.99	33.74	33.53	33.48	9.18
bc28	28310	35.06	5.49	.31	33.70	33.83	33.57	33.37	33.29	9.89
bc30	30440	34.98	6.80	.36	33.49	33.64	33.38	33.13	33.02	10.58
bc32	32490	35.02	7.50	.45	33.36	33.46	33.23	32.94	32.83	11.25
bc34	34430	34.98	6.74	.50	33.20	33.28	33.06	32.74	32.58	11.95
bc36	36280	35.05	8.07	.53	33.13	33.21	32.97	32.62	32.44	12.53
0.5% N ₂ Concentration										
bc18	18060	34.95	3.64	.62	33.56	33.51	33.25	33.03	33.18	6.35
bc22	22200	35.02	4.71	.71	33.36	33.31	33.06	32.77	32.91	7.77
bc26	26200	34.95	5.13	.86	33.11	33.06	32.81	32.42	32.63	9.14
bc30	30070	35.02	3.07	1.02	32.93	32.82	32.59	32.12	32.33	10.57
1.0% N ₂ Concentration										
bc18	18120	34.98	5.07	.83	33.38	33.26	32.95	32.76	32.98	6.32
bc22	22200	35.03	3.93	.92	33.24	33.12	32.82	32.53	32.75	7.78
bc26	26170	34.96	4.49	1.02	32.94	32.81	32.53	32.15	32.40	9.15
bc30	30210	34.98	4.41	.99	32.67	32.51	32.22	31.73	32.01	10.56
2.0% N ₂ Concentration										
bc18	18170	35.03	5.37	.93	32.97	32.75	32.39	32.20	32.47	6.33
bc22	22030	35.06	3.44	.94	32.82	32.60	32.25	31.98	32.25	7.74
bc26	26290	34.93	3.95	1.22	32.46	32.23	31.88	31.49	31.85	9.19
bc30	30350	35.04	4.89	1.32	32.37	32.11	31.77	31.32	31.66	10.57
5.0% N ₂ Concentration										
bc18	18220	34.95	3.42	1.58	31.83	31.32	30.91	30.74	31.20	6.37
bc22	22240	34.98	4.30	1.65	31.74	31.19	30.79	30.49	30.97	7.75
bc26	26290	35.06	4.10	1.77	31.61	31.09	30.65	30.26	30.75	9.16
bc30	30360	35.04	4.20	1.93	31.23	30.72	30.30	29.85	30.35	10.56

Table B.10: Water-side data for the Tu-Cii geometry with non-condensable gas contamination in HCFC-123 condensation

run	q W	$T_{bulk,in}$ °C	$T_{bulk,out}$ °C	LMTD °C	\dot{m}_{bulk} kg/min	\dot{m}_{tube} kg/min	Re	$\frac{h_i}{W}$ $\frac{W}{m^2 K}$
0% N ₂ Concentration, Run 1								
bc18	17900	29.39	31.38	4.59	129.05	5.16	8990	6600
bc24	23870	28.91	30.91	5.19	170.84	6.83	11780	8220
bc30	29900	28.37	30.35	5.72	216.80	8.67	14780	9890
bc36	35900	27.60	29.62	6.52	254.56	10.18	17070	11160
0% N ₂ Concentration, Run 2								
bc16	15630	29.98	31.77	4.04	125.24	5.01	8820	6470
bc18	17790	29.53	31.50	4.47	129.69	5.19	9060	6630
bc20	19950	29.29	31.27	4.68	145.24	5.81	10100	7240
bc22	21880	29.08	31.07	4.88	157.87	6.31	10930	7730
bc24	23850	29.00	30.99	5.10	172.81	6.91	11940	8300
bc26	25780	28.81	30.79	5.28	186.80	7.47	12850	8820
bc28	27770	28.57	30.55	5.53	201.53	8.06	13800	9350
bc30	30050	28.21	30.21	5.80	214.92	8.60	14600	9800
bc32	32140	28.02	30.02	6.04	231.30	9.25	15650	10380
bc34	33980	27.70	29.70	6.33	243.65	9.75	16370	10780
bc36	35630	27.56	29.56	6.55	255.29	10.21	17100	11180
0.5% N ₂ Concentration								
bc18	17930	28.64	30.63	5.37	129.24	5.17	8860	6550
bc22	22050	28.33	30.34	5.72	157.68	6.31	10740	7660
bc26	25790	27.85	29.82	6.15	187.55	7.50	12640	8760
bc30	30100	27.48	29.47	6.59	214.65	8.59	14350	9720
1.0% N ₂ Concentration								
bc18	17940	28.47	30.46	5.52	129.83	5.19	8870	6570
bc22	22270	28.08	30.11	5.96	157.96	6.32	10700	7650
bc26	26290	27.62	29.65	6.35	186.96	7.48	12540	8720
bc30	30370	27.16	29.19	6.86	215.34	8.61	14300	9710
2.0% N ₂ Concentration								
bc18	18050	28.04	30.04	6.02	129.92	5.20	8790	6540
bc22	22040	27.69	29.69	6.42	158.00	6.32	10610	7620
bc26	26270	27.11	29.12	6.86	187.11	7.48	12410	8680
bc30	30360	26.81	28.84	7.26	215.11	8.60	14170	9670
5.0% N ₂ Concentration								
bc18	18170	26.68	28.69	7.30	129.77	5.19	8520	6450
bc22	22210	26.33	28.35	7.69	158.02	6.32	10300	7520
bc26	26340	26.03	28.04	8.10	187.71	7.51	12150	8600
bc30	30460	25.48	27.50	8.61	215.72	8.63	13790	9560

Table B.11: Row data for the Tu-Cii geometry with non-condensable gas contamination in HCFC-123 condensation

run	row 1		row 2		row 3		row 4		row 5	
	$T_{w,out}$ °C	q'' W/m ²								
0% N ₂ Concentration, Run 1										
bc18	31.37	19880	31.42	20380	31.31	19280	31.27	18880	31.26	18780
bc24	30.91	26590	30.97	27380	30.85	25790	30.78	24860	30.77	24720
bc30	30.36	33570	30.40	34240	30.31	32730	30.22	31210	30.18	30530
bc36	29.65	40800	29.68	41400	29.59	39610	29.46	37040	29.40	35850
0% N ₂ Concentration, Run 2										
bc16	31.77	17440	31.83	18030	31.73	17050	31.69	16660	31.67	16470
bc18	31.48	19680	31.55	20380	31.45	19370	31.41	18970	31.38	18670
bc20	31.25	22150	31.31	22830	31.21	21700	31.16	21130	31.13	20790
bc22	31.05	24200	31.11	24940	31.02	23830	30.95	22970	30.94	22850
bc24	30.99	26760	31.05	27560	30.94	26090	30.87	25140	30.85	24880
bc26	30.79	28780	30.85	29650	30.75	28200	30.67	27030	30.65	26740
bc28	30.56	31200	30.61	31990	30.51	30420	30.43	29170	30.40	28690
bc30	30.23	33780	30.29	34780	30.19	33110	30.09	31440	30.05	30770
bc32	30.04	36170	30.08	36890	29.99	35280	29.88	33300	29.84	32580
bc34	29.75	38860	29.78	39430	29.70	37920	29.58	35640	29.52	34500
bc36	29.62	40920	29.65	41520	29.56	39730	29.43	37150	29.36	35750
0.5% N ₂ Concentration										
bc18	30.65	21020	30.63	20820	30.52	19710	30.43	18800	30.49	19410
bc22	30.36	24910	30.34	24660	30.24	23430	30.12	21960	30.18	22700
bc26	29.88	30210	29.86	29920	29.76	28460	29.61	26270	29.69	27440
bc30	29.54	34740	29.50	34070	29.41	32570	29.23	29560	29.31	30900
1.0% N ₂ Concentration										
bc18	30.52	20710	30.47	20200	30.34	18890	30.26	18080	30.35	18990
bc22	30.16	25560	30.11	24950	29.99	23480	29.87	22000	29.96	23110
bc26	29.70	30110	29.65	29390	29.54	27790	29.39	25600	29.49	27060
bc30	29.25	35020	29.19	34010	29.08	32170	28.89	28990	29.00	30830
2.0% N ₂ Concentration										
bc18	30.09	20720	30.00	19810	29.85	18300	29.77	17490	29.88	18600
bc22	29.75	25330	29.66	24220	29.52	22500	29.41	21150	29.52	22500
bc26	29.19	30280	29.10	28970	28.96	26930	28.81	24750	28.95	26790
bc30	28.92	35150	28.82	33480	28.69	31300	28.52	28460	28.65	30630
5.0% N ₂ Concentration										
bc18	28.80	21410	28.59	19290	28.42	17570	28.35	16860	28.54	18780
bc22	28.48	26440	28.26	23730	28.10	21760	27.98	20290	28.17	22630
bc26	28.17	31400	27.97	28480	27.80	26000	27.65	23810	27.84	26580
bc30	27.63	36090	27.44	32900	27.28	30220	27.11	27360	27.30	30550

Table B.12: Shell-side heat transfer coefficients and uncertainties for the Tu-Cii geometry with non-condensable gas contamination in HCFC-123 condensation

run	bundle				row 1		row 2		row 3		row 4		row 5	
	q''	q'	h_o	w										
	W/m^2	W/m	$\frac{W}{m^2 K}$	$\pm \%$										
0% N ₂ Concentration, Run 1														
bc18	20150	1190	26510	27.	24380	27.	29380	32.	20050	23.	17830	21.	17340	20.
bc24	26880	1600	24960	19.	23730	20.	28300	23.	20250	18.	17130	16.	16740	15.
bc30	33560	1990	23500	15.	23610	16.	26030	17.	21050	15.	17410	13.	16080	12.
bc36	40270	2390	20970	11.	22060	13.	23430	13.	19680	12.	15640	10.	14160	10.
0% N ₂ Concentration, Run 2														
bc16	17730	1050	29000	34.	26210	33.	34640	42.	22370	29.	19400	25.	18150	24.
bc18	20060	1190	29620	30.	25910	29.	34620	37.	23270	26.	20400	24.	18620	22.
bc20	22460	1340	28590	26.	26080	26.	32600	31.	22880	23.	19710	21.	18130	19.
bc22	24650	1460	28020	24.	25150	23.	30740	27.	22970	21.	18930	18.	18450	18.
bc24	26860	1600	26090	20.	25630	21.	30930	25.	22260	19.	18620	17.	17760	16.
bc26	29000	1720	25370	18.	24530	19.	29120	22.	22090	18.	18230	15.	17420	15.
bc28	31330	1860	24030	16.	23750	17.	27040	19.	21050	16.	17630	14.	16560	13.
bc30	33800	2010	23270	15.	23400	16.	27080	18.	21360	15.	17320	13.	16020	12.
bc32	36100	2140	22010	13.	22370	14.	24440	15.	20140	13.	16270	12.	15130	11.
bc34	38220	2270	20770	12.	22350	13.	23790	14.	20230	13.	16200	11.	14600	10.
bc36	40170	2380	20230	11.	21870	13.	23210	13.	19520	12.	15540	10.	13850	9.
0.5% N ₂ Concentration														
bc18	20110	1190	13570	14.	15760	17.	15060	16.	11940	14.	10060	12.	11260	13.
bc22	24720	1470	14940	13.	15420	14.	14810	14.	12220	12.	9900	11.	10980	11.
bc26	29050	1720	14760	11.	16890	13.	16260	13.	13550	11.	10550	10.	12030	10.
bc30	33620	2000	15170	10.	17000	12.	15850	11.	13630	10.	10310	9.	11640	9.
1.0% N ₂ Concentration														
bc18	20150	1190	11940	13.	13370	15.	12090	14.	9500	12.	8280	11.	9670	12.
bc22	24850	1470	13200	11.	14700	13.	13380	12.	10830	11.	8910	10.	10300	10.
bc26	29310	1740	13820	10.	15240	12.	13950	11.	11620	10.	9210	9.	10730	10.
bc30	33840	2010	13810	9.	15430	11.	14000	10.	11820	9.	8980	8.	10510	8.
2.0% N ₂ Concentration														
bc18	20240	1200	9510	10.	10310	11.	8890	10.	7050	9.	6270	9.	7380	9.
bc22	24620	1460	10500	9.	11520	11.	9990	10.	8100	9.	6920	8.	8100	9.
bc26	29360	1740	11330	8.	12490	10.	10900	9.	8910	8.	7250	7.	8790	8.
bc30	33920	2010	11990	8.	13390	9.	11580	8.	9670	8.	7710	7.	9160	8.
5.0% N ₂ Concentration														
bc18	20330	1200	6090	7.	6960	8.	5370	7.	4380	6.	4030	6.	5060	7.
bc22	24830	1470	7040	6.	8280	8.	6320	7.	5230	6.	4550	6.	5680	6.
bc26	29400	1740	7810	6.	9200	7.	7230	7.	5930	6.	4990	6.	6210	6.
bc30	33980	2020	8260	6.	9570	7.	7680	6.	6410	6.	5290	6.	6560	6.

Table B.13: Refrigerant-side data for the G-SC geometry with non-condensable gas contamination in HCFC-123 condensation

run	q W	T_{sat} °C	inlet outlet		middle tube $T_{s,o}$					\dot{m} kg/min
			sh °C	sc °C	row 1 °C	row 2 °C	row 3 °C	row 4 °C	row 5 °C	
0% N ₂ Concentration, Run 1										
bd18	18210	35.08	3.87	.09	33.40	33.48	33.14	33.55	33.29	6.42
bd24	24270	35.04	4.02	.19	32.75	32.86	32.59	32.95	32.67	8.54
bd30	30200	35.02	5.91	.30	32.19	32.22	31.90	32.28	31.96	10.54
bd36	36180	35.07	7.20	.39	31.48	31.57	31.30	31.66	31.33	12.55
0% N ₂ Concentration, Run 2										
bd16	16120	34.96	5.47	.04	33.51	33.56	33.22	33.61	33.40	5.64
bd18	18170	35.03	4.60	.10	33.35	33.43	33.09	33.51	33.25	6.38
bd20	20210	35.00	6.06	.11	33.13	33.29	33.00	33.37	33.11	7.06
bd22	22130	35.01	4.46	.12	33.04	33.12	32.87	33.22	32.93	7.77
bd24	24190	35.01	3.70	.08	32.84	32.95	32.70	33.00	32.73	8.53
bd26	26090	35.02	4.35	.20	32.65	32.76	32.51	32.82	32.54	9.16
bd28	28270	35.01	4.77	.17	32.42	32.50	32.27	32.56	32.27	9.91
bd30	30230	35.07	5.98	.22	32.34	32.43	32.17	32.49	32.20	10.55
bd32	32180	34.98	5.83	.26	32.08	32.11	31.91	32.17	31.88	11.23
bd34	34320	34.94	7.70	.35	31.81	31.87	31.60	31.90	31.60	11.88
bd36	36290	35.06	8.36	.35	31.60	31.66	31.42	31.72	31.42	12.53
0.5% N ₂ Concentration										
bd18	17870	35.03	4.29	.43	33.00	33.08	33.00	33.11	33.11	6.27
bd22	21920	35.08	2.29	.53	32.73	32.85	32.82	32.90	32.85	7.76
bd26	26160	34.99	3.95	.50	32.20	32.26	32.23	32.38	32.29	9.19
bd30	30220	35.07	3.72	.48	31.85	31.97	31.94	32.04	31.97	10.63
1.0% N ₂ Concentration										
bd18	17930	34.96	3.37	.46	32.75	32.80	32.69	32.80	32.83	6.31
bd22	22200	35.04	4.36	.51	32.48	32.51	32.48	32.57	32.57	7.78
bd26	26300	34.98	3.54	.55	32.02	32.08	32.02	32.14	32.11	9.25
bd30	30270	35.05	3.86	.67	31.72	31.78	31.69	31.81	31.78	10.63
2.0% N ₂ Concentration										
bd18	18100	34.92	3.76	.63	32.35	32.26	32.15	32.26	32.37	6.36
bd22	21880	35.02	1.49	.74	32.10	32.07	31.93	32.10	32.13	7.75
bd26	26200	35.06	3.81	.76	31.74	31.71	31.59	31.74	31.74	9.20
bd30	30360	35.07	3.88	.82	31.34	31.34	31.25	31.34	31.40	10.65
5.0% N ₂ Concentration										
bd18a	18140	34.98	4.15	1.35	31.21	30.84	30.56	30.73	30.96	6.33
bd22a	22090	35.02	3.46	1.33	30.81	30.46	30.23	30.40	30.61	7.74
bd26	26160	35.04	2.80	1.38	30.45	30.17	29.90	30.08	30.23	9.19
bd30a	30420	34.97	3.59	1.46	29.98	29.66	29.45	29.63	29.79	10.64

Table B.14: Water-side data for the G-SC geometry with non-condensable gas contamination in HCFC-123 condensation

run	q W	$T_{bulk,in}$ °C	$T_{bulk,out}$ °C	LMTD °C	\dot{m}_{bulk} kg/min	\dot{m}_{tube} kg/min	Re	$\frac{h_i}{m^2 K}$
0% N ₂ Concentration, Run 1								
bd18	17730	28.26	30.23	5.82	129.28	5.17	9610	6380
bd24	23780	27.37	29.35	6.68	172.19	6.89	12560	7950
bd30	29970	26.49	28.48	7.56	215.51	8.62	15410	9420
bd36	36110	25.47	27.53	8.60	252.02	10.08	17630	10570
0% N ₂ Concentration, Run 2								
bd16	15850	28.85	30.67	5.19	125.25	5.01	9420	6250
bd18	17950	28.25	30.24	5.78	129.92	5.20	9660	6400
bd20	19990	28.03	30.00	5.98	145.38	5.82	10760	6990
bd22	21930	27.74	29.74	6.27	157.76	6.31	11600	7440
bd24	24000	27.47	29.45	6.55	173.24	6.93	12660	7990
bd26	25950	27.20	29.19	6.83	187.47	7.50	13620	8490
bd28	28150	26.83	28.83	7.20	201.59	8.06	14530	8970
bd30	30190	26.68	28.68	7.41	216.03	8.64	15520	9460
bd32	32240	26.33	28.33	7.68	231.78	9.27	16520	9970
bd34	34450	25.92	27.95	8.03	243.31	9.73	17190	10320
bd36	36350	25.56	27.62	8.49	253.06	10.12	17740	10620
0.5% N ₂ Concentration								
bd18	17740	27.86	29.83	6.17	129.99	5.20	8590	5340
bd22	21850	27.35	29.34	6.74	157.86	6.31	10320	6210
bd26	26120	26.59	28.59	7.41	186.96	7.48	12020	7050
bd30	30250	26.11	28.12	7.97	215.52	8.62	13710	7860
1.0% N ₂ Concentration								
bd18	17840	27.55	29.52	6.42	130.03	5.20	8540	5320
bd22	22250	26.97	29.00	7.06	157.74	6.31	10230	6180
bd26	26250	26.40	28.40	7.59	187.71	7.51	12020	7060
bd30	30550	25.84	27.88	8.21	215.47	8.62	13630	7840
2.0% N ₂ Concentration								
bd18	17980	26.99	28.99	6.93	129.19	5.17	8380	5270
bd22	21770	26.66	28.64	7.38	157.69	6.31	10150	6160
bd26	26210	26.07	28.07	8.02	188.27	7.53	11960	7050
bd30	30700	25.38	27.44	8.69	214.61	8.58	13430	7780
5.0% N ₂ Concentration								
bd18a	18190	25.58	27.60	8.41	129.60	5.18	8150	5200
bd22a	22050	25.06	27.07	8.99	157.84	6.31	9800	6060
bd26	26210	24.55	26.56	9.53	188.11	7.52	11550	6930
bd30a	30730	23.80	25.84	10.19	215.84	8.63	13020	7680

Table B.15: Row data for the G-SC geometry with non-condensable gas contamination in HCFC-123 condensation

run	row 1		row 2		row 3		row 4		row 5	
	$T_{w,out}$ °C	q'' W/m ²								
0% N ₂ Concentration, Run 1										
bd18	30.21	19670	30.24	19970	30.11	18660	30.27	20270	30.17	19260
bd24	29.30	25930	29.34	26460	29.24	25130	29.37	26860	29.27	25530
bd30	28.44	32790	28.45	32950	28.34	31110	28.47	33290	28.36	31450
bd36	27.46	38930	27.49	39520	27.40	37760	27.52	40100	27.41	37950
0% N ₂ Concentration, Run 2										
bd16	30.64	17400	30.66	17600	30.53	16330	30.68	17790	30.60	17010
bd18	30.19	19560	30.22	19860	30.09	18550	30.25	20170	30.15	19160
bd20	29.93	21440	29.99	22120	29.88	20880	30.02	22450	29.92	21330
bd22	29.68	23750	29.71	24120	29.62	23020	29.75	24610	29.64	23260
bd24	29.40	25950	29.44	26490	29.35	25280	29.46	26760	29.36	25410
bd26	29.13	28080	29.17	28670	29.08	27360	29.19	28960	29.09	27500
bd28	28.77	30510	28.80	30980	28.72	29730	28.82	31290	28.72	29730
bd30	28.62	32700	28.65	33200	28.56	31690	28.67	33540	28.57	31860
bd32	28.27	35080	28.28	35260	28.21	34000	28.30	35620	28.20	33820
bd34	27.89	37210	27.91	37580	27.82	35880	27.92	37770	27.82	35880
bd36	27.56	39290	27.58	39680	27.50	38110	27.60	40070	27.50	38110
0.5% N ₂ Concentration										
bd18	29.71	18610	29.74	18910	29.71	18610	29.75	19020	29.75	19020
bd22	29.21	22850	29.25	23340	29.24	23220	29.27	23580	29.25	23340
bd26	28.46	27200	28.48	27500	28.47	27350	28.52	28080	28.49	27640
bd30	27.97	31190	28.01	31860	28.00	31700	28.03	32200	28.01	31860
1.0% N ₂ Concentration										
bd18	29.41	18820	29.43	19020	29.39	18620	29.43	19020	29.44	19120
bd22	28.87	23320	28.88	23440	28.87	23320	28.90	23690	28.90	23690
bd26	28.27	27310	28.29	27610	28.27	27310	28.31	27900	28.30	27750
bd30	27.74	31860	27.76	32190	27.73	31690	27.77	32360	27.76	32190
2.0% N ₂ Concentration										
bd18	28.90	19200	28.87	18900	28.83	18500	28.87	18900	28.91	19300
bd22	28.53	22950	28.52	22820	28.47	22210	28.53	22950	28.54	23070
bd26	27.95	27540	27.94	27400	27.90	26810	27.95	27540	27.95	27540
bd30	27.30	32070	27.30	32070	27.27	31560	27.30	32070	27.32	32400
5.0% N ₂ Concentration										
bd18a	27.57	19970	27.44	18660	27.34	17650	27.40	18250	27.48	19060
bd22a	27.01	23950	26.89	22480	26.81	21500	26.87	22230	26.94	23090
bd26	26.48	28250	26.39	26940	26.30	25620	26.36	26500	26.41	27230
bd30a	25.76	32920	25.66	31240	25.59	30070	25.65	31080	25.70	31920

Table B.16: Shell-side heat transfer coefficients and uncertainties for the G-SC geometry with non-condensable gas contamination in HCFC-123 condensation

run	bundle				row 1		row 2		row 3		row 4		row 5	
	q''	q'	h_o	w										
	W/m ²	W/m	$\frac{W}{m^2 K}$	± %										
0% N ₂ Concentration, Run 1														
bd18	20030	1240	13060	14.	12100	14.	12920	15.	9860	12.	13830	16.	11120	13.
bd24	26770	1660	12950	11.	11560	11.	12420	11.	10420	10.	13130	12.	10970	10.
bd30	33530	2080	12650	8.	11780	9.	11970	9.	10120	8.	12350	9.	10420	8.
bd36	40290	2490	12060	7.	10960	7.	11420	8.	10110	7.	11910	8.	10250	7.
0% N ₂ Concentration, Run 2														
bd16	17820	1100	13790	16.	12440	16.	13080	17.	9670	14.	13760	18.	11310	15.
bd18	20130	1250	13640	14.	12070	14.	12890	15.	9830	12.	13810	16.	11090	13.
bd20	22410	1390	14090	13.	11810	13.	13390	14.	10700	12.	14300	15.	11580	13.
bd22	24550	1520	14100	12.	12380	12.	13140	13.	11040	11.	14260	14.	11460	12.
bd24	26860	1660	13790	11.	12200	11.	13150	12.	11150	11.	13660	12.	11350	11.
bd26	29000	1790	13560	10.	12120	11.	13020	11.	11120	10.	13500	11.	11310	10.
bd28	31440	1950	13260	9.	11980	10.	12590	10.	11040	9.	13030	10.	11040	9.
bd30	33670	2080	13440	9.	12200	9.	12810	10.	11100	9.	13240	10.	11270	9.
bd32	35900	2220	13280	8.	12310	9.	12500	9.	11220	8.	12900	9.	11060	8.
bd34	38320	2370	13200	8.	12070	8.	12440	9.	10900	8.	12630	9.	10900	8.
bd36	40480	2510	12520	7.	11490	8.	11820	8.	10580	7.	12150	8.	10580	7.
0.5% N ₂ Concentration														
bd18	19890	1230	12140	13.	9360	12.	9940	13.	9360	12.	10140	13.	10140	13.
bd22	24450	1510	12680	11.	9890	11.	10640	11.	10450	11.	11050	11.	10640	11.
bd26	29210	1800	12470	9.	9880	9.	10210	9.	10040	9.	10910	10.	10380	9.
bd30	33780	2090	12480	8.	9800	8.	10420	9.	10260	8.	10750	9.	10420	9.
1.0% N ₂ Concentration														
bd18	19980	1230	10800	12.	8670	11.	8990	11.	8360	11.	8990	11.	9160	12.
bd22	24830	1530	11530	10.	9270	10.	9430	10.	9270	10.	9760	10.	9760	10.
bd26	29360	1810	11720	9.	9350	9.	9650	9.	9350	9.	9960	9.	9800	9.
bd30	33980	2100	11730	8.	9670	8.	9960	8.	9530	8.	10110	8.	9960	8.
2.0% N ₂ Concentration														
bd18	20150	1240	8870	10.	7560	10.	7200	9.	6760	9.	7200	9.	7690	10.
bd22	24380	1510	9600	9.	7970	9.	7850	9.	7270	8.	7970	9.	8100	9.
bd26	29280	1810	10000	8.	8370	8.	8250	8.	7790	8.	8370	8.	8370	8.
bd30	34110	2110	10300	7.	8660	7.	8660	7.	8320	7.	8660	7.	8900	7.
5.0% N ₂ Concentration														
bd18a	20300	1250	5560	6.	5350	7.	4540	7.	4020	6.	4330	6.	4770	7.
bd22a	24660	1520	6150	6.	5730	6.	4960	6.	4500	6.	4840	6.	5260	6.
bd26	29260	1810	6730	5.	6190	6.	5570	6.	5010	6.	5370	6.	5700	6.
bd30a	34160	2110	7220	5.	6630	6.	5910	6.	5460	5.	5850	6.	6190	6.

APPENDIX C. TABULATED HFC-134a INUNDATION DATA

Table C.1: Refrigerant-side data for the 26-fpi tube in HFC-134a inundation

run	quality	quality	T_{sat} °C	inlet	outlet	middle tube $T_{s,o}$					\dot{m} kg/min
	x_{in} %	x_{out} %		sh °C	sc °C	row 1 °C	row 2 °C	row 3 °C	row 4 °C	row 5 °C	
30 Tube Simulation											
af5t100	99.50	83.21	35.04	-41	-.02	33.14	33.19	32.82	33.03	33.19	10.87
af5t83	83.66	67.47	35.03	-35	.02	33.10	33.18	32.81	33.02	33.18	10.87
af5t67	67.54	51.31	35.00	-28	.00	33.11	33.17	32.82	33.01	33.14	10.84
af5t51	51.55	35.48	34.99	-21	.01	33.20	33.18	32.80	32.99	33.12	10.85
af5t35	35.77	19.33	35.05	-10	-.02	33.27	33.22	32.81	33.03	33.16	10.85
af5t19	20.07	3.57	35.02	-.02	-.02	33.14	33.19	32.79	32.98	33.11	10.82
15 Tube Simulation, Run 1											
af5t100	100.00	67.55	34.97	-20	-.15	31.09	30.94	30.23	30.51	30.89	10.80
af5t67	67.96	34.53	35.02	-.05	-.14	31.20	31.06	30.28	30.60	30.86	10.77
af5t35	35.68	2.70	34.99	.04	-.11	31.14	31.06	30.28	30.57	30.80	10.80
15 Tube Simulation, Run 2											
af5t100	99.43	66.71	34.98	-.31	-.04	31.14	30.94	30.30	30.68	30.94	10.87
af5t67	66.90	34.01	34.99	-.16	-.03	31.21	31.04	30.41	30.78	30.95	10.85
af5t35	35.81	2.68	35.07	-.04	-.02	31.20	31.06	30.37	30.74	30.94	10.80

Table C.2: Water-side data for the 26-fpi tube in HFC-134a inundation

run	q W	$T_{bulk,in}$ °C	$T_{bulk,out}$ °C	LMTD °C	\dot{m}_{bulk} kg/min	\dot{m}_{tube} kg/min	Re	h_i $\frac{W}{m^2 K}$
30 Tube Simulation								
af5t100	4930	28.54	30.31	5.60	40.04	8.01	14710	9460
af5t83	4900	28.54	30.30	5.60	39.97	7.99	14680	9440
af5t67	4900	28.54	30.30	5.57	39.99	8.00	14690	9450
af5t51	4850	28.58	30.32	5.53	39.99	8.00	14700	9450
af5t35	4960	28.51	30.29	5.64	39.95	7.99	14670	9440
af5t19	4960	28.46	30.24	5.66	39.93	7.99	14640	9430
15 Tube Simulation, Run 1								
af5f100	9930	22.49	25.49	10.97	47.59	9.52	15450	10250
af5f67	10030	22.46	25.49	11.05	47.57	9.51	15440	10250
af5t35	9920	22.50	25.50	11.00	47.51	9.50	15430	10240
15 Tube Simulation, Run 2								
af5f100	9930	22.49	25.49	10.97	47.59	9.52	15450	10250
af5f67	10030	22.46	25.49	11.05	47.57	9.51	15440	10250
af5t35	9920	22.50	25.50	11.00	47.51	9.50	15430	10240

Table C.3: Row data for the 26-fpi tube in HFC-134a inundation.

run	row 1			row 2			row 3			row 4			row 5		
	$T_{w,out}$ °C	q'' W/m ²	Rec												
30 Tube Simulation															
af5t100	30.24	26790	215	30.26	27100	217	30.12	24910	390	30.20	26160	402	30.26	27100	574
af5t83	30.22	26580	692	30.25	27050	695	30.11	24860	843	30.19	26110	856	30.25	27050	1003
af5t67	30.23	26600	1176	30.25	26910	1178	30.12	24880	1303	30.19	25970	1313	30.24	26750	1438
af5t51	30.29	26910	1661	30.28	26750	1659	30.14	24560	1761	30.21	25660	1768	30.26	26440	1871
af5t35	30.27	27660	2143	30.25	27350	2141	30.10	25010	2223	30.18	26260	2230	30.23	27040	2314
af5t19	30.19	27180	2606	30.21	27490	2608	30.06	25150	2663	30.13	26240	2674	30.18	27030	2732
15 Tube Simulation, Run 1															
af5f100	25.45	54940	410	25.40	54010	403	25.15	49350	758	25.25	51220	765	25.38	53640	1121
af5f67	25.47	55850	1376	25.42	54920	1369	25.15	49890	1680	25.26	51940	1689	25.35	53620	1997
af5t35	25.47	55220	2341	25.44	54660	2337	25.17	49640	2595	25.27	51500	2605	25.35	52990	2861
15 Tube Simulation, Run 2															
af5f100	25.45	54940	410	25.40	54010	403	25.15	49350	758	25.25	51220	765	25.38	53640	1121
af5f67	25.47	55850	1376	25.42	54920	1369	25.15	49890	1680	25.26	51940	1689	25.35	53620	1997
af5t35	25.47	55220	2341	25.44	54660	2337	25.17	49640	2595	25.27	51500	2605	25.35	52990	2861

Table C.4: Shell-side heat transfer coefficients and uncertainties for the 26-fpi tube in HFC-134a inundation.

run	bundle				row 1		row 2		row 3		row 4		row 5	
	q'' W/m ²	q' W/m	h_o $\frac{W}{m^2 K}$	w ± %										
30 Tube Simulation														
af5t100	27730	1630	16430	10.	14400	9.	15000	9.	11380	8.	13280	9.	15000	9.
af5t83	27520	1620	16140	10.	14080	9.	14980	9.	11360	8.	13260	9.	14980	9.
af5t67	27540	1620	16410	10.	14370	9.	14980	9.	11560	8.	13250	9.	14670	9.
af5t51	27220	1610	16190	10.	15410	10.	15090	10.	11400	8.	13060	9.	14470	9.
af5t35	27820	1640	16310	10.	15870	10.	15220	9.	11330	8.	13210	9.	14600	9.
af5t19	27810	1640	16120	10.	14740	9.	15360	9.	11440	8.	13070	9.	14440	9.
15 Tube Simulation, Run 1														
af5t100	55870	3300	15120	6.	14340	6.	13580	5.	10480	5.	11600	5.	13290	5.
af5t67	56410	3330	15300	6.	14830	6.	14040	5.	10620	5.	11860	5.	13030	5.
af5t35	55780	3290	15050	6.	14560	6.	14080	5.	10630	5.	11770	5.	12790	5.
15 Tube Simulation, Run 2														
af5t100	55870	3300	15120	6.	14340	6.	13580	5.	10480	5.	11600	5.	13290	5.
af5t67	56410	3330	15300	6.	14830	6.	14040	5.	10620	5.	11860	5.	13030	5.
af5t35	55780	3290	15050	6.	14560	6.	14080	5.	10630	5.	11770	5.	12790	5.

Table C.5: Refrigerant-side data for the 40-fpi tube in HFC-134a inundation

run	quality	quality	T_{sat} °C	inlet	outlet	middle tube $T_{s,o}$					\dot{m} kg/min
	x_{in} %	x_{out} %		sh °C	sc °C	row 1 °C	row 2 °C	row 3 °C	row 4 °C	row 5 °C	
30 Tube Simulation											
ag5t100	99.47	83.31	35.02	-30	-11	33.55	33.31	33.61	33.52	33.46	10.86
ag5t83	83.29	67.14	35.00	-22	-11	33.53	33.29	33.62	33.50	33.44	10.83
ag5t67	67.65	51.59	35.03	-18	-09	33.60	33.27	33.63	33.45	33.36	10.82
ag5t51	51.65	35.77	35.00	-11	-09	33.53	33.20	33.56	33.32	33.17	10.79
ag5t35	35.83	20.22	34.99	-02	-10	33.50	33.20	33.53	33.14	33.05	10.72
ag5t20	22.86	7.63	34.94	.01	-07	33.35	33.12	33.44	32.97	32.91	10.85
15 Tube Simulation											
ag5t100	99.39	66.68	35.06	-24	-11	31.97	31.42	31.84	31.65	31.39	10.85
ag5t67	67.08	35.01	35.04	-08	-11	31.79	31.38	31.76	31.15	31.31	10.84
ag5t35	35.49	4.62	34.96	.05	-10	31.52	31.27	31.59	30.40	31.17	10.86

Table C.6: Water-side data for the 40-fpi tube in HFC-134a inundation

run	q W	$T_{bulk,in}$ °C	$T_{bulk,out}$ °C	LMTD °C	\dot{m}_{bulk} kg/min	\dot{m}_{tube} kg/min	Re	h_i $\frac{W}{m^2 K}$
30 Tube Simulation								
ag5t100	4890	28.51	30.26	5.65	40.03	8.01	13390	7580
ag5t83	4880	28.49	30.24	5.65	40.01	8.00	13380	7580
ag5t67	4840	28.50	30.24	5.68	40.02	8.00	13380	7580
ag5t51	4770	28.49	30.20	5.70	40.00	8.00	13370	7580
ag5t35	4660	28.52	30.19	5.69	40.00	8.00	13370	7580
ag5t20	4590	28.46	30.11	5.71	40.00	8.00	13350	7570
15 Tube Simulation								
ag5t100	9890	22.59	25.54	11.05	48.05	9.61	14240	8300
ag5t67	9700	22.60	25.50	11.03	47.97	9.59	14210	8280
ag5t35	9360	22.62	25.42	10.95	47.97	9.59	14200	8280

Table C.7: Row data for the 40-fpi tube in HFC-134a inundation.

run	row 1			row 2			row 3			row 4			row 5		
	$T_{w,out}$ °C	q'' W/m ²	Re_c												
30 Tube Simulation															
ag5t100	30.19	26320	213	30.11	25070	204	30.21	26630	403	30.18	26160	390	30.16	25850	577
ag5t83	30.17	26310	700	30.09	25060	691	30.20	26770	866	30.16	26150	852	30.14	25840	1017
ag5t67	30.20	26620	1172	30.09	24910	1159	30.21	26780	1315	30.15	25850	1296	30.12	25380	1440
ag5t51	30.17	26300	1646	30.06	24590	1633	30.18	26450	1763	30.10	25210	1741	30.05	24430	1858
ag5t35	30.18	25990	2105	30.08	24430	2094	30.19	26140	2197	30.06	24120	2170	30.03	23650	2265
ag5t20	30.09	25520	2514	30.01	24280	2505	30.12	25990	2584	29.96	23500	2556	29.94	23190	2629
15 Tube Simulation															
ag5t100	25.49	54230	426	25.32	51050	402	25.45	53480	807	25.39	52360	776	25.31	50860	1149
ag5t67	25.45	53020	1390	25.32	50590	1372	25.44	52830	1718	25.25	49280	1674	25.30	50220	2009
ag5t35	25.38	51340	2330	25.30	49840	2319	25.40	51710	2602	25.03	44800	2539	25.27	49280	2842

Table C.8: Shell-side heat transfer coefficients and uncertainties for the 40-fpi tube in HFC-134a inundation.

run	bundle				row 1		row 2		row 3		row 4		row 5	
	q'' W/m ²	q' W/m	h_o $\frac{W}{m^2 K}$	w ± %										
30 Tube Simulation														
ag5t100	27250	1610	22010	14.	18420	12.	15010	11.	19460	13.	17930	12.	17010	12.
ag5t83	27240	1610	21950	14.	18370	12.	14980	11.	19960	13.	17880	12.	16970	12.
ag5t67	27090	1610	21000	13.	19150	12.	14470	10.	19690	13.	16770	11.	15550	11.
ag5t51	26610	1580	19520	13.	18350	12.	13930	10.	18860	12.	15330	11.	13610	10.
ag5t35	25990	1540	17960	12.	17840	12.	13890	10.	18330	12.	13260	10.	12390	10.
ag5t20	25680	1530	17000	12.	16460	11.	13550	10.	17800	12.	12100	9.	11580	9.
15 Tube Simulation														
ag5t100	55160	3280	19220	7.	17890	7.	14250	6.	16920	7.	15610	7.	14080	6.
ag5t67	54140	3210	17990	7.	16600	7.	13990	6.	16370	7.	12830	6.	13650	6.
ag5t35	52270	3100	16180	7.	15180	6.	13690	6.	15590	7.	9920	5.	13180	6.

Table C.9: Refrigerant-side data for the Tu-Cii in HFC-134a inundation

run	quality	quality	T_{sat} °C	inlet	outlet	middle tube $T_{s,o}$					\dot{m} kg/min
	x_{in} %	x_{out} %		sh °C	sc °C	row 1 °C	row 2 °C	row 3 °C	row 4 °C	row 5 °C	
30 Tube Simulation											
ac5t100	100.00	83.03	35.02	-30	-14	34.35	34.53	34.33	34.17	34.33	10.87
ac5t83	83.05	66.02	35.02	-22	-11	34.21	34.44	34.29	34.08	34.19	10.83
ac5t66	66.29	50.06	34.98	-18	-09	34.06	34.24	34.19	33.91	33.86	10.88
ac5t50	50.59	34.58	35.02	-10	-10	34.12	34.19	34.14	33.93	33.62	10.84
ac5t35	35.66	19.91	35.02	-02	-10	34.07	34.15	34.13	33.63	33.53	10.82
ac5t20	21.41	5.56	35.00	.02	-08	33.82	34.13	34.08	33.40	33.61	10.48
15 Tube Simulation											
ac5t100	99.92	67.05	35.03	-24	-13	33.66	33.82	33.42	33.10	33.31	10.84
ac5t67	67.70	36.52	35.00	-07	-14	33.44	33.41	33.28	32.72	32.39	10.80
ac5t37	37.08	7.33	35.00	.04	-12	33.18	33.15	33.02	32.16	31.84	10.80

Table C.10: Water-side data for the Tu-Cii in HFC-134a inundation

run	q W	$T_{bulk,in}$ °C	$T_{bulk,out}$ °C	LMTD °C	\dot{m}_{bulk} kg/min	\dot{m}_{tube} kg/min	Re	h_i $\frac{W}{m^2 K}$
30 Tube Simulation								
ac5t100	5220	30.02	31.68	4.13	45.02	9.00	15840	10340
ac5t83	5140	30.00	31.65	4.16	44.98	9.00	15820	10330
ac5t66	4920	29.99	31.56	4.21	44.97	8.99	15800	10330
ac5t50	4830	29.99	31.53	4.30	45.02	9.00	15810	10330
ac5t35	4750	29.99	31.51	4.31	45.01	9.00	15810	10330
ac5t20	4620	30.03	31.50	4.25	45.00	9.00	15810	10330
15 Tube Simulation								
ac5t100	9950	25.51	28.52	8.00	47.54	9.51	15380	10390
ac5t67	9390	25.53	28.37	8.14	47.54	9.51	15360	10380
ac5t37	8950	25.51	28.21	8.27	47.51	9.50	15310	10360

Table C.11: Row data for the Tu-Cii in HFC-134a inundation.

run	row 1			row 2			row 3			row 4			row 5		
	$T_{w,out}$ °C	q'' W/m ²	Rec												
30 Tube Simulation															
ac5t100	31.68	29250	219	31.75	30470	229	31.67	29070	427	31.61	28020	428	31.67	29070	624
ac5t83	31.62	28350	723	31.71	29920	734	31.65	28870	904	31.57	27470	904	31.61	28170	1070
ac5t66	31.55	27470	1224	31.62	28690	1234	31.60	28340	1376	31.49	26420	1370	31.47	26070	1503
ac5t50	31.57	27850	1697	31.60	28370	1701	31.58	28020	1823	31.50	26620	1816	31.38	24520	1916
ac5t35	31.56	27490	2140	31.59	28020	2144	31.58	27840	2243	31.39	24510	2221	31.35	23810	2310
ac5t20	31.48	25560	2479	31.60	27660	2495	31.58	27310	2560	31.32	22760	2541	31.40	24160	2614
15 Tube Simulation															
ac5t100	28.52	55670	421	28.58	56780	429	28.43	54010	806	28.31	51790	797	28.39	53270	1166
ac5t67	28.45	54010	1374	28.44	53830	1373	28.39	52900	1703	28.18	49020	1673	28.06	46800	1970
ac5t37	28.34	52310	2280	28.33	52130	2279	28.28	51200	2551	27.96	45290	2505	27.84	43070	2747

Table C.12: Shell-side heat transfer coefficients and uncertainties for the Tu-Cii in HFC-134a inundation.

run	bundle				row 1		row 2		row 3		row 4		row 5	
	q'' W/m ²	q' W/m	h_o $\frac{W}{m^2 K}$	w ± %										
30 Tube Simulation														
ac5t100	29070	1720	45530	23.	47040	24.	69890	34.	44840	23.	34700	19.	44840	23.
ac5t83	28870	1710	42280	22.	37180	20.	57140	28.	42280	22.	30700	17.	35710	19.
ac5t66	27470	1630	31950	18.	31590	17.	41940	22.	38450	20.	25680	15.	24100	14.
ac5t50	26970	1600	27440	16.	32360	18.	36330	19.	33600	18.	25450	15.	17990	12.
ac5t35	26620	1580	25680	15.	30400	17.	33970	18.	32710	18.	18110	12.	16310	11.
ac5t20	25730	1530	23290	14.	22390	14.	33580	18.	31150	17.	14550	11.	17860	12.
15 Tube Simulation														
ac5t100	55670	3310	43070	13.	43070	13.	50330	15.	35090	11.	27730	10.	32310	11.
ac5t67	52530	3110	30740	10.	36250	12.	35470	12.	31980	11.	21990	8.	18300	7.
ac5t37	49910	2960	23670	8.	29840	10.	29280	10.	26710	9.	16220	7.	13800	6.

Table C.13: Refrigerant-side data for the G-SC in HFC-134a inundation

run	quality	quality	T_{sat} °C	inlet		middle tube $T_{s,o}$					\dot{m} kg/min
	x_{in} %	x_{out} %		sh °C	sc °C	row 1 °C	row 2 °C	row 3 °C	row 4 °C	row 5 °C	
30 Tube Simulation, Run 1											
ad5t100	99.61	83.17	34.97	-31	-12	33.41	33.58	33.38	33.67	33.44	10.84
ad5t83	83.33	66.98	34.99	-21	-10	33.20	33.53	33.39	33.65	33.39	10.82
ad5t67	67.27	50.98	35.01	-17	-10	33.24	33.50	33.38	33.61	33.30	10.81
ad5t51	51.26	35.15	35.00	-11	-08	33.24	33.47	33.36	33.52	33.27	10.79
ad5t35	35.56	19.55	35.00	-01	-10	33.22	33.48	33.31	33.42	33.17	10.73
ad5t19	19.87	4.02	34.99	.04	-09	33.14	33.42	33.25	33.28	33.05	10.81
30 Run Simulation, Run 2											
ad5t100	99.47	83.01	35.01	-35	-07	33.40	33.54	33.37	33.63	33.40	10.85
ad5t83	83.60	67.36	35.00	-27	-05	33.37	33.49	33.35	33.60	33.32	10.84
ad5t67	67.69	51.48	35.02	-20	-06	33.34	33.48	33.34	33.59	33.28	10.83
ad5t51	51.73	35.72	34.97	-12	-07	33.13	33.41	33.30	33.50	33.21	10.77
ad5t35	35.66	19.86	34.92	-06	-05	33.10	33.32	33.21	33.30	33.04	10.78
ad5t20	21.92	5.89	35.00	-01	-04	32.80	33.39	33.19	33.28	33.05	10.57
15 Tube Simulation											
ad5t100	99.56	67.06	34.99	-33	-01	31.53	31.74	31.47	31.98	31.44	10.84
ad5t67	67.64	35.57	35.00	-19	.01	31.41	31.62	31.41	31.77	31.14	10.83
ad5t35	35.84	4.37	34.96	-06	.00	31.18	31.54	31.27	31.39	30.88	10.81

Table C.14: Water-side data for the G-SC in HFC-134a inundation

run	q W	$T_{butk,in}$ °C	$T_{butk,out}$ °C	LMTD °C	\dot{m}_{butk} kg/min	\dot{m}_{tube} kg/min	Re	$\frac{h_1}{W}$ $\frac{W}{m^2 K}$
30 Tube Simulation, Run 1								
ad5t100	4970	28.47	30.25	5.58	40.04	8.01	14930	9060
ad5t83	4930	28.48	30.25	5.60	40.03	8.01	14920	9060
ad5t67	4910	28.47	30.23	5.65	40.03	8.01	14920	9050
ad5t51	4850	28.47	30.21	5.65	40.02	8.00	14910	9050
ad5t35	4780	28.51	30.23	5.64	39.98	8.00	14910	9050
ad5t19	4770	28.42	30.14	5.72	40.00	8.00	14890	9040
30 Run Simulation, Run 2								
ad5t100	4970	28.43	30.21	5.66	40.04	8.01	14910	9050
ad5t83	4900	28.46	30.22	5.64	40.04	8.01	14920	9060
ad5t67	4880	28.45	30.20	5.69	40.00	8.00	14900	9050
ad5t51	4800	28.47	30.20	5.63	39.99	8.00	14900	9050
ad5t35	4740	28.41	30.11	5.66	39.93	7.99	14850	9030
ad5t20	4710	28.47	30.17	5.68	39.92	7.98	14870	9030
15 Tube Simulation								
ad5t100	9820	22.69	25.62	10.81	48.04	9.61	15910	9920
ad5t67	9670	22.65	25.55	10.90	48.03	9.61	15890	9910
ad5t35	9470	22.64	25.47	10.92	48.05	9.61	15880	9910

Table C.15: Row data for the G-SC in HFC-134a inundation.

run	row 1			row 2			row 3			row 4			row 5		
	$T_{w,out}$ °C	q'' W/m ²	Re_c												
30 Tube Simulation, Run 1															
ad5t100	30.21	27190	216	30.27	28120	223	30.20	27040	409	30.30	28590	427	30.22	27350	594
ad5t83	30.14	25940	696	30.26	27810	710	30.21	27030	865	30.30	28430	888	30.21	27030	1025
ad5t67	30.15	26250	1180	30.24	27650	1191	30.20	27030	1325	30.28	28270	1344	30.17	26560	1459
ad5t51	30.15	26250	1658	30.23	27490	1667	30.19	26870	1778	30.25	27800	1793	30.16	26400	1888
ad5t35	30.17	25910	2115	30.26	27310	2126	30.20	26380	2208	30.24	27000	2223	30.15	25600	2291
ad5t19	30.08	25920	2601	30.18	27470	2612	30.12	26540	2671	30.13	26700	2683	30.05	25460	2729
30 Run Simulation, Run 2															
ad5t100	30.18	27350	222	30.23	28120	227	30.17	27190	415	30.26	28590	431	30.18	27350	601
ad5t83	30.19	27040	697	30.23	27660	702	30.18	26880	865	30.27	28280	880	30.17	26730	1023
ad5t67	30.17	26850	1174	30.22	27630	1180	30.17	26850	1318	30.26	28250	1334	30.15	26540	1452
ad5t51	30.11	25610	1636	30.21	27160	1648	30.17	26540	1754	30.24	27620	1773	30.14	26070	1862
ad5t35	30.06	25720	2118	30.14	26960	2127	30.10	26340	2210	30.13	26810	2222	30.04	25410	2291
ad5t20	30.00	23700	2471	30.21	26960	2495	30.14	25870	2542	30.17	26340	2569	30.09	25100	2604
15 Tube Simulation															
ad5t100	25.58	53890	419	25.65	55200	429	25.56	53520	801	25.73	56690	834	25.55	53330	1163
ad5t67	25.52	53320	1375	25.59	54630	1385	25.52	53320	1708	25.64	55560	1734	25.43	51640	2011
ad5t35	25.43	52040	2317	25.55	54280	2334	25.46	52600	2597	25.50	53340	2619	25.33	50170	2845

Table C.16: Shell-side heat transfer coefficients and uncertainties for the G-SC in HFC-134a inundation.

run	bundle				row 1		row 2		row 3		row 4		row 5	
	q'' W/m ²	q' W/m	h_o W/m ² K	w ± %										
30 Tube Simulation, Run 1														
ad5t100	27660	1640	19630	12.	18070	11.	21100	13.	17630	11.	22930	13.	18530	11.
ad5t83	27500	1630	18960	12.	14850	10.	19830	12.	17480	11.	22070	13.	17480	11.
ad5t67	27340	1620	18110	11.	15260	10.	18910	12.	17140	11.	20990	12.	15980	10.
ad5t51	27020	1610	17320	11.	15320	10.	18530	11.	16810	11.	19490	12.	15670	10.
ad5t35	26690	1590	16850	11.	14920	10.	18470	11.	15980	10.	17570	11.	14270	10.
ad5t19	26700	1590	16090	11.	14300	10.	18010	11.	15640	10.	16000	10.	13410	9.
30 Run Simulation, Run 2														
ad5t100	27660	1640	18550	11.	17560	11.	19890	12.	17140	11.	21520	13.	17560	11.
ad5t83	27350	1620	18150	11.	17180	11.	18960	12.	16780	11.	21040	12.	16390	11.
ad5t67	27160	1610	17260	11.	16360	10.	18450	11.	16360	10.	20420	12.	15630	10.
ad5t51	26850	1600	17230	11.	14250	10.	17980	11.	16330	11.	19390	12.	15230	10.
ad5t35	26340	1570	15930	11.	14470	10.	17410	11.	15840	10.	17000	11.	13850	10.
ad5t20	26340	1570	15700	10.	10950	8.	17240	11.	14670	10.	15700	10.	13160	9.
15 Tube Simulation														
ad5t100	54640	3250	16680	6.	15860	6.	17340	7.	15470	6.	19300	7.	15280	6.
ad5t67	54070	3220	15840	6.	15120	6.	16490	6.	15120	6.	17590	7.	13580	6.
ad5t35	52790	3140	14670	6.	13990	6.	16190	6.	14500	6.	15220	6.	12460	5.

APPENDIX D. TABULATED HCFC-123 SHEAR AND INUNDATION DATA

Table D.1: Refrigerant-side data for the 26-fpi tube in HCFC-123 inundation

run	quality	quality	T_{sat} °C	inlet	outlet	middle tube $T_{s,o}$					\dot{m} kg/min
	x_{in} %	x_{out} %		sh °C	sc °C	row 1 °C	row 2 °C	row 3 °C	row 4 °C	row 5 °C	
Velocity 1											
BA96V26	96.35	78.24	35.05	.12	-3.30	33.85	33.87	33.52	33.70	33.77	6.12
BA79V26	79.32	61.42	35.01	.14	-.25	33.80	33.77	33.47	33.62	33.70	6.11
BA61V26	61.36	43.61	34.95	.15	-.21	33.72	33.75	33.45	33.57	33.65	6.13
BA43V26	43.90	25.89	35.03	.16	-.20	33.70	33.83	33.47	33.62	33.70	6.12
BA25V26	25.39	7.89	35.02	.11	-.16	33.64	33.74	33.31	33.36	33.59	6.13
Velocity 2											
BA98V35	98.29	79.96	34.94	.01	-.95	33.00	33.08	32.66	32.87	33.02	8.20
BA80V35	80.32	62.00	34.96	.05	-.22	33.03	33.08	32.66	32.85	32.98	8.18
BA62V35	62.70	44.42	34.97	.09	-.20	32.94	33.10	32.66	32.81	32.94	8.20
BA44V35	44.58	26.50	35.04	.11	-.19	33.03	33.10	32.61	32.71	32.87	8.20
BA26V35	26.32	9.24	34.98	.09	-.15	32.87	32.93	32.09	32.01	32.64	8.19
Velocity 3											
BA97V43	97.74	79.25	35.06	-.10	-.37	32.44	32.47	32.01	32.25	32.44	10.25
BA79V43	79.89	61.89	34.93	-.05	-.18	32.33	32.42	31.93	32.17	32.33	10.27
BA61V43	61.49	43.36	34.96	.02	-.19	32.23	32.37	31.88	32.10	32.23	10.24
BA43V43	43.72	25.64	35.01	.06	-.18	32.39	32.39	31.82	31.93	32.12	10.25
BA25V43	25.65	9.06	35.02	.04	-.13	32.30	32.13	30.97	31.02	31.92	10.25

Table D.2: Water-side data for the 26-fpi tube in HCFC-123 inundation

run	q W	$T_{bulk,in}$ °C	$T_{bulk,out}$ °C	LMTD °C	\dot{m}_{bulk} kg/min	\dot{m}_{tube} kg/min	Re	h_i $\frac{W}{m^2 K}$
Velocity 1								
BA96V26	3130	29.98	31.50	4.29	29.77	5.95	11250	7560
BA79V26	3090	29.97	31.48	4.26	29.73	5.95	11230	7550
BA61V26	3080	29.97	31.47	4.21	29.76	5.95	11240	7560
BA43V26	3100	30.00	31.52	4.26	29.72	5.94	11240	7550
BA25V26	3000	29.99	31.46	4.28	29.72	5.94	11230	7550
Velocity 2								
BA98V35	4300	28.48	30.26	5.55	35.09	7.02	12870	8500
BA80V35	4300	28.47	30.24	5.59	35.10	7.02	12870	8500
BA62V35	4280	28.47	30.23	5.62	35.09	7.02	12870	8500
BA44V35	4210	28.52	30.26	5.65	35.07	7.01	12870	8500
BA26V35	3940	28.47	30.09	5.69	35.11	7.02	12860	8500
Velocity 3								
BA97V43	5500	27.23	29.21	6.82	40.20	8.04	14380	9370
BA79V43	5400	27.21	29.15	6.74	40.17	8.03	14360	9360
BA61V43	5380	27.19	29.12	6.80	40.18	8.04	14350	9360
BA43V43	5310	27.18	29.09	6.89	40.21	8.04	14360	9360
BA25V43	4830	27.20	28.94	6.92	40.14	8.03	14310	9340

Table D.3: Row data for the 26-fpi tube in HCFC-123 inundation.

run	row 1			row 2			row 3			row 4			row 5		
	$T_{w,out}$ °C	q'' W/m ²	Re_c												
Velocity 1															
BA96V26	31.50	17820	95	31.51	17940	95	31.37	16310	150	31.44	17120	153	31.47	17470	206
BA79V26	31.48	17560	235	31.47	17450	235	31.35	16050	282	31.41	16750	284	31.44	17100	330
BA61V26	31.45	17230	384	31.46	17350	384	31.34	15950	423	31.39	16530	425	31.42	16880	463
BA43V26	31.46	16980	528	31.51	17560	530	31.37	15930	560	31.43	16630	564	31.46	16980	594
BA25V26	31.43	16740	682	31.47	17210	684	31.30	15230	704	31.32	15460	706	31.41	16510	729
Velocity 2															
BA98V35	30.20	23480	104	30.23	23890	106	30.07	21690	178	30.15	22790	183	30.21	23610	255
BA80V35	30.20	23760	305	30.22	24030	306	30.06	21830	369	30.13	22800	374	30.18	23480	436
BA62V35	30.16	23340	500	30.22	24160	503	30.05	21830	555	30.11	22650	560	30.16	23340	612
BA44V35	30.23	23460	703	30.26	23870	704	30.07	21270	745	30.11	21820	749	30.17	22640	791
BA26V35	30.14	22940	903	30.16	23210	904	29.84	18820	926	29.81	18410	926	30.05	21700	959
Velocity 3															
BA97V43	29.15	30040	141	29.16	30200	141	28.99	27520	234	29.08	28940	240	29.15	30040	332
BA79V43	29.09	29550	388	29.12	30020	389	28.94	27190	467	29.03	28600	474	29.09	29550	552
BA61V43	29.04	29080	641	29.09	29870	644	28.91	27040	708	28.99	28300	715	29.04	29080	778
BA43V43	29.09	30050	893	29.09	30050	893	28.88	26740	946	28.92	27370	948	28.99	28470	1003
BA25V43	29.07	29370	1142	29.01	28430	1139	28.58	21670	1164	28.60	21990	1162	28.93	27170	1205

Table D.4: Shell-side heat transfer coefficients and uncertainties for the 26-fpi tube in HCFC-123 inundation.

run	bundle				row 1		row 2		row 3		row 4		row 5	
	q'' W/m ²	q' W/m	h_o $\frac{W}{m^2 K}$	w ± %										
Velocity 1														
BA96V26	17700	1050	15050	19.	15360	19.	15810	20.	10900	15.	13020	17.	14120	18.
BA79V26	17560	1040	14980	19.	14980	19.	14560	19.	10650	15.	12380	17.	13410	18.
BA61V26	17460	1030	15400	20.	14530	19.	14960	19.	10860	16.	12330	17.	13370	18.
BA43V26	17670	1040	15540	20.	13140	17.	15090	19.	10450	15.	12140	17.	13140	17.
BA25V26	17090	1010	13540	18.	12490	17.	13910	18.	9090	14.	9530	14.	11860	16.
Velocity 2														
BA98V35	24440	1500	14110	14.	12300	12.	13060	13.	9620	11.	11160	12.	12550	12.
BA80V35	24310	1490	13610	13.	12550	12.	13070	13.	9640	11.	10960	11.	12070	12.
BA62V35	24160	1480	13280	13.	11730	12.	13210	13.	9560	11.	10670	11.	11730	12.
BA44V35	23870	1470	12620	13.	11900	12.	12620	12.	8870	10.	9520	10.	10620	11.
BA26V35	22250	1370	10080	11.	11060	11.	11480	12.	6550	9.	6230	9.	9370	10.
Velocity 3														
BA97V43	31140	1840	13010	10.	11660	9.	11840	10.	9120	8.	10450	9.	11660	9.
BA79V43	30490	1800	12710	10.	11530	10.	12100	10.	9140	8.	10490	9.	11530	10.
BA61V43	30340	1790	12300	10.	10820	9.	11710	10.	8880	8.	10020	9.	10820	9.
BA43V43	30050	1770	11610	10.	11610	9.	11610	9.	8450	8.	8960	8.	9950	9.
BA25V43	27330	1610	8980	9.	10930	9.	9970	9.	5370	7.	5530	7.	8850	8.

Table D.5: Refrigerant-side data for the 40-fpi tube in HCFC-123 inundation

run	quality	quality	T_{sat} °C	inlet		middle tube $T_{s,o}$					\dot{m} kg/min
	x_{in} %	x_{out} %		sh °C	sc °C	row 1 °C	row 2 °C	row 3 °C	row 4 °C	row 5 °C	
Velocity 1											
BB95V1	95.01	77.60	35.01	.10	-1.26	34.06	33.89	33.98	34.00	33.92	6.09
BB77V1	77.85	60.77	34.96	.12	-.21	33.98	33.84	33.93	33.93	33.84	6.10
BB60V1	60.72	43.52	35.04	.12	-.18	33.99	33.85	33.91	33.88	33.82	6.11
BB43V1	44.23	27.16	35.04	.14	-.18	34.01	33.84	33.87	33.81	33.73	6.11
BB26V1	26.36	10.15	34.98	.12	-.15	33.93	33.76	33.67	33.53	33.37	6.11
Velocity 2											
BB98V2	98.00	79.84	35.00	.00	-.87	33.52	33.29	33.46	33.43	33.26	8.20
BB80V2	80.49	62.59	35.01	.05	-.19	33.49	33.29	33.43	33.40	33.23	8.21
BB62V2	62.26	44.57	34.96	.08	-.19	33.40	33.20	33.29	33.20	33.08	8.22
BB44V2	44.85	27.42	35.04	.10	-.18	33.42	33.25	33.28	33.07	32.96	8.21
BB26V2	26.98	10.38	35.00	.08	-.14	33.33	33.13	33.02	32.61	32.44	8.19
Velocity 3											
BB98V3	97.96	79.62	35.00	-.09	-.42	32.99	32.69	32.90	32.87	32.63	10.35
BB80V3	80.42	62.32	35.02	-.04	-.19	32.97	32.70	32.88	32.79	32.55	10.35
BB62V3	62.83	44.95	34.97	.01	-.20	32.88	32.61	32.70	32.58	32.37	10.32
BB44V3	45.20	27.57	35.05	.07	-.19	32.86	32.62	32.59	32.26	32.17	10.32
BB26V3	27.13	10.73	35.01	.07	-.15	32.72	32.45	32.27	31.52	31.49	10.27

Table D.6: Water-side data for the 40-fpi tube in HCFC-123 inundation

run	q W	$T_{bulk,in}$ °C	$T_{bulk,out}$ °C	LMTD °C	\dot{m}_{bulk} kg/min	\dot{m}_{tube} kg/min	Re	$\frac{h_i}{W}$ $\frac{m^2}{K}$
Velocity 1								
BB95V1	3000	30.15	31.59	4.15	30.33	6.07	10480	6170
BB77V1	2950	30.13	31.55	4.14	30.28	6.06	10450	6160
BB60V1	2970	30.11	31.54	4.23	30.29	6.06	10450	6160
BB43V1	2940	30.10	31.51	4.27	30.27	6.05	10440	6150
BB26V1	2780	30.10	31.44	4.28	30.25	6.05	10430	6150
Velocity 2								
BB98V2	4250	28.59	30.34	5.57	35.01	7.00	11730	6820
BB80V2	4220	28.59	30.33	5.59	35.02	7.00	11730	6820
BB62V2	4160	28.53	30.25	5.62	34.97	6.99	11700	6810
BB44V2	4070	28.59	30.26	5.68	35.00	7.00	11720	6810
BB26V2	3840	28.55	30.13	5.76	34.96	6.99	11680	6800
Velocity 3								
BB98V3	5520	27.17	29.16	6.89	39.81	7.96	12960	7460
BB80V3	5480	27.15	29.14	6.94	39.77	7.95	12950	7450
BB62V3	5370	27.12	29.06	6.94	39.81	7.96	12940	7450
BB44V3	5230	27.13	29.02	7.06	39.78	7.96	12930	7450
BB26V3	4790	27.17	28.91	7.10	39.72	7.94	12900	7430

Table D.7: Row data for the 40-fpi tube in HCFC-123 inundation.

run	row 1			row 2			row 3			row 4			row 5		
	$T_{w,out}$ °C	q'' W/m ²	Rec												
Velocity 1															
BB95V1	31.54	16400	101	31.48	15690	98	31.51	16050	155	31.52	16160	153	31.49	15810	205
BB77V1	31.50	16140	242	31.45	15550	240	31.48	15900	288	31.48	15900	286	31.45	15550	331
BB60V1	31.49	16260	385	31.44	15670	383	31.46	15910	425	31.45	15790	422	31.43	15550	460
BB43V1	31.49	16370	523	31.43	15660	520	31.44	15780	555	31.42	15540	551	31.39	15190	583
BB26V1	31.46	16000	669	31.40	15300	667	31.37	14950	691	31.32	14360	686	31.26	13650	706
Velocity 2															
BB98V2	30.28	23020	106	30.20	21930	102	30.26	22750	184	30.25	22610	180	30.19	21790	255
BB80V2	30.27	22890	301	30.20	21930	298	30.25	22620	369	30.24	22480	365	30.18	21660	430
BB62V2	30.20	22720	504	30.13	21770	501	30.16	22180	560	30.13	21770	555	30.09	21220	610
BB44V2	30.24	22600	698	30.18	21790	695	30.19	21920	744	30.12	20970	737	30.08	20420	781
BB26V2	30.19	22310	894	30.12	21350	890	30.08	20810	926	29.94	18910	915	29.88	18090	946
Velocity 3															
BB98V3	29.10	29890	138	29.00	28340	132	29.07	29430	239	29.06	29270	233	28.98	28030	330
BB80V3	29.08	29860	385	28.99	28470	379	29.05	29400	473	29.02	28930	467	28.94	27700	551
BB62V3	29.03	29580	629	28.94	28190	624	28.97	28650	703	28.93	28030	695	28.86	26950	766
BB44V3	29.03	29410	876	28.95	28170	872	28.94	28010	935	28.83	26310	925	28.80	25850	984
BB26V3	29.01	28430	1121	28.92	27040	1116	28.86	26120	1161	28.61	22250	1142	28.60	22100	1184

Table D.8: Shell-side heat transfer coefficients and uncertainties for the 40-fpi tube in HCFC-123 inundation.

run	bundle				row 1		row 2		row 3		row 4		row 5	
	q'' W/m ²	q' W/m	h_o W/m ² K	w ± %										
Velocity 1														
BB95V1	16990	1010	22070	29.	17970	25.	14470	21.	16070	23.	16670	23.	14980	22.
BB77V1	16730	990	20840	28.	17070	24.	14290	21.	15860	23.	15860	23.	14290	21.
BB60V1	16850	1000	19470	26.	16130	23.	13610	20.	14540	21.	14070	20.	13190	20.
BB43V1	16600	980	17630	24.	16380	23.	13380	20.	13820	20.	12970	19.	11830	18.
BB26V1	15770	930	14580	22.	15620	22.	12800	19.	11670	18.	10080	17.	8560	15.
Velocity 2														
BB98V2	23840	1410	18890	19.	16000	16.	13100	14.	15190	16.	14810	15.	12790	14.
BB80V2	23710	1400	18140	18.	15430	16.	12980	14.	14660	15.	14300	15.	12390	14.
BB62V2	23400	1380	17020	17.	14920	16.	12590	14.	13520	15.	12590	14.	11490	13.
BB44V2	22740	1350	14720	16.	14270	15.	12370	14.	12660	14.	10820	13.	9940	12.
BB26V2	21490	1280	11890	14.	13680	15.	11630	13.	10650	12.	7990	11.	7110	10.
Velocity 3														
BB98V3	30820	1830	17220	14.	15160	12.	12450	11.	14260	12.	13980	12.	12000	11.
BB80V3	30790	1830	16860	13.	14870	12.	12480	11.	14000	12.	13210	11.	11380	10.
BB62V3	30050	1780	15400	13.	14480	12.	12170	11.	12880	11.	11950	11.	10530	10.
BB44V3	29250	1740	13400	12.	13660	11.	11760	10.	11550	10.	9530	9.	9070	9.
BB26V3	26890	1600	10510	10.	12610	11.	10700	10.	9640	9.	6410	8.	6310	8.

Table D.9: Refrigerant-side data for the Tu-Cii in HCFC-123 inundation

run	quality	quality	T_{sat} °C	inlet outlet		middle tube $T_{s,o}$					\dot{m} kg/min
	x_{in} %	x_{out} %		sh °C	sc °C	row 1 °C	row 2 °C	row 3 °C	row 4 °C	row 5 °C	
Velocity 1											
BC93V1	93.04	74.97	35.00	.11	-.42	34.60	34.69	34.48	34.40	34.50	6.08
BC75V1	75.33	57.85	34.99	.12	-.21	34.52	34.64	34.45	34.30	34.42	6.08
BC57V1	57.98	40.88	34.96	.11	-.17	34.35	34.54	34.33	34.16	34.28	6.09
BC40V1	40.94	24.12	35.03	.09	-.14	34.31	34.50	34.26	34.02	34.12	6.08
BC24V1	24.17	8.76	34.96	.09	-.14	34.23	34.38	33.97	33.61	33.68	6.10
Velocity 2											
BC98V2	97.97	80.02	35.01	.00	-.55	34.11	34.43	34.21	34.06	34.18	8.22
BC80V2	80.17	62.76	35.02	.03	-.19	34.10	34.38	34.13	33.93	34.10	8.23
BC62V2	62.78	45.44	35.04	.07	-.18	34.09	34.29	34.07	33.79	33.97	8.24
BC45V2	45.84	29.44	34.96	.09	-.16	33.92	34.12	33.84	33.47	33.60	8.23
BC29V2	29.31	13.88	34.98	.07	-.13	33.88	33.98	33.68	33.16	33.21	8.24
Velocity 3											
BC98V3	97.52	79.31	35.00	-.08	-.38	33.69	34.05	33.84	33.61	33.82	10.38
BC80V3	80.29	62.52	35.02	-.03	-.20	33.80	34.03	33.80	33.49	33.72	10.40
BC62V3	62.83	45.63	34.98	.02	-.21	33.67	33.88	33.60	33.27	33.44	10.39
BC45V3	45.74	29.16	34.97	.07	-.19	33.57	33.67	33.42	32.85	33.13	10.38
BC29V3	29.65	14.19	35.04	.07	-.16	33.43	33.43	33.23	32.41	32.51	10.39

Table D.10: Water-side data for the Tu-Cii in HCFC-123 inundation

run	q W	$T_{bulk,in}$ °C	$T_{bulk,out}$ °C	LMTD °C	\dot{m}_{bulk} kg/min	\dot{m}_{tube} kg/min	Re	h_1 $\frac{W}{m^2 K}$
Velocity 1								
BC93V1	3110	30.94	32.46	3.28	30.06	6.01	10770	7550
BC75V1	3010	31.01	32.47	3.23	30.01	6.00	10760	7540
BC57V1	2940	30.95	32.39	3.27	30.03	6.01	10750	7540
BC40V1	2880	30.96	32.37	3.37	29.97	5.99	10730	7530
BC24V1	2640	30.98	32.27	3.39	29.96	5.99	10720	7520
Velocity 2								
BC98V2	4210	30.00	31.74	4.12	35.02	7.00	12330	8460
BC80V2	4120	30.02	31.73	4.12	35.04	7.01	12340	8470
BC62V2	4090	29.98	31.66	4.21	35.05	7.01	12330	8460
BC45V2	3840	29.98	31.56	4.21	35.03	7.01	12310	8450
BC29V2	3600	29.99	31.48	4.31	35.02	7.00	12290	8450
Velocity 3								
BC98V3	5500	28.89	30.88	5.09	39.86	7.97	13740	9290
BC80V3	5420	28.90	30.86	5.13	39.84	7.97	13730	9290
BC62V3	5200	28.90	30.78	5.14	39.82	7.96	13710	9280
BC45V3	4940	28.87	30.67	5.23	39.84	7.97	13700	9280
BC29V3	4580	28.86	30.52	5.44	39.81	7.96	13670	9270

Table D.11: Row data for the Tu-Cii in HCFC-123 inundation.

run	row 1			row 2			row 3			row 4			row 5		
	$T_{w,out}$ °C	q'' W/m ²	Rec												
Velocity 1															
BC93V1	32.45	17770	122	32.49	18240	124	32.40	17190	179	32.37	16840	179	32.41	17310	234
BC75V1	32.46	17040	266	32.51	17630	268	32.43	16690	314	32.37	15990	313	32.42	16580	359
BC57V1	32.36	16470	407	32.44	17410	411	32.35	16360	447	32.28	15540	447	32.33	16120	484
BC40V1	32.35	16210	547	32.43	17140	550	32.33	15970	578	32.23	14810	577	32.27	15270	605
BC24V1	32.33	15730	685	32.39	16430	688	32.22	14450	704	32.07	12700	700	32.10	13050	717
Velocity 2															
BC98V2	31.65	22480	105	31.78	24250	111	31.69	23020	184	31.63	22210	187	31.68	22890	259
BC80V2	31.66	22360	303	31.77	23860	309	31.67	22490	371	31.59	21400	372	31.66	22360	434
BC62V2	31.63	22500	499	31.71	23590	503	31.62	22360	556	31.51	20860	554	31.58	21820	608
BC45V2	31.56	21530	684	31.64	22620	688	31.53	21120	727	31.38	19080	723	31.43	19760	763
BC29V2	31.55	21250	869	31.59	21800	871	31.47	20160	899	31.26	17300	891	31.28	17570	919
Velocity 3															
BC98V3	30.76	29000	141	30.90	31170	149	30.82	29930	244	30.73	28530	246	30.81	29770	341
BC80V3	30.81	29600	387	30.90	31000	392	30.81	29600	476	30.69	27740	474	30.78	29140	559
BC62V3	30.76	28810	630	30.84	30050	634	30.73	28350	702	30.60	26340	699	30.67	27420	768
BC45V3	30.70	28360	869	30.74	28980	871	30.64	27430	926	30.42	24020	915	30.53	25730	974
BC29V3	30.64	27570	1094	30.64	27570	1094	30.56	26330	1136	30.24	21370	1118	30.28	21990	1160

Table D.12: Shell-side heat transfer coefficients and uncertainties for the Tu-Cii in HCFC-123 inundation.

run	bundle				row 1		row 2		row 3		row 4		row 5	
	q'' W/m ²	q' W/m	h_o $\frac{W}{m^2 K}$	w ± %										
Velocity 1														
BC93V1	17770	1060	51710	62.	50260	61.	71720	84.	35990	45.	30510	39.	38220	47.
BC75V1	17040	1010	41060	52.	40100	51.	58560	71.	33430	43.	24690	33.	31630	41.
BC57V1	16820	1000	34200	44.	29090	38.	47310	58.	27680	37.	20340	29.	25170	34.
BC40V1	16440	970	26380	35.	24090	32.	36100	45.	22120	30.	15280	23.	17550	25.
BC24V1	15040	890	18020	27.	22930	32.	30560	40.	15090	23.	9570	17.	10420	18.
Velocity 2														
BC98V2	23710	1400	37850	35.	26280	26.	46240	42.	30550	29.	24500	24.	29370	28.
BC80V2	23310	1380	34030	32.	25900	26.	40910	37.	26850	26.	20550	21.	25900	26.
BC62V2	22910	1360	27830	27.	25010	25.	33900	31.	24180	24.	17320	19.	21250	22.
BC45V2	21530	1280	21560	22.	21560	22.	28450	28.	19650	21.	13110	16.	14870	17.
BC29V2	20300	1200	16430	18.	20090	21.	22790	23.	15990	18.	9650	13.	10080	13.
Velocity 3														
BC98V3	30860	1830	32540	24.	22980	18.	34790	25.	27080	20.	21290	17.	26320	20.
BC80V3	30380	1810	29150	22.	25240	19.	33060	24.	25240	19.	18670	15.	23290	18.
BC62V3	29120	1730	24190	19.	22940	18.	28690	21.	21240	17.	15740	14.	18390	15.
BC45V3	27900	1650	19410	16.	20870	17.	23110	18.	18110	15.	11500	11.	14280	13.
BC29V3	25710	1530	13660	13.	17570	15.	17570	15.	14810	13.	8190	9.	8770	10.

Table D.13: Refrigerant-side data for the G-SC tube in HCFC-123 inundation

run	quality	quality	T_{sat} °C	inlet		middle tube $T_{s,o}$					\dot{m} kg/min
	x_{in} %	x_{out} %		sh °C	sc °C	row 1 °C	row 2 °C	row 3 °C	row 4 °C	row 5 °C	
Velocity 1											
BD93V1	93.30	75.43	35.04	.10	-.48	33.99	34.07	33.94	34.09	33.96	6.16
BD75V1	75.60	57.82	35.00	.12	-.21	33.90	34.01	33.85	34.01	33.85	6.17
BD58V1	59.05	41.64	34.99	.11	-.17	33.85	33.96	33.80	33.93	33.77	6.16
BD40V1	40.37	23.20	34.99	.11	-.15	33.81	33.92	33.71	33.81	33.60	6.16
bd21v1	21.43	5.26	34.95	.07	-.12	33.70	33.78	33.49	33.41	33.25	6.17
Velocity 2											
bd98v2	98.19	80.12	35.02	.01	-.99	33.49	33.65	33.51	33.70	33.46	8.22
bd80v2	80.50	62.77	35.02	.06	-.22	33.45	33.58	33.45	33.61	33.39	8.25
bd62v2	62.77	45.15	35.03	.09	-.20	33.32	33.54	33.38	33.54	33.27	8.24
bd45v2	45.87	28.80	34.97	.10	-.18	33.28	33.42	33.26	33.34	33.06	8.22
bd28v2	28.95	12.55	34.93	.09	-.14	33.15	33.32	33.02	32.99	32.69	8.24
Velocity 3											
bd98v3	98.12	80.11	35.00	-.10	-.46	32.80	33.11	33.00	33.19	32.88	10.34
bd80v3	80.83	63.18	34.97	-.05	-.19	32.77	33.03	32.88	33.08	32.80	10.32
bd63v3	63.02	45.51	34.99	.01	-.20	32.60	33.00	32.80	33.00	32.66	10.33
bd45v3	46.05	28.80	35.01	.07	-.20	32.50	32.92	32.75	32.84	32.41	10.35
bd29v3	29.85	13.29	35.01	.07	-.16	32.57	32.80	32.46	32.37	31.98	10.32

Table D.14: Water-side data for the G-SC tube in HCFC-123 inundation

run	q W	$T_{bulk,in}$ °C	$T_{bulk,out}$ °C	LMTD °C	\dot{m}_{bulk} kg/min	\dot{m}_{tube} kg/min	Re	$\frac{h_i}{W}$ $\frac{m^2}{K}$
Velocity 1								
BD93V1	3120	30.05	31.55	4.22	30.05	6.01	11560	7300
BD75V1	3100	29.96	31.46	4.27	30.06	6.01	11540	7300
BD58V1	3030	30.00	31.46	4.25	30.02	6.00	11530	7290
BD40V1	2980	29.97	31.41	4.29	30.03	6.01	11520	7290
bd21v1	2790	29.97	31.32	4.33	30.01	6.00	11500	7280
Velocity 2								
bd98v2	4250	28.74	30.49	5.38	35.03	7.01	13130	8160
bd80v2	4210	28.73	30.46	5.40	35.02	7.00	13120	8160
bd62v2	4150	28.74	30.45	5.43	35.02	7.00	13120	8160
bd45v2	3990	28.76	30.40	5.39	34.97	6.99	13100	8150
bd28v2	3820	28.71	30.29	5.46	34.94	6.99	13060	8130
Velocity 3								
bd98v3	5420	27.47	29.43	6.53	39.87	7.97	14570	8940
bd80v3	5340	27.47	29.40	6.52	39.85	7.97	14560	8940
bd63v3	5260	27.47	29.37	6.57	39.80	7.96	14530	8930
bd45v3	5130	27.48	29.34	6.63	39.83	7.97	14540	8930
bd29v3	4870	27.47	29.24	6.72	39.76	7.95	14500	8910

Table D.15: Row data for the G-SC tube in HCFC-123 inundation.

run	row 1			row 2			row 3			row 4			row 5		
	$T_{w,out}$ °C	q'' W/m ²	Re_c												
Velocity 1															
BD93V1	31.53	17260	119	31.56	17610	120	31.51	17030	176	31.57	17720	180	31.52	17140	230
BD75V1	31.44	17260	268	31.48	17730	269	31.42	17030	317	31.48	17730	321	31.42	17030	364
BD58V1	31.44	16890	404	31.48	17360	406	31.42	16660	445	31.47	17240	449	31.41	16540	484
BD40V1	31.42	16780	560	31.46	17250	562	31.38	16310	592	31.42	16780	596	31.34	15850	621
bd21v1	31.37	16300	718	31.40	16650	719	31.29	15370	738	31.26	15020	738	31.20	14320	754
Velocity 2															
bd98v2	30.46	23380	106	30.52	24200	109	30.47	23520	187	30.54	24470	193	30.45	23250	263
bd80v2	30.44	23240	304	30.49	23920	306	30.44	23240	374	30.50	24050	379	30.42	22970	440
bd62v2	30.40	22560	499	30.48	23650	503	30.42	22830	558	30.48	23650	565	30.38	22290	613
bd45v2	30.40	22260	686	30.45	22930	688	30.39	22120	733	30.42	22530	736	30.32	21170	774
bd28v2	30.32	21830	874	30.38	22640	877	30.27	21150	908	30.26	21020	911	30.15	19520	935
Velocity 3															
bd98v3	29.34	28930	132	29.45	30640	139	29.41	30020	236	29.48	31100	246	29.37	29400	332
bd80v3	29.33	28760	374	29.42	30160	379	29.37	29380	463	29.44	30470	472	29.34	28920	546
bd63v3	29.27	27800	621	29.41	29960	629	29.34	28880	696	29.41	29960	707	29.29	28110	764
bd45v3	29.24	27200	858	29.39	29520	867	29.33	28600	921	29.36	29060	930	29.21	26740	973
bd29v3	29.26	27620	1085	29.34	28850	1089	29.22	27000	1130	29.19	26540	1133	29.05	24380	1163

Table D.16: Shell-side heat transfer coefficients and uncertainties for the G-SC tube in HCFC-123 inundation.

run	bundle				row 1		row 2		row 3		row 4		row 5	
	q'' W/m ²	q' W/m	h_o $\frac{W}{m^2 K}$	w ± %										
Velocity 1														
BD93V1	17490	1040	18280	24.	17070	22.	18940	24.	15980	21.	19640	25.	16510	22.
BD75V1	17500	1040	17460	23.	16350	21.	18710	24.	15340	20.	18710	24.	15340	20.
BD58V1	17010	1010	16100	22.	15450	21.	17630	23.	14520	20.	17040	22.	14080	19.
BD40V1	16780	1000	14700	20.	14820	20.	16850	22.	13150	18.	14820	20.	11750	17.
bd21v1	15720	930	11680	17.	13470	19.	14750	20.	10770	16.	9960	15.	8580	14.
Velocity 2														
bd98v2	23790	1410	16980	17.	15750	16.	18370	18.	16140	16.	19400	18.	15360	15.
bd80v2	23510	1390	16030	16.	15260	15.	17300	17.	15260	15.	17750	17.	14550	15.
bd62v2	23240	1380	15240	16.	13560	14.	16420	16.	14200	15.	16420	16.	12960	14.
bd45v2	22260	1330	13580	15.	13580	14.	15300	16.	13270	14.	14230	15.	11370	13.
bd28v2	21420	1280	11800	13.	12610	14.	14480	15.	11300	13.	11070	13.	8850	11.
Velocity 3														
bd98v3	30330	1810	16040	13.	13460	11.	16720	13.	15410	12.	17810	14.	14250	12.
bd80v3	29850	1780	15270	12.	13340	11.	15900	13.	14400	12.	16560	13.	13590	11.
bd63v3	29350	1750	14260	12.	11850	10.	15420	12.	13470	11.	15420	12.	12280	11.
bd45v3	28750	1710	13140	11.	10990	10.	14450	12.	12900	11.	13640	11.	10440	10.
bd29v3	27310	1620	11130	10.	11530	10.	13320	11.	10750	10.	10220	10.	8130	9.